Anal. Method Environ. Chem. J. 3 (2) (2020) 5-20

AMECJ

Research Article, Issue 2
Analytical Methods in Environmental Chemistry Journal
Journal home page: www.amecj.com/ir

Determination and prediction of peptide mobilities by micellar electro-kinetic chromatography using adaptive neuro-fuzzy inference system as a feature selection method

Mostafa Hassanisadi [a,*], Morteza G. Khaledi [b] and Mehdi Jalali-Heravi [c]

[a]*Nanotechnology Research Center, Research Institute of Petroleum Industry, Tehran, Iran.*
[b]*Department of Chemistry, Sharif University of Technology, P.O.Box9516-11365, Tehran, Iran*
[c]*Department of Chemistry, North Carolina State University, NC8204-27695, USA*

ARTICLE INFO:

Received 5 Mar 2020
Revised form 28 Apr 2020
Accepted 27 May 2020
Available online 28 Jun 2020

Keywords:
Peptide mobilities,
Micellar ElectroKinetic Chromatography,
Artificial neural networks,
Adaptive neuro-fuzzy inference system

ABSTRACT

Mobility of 128 peptides composed of up to 14 amino acids is determined for sodium dodecyl sulfate (SDS) micellar systems using micellar electrokinetic chromatography (MEKC). The mobilities of these peptides are predicted using back propagation of error artificial neural networks (BP-ANNs). Adaptive neuro-fuzzy inference system (ANFIS) which can deal with linear and nonlinear phenomena is used to select the inputs of BP-ANN. A 3:4:1 BP-ANN model with four variables of Kappa substituent constant, Kappa(H), number of peptide bonds, (lnN), molar refractivity of C-terminal, MRC, and steric effects at N-terminal, ES,N, which incorporate substituent, steric and molar refractivity effects as its inputs was developed. Comparison of Multiple Linear Regression (MLR) and ANN results shows the nonlinear characteristic of the phenomena. The nonlinear model was successful in predicting the mobilities of 120 peptides except for the ones (8 peptides) with negatively charged amino acids. It is shown that that most outlier peptides contain middle glutamic acid (E) and aspartic acid (D) amino acids and their mobilities follow a similar mechanism in MEKC.

1. Introduction

Micellar electrokinetic chromatography (MEKC) is a widely used technique in capillary electrophoresis (CE) and is capable of separating neutral compounds as well as charged solutes by including a pseudo-stationary phase [1-6]. This technique has great utility in separating mixtures that contain both ionic and neutral species, and has become a valuable tool in separating very hydrophobic pharmaceuticals from their very polar metabolites. The creation of the pseudo-stationary phase is most easily achieved using micelles of surfactants and depending on the hydrophobicity, analytes partition between these micelles and the mobile phase. The significant features of MEKC are the availability of a wide range of pseudo-stationary phases that provide unique selectivities for peptides and feasibility of manipulating the comparison of the pseudo-phases since it is a completely solution-based technique. Therefore, selectivity in MEKC can be varied by altering the nature of the micelles [6-8]. This could be achieved by altering the surfactant and changing the size, charge or geometry of the micelles. It is shown that not only the predominant hydrophobic interaction but also other important solute-micelle

* Corresponding Author: Mostafa Hassanisadi
Email: mhsaadi@ripi.ir
https://doi.org/10.24200/amecj.v3.i02.98

interactions such as electrostatic and hydrogen bonding could manipulate the separation. In most MEKC studies, sodium dodecyl sulphate (SDS) which is an anionic micelle has been successfully used to separate the hydrophobic and cationic analytes. An important parameter for the separation of the peptides and modeling of the electropherograms in CE and MEKC is their mobilities. This parameter can be converted to migration time and then electropherograms can be simulated using gaussian function. A long-range goal of our laboratory is developing experimental and theoretical methods for peptide separations, and mapping two-dimensional MEKC-CZE schemes. Reaching this goal requires an in-depth understanding of the effects of different factors on the CZE and MEKC peptide mobilities. Quantitative models such as quantitative structure-mobility relationships (QSMR) can help us to gain this knowledge. We have started with the prediction of electrophoretic mobilities of 125 peptides using CZE technique [9]. A QSMR model has been developed using Offord's charge-over-mass term (Q/M2/3) together with the corrected steric substituent constant (ES,C)and molar refractivity (MR) as descriptors. The latter two parameters, account for the steric effects and bulkiness of amino acid side chains, respectively [9]. The robustness of this work was shown by artificial neural network (ANN) modeling of the mobilities of 102 larger peptides – up to 42 amino acid residues – that also included highly charged and hydrophobic peptides [10]. Besides, to explore the utility of the ANN model in simulation of peptide maps, the profile for the endoproteinase digest of the melittin, glucagon and horse cytochrome C, was also studied in the latter work [10]. We intended to examine the same route for the MEKC modeling as we did for the CZE. Therefore, the main aim of the present work was the determination of the mobilities of a set of small peptides – up to 14 amino acid residues – using MEKC and then modeling the mobilities by applying different chemometric techniques. Artificial neural networks (ANNs) are among the most popular methods for modeling of the linear/nonlinear phenomena [11]. ANN-based approaches have the ability of modeling the complex data without the need for a detailed understanding of the underlying phenomena. Back propagation (BP) learning rule is the most popular learning algorithm adopted in neural network technology. Hence in the present research, a back-propagation of error artificial neural network (BP-ANN) was used to predict the mobilities of 128 peptides obtained using MEKC with SDS micellar system. However, the main problem in developing the ANNs, is the selection of suitable descriptors for their inputs. This is especially serious when the mechanism of the phenomenon is complex or unknown. In order to overcome this problem one needs to use a powerful method for the feature selection. Therefore, in the present work we have chosen adaptive neuro-fuzzy inference system (ANFIS) for selecting the most effective parameters on MEKC mobilities. This method is capable in dealing with linear and nonlinear phenomena. Success in modeling of the electrophoretic mobilities of peptides using MEKC, together with our previous achievements in modeling of CZE mobilities might pave the way for developing and predicting the two-dimensional MEKC-CZE maps of peptides.

2. Experimental

2.1. Chemicals and Materials

Sodium dodecyl sulfate (SDS), decanophenone, sodium phosphate monobasic ($NaH_2PO_4.H_2O$), hexanol, and peptides were obtained from Sigma Chemical Co. (St. Louis, MO). Different concentrations of 40, 60 and 80 mM SDS were prepared in 20 mM phosphate buffer at pH 7 with 1.15 % (v/v) hexanol. The solutions were filtered through 0.2 μm acrodisc filter (STRL, Eatontown, NJ) before use. All experiments were carried out on a home-built CE system comprised of a 0-30 kV high voltage power supply (Series EH, Glassman High Voltage, Inc., White house Station, NJ). Fused silica capillary (Polymicro Technologies, Phoenix, AZ), with an inner diameter of 50 μm and an outer diameter of 375 μm was used. The total capillary length and the length from the inlet to the detector were 71 and 47 cm, respectively. A circulating mineral oil bath was used to maintain the temperature of the two buffer reservoirs and the capillary at a designed temperature in this experiment. A positive voltage of 25 kV was applied during the experiments. A variable-wavelength UV detector (Model 200,

Scientific System, Inc., State College, PA) was used, and a wavelength of 214 nm was set in this work. The chromatograms were collected using acquisition software written in LabView (Austin, TX). Before any injection was made, the untreated capillary was conditioned by rinsing with deionized (DI) water for 20 minutes, sodium hydroxide dissolved in methanol for 10-12 minutes, DI water for 20 minutes and finally with the buffer for 15 minutes. The capillary was vacuum rinsed with the buffer solution between each injection.

2.2. Determination of mobility by measurement of migration time of peptides

Electrophoretic mobility at a micelle concentration can be determined from the migration times using equation 10 [2,20]:

$$\mu = \frac{L_t L_d}{V}\left(\frac{1}{t_r} - \frac{1}{t_o}\right) \qquad (10)$$

where Lt is the total length of the capillary, Ld is the separation length (from the upstream end of the capillary to the detection window). V is the applied voltage. tr is the retention time of a solute at a given micelle concentration, and to is the retention time of an unretained solute. The determined mobility values of peptides in 40, 60 and 80 mM SDS solutions together with the peptides studied in this work are shown in Table 1.

Table 1. The values of electrophoretic mobilities of peptides using MEKC with different SDS concentrations together with the calculated values of descriptors

		Descriptors				Mobility		
#	Peptide	$E_{S,C}$	MR_n	ln(N)	Kappa(H)	SDS 80 mM	SDS 60mM	SDS 40mM
1	A_LY_L	-0.70	5.65	0.69	0.67	-6.38	-6.10	-5.73
2	GY	-0.50	1.03	0.69	0.46	-6.49	-5.55	-4.31
3	AY	-0.70	5.65	0.69	0.67	-6.88	-6.23	-4.76
4	ASTTTNYT	-3.88	5.65	2.08	-0.22	-8.71	-7.36	-5.15
5	VY	-1.79	14.95	0.69	1.09	-8.74	-8.13	-6.60
6	YV	-1.79	31.83	0.69	1.09	-10.04	-9.60	-8.58
7	YA	-0.70	31.83	0.69	0.67	-10.17	-9.30	-8.12
8	GGF	-0.30	1.03	1.10	1.06	-10.92	-9.61	-7.10
9	GF	-0.50	1.03	0.69	1.06	-12.09	-10.49	-8.30
10	YY	-1.40	31.83	0.69	0.92	-12.16	-11.49	-9.88
11	YG	-0.50	31.83	0.69	0.46	-12.23	-10.71	-8.12
12	IY	-2.31	19.59	0.69	1.41	-12.86	-11.42	-8.88
13	AF	-0.70	5.65	0.69	1.27	-13.18	-11.25	-7.89
14	HY	-1.36	23.79	0.69	0.90	-13.20	-11.63	-8.66
15	YI	-2.31	31.83	0.69	1.41	-13.52	-11.70	-9.80
16	LY	-1.94	19.59	0.69	1.40	-13.60	-11.97	-8.53
17	YGG	-0.30	31.83	1.10	0.46	-16.03	-14.47	-11.45
18	FA	-0.70	30.01	0.69	1.27	-16.43	-14.56	-11.52
19	FV	-1.79	30.01	0.69	1.69	-16.43	-14.65	-11.79
20	YL	-1.94	31.83	0.69	1.40	-16.72	-15.05	-11.45
21	GW	-0.46	1.03	0.69	1.01	-16.79	-14.85	-10.49
22	AW	-0.66	5.65	0.69	1.22	-17.89	-15.65	-11.99
23	VF	-1.79	14.95	0.69	1.69	-19.52	-16.75	-12.04
24	YAG	-0.50	31.83	1.10	0.67	-19.89	-17.00	-12.17
25	YYY	-2.10	31.83	1.10	1.38	-20.00	-18.09	-13.31
26	WS	-0.94	39.81	0.69	0.90	-20.57	-18.21	-13.89
27	FG	-0.50	30.01	0.69	1.06	-21.47	-18.60	-15.43
28	PW	-0.66	13.95	0.69	1.56	-21.78	-17.65	-13.05

29	VW	-1.75	14.95	0.69	1.64	-22.08	-19.31	-13.51
30	FI	-2.31	30.01	0.69	2.01	-22.10	-19.09	-15.68
31	WD	-1.44	39.81	0.69	1.45	-22.22	-22.25	-19.11
32	DF	-1.48	11.58	0.69	1.50	-22.54	-22.18	-21.82
33	WA	-0.66	39.81	0.69	1.22	-22.60	-19.65	-14.85
34	D_LF_L	-1.48	11.58	0.69	1.50	-23.16	-22.61	-21.64
35	FM	-1.53	30.01	0.69	1.66	-23.23	-20.79	-15.57
36	GGFM	-1.13	1.03	1.39	1.66	-23.74	-20.27	-14.12
37	WV	-1.75	39.81	0.69	1.64	-23.83	-20.62	-16.14
38	FGG	-0.30	30.01	1.10	1.06	-24.86	-22.50	-16.57
39	YGGF	-1.00	31.83	1.39	1.52	-25.14	-23.13	-15.69
40	EW	-1.28	16.23	0.69	1.43	-25.54	-22.75	-21.33
41	YW	-1.36	31.83	0.69	1.47	-25.54	-21.90	-18.32
42	YYL	-2.64	31.83	1.10	1.86	-25.68	-23.87	-16.44
43	DW	-1.44	11.58	0.69	1.45	-25.77	-22.99	-21.18
44	MW	-1.49	23.12	0.69	1.61	-25.77	-21.96	-18.07
		Descriptors				Mobility		
#	**Peptide**	**$E_{S,C}$**	**MR_n**	**ln(N)**	**Kappa(H)**	**SDS 80 mM**	**SDS 60 mM**	**SDS 40 mM**
45	WE	-1.28	39.81	0.69	1.43	-26.89	-21.82	-18.29
46	FL	-1.94	30.01	0.69	2.00	-28.13	-25.32	-18.93
47	WG	-0.46	39.81	0.69	1.01	-28.40	-25.57	-19.98
48	IW	-2.27	19.59	0.69	1.96	-28.84	-25.41	-18.06
49	IF	-2.31	19.59	0.69	2.01	-29.15	-25.04	-19.64
50	PPGFSP	-0.78	13.95	1.79	2.60	-29.19	-25.75	-17.08
51	GGFL	-1.54	1.03	1.39	2.00	-29.26	-26.34	-19.32
52	WM	-1.49	39.81	0.69	1.61	-29.56	-26.25	-20.98
53	LF	-1.94	19.59	0.69	2.00	-31.16	-28.17	-20.70
54	WP	-0.66	39.81	0.69	1.56	-31.20	-27.36	-21.35
55	KF	-1.32	25.05	0.69	2.20	-31.69	-29.11	-21.43
56	YPF	-1.40	31.83	1.10	2.07	-31.97	-28.32	-20.78
57	WY	-1.36	39.81	0.69	1.47	-32.60	-26.46	-20.86
58	L_LW_L	-1.90	19.59	0.69	1.95	-32.61	-28.95	-22.63
59	FF	-1.40	30.01	0.69	2.12	-32.72	-29.83	-22.99
60	F_LF_L	-1.40	30.01	0.69	2.12	-32.84	-30.44	-23.48
61	K_LF_L	-1.32	25.05	0.69	2.20	-32.87	-30.20	-21.63
62	LW	-1.90	19.59	0.69	1.95	-33.11	-29.65	-21.60
63	GLF	-1.74	1.03	1.10	2.00	-33.96	-31.49	-23.70
64	WGG	-0.26	39.81	1.10	1.01	-34.06	-30.35	-24.09
65	GFL	-1.74	1.03	1.10	2.00	-34.55	-31.48	-24.40
66	FW	-1.36	30.01	0.69	2.07	-35.09	-32.21	-26.14
67	YGGFM	-1.83	31.83	1.61	2.12	-35.13	-31.37	-22.40
68	WL	-1.90	39.81	0.69	1.95	-35.27	-31.65	-25.71
69	MLF	-2.77	23.12	1.10	2.60	-35.62	-32.99	-26.10
70	WGY	-1.16	39.81	1.10	1.47	-36.11	-32.72	-26.61
71	YAGFL	-2.44	31.83	1.61	2.67	-37.52	-34.85	-26.72
72	YGGFL	-2.24	31.83	1.61	2.46	-37.59	-36.08	-26.09
73	WGGGY	-0.76	39.81	1.61	1.47	-38.83	-35.78	-29.77
74	KW	-1.28	25.05	0.69	2.15	-38.88	-36.79	-30.76
75	WGGY	-0.96	39.81	1.39	1.47	-38.88	-35.47	-29.39
76	FGGF	-1.00	30.01	1.39	2.12	-38.95	-35.19	-29.22
77	WF	-1.36	39.81	0.69	2.07	-39.97	-37.28	-31.14
78	YSGFLT	-3.25	31.83	1.79	2.20	-39.98	-35.47	-28.51

79	WW	-1.32	39.81	0.69	2.02	-41.50	-39.25	-33.67
80	TRSAW	-2.09	11.82	1.61	2.53	-41.52	-40.67	-33.07
81	YGGWL	-2.20	31.83	1.61	2.41	-42.21	-40.85	-32.63
82	FGFG	-1.00	30.01	1.39	2.12	-42.78	-39.83	-34.28
83	RW	-1.28	30.05	0.69	2.58	-43.08	-41.39	-33.55
84	FFF	-2.10	30.01	1.10	3.18	-44.33	-43.35	-38.04
85	RPPGK	-1.04	30.05	1.61	3.81	-44.43	-42.77	-35.55
86	DRVYIHP	-5.46	11.58	1.95	5.04	-44.53	-43.75	-37.60
87	KYK	-1.94	25.05	1.10	2.74	-45.47	-45.20	-41.39
88	RPPGFSP	-1.40	30.05	1.95	4.17	-45.63	-45.23	-41.06
89	WR	-1.28	39.81	0.69	2.58	-46.11	-44.77	-38.45
90	DRVYIHPF	-6.16	11.58	2.08	6.10	-46.54	-45.96	-41.39
91	ELYENKPRRPY	-6.52	16.23	2.40	7.90	-46.61	-46.27	-43.06
92	DRVYVHPFHL	-7.54	11.58	2.30	7.16	-47.11	-47.08	-45.15
93	NRVYVHPF	-5.64	14.46	2.08	5.16	-47.12	-47.29	-44.15
		Descriptors				Mobility		
#	Peptide	$E_{S,C}$	MR_n	ln(N)	**Kappa(H)**	**SDS 80 mM**	**SDS 60 mM**	**SDS 40 mM**
94	YMEHFRW	-4.79	31.83	1.95	5.56	-47.21	-46.98	-43.99
95	RYLGYL	-4.30	30.05	1.79	4.37	-47.31	-46.99	-45.06
96	ELYENKPRRPYIL	-9.37	16.23	2.56	9.79	-47.31	-46.57	-44.76
97	FFFF	-2.80	30.01	1.39	4.24	-47.35	-47.43	-44.36
98	CGYGPKKKRKVGG	-4.09	13.90	2.56	9.05	-47.48	-46.26	-41.74
99	RPKPQQFFGLM	-5.75	30.05	2.40	7.59	-47.55	-47.82	-46.31
100	YRPPGFSPFR	-3.42	31.83	2.30	7.26	-47.55	-47.82	-46.31
101	MEHFRWG	-3.89	23.12	1.95	5.10	-47.56	-47.47	-43.97
102	DRVYIHPFHL	-8.06	11.58	2.30	7.48	-47.66	-46.85	-43.59
103	ELYENKPRRPFIL	-9.37	16.23	2.56	10.39	-47.71	-46.77	-44.90
104	AGCKNFFWKTFTSC	-5.92	5.65	2.64	8.65	-47.71	-47.66	-45.63
105	RPKPQQF	-3.18	30.05	1.95	4.99	-47.83	-47.28	-44.08
106	RPPGFSPFR	-2.72	30.05	2.20	6.80	-47.85	-47.71	-46.02
107	RVYIHPI	-6.29	30.05	1.95	5.55	-47.86	-47.41	-46.15
108	SYSMEHFRWG	-5.15	7.20	2.30	5.34	-47.88	-47.54	-44.80
109	RVYVHPF	-4.86	30.05	1.95	5.34	-47.92	-47.27	-45.34
110	FFFFF	-3.50	30.01	1.61	5.30	-47.92	-48.27	-46.11
111	RPGFSPFR	-2.72	30.05	2.08	6.25	-48.07	-46.91	-44.71
112	DRVYIHPFHLVIHN	-12.20	11.58	2.64	9.32	-48.10	-47.43	-45.25
113	WQPPRARI	-4.13	39.81	2.08	6.47	-48.11	-47.40	-45.77
114	RGPFPI	-2.73	30.05	1.79	4.68	-48.12	-47.14	-42.36
115	IARRHPYFL	-6.15	19.59	2.20	7.75	-48.21	-47.30	-44.58
116	WHWLQL	-5.08	39.81	1.79	4.40	-48.28	-48.46	-45.62
117	PPGFSPFR	-2.10	13.95	2.08	5.23	-48.42	-47.61	-45.54
118	YGGFMRF	-3.15	31.83	1.95	4.75	-48.49	-47.09	-44.86
119	EGKRPWIL	-5.17	16.23	2.08	6.58	-48.57	-47.47	-45.87
120	WWW	-1.98	39.81	1.10	3.03	-48.66	-48.09	-45.97
121	HW	-1.32	23.79	0.69	1.45	-40.97	-38.71	-31.77
122	RRPYIL	-4.79	30.05	1.79	6.04	-32.39	-29.11	-22.96
123	YPFVEPI	-4.72	31.83	1.95	4.62	-32.39	-29.11	-22.96
124	YLEPGPVTA	-3.98	31.83	2.20	3.61	-18.05	-16.71	-14.09
125	RKDVY	-3.81	30.05	1.61	4.24	-42.31	-40.11	-33.63
126	RFDS	-2.38	30.05	1.39	2.96	-31.80	-28.57	-19.86
127	FLEEI	-4.79	30.01	1.61	3.79	-27.60	-27.03	-25.53
128	VEPIPY	-4.02	14.95	1.79	3.56	-14.58	-14.09	-12.70

2.3. Sequential forward search for input selection using ANFIS

In this work, ANFIS-based sequential variable selection program written in MATLAB is used as a feature selection method [21]. The algorithm is based on selecting the best descriptor which minimizes standard errors of calibration and prediction and then repeatedly adds next best descriptor to the previous one(s). In the first step after sorting the dataset based on the mobility values (Table 1), training and test sets in a ratio of 4:1 were randomly chosen such that the test set adequately represented the training set. Then based on three iterations and two Gaussian bell membership functions, 5 out of 41 descriptors were selected using ANFIS. The selected parameters were used as inputs for developing ANN models. Analysis of the results obtained by the ANN model showed some outliers. These outliers were removed from the original dataset and the sequential variable selection was repeated using the remaining peptides of the dataset. In the final stage, a total of four descriptors were selected for developing neural networks and further studies. The values of these parameters are given in Table 1 for all peptides studied in this work.

2.4. Descriptors

The following structural parameters for amino acids were considered for calculating the descriptors of peptides: The substituent constants (κ), steric effects (ES,C) and molecular refractivity (MR) [22,23]. The values of these descriptors for twenty amino acids are listed in Table 2. Molar refractivity and residues mass are scaled by a factor of 0.1, such that they will have the same scale according to Hansch and Leo [18]. Taft defined the steric constant, ES, as log (k/ko), where k and ko are the rate constants for the acidic hydrolysis of a substituted ester and of a reference ester (methyl group is usually used as the reference, but H is sometimes used), respectively [24]. Hankcock has stated that there is contribution of hyper conjugation (α-hydrogen bonding) to the Taft Es; therefore, it must be corrected as defined by [25]:

$$ES,C = ES + 0.306\ (n-3) \quad (11)$$

where ES,C is a corrected steric substituent constant and Es is the "revised" Taft steric constant[26]; n is the number of α-hydrogens. As can be seen in Table 2, a small value of steric effect was observed for "crowded" structures of α-branched side chain (V, I, L). This means that they are large resistance to the hydrolysis.

Table 2. Physicochemical substituent parameters for amino acids

AA Side Chains	K	$E_{S,C}$	MR
alanine (A)	0.21	0.00	0.57
arginine (R)	1.57	-0.62	3.01
asparagine (N)	-0.18	-0.78	1.45
aspartic acid (D)	0.44	-0.78	1.16
cysteine (C)	1.28	0.00	0.00
glutamine (Q)	0.06	-0.62	1.91
glutamic acid (E)	0.42	-0.62	1.62
glycine (G)	0.00	0.20	0.10
histidine (H)	0.44	-0.66	2.38
isoleucine (I)	0.95	-1.61	1.96
leucine (L)	0.94	-1.24	1.96
lysine (K)	1.14	-0.62	2.51
methionine (M)	0.60	-0.83	2.31
phenylalanine (F)	1.06	-0.70	3.00
proline (P)	0.55	0.00	1.40
serine (S)	-0.11	-0.28	1.18
threonine (T)	-0.15	-0.53	1.18
tryptophan (W)	1.01	-0.66	3.98
tyrosine (Y)	0.46	-0.70	3.18
valine (V)	0.63	-1.09	1.50

2.5. Artificial neural network

In the present work, the feed forward back propagation of error artificial neural network (BP-ANN) is written in C++. The input layer consisted of the four parameters selected by ANFIS. The output layer represents the electrophoretic mobilities of the peptides. In this investigation, the bipolar sigmoid function, i.e., f (x) = (1-exp (-x)) / (1+exp (-x)), is used as the transfer function. The initial weights were chosen randomly, and were optimized based

on the delta rule through back propagation of errors. The program is written in such a way that the range for initialization of the weights depends on the number of input and hidden nodes. Before training, the inputs were normalized between -2 and 2 and the output between 0 and 1. The network parameters such as the number of hidden layer nodes, learning rate and momentum were optimized. Optimizations of these parameters were based on obtaining the minimum standard error of calibration and prediction. Program automatically avoids overfitting by stopping the training when the increase in standard error of prediction commences. After the analysis of ANN results and removing the outliers, the new dataset consisted of 118 peptides were sorted based on mobility values. This set was divided into training, test and validation sets (in a ratio of 4:1:1). However, in order to test the stability of the model and making sure that the results are not due to the chance, six different sets of training, test and validation sets for each concentration of SDS were created.

2.6. Methodology

The present work consists of three steps: (1) experimental determination of the mobilities of peptides using CE system in 40, 60 and 80 mM SDS solutions for two purposes. First, to investigate the effects of change of surfactant concentration on the mobilities of peptides and secondly, exploration of the ability and robustness of the generated theoretical models in the prediction of the MEKC mobilities at different SDS concentrations. (2) Selecting the structural parameters which play the major role in the migration behavior of peptides in MEKC experiments. This is a challenging process, since the mechanism of partitioning of the peptides into the micelles and migration of the micelles due to the electrophoretic and electroosmotic phenomena are complex. In modeling, choosing suitable features/descriptors is critical, because without success in this step the development of a robust and interpretable model is impossible. Therefore, we were very anxious to search for a powerful method as a feature selection technique. We have chosen a neurofuzzy system for this purpose, which is a combination of the neural network and fuzzy rules. A neural network can model a process by means of a linear/nonlinear regression algorithm, for which the result is a network with adjusted weights and approximates the property of interest. However, the problem is that the knowledge is stored in an opaque fashion; the learning result is a set of parameter values, almost impossible to interpret them in words. Conversely, a fuzzy rule-base consists of readable if-then statements which are very close to natural language, but cannot learn the rules. These two are combined in neurofuzzy systems in order to achieve readability and learning ability at the same time. In this work a sequential ANFIS is used as feature selection technique. We have chosen ANFIS because of its much faster convergence, much more repeatability and much less preprocessing compared with ANN. (3) In order to develop a model for predicting the MEKC mobilities of peptides and also inspecting the linear/nonlinear characteristics of the migration behavior of peptides in MEKC, simple MLR as a linear method and BP-ANN as a nonlinear method are used. In both cases we use ANFIS for selecting the features. These methods are very common and frequently have been used in our laboratory and by several other researchers [12-16]. Therefore, for the sake of brevity their description is not given here.

2.6.1.Adaptive Neuro-Fuzzy Inference System (ANFIS)

By definition fuzzy logic is a type of logic that recognizes more than simple true and false values [17]. Fuzzy logic can represent propositions by degrees of truthfulness and falsehood and has proved to be particularly useful in expert systems and other artificial intelligence applications. One of the hallmarks of fuzzy logic is that it allows nonlinear input/output relationships to be expressed by a set of qualitative “if-then” rules. The theory of fuzzy logic provides a mathematical morphology to emulate certain perceptual and linguistic attributes associated with human cognition. Most fuzzy systems are hand-crafted by a human expert to

capture some desired input/output relationships that the expert has in mind. However, often an expert cannot express his or her knowledge explicitly; and, for many applications, an expert may not even exist. Hence, there is considerable interest in being able to automatically extract fuzzy rules from experimental input/output data. While fuzzy theory provides an inference mechanism under cognitive uncertainty, computational neural networks offer exciting advantages such as learning, adaptation, fault-tolerance, parallelism and generalization. The computational neural networks are capable of coping with computational complexity, nonlinearity and uncertainty. In fact, the neural network approach fuses well with fuzzy logic and by combining these two techniques, benefits of both would be acquired. Fuzzy inference is the process of formulating the mapping from a given input to an output using fuzzy logic (Fig. 1). The mapping then provides a basis from which decisions can be made, or patterns discerned. One type of fuzzy inference systems is based on Takagi-Sugeno model [18]. In the Takagi-Sugeno model the idea is that each rule in a rule-base defines a region for a model, which can be linear. The left-hand side of each rule defines a fuzzy validity region for the linear model on the right-hand side. The inference mechanism interpolates smoothly between each local model to provide a global model. As an example consider a single input, single output system with the following two rules: 1) IF input is large THEN output is line 1. 2) IF input is small THEN output is line 2. Where line 1 is defined as 0.2 * input + 90 and line 2 is 0.6 * input + 20. The rules interpolate between the two lines in the region where the membership functions overlap (Fig. 2). Outside of that region the input is a linear function of the error.

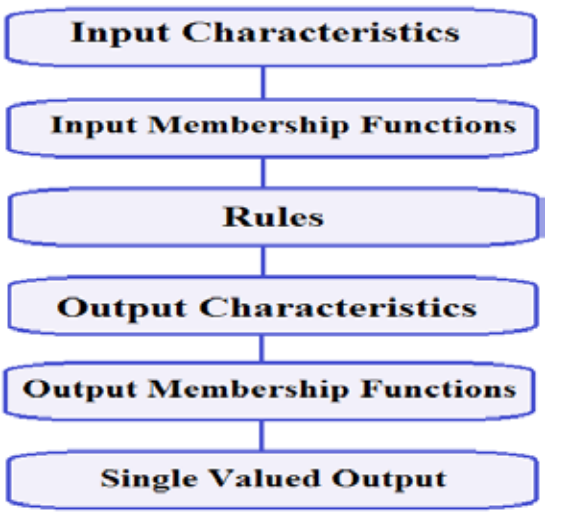

Fig. 1. The basic structure of fuzzy inference system

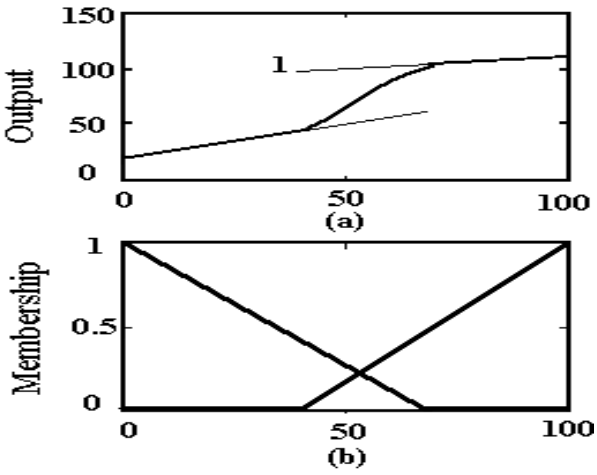

Fig. 2. Interpolation between two lines (top) in the overlap of input sets (bottom).

2.6.2.ANFIS architecture

Without loss of generality we assume two inputs, u1 and u2, and one output, y. Assume for now a first order Sugeno type rule-base composed of the following two rules [19]:

If u_1 is A_1 and u_2 is B_1 then

$$y_1 = c_1 u_1 + c_2 u_2 + c_0 \quad (1)$$

If u_1 is A_2 and u_2 is B_2 then

$$y_2 = c_2 u_1 + c_2 u_2 + c_0 \quad (2)$$

Incidentally, this fuzzy controller could interpolate between two linear controllers depending on the current state. If the firing strengths of the rules are α1 and α2 respectively, for two particular values of the inputs u1 and u2, then the output is computed as a weighted average

$$y = \frac{\alpha_1 y_{1+} \alpha_2 y_2}{\alpha_{1+} \alpha_2} = \overline{\alpha}_1 y_{1+} \overline{\alpha}_2 y_2 \quad (3)$$

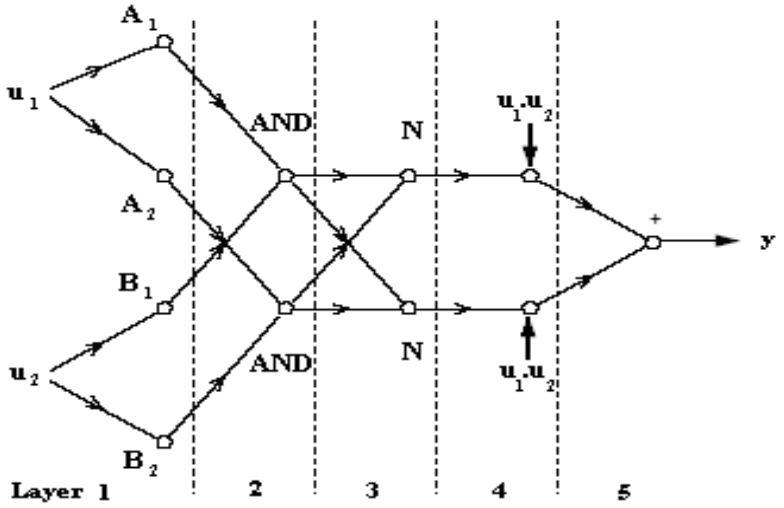

Fig. 3. Structure of the ANFIS network

Figure 3 shows corresponding ANFIS network. The descriptions for the layers shown in the network are as follows:

1. Each neuron i in layer one is adaptive with a parametric activation function. Its output is the grade of membership to which the given input satisfies the membership function, i.e.,

$$\mu_{A_1}(u_1),\ \mu_{B_1}(u_2),\ \mu_{A_2}(u_1) \text{ or } \mu_{B_2}(u_2).$$

An example of a membership function is the generalized bell function:

$$\mu(x) = \frac{1}{1+\left|\frac{x-c}{a}\right|^{2b}} \qquad (4)$$

where {a, b, c} is the parameter set. As the values of the parameters change, the shape of the bell-shaped function varies. Parameters in that layer are called premise parameters.

2. Every node in layer two is a fixed node, whose output is the product of all incoming signals. In general, any other fuzzy AND operation can be used. Each node output represents the firing strength αi of the ith rule.

3. Every node in layer three is a fixed node which calculates the ratio of the ith rule's firing strength relative to the sum of all rule's firing strengths,

$$\overline{\alpha}_i = \frac{\alpha_i}{\sum_{i=1,2}\alpha_i} \qquad (5)$$

The result is a normalized firing strength.

4. Every node in layer four is an adaptive node with a node output

$$\overline{\alpha}_i y_i = \overline{\alpha}_i (c_{i1}u_1 + c_{i2}u_2 + c_{i0}) \quad i = 1,2 \qquad (6)$$

where i is the normalized firing strength from layer three and {ci1, ci2, ci0} is the parameter set of this node. Parameters in this layer are called consequent parameters.

5. Every node in layer five is a fixed node which sums all incoming signals. It is straightforward to generalize the ANFIS architecture in Figure 3 to a rule-base with more than two rules.

2.6.3. The ANFIS learning algorithm

When the premise parameters are fixed, the overall output is a linear combination of the consequent parameters. In symbols, the output y can be written as:

$$y = \frac{\alpha_1}{\alpha_{1+}\alpha_2} y_1 + \frac{\alpha_2}{\alpha_{1+}\alpha_2} y_2 \qquad (7)$$

$$y = \overline{\alpha}_1(c_1 u_1 + c_2 u_2 + c_0) + \overline{\alpha}_2(c_2 u_1 + c_2 u_2 + c_0) \qquad (8)$$

$$y = (\overline{\alpha}_1 u_1)c_1 + (\overline{\alpha}_1 u_2)c_2 + \overline{\alpha}_1 c_0 + (\overline{\alpha}_2 u_1)c_2 + (\overline{\alpha}_2 u_2)c_2 + \overline{\alpha}_2 c_0 \qquad (9)$$

Which is linear in the consequent parameters cij (i=1, 2; j=0, 1, 2). A hybrid algorithm adjusts the consequent parameters cij in a forward pass and the premise parameters {ai, bi, ci} in a backward pass. In the forward pass the network inputs propagate forward up to layer 4, where the consequent parameters are identified by the least-squares method. In the backward pass, the error signals propagate backwards and the premise parameters are updated by gradient descent. Because the update rules for the premise and consequent parameters are decoupled in the hybrid learning rule, a computational speedup may be possible by using variants of the gradient method or other optimization techniques on the premise parameters.

3. Results and discussion

The main goal of this work was to study the mechanism of the migration of peptides in MEKC. We hope that the results of this work together with our previous works on CZE could pave the way for further studies on the 2D MEKC-CZE simulations. However, the best way of studying the mechanism is gathering a set of the general parameters which are responsible for the migration of the peptides in MEKC. To achieve this, the mobility of a set of different classes of peptides has to be modeled. Mobilities of a set of 128 peptides composed of up to 14 amino acids in 40, 60 and 80 mM solutions of SDS was measured. The general strategy of modeling the mobilities was as follows: Feature selection using sequential ANFIS algorithm; developing MLR and BP-ANN models using the selected descriptors as the inputs; and analysis and evaluation of the best model.

3.1. Application of ANFIS as feature selection method

After obtaining the values of the mobilities of 128 peptides using MEKC method and calculating 41 descriptors for each one, the dataset was divided into training (102 peptides) and test sets (26 peptides). Then by applying ANFIS, five descriptors of Kappa(H), ln(N), ARM, MRC and ES,N which minimized the standard errors of calibration and prediction were selected. These descriptors were used as the inputs to develop a network for modeling the mobility of peptides. The results of the ANN showed that the network is not able to predict accurately the mobility of ten peptides and therefore they can be considered as statistical outliers. These peptides were DF, DLFL, DW, WD, EW, WE, FLEEI, VEPIPY, YPFVEPI and YLEPGPVTA. This means that these peptides have different characteristics compared with the rest of the dataset, and the ANN model is unable to learn and predict their behavior. Consequently, due to the special characteristics of the above-mentioned peptides there is the possibility of misleading the ANFIS and this method may model the noise. Hence, these peptides were removed from the dataset and selection of the features was repeated. Finally four descriptors (Kappa (H), ln (N), MRn and ES,C) which could model the mobility were chosen. The behavior of the outliers will be discussed later in this section.

3.2. Modeling and prediction by Artificial Neural Network

The investigations were started using SDS 80 mM dataset. Even though we had removed the ten outliers in feature selection step, in order to study the results of ANN calculations, we added them to the dataset again. Then the dataset was divided into training, test and validation sets. The network was trained and the results were studied. Results showed that some peptides cause instability and premature training of the network. Therefore, the outliers were removed one at a time and entered into the validation set in order to study their behavior when the network is completely trained with the remaining peptides. It is obvious that after removing the outliers the remaining peptides were divided into new training, test and validation sets. These sets are composed of random and representative samples, but the validation set encompasses the entered samples as well. In the final stage eight statistical outliers were obtained which were HW, RRPYIL, RFDS, RKDVY FLEEI, VEPIPY, YPFVEPI and YLEPGPVTA.

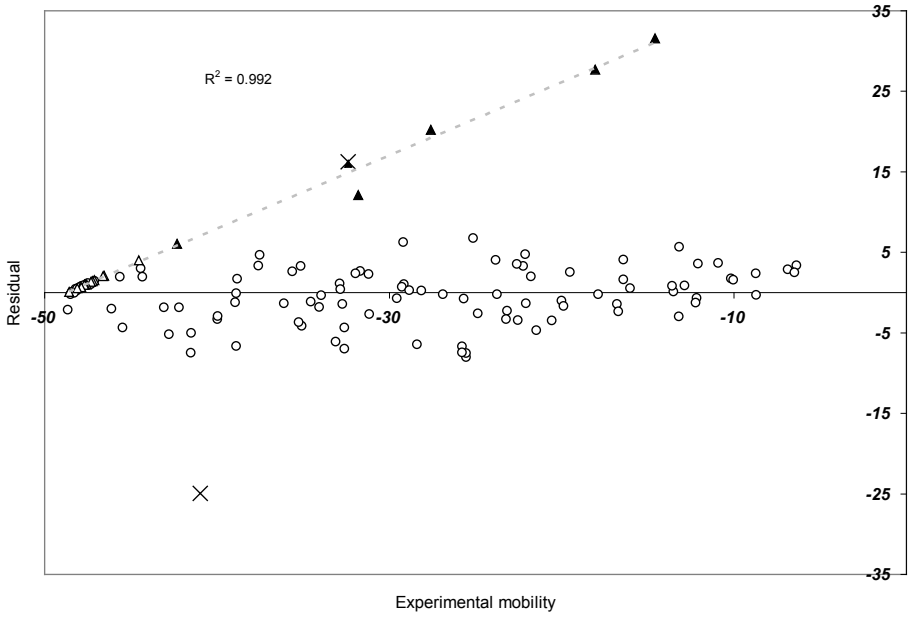

Fig. 4. Residuals of calculated ANN values of mobilities versus the experimental values. Δ, peptides containing negatively charged middle amino acids (E and D); ×, HW and RRPYIL; ▲, outliers

3.3. Analysis of residuals

Figure 4 depicts the residuals of ANN calculated values versus the experimental mobilities. It can be seen from this figure that the developed ANN is not able to predict accurately the mobilities of HW and RRPYIL. Also it can be seen that the residuals of all of the outliers are located above the zero axis. Statistically this means that there should be a systematic error in the calculated results of the ANN model. However, inspection of the residuals reveals that the peptides containing middle E and D amino acids together with the six outliers lie on a line with a correlation of R2= 0.992. This implies that the mobility of these peptides follows a similar mechanism which is different from the mechanism for the remaining peptides. Presumably a parameter appropriate for accounting the influence of charge is missing. Fundamentally a charge descriptor should be able to introduce this characteristic to the model. However, due to the small number of these type of peptides in the dataset (18 peptides), the network was not being able to receive enough information to learn their behavior. On the other hand, positive values of the residuals show that the ANN model overestimates the mobilities of these peptides. The repulsion between the negatively charged D and E amino acids and the anionic SDS surfactant could be responsible for this overestimation. Because of this repulsion, these peptides spend a shorter time in the micellar phase and move slower. Consequently, one expects that in more dilute solutions of SDS, this effect be more pronounced.

3.4. Effect of SDS concentration on peptide mobilities

In order to investigate the effect of concentration on the migration of peptides, in addition to the original model which was developed based on the 80 mM SDS solution, two other models were developed using the same descriptors and same settings of the network for 40 and 60 mM SDS solutions. Figure 5 presents the predicted results (validation set) versus the experimental values for 80, 60 and 40 mM SDS solutions. Inspection of the figures reveals that by decreasing the SDS concentration the spread of points around the correlation line has increased. Therefore, a question arises regarding the effect of the SDS

concentration on the mobility behavior of the peptides. To explain the grounds, we refer to Figures 6 which are obtained using purely experimental values. These figures show the trend of mobility changes due to changes in SDS concentration. The vertical axis shows the change in mobility for two solutions of SDS and the horizontal axis is the mobility of the more concentrated one. By inspection of these figures one may conclude that: (1) Concentration increments have a profound effect on the curvatures of the mobility trends. Figure 6C with the highest concentration gradient shows a high curvature. On the other hand, although the concentration gradients are equal in figures 6A and 6B (20mM), Figure 6A shows a very small curvature compared with Figure 6B. This shows that 40 and 60 mM solutions are below the optimum level of SDS concentration. This may be due to the fact that when the solution is more dilute the effect of micelles is less profound, and CZE mechanism prevails over MEKC. Since the ANN model is trained based on the MEKC data, the calculated values for the more dilute solutions show a broader spread. (2) The compounds which include E and D amino acids behave different in comparison with the other peptides. This is more pronounced for the dipeptides. Points marked with hollow squares in Figures 6 belong to FLEEI, DW, WD, WE, EW, DF and DLFL. The figures show that these peptides do not obey the general

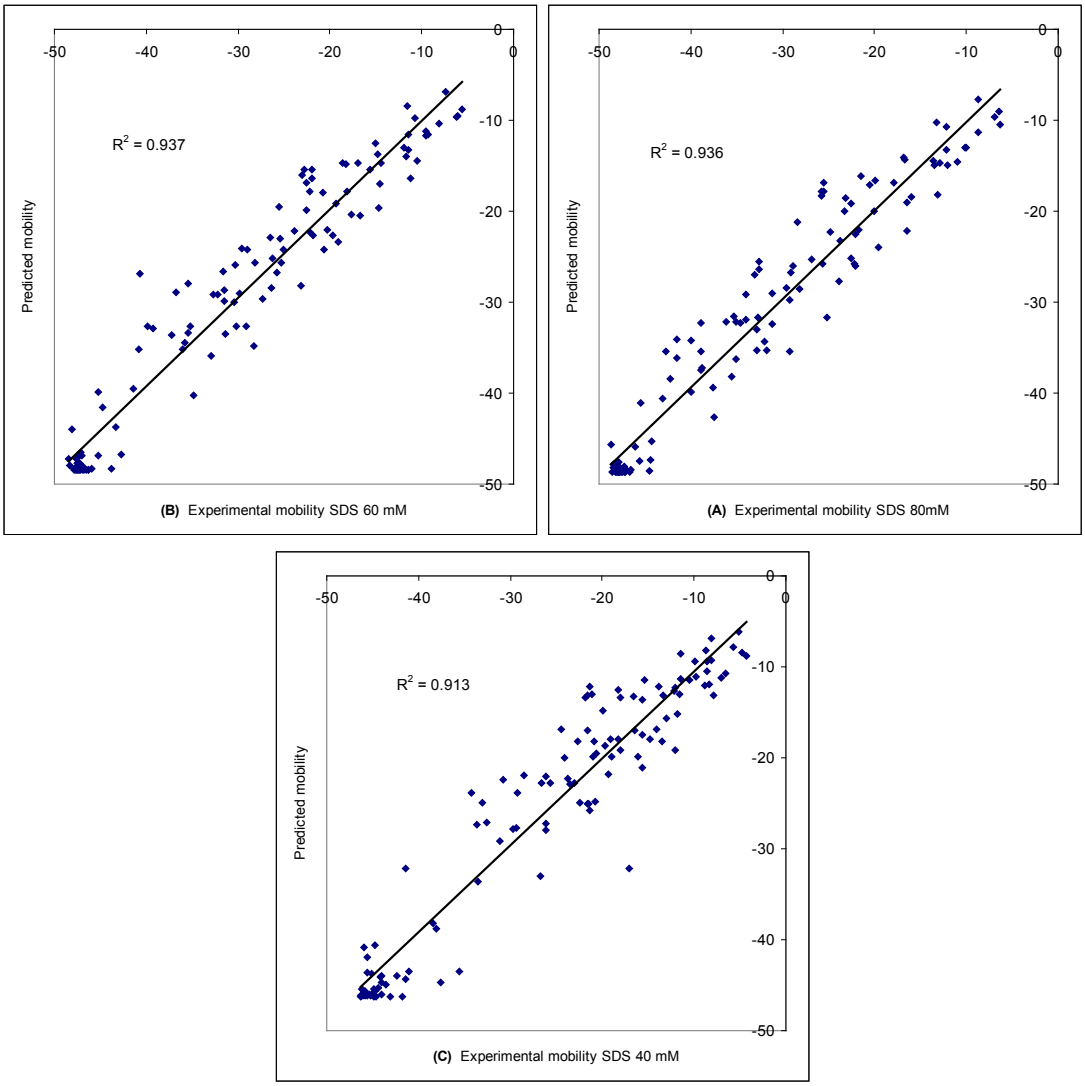

Fig. 5. Predicted values obtained by ANN model for the all 6 batches. 80 mM, (B) 60 mM and (C) 40 mM SDS solutions.

trend of mobility changes which exists for the other peptides. FLEEI is the only peptide in the dataset which contains two E amino acids, so it would suffer more of the repulsion forces which exists between E amino acids and the anionic surfactant. The footprint of this interaction exits in the outliers of the ANN (RFDS, RKDVY, FLEEI, VEPIPY, YPFVEPI and YLEPGPVTA), and ANFIS (DF, DLFL, DW, WD, EW, WE, FLEEI, VEPIPY, YPFVEPI and YLEPGPVTA) as well.

3.5. Comparison of MLR and ANN results

To investigate the linear/nonlinear characteristics of the relation between mobility and the descriptors, a similar MLR model was developed. For a meaningful comparison, both the ANN and MLR methods has to be trained using the same training set and verified by the same validation set. Despite the fact that we have used all of the peptides (outliers of the ANN model were excluded) in the regression step, the MLR calculated results for the training set show a poor correlation of 0.71. This demonstrates the inadequacy of MLR method for the modeling of the peptide mobilities, and irrational trend of residuals (Fig. 7). This could be due to nonlinear characteristics of the mobilities. Such a trend is absent in ANN residuals (Fig. 4). In order to assess the role of each variable in nonlinear characteristics of the peptide mobilities, the MLR residuals for the variables are depicted in Figure 8. These figures suggest that, kappa could be the parameter responsible for the nonlinearity, because the trend in its residuals is very similar to the trend of the MLR residual plot.

3.6. Robustness of the ANN models

After the training of the ANN for the prediction of peptide mobilities in different concentrations of SDS, the outliers were expelled and the remaining peptides were divided into six different batches of training, test and validation sets. These batches were chosen in a way that in each one every peptide appeared in the test and validation sets once. Then all six batches of training, test and validation sets

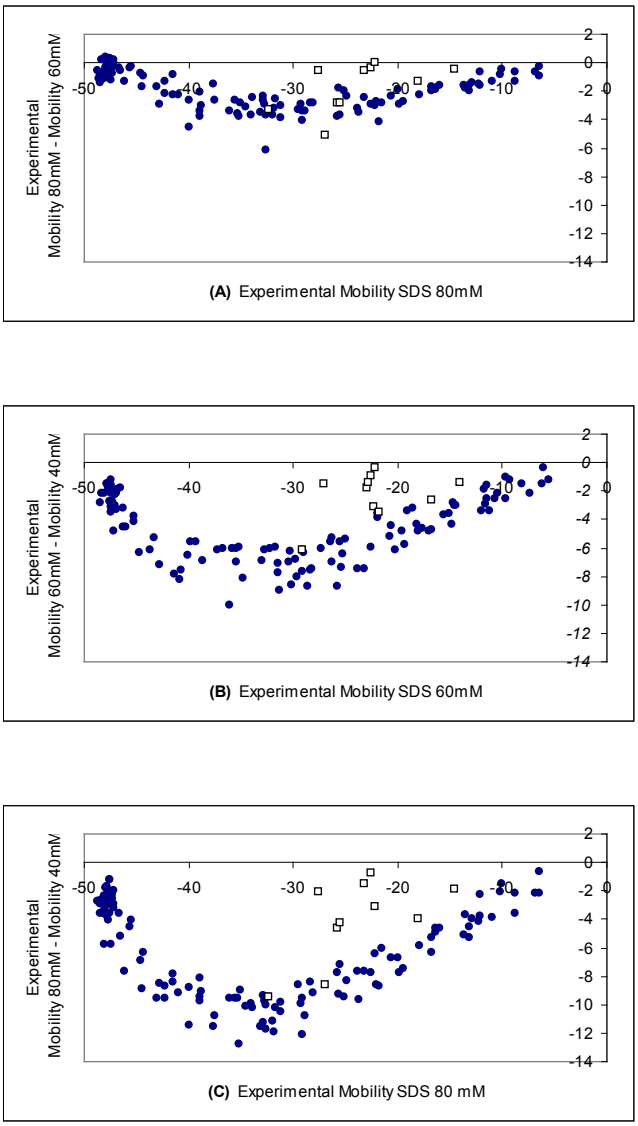

Fig. 6. Change in mobility due to SDS concentrations changes.
the peptides with E and D amino acids

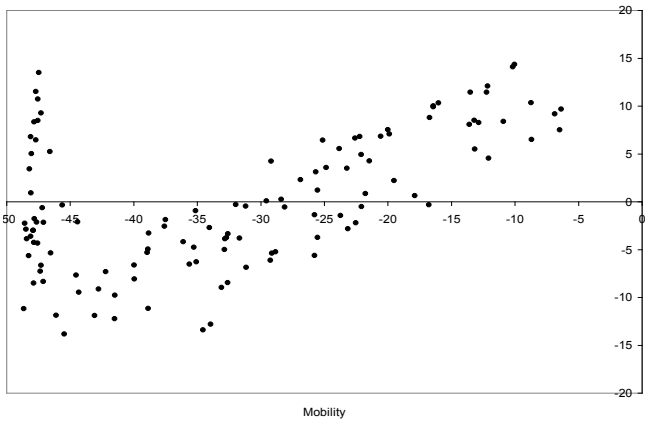

Fig. 7. MLR prediction residual plot.

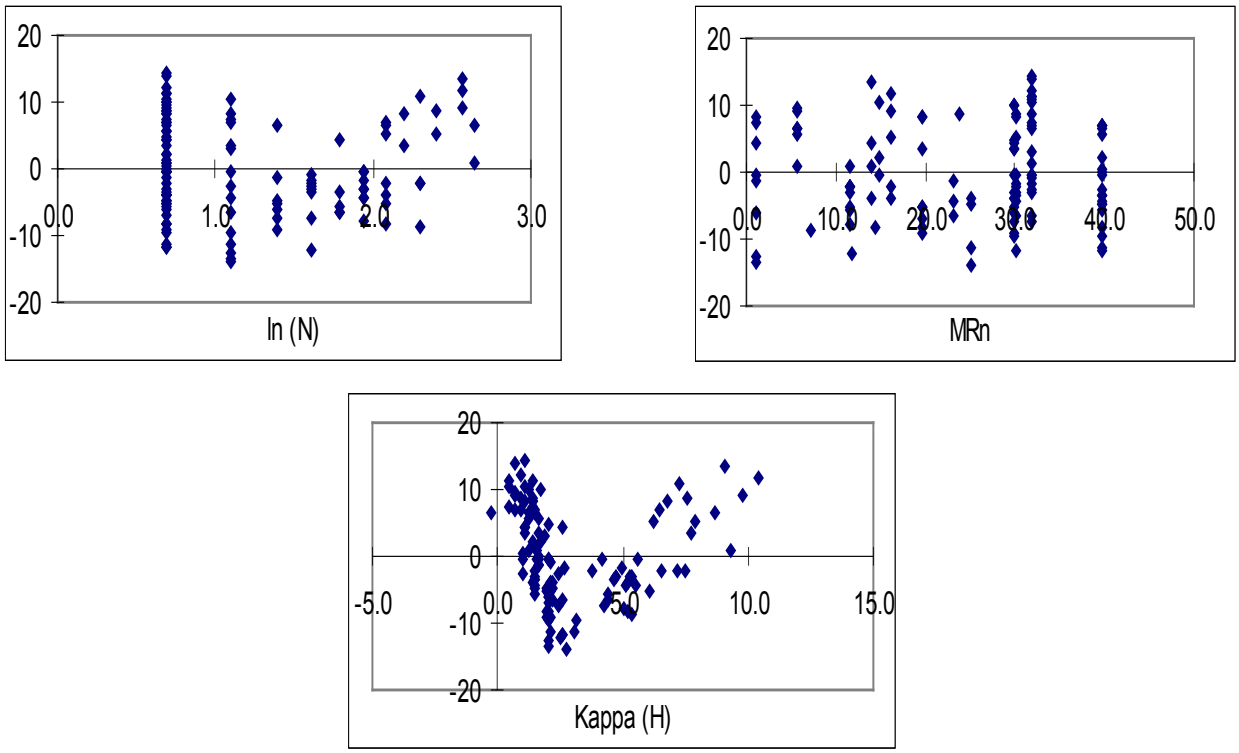

Fig. 8. MLR variables residual plots

were trained and applied for predicting the peptide mobilities in solutions with different concentrations of SDS. It can be seen from Figures 5 and Tables 3 and 4 that the residuals are promising for all of the six batches. Table 3 is devoted to correlation values for training, test and validation sets of each batch. The values for the correlations were in the range of 0.849 to 0.969 for all batches with different concentrations of SDS, which show the robustness of the model. Table 4 shows the average deviation (AD), average absolute deviation (AAD) and standard deviation (SD) of the ANN predicted values (validation sets) which have been calculated through equations 12-14.

$$AD = \frac{1}{n}\sum_{i=1}^{n}(y_i - \hat{y}_i) \quad (12)$$

$$AAD = \frac{1}{n}\sum_{i=1}^{n}|y_i - \hat{y}_i| \quad (13)$$

$$SD = \sqrt{\left(\frac{1}{n-1}\sum_{i=1}^{n}(y_i - \hat{y}_i)^2\right)} \quad (14)$$

in these equations yi are calculated mobilities, ŷi represents experimental mobilities and n is the number of samples of the set. In these calculations we have not considered the outlier peptides of the validation sets which were outliers. The small values of the deviations reveal the lack of systematic errors in the model. It is noteworthy that the SD shows a range of 3.410 to 4.040 which is close to the experimental errors. These deviations also confirm the predictive ability and robustness of the model.

4. Conclusion

A long-range goal of our laboratory is the development of experimental and theoretical methods for peptide separations and mapping in two-dimensional MEKC-CZE scheme. We have considered the specifications of simplicity, accuracy and robustness of the models in predicting the CZE and MEKC mobilities of the peptides. In our previous works [9-10], we showed the ability of the artificial neural networks in modeling of the CZE mobilities. This paper focuses on MEKC with more complicated mechanism compared to the CZE. Adaptive neuro-fuzzy inference system (ANFIS) was successfully used to select the most

Table 3. Statistical correlations using the ANN model for six different batches

	batch I	batch II	batch III	batch IV	batch V	batch VI	average
80 mM SDS							
Training	0.956	0.952	0.951	0.964	0.951	0.949	0.954
test	0.955	0.969	0.941	0.924	0.947	0.947	0.947
prediction	0.921	0.943	0.947	0.943	0.963	0.939	0.943
60 mM SDS							
Training	0.964	0.953	0.956	0.962	0.951	0.952	0.956
test	0.956	0.969	0.951	0.913	0.953	0.953	0.949
prediction	0.900	0.953	0.954	0.958	0.956	0.947	0.945
40 mM SDS							
Training	0.937	0.941	0.948	0.953	0.948	0.945	0.945
test	0.953	0.961	0.932	0.900	0.942	0.924	0.935
prediction	0.849	0.944	0.924	0.928	0.954	0.931	0.922

Table 4. Statistical deviations for the ANN predicted values of the peptide nobilities

Prediction[a]	batch I	batch II	batch III	batch IV	batch V	batch VI	average
80 mM SDS							
AD	-1.143	-0.361	-1.712	-0.489	0.057	1.144	-0.417
AAD	3.467	2.527	2.536	2.283	1.935	2.879	2.605
SD	4.208	3.262	3.652	3.257	2.477	3.605	3.410
60 mM SDS							
AD	-1.754	0.029	-1.353	-0.769	-0.093	1.126	-0.469
AAD	3.871	2.542	2.383	2.174	2.196	2.693	2.643
SD	5.076	3.114	3.377	2.937	2.795	3.413	3.452
40 mM SDS							
AD	-0.222	-0.266	-1.724	-0.351	0.255	1.105	-0.201
AAD	4.299	2.610	3.016	2.696	2.312	2.989	2.987
SD	5.745	3.521	4.402	3.771	2.949	3.853	4.040

[a] The notations AD, AAD and SD stand for average deviation, average absolute deviation and standard deviation, respectively.

appropriate variables as ANN inputs. It is shown that except for the peptides including negatively charged amino acids the model holds promise for application in predicting the peptide mobilities in MEKC systems. However, researches are underway in our laboratory to combine the CZE and MEKC models to map the peptides in 2D CZE/MEKC scheme.

5. Acknowledgement

A research grant from the U.S. National Institutes of Health (GM 38738) is gratefully acknowledged.

6. References

[1] A.H. Rageh, U. Pyell, Pseudostationary ion-exchanger" sweeping as an online enrichment technique in teh determination of nucleosides in urine via micellar electrokinetic chromatography, Chromatogra., 82 (2019) 325–345.

[2] A.H. Rageh, U. Pyell, Imidazolium-based ionic liquid-type surfactant as pseudostationary phase in micellar electrokinetic chromatography of highly hydrophilic urinary nucleosides, J Chromatogr., A 1316 (2013)135–146.

[3] R.B. Yu, J. P. Quirino, Chiral Selectors in capillary electrophoresis: trends during 2017–2018, Molecules, 24 (2019) 1135.

[4] J. Fiori, B. Pasquini, C. Caprini, S. Orlandini, S. Furlanetto, R. Gotti, Chiral analysis of theanine and catechin in characterization of green tea by cyclodextrin-modified micellar electrokinetic chromatography and high performance liquid chromatography, J. Chromatogr. A, 1562 (2018) 115–122.

[5] Y. Liu, X. Wang, Enantioseparation of ofloxacin and

its four related substances with ligand exchange–micellar electrokinetic chromatography using copper (II)-L-isoleucine complex as chiral selector, Chirality., 29 (2017) 422–429.

[6] I.J. Stavrou, E.A. Agathokleous, C.P. Kapnissi-Christodoulou, Chiral selectors in CE: Recent development and applications, Electrophoresis, 38 (2017) 786–819.

[7] V. Patel , S. A. Shamsi, Carbohydrate based polymeric surfactants for chiral micellar electrokinetic chromatography (CMEKC) coupled to mass spectrometry, Methods Mol. Biol., 1985 (2019) 417–444.

[8] Y. Liu, S.A. Shamsi, Development of novel micellar electrokinetic chromatography mass spectrometry for simultaneous enantioseparation of venlafaxine and dimethyl-venlafaxine: Application to analysis of drug-drug interactions, J. Chromatogr. A, 1420 (2015) 119–128.

[9] R. L. C. Voeten, I. K. Ventouri, R. Haselberg, G. W. Somsen, Capillary electrophoresis: trends and recent Advances, Anal Chem., 90 (2018) 1464–1481.

[10] C.-R. Chung, J.-H. Jhong, Z. Wang, S. Chen, Y. Wan, Characterization and identification of natural antimicrobial peptides on different organisms, Int. J. Mol. Sci., 21(2020) 986. doi:10.3390/ijms21030986

[11] Fausett, L, Fundamentals of neural networks, architectures, algorithms, and applications, Prentice-Hall, inc., New Jersey, 1994.

[12] M. Sugimoto, S. Kikuchi, M. Arita, T. Soga, T. Nishioka, M. Tomita, Large-scale prediction of cationic metabolite identity and migration time in capillary electrophoresis mass spectrometry using artificial neural networks, Anal. Chem., 77 (2005) 78-84

[13] K. Shinoda, M. Sugimoto, N. Yachie, N. Sugiyama, T. Masuda, M. Robert, T Soga, M. Tomita, Prediction of liquid chromatographic retention times of peptides generated by protease digestion of the Escherichia coli proteome using artificial neural networks, J. Proteome Res., 5 (2006) 3312-3317.

[14] K. Khan, K. Roy, Ecotoxicological modelling of cosmetics for aquatic organisms: A QSTR approach, SAR QSAR Environ. Res., 28 (2017) 567-594.

[15] F. Yang, J. Tian, Y. Xiang, Z. Zhang, P. de B. Harrington, Near infrared spectroscopy combined with least squares support vector machines and fuzzy rule-building expert system applied to diagnosis of endometrial carcinoma, Cancer Epidemiol., 36 (2012) 317-323.

[16] R. Darnag, B.Minaoui, M. Fakir, QSAR models for prediction study of HIV protease inhibitors using support vector machines, neural networks and multiple linear regression, Arab. J. Chem., 10 (2017) S600-S608.

[17] G.J. Klir, B.Yuan, Fuzzy sets and fuzzy logic, theory and applications. Prentice-Hall, inc., New Jersey, 1995.

[18] H. Zarei, A. Khastan, A. Zafar, Optimal control of linear fuzzy time-variant controlled systems, Iran. J. Fuzzy Sys., 17 (2020) 1-12.

[19] J. Jantzen, Neurofuzzy modeling technical report no 98-H-874, 1998.

[20] M. G. Khaledi, Micellar electrokinetic chromatography in high performance capillary electrophoresis: theory, technique and applications, Wiley, New York, 1998.

[21] Fuzzy toolbox; Copyright 1994-2002, the math works, Inc. revision: 1.8; Roger Jang, Aug. 1997.

[22] J. Liu, H. Wang, LingZhi oligopeptides amino acid sequence analysis and anticancer potency evaluation, RSC Adv., 10 (2020) 8377-8384.

[23] C. Hansch, A. Leo, D. Hoekman, Exploring QSAR, hydrophobic, electronic, and steric constants, ACS, Washington DC., 1995.

[24] R. W. Taft, Steric effects in organic chemistry, John Wiley and Sons Inc.; New York, 1956.

[25] S. S. Samanta, S. P. Roche, Synthesis and reactivity of α-haloglycine esters: hyperconjugation in action, Eur. J. Inorg. Chem., 2019 (2019) 6597-6605.

[26] J.A. Macphee, A. Panaye, J.E. Dubois, Steric effects-I: A critical examination of the taft steric parameter-Es, definition of a revised, broader and homogeneous scale, extension to highly congested alkyl groups, Tetrahedron., 34 (1978) 3553-3562

Anal. Method Environ. Chem. J. 3 (2) (2020) 21-33

AMECJ

Research Article, Issue 2
Analytical Methods in Environmental Chemistry Journal
Journal home page: www.amecj.com/ir

Separation and determination of mercury from nail and hair in petrochemical workers based on silver carbon nanotubes by microwave-assisted headspace sorbent trap

Daniel Soleymani[a], Sahar Zargari[b] and Ali Faghihi-Zarandi[a,*]

[a] *Occupational Health Engineering Department, Modeling in Health Research Center, Institute for Futures Studies in Health,Kerman University of Medical sciences, Kerman, Iran*
[b]*Software Engineer, Statistical sciences and engineering, Department of Web development and software engineering, Research Institute of Petroleum Industry, Tehran, Iran*

ARTICLE INFO:

Received 29 Feb 2020
Revised form 17 Apr 2020
Accepted 14 May 2020
Available online 27 Jun 2020

Keywords:
Mercury,
Nail and Hair,
Silver multi-walled carbon nanotubes,
Microwave-assisted headspace removal

ABSTRACT

In this work, the occupational analytical chemistry was developed for determination of chronic exposure of mercury in nail and hair in petrochemical workers (Age: 30-50, Men). By experimental procedure, 100 mg of hair and nail of workers was prepared by washing / grinding and then the powder was dried in oven for 20 min at 95°C. 20 mg of hair or nail samples added to reagents (HNO_3/H_2O_2; 5:1) in polyethylene tube (PET) of microwave digestion and the mercury in resulting solution was removed with silver nanoparticles pasted on multi-walled carbon nanotubes (Ag-MWCNTs) which were placed in head space of separator. After microwave digestion for 25 min, the mercury vapor was removed by *Ag-MWCNTs* as the headspace sorbent trap (HSST) under hood conditions. Finally, the mercury in sorbent was online determined by cold vapor atomic absorption spectrometry (CV-AAS) after heat process at 250°C in presence of Ar gas. The capacity adsorptions of *Ag-MWCNTs* and *MWCNTs* for mercury removal from air were obtained 205.4 mg g^{-1} and 63.7 mg g^{-1}, respectively. The mean of mercury in nail and hair in workers and healthy peoples was achieved (15.2±3.7 µg g^{-1}; 11.6± 2.6 µg g^{-1}) and (0.16±0.05 µg g^{-1}; 0.24± 0.03 µg g^{-1}), respectively (RSD<5%). The validation of method was done by certified reference material (CRM).

1. Introduction

Mercury, as a trace heavy metal element, is the only common metal which is liquid at ordinary temperatures and has a high vapor pressure [1]. Atmospheric mercury is present in three forms: metallic or elemental mercury (Hg0), oxidized or inorganic mercury (Hg^{2+}) and particulate-bound mercury with organic materials such as methyl (R-Hg) [2]. Each of these forms has different impacts on health surveillance and requires different countermeasures to avoid exposure. Hg0 is oxidized to inorganic forms of Hg^{2+}, when entering the atmosphere. Elemental mercury in its gaseous form is the main form of mercury in the atmosphere with atmospheric lifetime of approximately 6–24 months [3]. It is a pollutant of great concern due to its volatility, toxicity, persistence, and bioaccumulation in the environment and its neurotoxic impact on human health [4,5]. Mercury vapors are well absorbed into blood through the lungs (approximately 80%) and can easily cross the blood-brain barrier as a lipid-soluble substance in human body tissues such as brain and

* Corresponding Author: Ali Faghihi-Zarandi
Email: alifaghihi60@yahoo.com
https://doi.org/10.24200/amecj.v3.i02.99

renal [6]. Chlor-alkali factories using mercury metal as a liquid electrode in the manufacturing of chlorine (Cl2) and sodium hydroxide (NaOH) by electrolysis release of the mercury vapor in air and so, it causes to disease in workers by exposure of the workers to mercury [7]. Chlor–alkali plants (CAP) which use mercury (Hg) in electrolytic cell manufacture has been identified as one of the main sources of Hg pollution in environmental air. Although alternative methods were established to replace the Hg-cell process, many older plants are still in operation in some undeveloped areas. In addition, many amounts of mercury enter to environment by different sources such as chemical factories, petrochemical activity, volcanoes, forest fires, and fossil fuels [8]. Bioaccumulation of mercury in the human body changes the normal cell/tissues/organs and cause to cancer. It can damage the physiological activities of the human body especially in the brain and renal, even at very low concentrations of mercury [9]. The primary target for Hg exposure is the central nervous system (CNS) and then, it can also damage many organ systems such as liver and renal through its ephemeral and residual systemic distribution [10] Finally, the chronic mercury exposure can be damaged the cells of kidney [11] and central nervous system (CNS) [12]. In addition, the other organs/systems such as the immune system, reproduction and cardiovascular system can also be affected by mercury exposure [13]. The mercury exposure has adverse health effect in human body and can depend on the form of the mercury, time and dose of exposure [14]. Acute, high-dose exposure to elemental mercury vapor may cause to pneumonitis. At low levels, the acute lung injury, insomnia, headaches, disturbances in sensations and changes in nerve responses is obtained and then, the chronic inhalation cause to many problems include, tremor, gingivitis, particularly irritability, depression, short-term memory loss, fatigue, anorexia, and sleep disturbance [15]. In the general population, the total blood mercury concentration is due mostly to the dietary intake of organic forms, particularly methyl mercury and urinary mercury consists mostly of inorganic mercury forms [15]. Several studies identified a significant positive association between mercury in hair samples and hypertension (blood pressure); whereby the exposure dose is an important factor for determining the toxic effects of mercury [16]. Hair mercury concentration as a biomarker of organic and inorganic mercury exposure can be provided the information over a definable period of time, based upon sequential analyses of hair segments, to represent both the magnitude and timing of past exposure. However, the mercury analysis in hair have two problems. The first concerns the origin of the measured elements, and the second concerns the biological significance that may be given to the level of the elements. Unlike hair, total blood mercury levels also include inorganic mercury, which may be of importance in certain contexts. It is generally considered the appropriate indicator of the absorbed dose. Urinary mercury concentrations are widely used as a biomarker of mercury exposure from elemental or inorganic mercury [17]. Note, the inorganic mercury can be changed to organic forms by high concentration of mercury or chronic exposure of mercury. It is very important to develop a novel analytical method for determination of heavy metals in environment and biological samples for monitoring the severity of heavy metal pollution. At the present time, the most well-known methods for detecting heavy metals are atomic absorbance spectrometry (AAS) [18], atomic fluorescence spectrometry (AFS) [19], electrochemical analysis, inductively coupled plasma (ICP) [20], high performance liquid chromatography (HPLC) [21] and capillary electrophoresis [22]. However, these methods generally need a sample preparation or extraction procedure [23]. Recently, the cold vapor atomic absorption spectrometry (CV-AAS) was used as a favorite analytical technique for mercury analyses in various types of samples [24], but it has been necessary to develop with preconcentration methods that allow mercury determination at ultra-trace levels [25]. Liquid-liquid extraction/micro extraction (LLE/LLME) and solid-phase extraction/ micro solid-phase extraction (SPE&MSPE) are the most commonly employed methods to achieve the separation and preconcentration of metal ions [26-28]. In this study, the chronic exposure of mercury in nail and hair of petrochemical workers was determined

by microwave-assisted headspace removal procedure (MAHR). By procedure, the microwave based on silver nanoparticles passed on multi-walled carbon nanotubes (Ag-MWCNTs) was used as head space removal and mercury concentration was determined by CV-AAS.

2. Experimental

2.1. Instrumental

Mercury was measured by an atomic absorption spectrometer (AAS, GBC 932, Australia) equipped with a flow injection cold vapor accessory (FI-CV). The background correction with a deuterium-lamp and hollow-cathode lamp of mercury was used. The circulating cooling unit (CCU) caused to generation of vapour of mercury in cold conditions. NaBH4 / NaOH or SnCl2/HCl was used as reduction agents for generating of mercury hydride which was moved to liquid –gas separator by Ar. The conditions of FI-CVAAS were shown in Table 1. The pH ranges in liquid phase were adjusted and determined by a Metrohm pH meter (744, Switzerland). The multi-wave microwave system (MMS, Anton Paar 3000, Austria) was used for digestion of hair and nail samples which was converted the organic mercury to inorganic mercury. Anton Paar's 8-position rotor (8SXQ80) and respective reaction vessels individually equipped with variable temperature and ultraviolet (UV) radiations. The temperature and pressure of MMS were 220°C and 35 bar, respectively.

Table 1. The conditions of mercury determination by FI-CVAAS with closed cell

Features	Value
Linear range	0.5-65 µg L^{-1}
Working range	0.5-150 µg L^{-1}
Wavelength	253.7 nm
Lamp current	4.0 mA
Slit	0.5 nm
Mode	Peak Area surface
HCl carrier solution 37%	3.4 mol L^{-1}
NaBH4 reducing agent, % (m/v)	0.6 (0.5% NaOH)
Argon flow rate	15.0 mL min^{-1}
Sample flow rate	4.0 mL min^{-1}
Reagent flow rate	mL min^{-1}

2.2. Reagents

All reagents with high purity as an analytical grade were purchased from Merck (Darmstadt, Germany). All samples were prepared with the deionized water (DW) from Millipore water system (USA). The standard stock solution of inorganic mercury (1000 mg L-1 Hg(II) in 1% nitric acid) was purchased from Fluka, Switzerland. The working standard solutions were prepared daily by diluting of standard solutions with DW. The solutions were freshly prepared and stored just in a fridge (4 °C) to prevent decomposition. First, 0.6% (w/v) NaBH4 solution was prepared daily by dissolving in 0.5% (w/v) sodium hydroxide (NaOH) and used as a reducing agent. The glassware and plastics of laboratory were cleaned by nitric acid (15%, v/v) for at least 12 h and then washed with DW. Silver nitrate, ammonia, formalin, and ethanol were purchased from Merck Company (Germany).

2.3. Synthesis of AgNPs-MWCNTs

The silver nanoparticles passed on MWCNTs have prepared. First, the mixture of MWCNTs (10 mg) in 100 mL of DW solution was prepared and then, 0.3 g of T-X100 as a surfactant was dispersed in mixture at 300 rpm stirring speed. The 0.5 g of silver nitrate was added to the mixture (MWCNTs/AgNO3/TX-100/DW) without heat in same stirring speed (300 rpm). Finally, 2 mL of the ammonia solution was added to above solution and diluted with DW up to 0.5 L by stirring at 15 minute. Then, 12 mL of formalin as a reducing agent was added to product in 5 min and by increasing the speed of stirring (600-800 rpm), the AgNPs (20-100 nm) were coated on the MWCNTs. For cleaning of the MWCNTs from CH_2O and NH_3, the product was washed with DW for 10 times. For preventing of silver oxidation, the product (AgNPs-MWCNTs) washed with Ethanol or increasing temperature up to 180°C.

2.4. Procedure

As Figure 1, 20 mg of hair or nail samples and reagents (HNO_3 / H_2O_2; 5:1) was put into PET of microwave digestion at UV/@220°C for 30 min.

After digestion, the resulting solution was diluted with DW up to 10 mL mixed with reducing reagents ($NaBH_4$/NaOH) in mixer. Then, the hydride form of mercury in liquid phase was generated by reaction loop before moved to separator by flowrate of 100 ml min-1. As ultra-trace mercury (sub ppb), the mercury was preconcentrated by Ag-MWCNTs trap in head space of separator. Finally, the concentration mercury was online determined by closed cell FI-CV-AAS after thermal desorption by heat accessory at 185°C in presence of Ar gas. The peak area of absorption was calculated as concentration of mercury in nail or hair samples by Avanta software of FI-CV-AAS. The conditions of procedure were shown in Table 2.

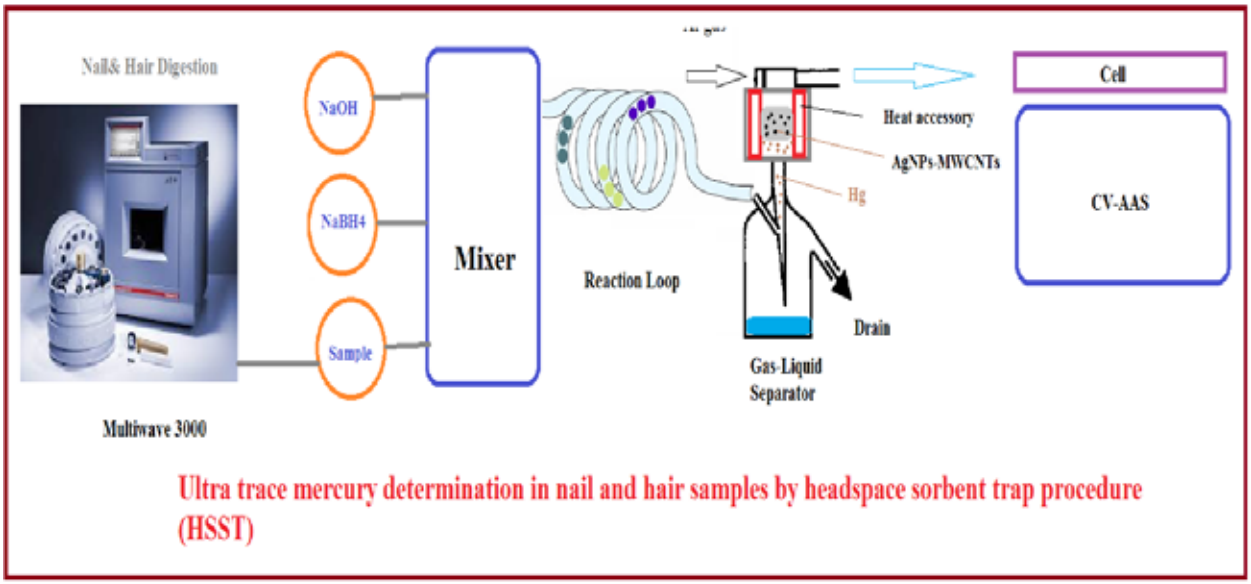

Fig.1. Determination mercury in nail and hair based on Ag-MWCNTs by HSST method

The Ethical Committee of Kerman University of Medical Science (E.C.:IR.KMU.REC.1400.143) was approved the project of human nail and hair samples which was considered based on guiding physicians in human body research in human tissue by the world medical association declaration of Helsinki.

Table 2. The conditions of the headspace sorbent trap (HSST) method in nail, hair and water samples by Ag-MWCNTs sorbent

Parameter	Nail/Hair sample	Water sample
PF[a]	32.2	35.1
LOD[b] (n=10, ng L^{-1})	5.3	4.5
RSD[c] (%)	2.4	1.9
Linear range (µg L^{-1})	0.015– 2.1	0.013-1.85
Working range(µg L^{-1})	0.015– 4.7	0.013-4.4
Correlation coefficient	0.9991	0.9995

[a] Preconcentration factor, [b] Limit of detection,
[c] Relative standard deviation.

3. Results and Discussion

As chronic exposure of mercury in nail and hair in petrochemical workers, the novel method based on Ag-MWCNTs sorbent was used for mercury determination by microwave-headspace sorbent trap (MW-HSST) procedure. For optimization recovery, the parameters such as, temperature, flowrate, adsorption capacity was studied. On the other hand, validation of proposed method was achieved based on spiking samples and Microwave digestion coupled to gold MC-3000 as ultra-trace analyzer of mercury (ppt). Based on results, the recovery of Ag-MWCNTs and MWCNTs sorbents was obtained 38.5 and 98.3, respectively. The recoveries in Ag-MWCNTs and MWCNTs sorbents were determined by MW-HSST procedure (equation I). Furthermore, the adsorption capacity of sorbents was considered by equation of II.

$$Recovery = \frac{a}{b} \times 100 \quad \text{(Eq. I)}$$

$$Adsorption\ Capacity = \frac{(C_1 - C_2) \times v}{m} \quad \text{(Eq. II)}$$

As equation I, a is the primary concentration of mercury and b is the final concentration of mercury, the adsorption capacity (mg g^{-1}) was shown in equation of II and and (mg L^{-1}) are before and after adsorption of mercury concentration by Ag-MWCNTs, V is the air volume as flowrate and (g) is the mass of Ag-MWCNTs.

3.1. Characterization

The specific surface area (SBET) of Ag-MWCNT and MWCNTs were obtained from the BET equation at 20^{oC}. Decreasing of BET surface area of Ag-MWCNT in comparison with initial MWCNT was due to the grafting of silver nanoparticles on walls of MWCNTs.

The SEM micrographs of MWCNTs and Ag-MWCNTs were shown in Figure 2a and 2b. The diameter of MWCNTs and Ag-MWCNTs is approximately between 30-100 nm. The XRD patterns of MWNTs and Ag-MWCNTs were shown in Figure 3. The TEM micrographs (Germany, Philips CM30, 250 kV) showed the morphology of the MWCNTs and Ag-MWCNTs particles. Nano particles of MWNTs and Ag-MWCNTs were dissolved in ethanol by shaking for 15 min and a drop of the ethanol was used by TEM instrument. The similar TEM micrographs for MWNTs and Ag-MWCNTs were obtained about 40 nm (Fig. 4a and 4b).

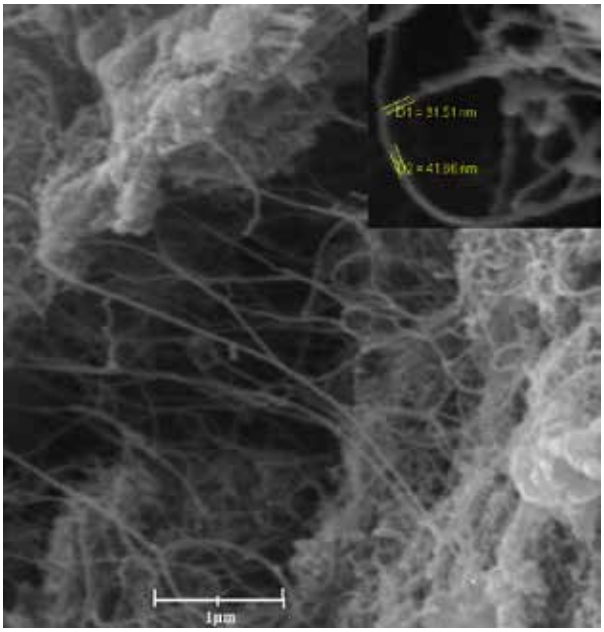

Fig. 2a. The SEM of MWCNTs.

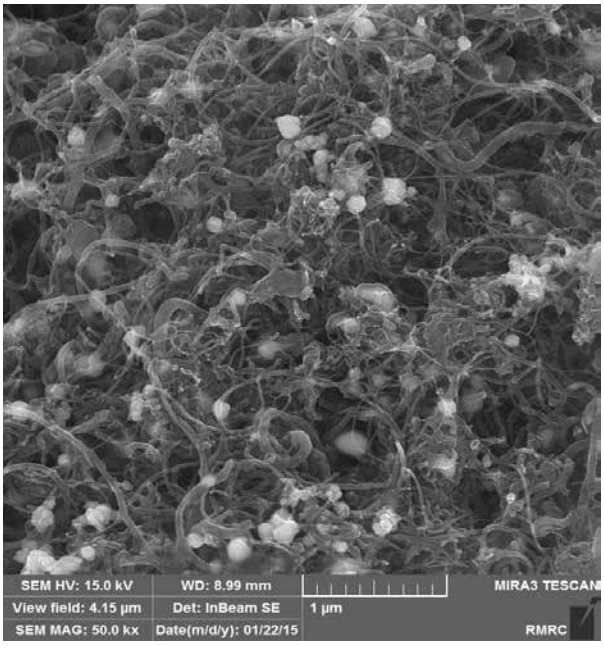

Fig. 2b. The SEM of Ag-MWCNTs.

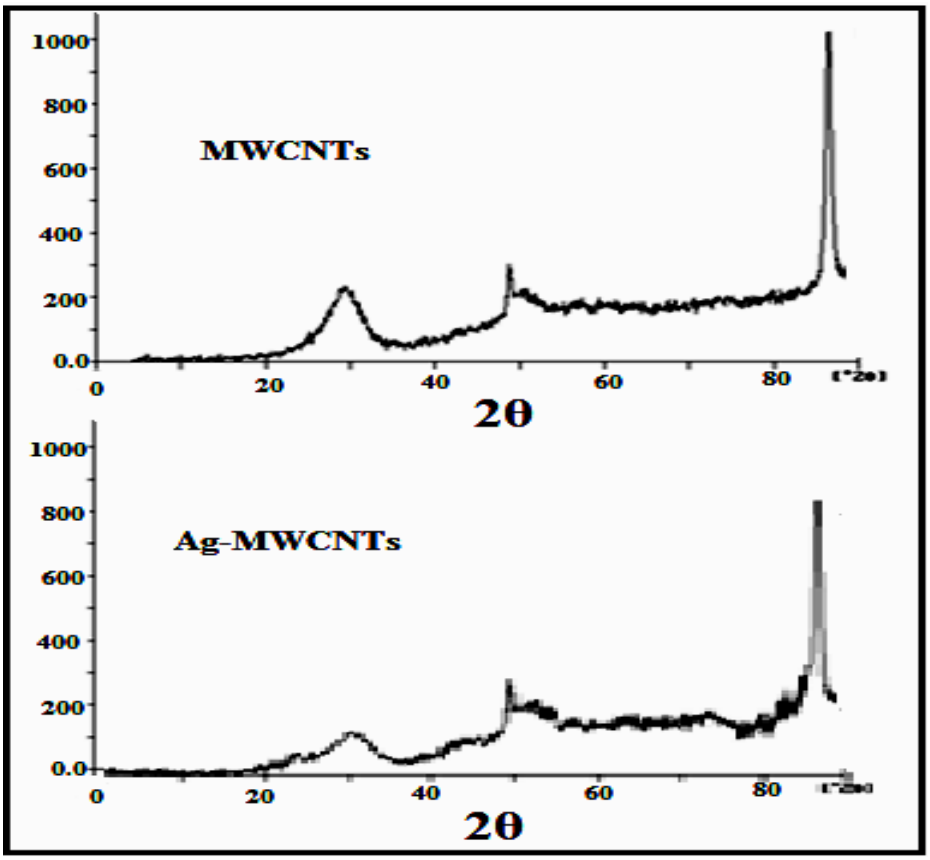

Fig. 3. The XRD of MWCNTs and Ag-MWCNTs

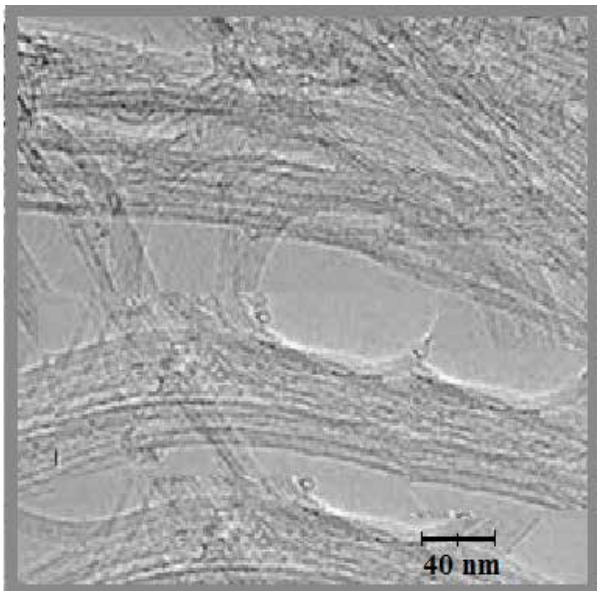

Fig. 4a. The TEM of MWCNTs.

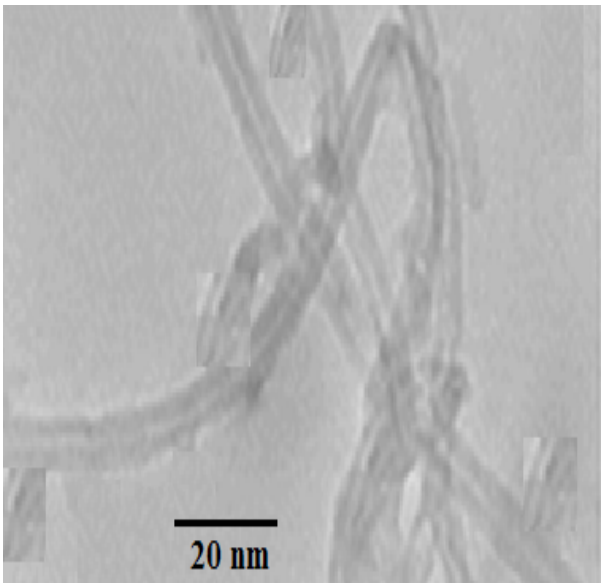

Fig. 4b. The TEM of Ag-MWCNTs

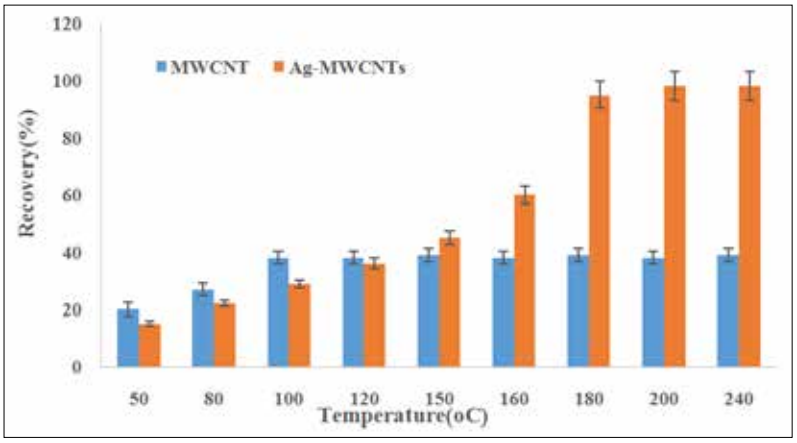

Fig. 5. The effect of temperature on desorption mercury from Ag-MWCNTs and MWCNTs sorbents by HSST method.

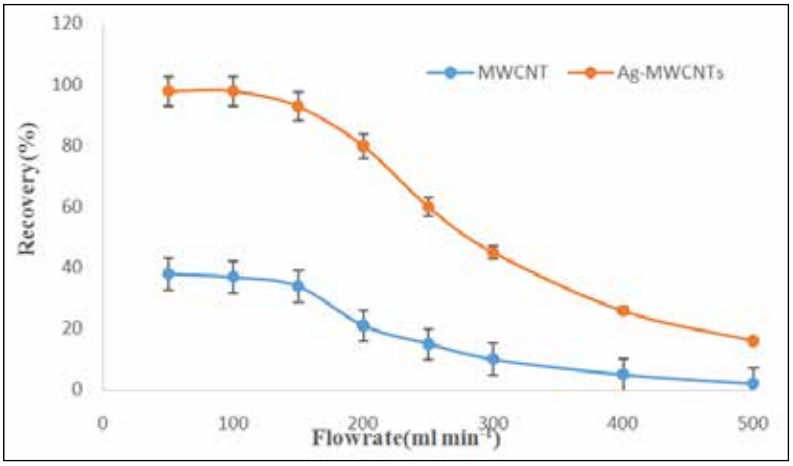

Fig. 6. The effect of flow rate on removal of mercury vapor from liquid phase by Ag-MWCNTs and MWCNTs sorbents

3.2. Effect of temperature

The effect of temperature for absorption and desorption mercury by Ag-MWCNTs sorbent was investigated. The temperatures between 20-2000C was studied for procedure. As results, the recovery of Ag-MWCNTs and MWCNTs was decreased in high temperature and the mercury can be desorbed from Ag-MWCNTs and MWCNTs at 185oC and more than 80oC. The results showed, the optimum temperature for adsorption and desorption mercury from Ag-MWCNTs sorbent was obtained 25-35oC and 185oC (Fig. 5).

At temperature more than 35oC, the removal efficiency of mercury by Ag-MWCNTs were decreased. Temperature had more effected on mercury removal by Ag-MWCNTs as compared to humidity.

3.3. Effect of flow rate

The main factor for adsorption of mercury on Ag-MWCNTs sorbent was depended on flowrate of Argon gas which was caused to increase interaction Hg with Ag as amalgamation form (Ag-Hg). As optimized conditions for removal of mercury by headspace sorbent trap (HSST) method, the flow rates must be evaluated. So, the flow rates between 50 - 500 mL min-1 were optimized for Ag-MWCNTs and MWCNTs at room temperature. The flow rate was determined by a rotameter accessory in room temperature. In high and low flowrate, the rate of adsorption was reduced and increased, respectively. The results showed that maximum recovery for mercury removal was achieved by Ag-MWCNTs at flowrate 100 ml min-1. Figure 6 showed the effects of flow rate on the removal efficiency of mercury by HSST method.

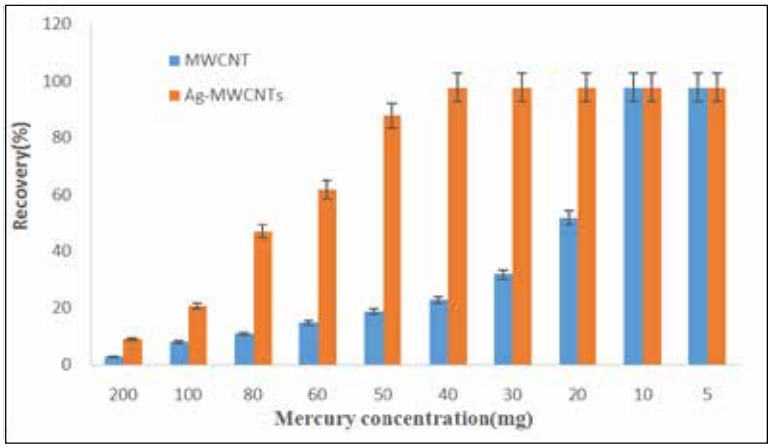

Fig. 7. The absorption capacity of mercury by Ag-MWCNTs and MWCNTs sorbents by HSST method

3.4. Adsorption capacity

In this study, the adsorption capacity of mercury by Ag-MWCNTs, and MWCNTs in batch system has obtained 205.4 mg g^{-1}, 63.7 mg g^{-1}, respectively which was shown in Figure 7. The closed special vial (10 mL) was used with 5 mL of liquid standard mercury value (100 mg), 0.2 g of Ag-MWCNTs, and MWCNTs sorbents in head space of vial and reducing agents which was added by syringe with beside input port. After 5, 10, 15, 20 min, the mercury in sorbent determined by CV-AAS. The results showed us, the maximum removal was achieved by Ag-MWCNTs after 15 min. By procedure, the final concentration in sorbent was obtained 41.1 mg of mercury after thermal desorption.

3.5. Validation

The accurate and precise results for mercury determination in nail /hair are important factor for human samples. So, the mercury results based on Ag-MWCNTs must be validated by MW-HSST procedure. First, the different concentration of standard mercury solutions from 0.5 to 5 µg L^{-1} was prepared. For validation, the different concentrations of mercury were used for spiking of nail, hair and water samples by Ag-MWCNTs sorbents (Table 3). The removal efficiency of sorbents based on MW-HSST was evaluated. For method validation ICP analyzer was used for nail and hair samples after sample digestion (Table 4). In addition, the removal efficiency of mercury in water and gas phase by different sorbents was compared to MW-HSST procedure (Table 5). According to table5, the Ag-MWCNTs have more efficiency than other sorbents. The Ethical Code for human nail and hair samples approved by Kerman University of Medical Science (E.C.: IR.KMU.REC. 1400.143).

Table 3. Validation of MW-HSST procedure for total mercury determination in nail, hair and water samples by spiking of real samples

Sample	Added (µg L^{-1})	Found (µg L^{-1})	Recovery(%)
Human Nail	------	1.43 ± 0.05	------
	1.5	2.91 ± 0.12	98.6
Human Nail	------	0.17 ± 0.01	------
	0.2	0.36 ± 0.02	95.0
Human Hair	------	1.98 ± 0.08	------
	2.0	4.02 ± 0.17	102
Human Hair	------	0.55 ± 0.02	------
	0.5	1.03 ± 0.04	95.8
Well Water	------	0.38 ± 0.01	------
	0.5	0.86 ± 0.03	96.0

Table 4. ICP analyzer was used for validation of proposed method for mercury determination in nail and hair samples after sample digestion

Sample	ICP-MS (μg L^{-1})	Added (μg L^{-1})	Found (μg L^{-1})	Recovery (%)
Nail	1.24 ± 0.03	------	1.20 ± 0.05	96.8
	------	1.0	2.17 ± 0.09	97.0
Hair	0.52	------	0.54 ± 0.03	103.8
	------	0.5	1.02 ± 0.04	96.0

Table 5. Comparing of Ag-MWCNTs based on MW-HSST procedure with different sorbents by published method

Sorbents	Matrix	Technique	Absorption Capacity (mg g^{-1})	Recovery	Reference
Solid-phase extraction with multiwalled carbon nanotubes	Real waters	Adsorption	0.70–3.83	----	[29]
Ag-CNT	Flue gases	Amalgamation	9.3	----	[30]
Silver nano particles/ MGBs	Air/Artificial air	Amalgamation/ SPGE	91.8	98%	[31]
Mn/zeolite catalyst	Flue gas	Microwave assisted catalytic	----	35.3%	[32]
Porous carbon-supported $CuCl_2$	Gas	----	----	98.5%	[33]
Nano-ZnS	Coal Combustion Fuel Gas	Adsorption	497.84 (μg·g^{-1})	----	[34]
nano-ceramic	Flue gas	Chemisorption	----	75.58%	[35]
Au NP–Al_2O_3	Natural Waters	Adsorption	145 (μmol g^{-1})	97%	[36]
Silver/quartz nanocomposite	Aqueous solutions	----	376.3	96%	[37]
magnetic nanoparticles coated with yam peel biomass (MNP-YP)	Water	Complexation	----	75%	[38]
Reduced graphene oxide	Water	SPE/Anodic Stripping Voltammetry	77.0	96.4	[40]
Ag-MWCNTs	Nail/Hair	MW-HSST	205.4	98.8	This work

3.6. Discussion

Krawczyk et al was used TiO_2 nanoparticles (NPs) as adsorbent for preconcentration and determination of mercury species (Hg total, Hg^{2+} and CH_3Hg^+) in biological, environmental and water samples. The mercury extracted based on ultrasound-assisted dispersive micro solid-phase extraction (USA DMSPE) and determined by cold vapor atomic absorption spectrometry (CV AAS). The detection limit of the method for Hg^{2+} and relative standard deviations (RSD%) was obtained 4 ng L^{-1} and 4–20%, respectively. The mercury was separated from liquid phase with 10 mg of TiO_2 at pH 7.5[39]. In addition, Ma et al showed that the mercaptopropyl

trimethoxysilane (MPTS) modified on Fe_3O_4@SiO_2 as a magnetic nanoparticles (MNPs) can used for the speciation of mercury in environmental water and human hair samples. The characterization of (MPTS-MNPs) was obtained by Fourier transform infrared spectrometer (FT-IR), transmission electron microscope (TEM) and vibrating sample magnetometer (VSM). In the optimized conditions, the limits of detection (LOD) for CH_3Hg^+ and total Hg were achieved 1.6 and 1.9 ng L^{-1}, respectively. This method successfully applied for the speciation of CH_3Hg^+ and Hg^{2+} in water and hair samples [40]. A novel Fe_3O_4@SiO_2@polythiophene magnetic nanocomposite was synthesized by Abolhasani et al. They could determine the Hg(II) ions in sea food samples. After sample digestion, the mercury was determined by cold vapor atomic absorption spectrometry (CV AAS). Under the optimum condition, the LOD (20 ng L^{-1}) and RSD% (9.2 %) were obtained. The capacity adsorption of Fe_3O_4@ SiO_2@polythiophene magnetic nanocomposite was 59 mg g^{-1} which was lower than our proposed method base on Ag-MWCNTs (184.3 mg g^{-1}) [41]. In other study, Akbar et al was reported a SPE method based on mGO@SiO_2@2-MPATD nanocomposite for determination of mercury in the water and seafood samples. The characterization was obtained by FT-IR, SEM, and elemental analysis techniques. After adsorption and elution steps, the concentration of Hg (II) was measured by CV-AAS. Under the optimized conditions, the limit of detection was 8 ng L^{-1}. The capacity adsorption of mGO@SiO_2@2-MPATD was obtained 236 mg g^{-1} which was higher than proposed method by Ag-MWCNTs [42]. Also, Krawczyk et al introduced the silver nanoparticles (AgNPs) as solid sorbent for preconcentration and determination of Hg^{2+} ions in water samples. The limit of detection and RSD% was achieved 5 ng L^{-1} and 6-11%, respectively [43].

4. Conclusions

In this study, a robust analytical method based on microwave coupled to headspace sorbent trap (HSST) was developed for determination mercury in nail and hair in petrochemical male workers aged 30 to 60 years. Results showed the capacity adsorptions of Ag-MWCNTs and MWCNTs for mercury removal from the air were obtained 205.4 mg g^{-1} and 63.7 mg g^{-1}, respectively. It means that mercury removal from the air was increased dramatically by silver nanoparticles pasted on multi-walled carbon nanotubes. After nail/hair digestion, the mercury in liquid phase converted to hydride form (HgH_2) and captured by silver nanoparticles on MWCNTs as a sorbent trap in head space of separator. The LOD and LOQ of proposed procedure was obtained 5 ng L^{-1} and 15 ng L^{-1}, respectively. Also, the mean of mercury in nail and hair in workers and control group was achieved (15.2 ±3.7 µg g^{-1}; 11.6 ± 2.6 µg g^{-1}) and (0.16 ± 0.05 µg g^{-1}; 0.24 ± 0.03 µg g^{-1}), respectively (RSD<5%). Regardless of the interfering factors, the difference between these values is due to high exposure with mercury.

5. References

[1] H. Satoh, Occupational and environmental toxicology of mercury and its compounds, Industrial. Health, 38 (2000) 153-164.

[2] B. Zhao, H.H. Yi, X.L. Tang, Q. Li, D.D. Liu, F.Y. Gao, Copper modified activated coke for mercury removal from coal-fired flue gas, Chem. Eng. J., 286 (2016) 585-593.

[3] UN Environment Document Repository, Global mercury modelling: update of modelling results in the global mercury assessment 2013. https://wedocs.unep.org/handle/20.500.11822/13772 , 2015.

[4] Y.S. Gao, Z. Zhang, J.W. Wu, L.H. Duan, A. Umar, L.Y. Sun, Z.H. Guo, Q. Wang, A critical review on the heterogeneous catalytic oxidation of elemental mercury in flue gases, Environ. Sci. Technol., 47 (2013) 10813–10823.

[5] S.L. Tang, L.N. Wang, X.B. Feng, Z.H. Feng, R.Y. Li, H.P. Fan, K. Li, Actual mercury speciation and mercury discharges from coal-fired power plants in Inner Mongolia, northern China, Fuel, 180 (2016) 194–204.

[6] M. Sakamoto, N. Tatsuta, K. Izumo, P.T. Phan, L.D. Vu, M. Yamamoto, M. Nakamura, K. Nakai, K. Murata, Health impacts and biomarkers of prenatal exposure to methylmercury: Lessons from Minamata, Japan, Toxic., 6 (2018).

[7] G.J. Zagury, C.-M. Neculita, C. Bastien, L. Deschênes, Mercury fractionation, bioavailability, and ecotoxicity in highly contaminated soils from chlor-alkali plants, Environ. Toxicol. Chem., 25 (2006) 1138-1147.

[8] C. Feng, Z. Zayas, L. Lima, S. Olivares, D. De La Rosa, S. Berail, E. Tessier, F. Pannier, D. Amouroux, Assessment of Hg contamination by a chlor-alkali plant in riverine and coastal sites combining Hg speciation and isotopic signature (Sagua la Grande River, Cuba), J. Hazard. Mater., 371 (2019) 558-65.

[9] L.-n. Liang, J.-b. Shi, B. He, G.-b. Jiang, C.-g. Yuan, Investigation of methyl mercury and total mercury contamination in mollusk samples collected from Coastal sites along the Chinese Bohai sea, J. Agric. Food. Chem., 51 (2003) 7373-7378.

[10] C. Gundacker, S. Fröhlich, K. Graf-Rohrmeister, B. Eibenberger, V. Jessenig, D. Gicic, S. Prinz, K.J. Wittmann, H. Zeisler, B. Vallant, A. Pollak, P. Husslein, Perinatal lead and mercury exposure in Austria, Sci. Total. Environ., 408 (2010) 5744-5749.

[11] S.E. Orr, C.C. Bridges, Chronic kidney disease and exposure to nephrotoxic metals, Int. J. Mol. Sci., 18 (2017).

[12] H. Lohren, J. Bornhorst, R. Fitkau, G. Pohl, H.-J. Galla, T. Schwerdtle, Effects on and transfer across the blood-brain barrier in vitro—Comparison of organic and inorganic mercury species, BMC. Pharmacol. Toxicol., 17 (2016) 63.

[13] G. Genchi, M.S. Sinicropi, A. Carocci, G. Lauria, A. Catalano, Mercury exposure and heart diseases, Int. J. Environ. Res. Public. Health, 14 (2017) 74.

[14] F. Ruggieri, C. Majorani, F. Domanico, A. Alimonti, Mercury in children: current state on exposure through human biomonitoring studies, Int. J. Environ. Res. Public. Health, 14 (2017).

[15] Centers for Disease Control and Prevention, National biomonitoring program: mercury, 2017. https://www.cdc.gov/biomonitoring/Mercury_BiomonitoringSummary.html/

[16] X.F. Hu, K. Singh, H.M. Chan, Mercury exposure, blood pressure, and hypertension: A systematic review and dose-response meta-analysis, Environ. Health. Perspect., 126 (2018) 076002.

[17] L.T. Budnik, L. Casteleyn, Mercury pollution in modern times and its socio-medical consequences, Sci. Total. Environ., 654 (2019) 720-734.

[18] M.A. Kamyabi, A. Aghaei, A simple and selective approach for determination of trace Hg (II) using electromembrane extraction followed by graphite furnace atomic absorption spectrometry, Spectrochim. Acta Part B: At. Spect., 128 (2017) 17-21.

[19] S.L.C. Ferreira, J.P. dos Anjos, C.S.A. Felix, M.M. da Silva Junior, E. Palacio, V. Cerda, Speciation analysis of antimony in environmental samples employing atomic fluorescence spectrometry–Review, Trends. Anal. Chem., 110 (2019) 335-343.

[20] M.-L. Lin, S.-J. Jiang, Determination of As, Cd, Hg and Pb in herbs using slurry sampling electrothermal vaporisation inductively coupled plasma mass spectrometry, Food. Chem., 141 (2013) 2158-2162.

[21] M. Thirumalai, S.N. Kumar, D. Prabhakaran, N. Sivaraman, M.A. Maheswari, Dynamically modified C18 silica monolithic column for the rapid determinations of lead, cadmium and mercury ions by reversed-phase high-performance liquid chromatography, J. Chromatogr. A, 1569 (2018) 62-69.

[22] S. Wang, X. Song, J. Hu, R. Zhang, L. Men, M. Wei, T. Xie, J. Cao, Direct speciation analysis of organic mercury in fish and kelp by on-line complexation and stacking using

capillary electrophoresis, Food. Chem., 281 (2019) 41-48.

[23] Y. Wu, X. Wen, Z. Fan, An AIE active pyrene based fluorescent probe for selective sensing Hg2+ and imaging in live cells, Spectrochim. Acta. A. Mol. Biomol. Spec., 223 (2019) 117315.

[24] A.A. Elezz, H. Mustafa Hassan, H. Abdulla Alsaadi, A. Easa, S. Al-Meer, K. Elsaid, Z.K. Ghouri, A. Abdala, Validation of total mercury in marine sediment and biological samples, using cold vapour atomic absorption spectrometry, Method. Protoc., 1 (2018) 31.

[25] F. Mercader-Trejo, R. Herrera-Basurto, E.R. de San Miguel, J. de Gyves, Mercury determination in sediments by CVAAS after on line preconcentration by solid phase extraction with a sol-gel sorbent containing CYANEX 471X, Int. J. Environ. Anal. Chem., 91 (2011) 1062-1076.

[26] V. Camel, Solid phase extraction of trace elements, Spectrochim. Acta. Part. B: At. Spec., 58 (2003) 1177-1233.

[27] A.E. Visser, R.P. Swatloski, S.T. Griffin, D.H. Hartman, R.D. Rogers, Liquid-liquid extraction of metal ions in room temperature ionic liquids, Sep. Sci. Technol., 36 (2001) 785-804.

[28] W.I. Mortada, I.M.M. Kenawy, Y.G. Abou El-Reash, A.A. Mousa, Microwave assisted modification of cellulose by gallic acid and its application for removal of aluminium from real samples, Int. J. Biol. Macromol., 101 (2017) 490-501.

[29] A.H. El-Sheikh, Y.S. Al-Degs, R.M. Al-As'ad, J.A. Sweileh, Effect of oxidation and geometrical dimensions of carbon nanotubes on Hg(II) sorption and preconcentration from real waters, Desalination, 270 (2011) 214-220.

[30] G. Luo, H. Yao, M. Xu, X. Cui, W. Chen, R. Gupta, Z. Xu, Carbon Nanotube-Silver Composite for Mercury Capture and Analysis, Energ. Fuels, 24 (2010) 419-426.

[31] H. Shirkhanloo, M. Osanloo, M. Ghazaghi, H. Hassani, Validation of a new and cost-effective method for mercury vapor removal based on silver nanoparticles coating on micro glassy balls, Atmos. Pollut. Res., 8 (2017) 359-365.

[32] Z. Wei, Y. Luo, B. Li, Z. Cheng, J. Wang, Q. Ye, Microwave assisted catalytic removal of elemental mercury from flue gas using Mn/zeolite catalyst, Atmos. Pollut. Res., 6 (2015) 45-51.

[33] F. Shen, J. Liu, Y. Dong, D. Wu, C. Gu, Z. Zhang, Elemental mercury removal from syngas by porous carbon-supported CuCl2 sorbents, Fuel, 239 (2019) 138-144.

[34] H. Li, L. Zhu, J. Wang, L. Li, K. Shih, Development of nano-sulfide sorbent for efficient removal of elemental mercury from coal combustion fuel gas, Environ. Sci. Technol., 50 (2016) 9551-9557.

[35] T. Zhu, W. Jing, X. Zhang, W. Bian, Y. Han, T. Liu, Y. Hou, Z. Ye, Gas-phase elemental mercury removal by nano-ceramic material, Nanomater. Nanotechnol., 10 (2020) 1847980419899759.

[36] S.-I. Lo, P.-C. Chen, C.-C. Huang, H.-T. Chang, Gold nanoparticle–aluminum oxide adsorbent for efficient removal of mercury species from natural waters, Environ. Sci. Technol., 46 (2012) 2724-2730.

[37] R.S. El-Tawil, S.T. El-Wakeel, A.E. Abdel-Ghany, H.A.M. Abuzeid, K.A. Selim, A.M. Hashem, Silver/quartz nanocomposite as an adsorbent for removal of mercury (II) ions from aqueous solutions, Heliyon, 5 (2019) e02415.

[38] W. Marimón-Bolívar, L. Tejeda-Benítez, A.P. Herrera, Removal of mercury (II) from water using magnetic nanoparticles coated with amino organic ligands and yam peel biomass, Environ. Nanotechnol. Monit. Manage., 10 (2018) 486-493.

[39] M. Krawczyk, E. Stanisz, Ultrasound-assisted dispersive micro solid-phase extraction with nano-TiO2 as adsorbent for the determination of mercury species, Talanta, 161 (2016) 384-391.

[40] S. Ma, M. He, B. Chen, W. Deng, Q. Zheng, B.

Hu, Magnetic solid phase extraction coupled with inductively coupled plasma mass spectrometry for the speciation of mercury in environmental water and human hair samples, Talanta, 146 (2016) 93-99.

[41] J. Abolhasani, R. Hosseinzadeh Khanmiri, M. Babazadeh, E. Ghorbani-Kalhor, L. Edjlali, A. Hassanpour, Determination of Hg(II) ions in sea food samples after extraction and preconcentration by novel Fe3O4@SiO2@ polythiophene magnetic nanocomposite, Environ. Monit. Assess., 187 (2015) 554.

[42] M. Akbar, M. Manoochehri, An efficient 2-mercapto-5-phenylamino-1,3,4-thiadiazole functionalized magnetic graphene oxide nanocomposite for preconcentrative determination of mercury in water and seafood samples, Inorg. Chem. Commun., 103 (2019) 37-42.

[43] M. Krawczyk, E. Stanisz, Silver nanoparticles as a solid sorbent in ultrasound-assisted dispersive micro solid-phase extraction for the atomic absorption spectrometric determination of mercury in water samples, J. Anal. At. Spectrom., 30 (2015) 2353-2358.

Anal. Method Environ. Chem. J. 3 (2) (2020) 34-58

AMECJ

Research Article, Issue 2
Analytical Methods in Environmental Chemistry Journal
Journal home page: www.amecj.com/ir

A Review, Methods for removal and adsorption of volatile organic compounds from environmental matrixes

Shahnaz Teimoori[a], Amir Hessam Hassani[b,*] Mostafa Panahi[c] and Nabiollah Mansouri[d]

[a] *PhD student of environmental engineering, Faculty of Natural Resources and Environment, Science and Research Branch, Islamic Azad University, Tehran, Iran*
[b] *Department of environmental engineering, Faculty of Natural Resources and Environment, Science and Research Branch, Islamic Azad University, Tehran, Iran*
[C] *Department of environmental engineering, Faculty of Natural Resources and Environment, Science and Research Branch, Islamic Azad University, Tehran, Iran*
[d] *Department of environmental engineering, Faculty of Natural Resources and Environment, Science and Research Branch, Islamic Azad University, Tehran, Iran*

ARTICLE INFO:

Received 6 Mar 2020
Revised form 5 May 2020
Accepted 30 May 2020
Available online 30 Jun 2020

Keywords:
Volatile organic compounds,
Chemistry and biochemistry method,
Removal,
Adsorption,
Water and air

ABSTRACT

The volatile organic compounds (VOCs) have toxic effects on human health and environmental matrices. So, determination and removal of VOCs from the environmental samples such as water, wastewater and air are very important as they exert toxic effects on human. Many chemical techniques such as; analytical methods for sorbents (extraction, adsorption), sole gel method, pervaporation, regenerative catalytic oxidation (RCO), recuperative catalytic oxidation (CO), adsorptive concentration-catalytic oxidation, photocatalytic oxidation (PCO), ozonation-catalytic oxidation and non-thermal plasma-catalytic oxidation, have been used for removal and reduction of VOCs from different matrices. This review study has been conducted to collect the adsorbents and applied chemistry methods which have been recently used in different works for the elimination of VOCs from air and water samples.

1. Introduction

Volatile organic compounds (VOCs) enter the environment through various sources, leaving severe environmental and health impacts [1]. The production of industrial wastewater is the main origin of VOCs which is considered as a negative aspect of industrial activity, exerting several adverse effects on the environment and human health [2-6]. Volatile organic compounds are one of the most widely used materials in the production of refrigerants, plastics, adhesives, paints, and petroleum products [3, 5, 7-12]. Benzene and toluene are regarded as the most hazardous materials in the volatile organic compounds family and regarding their importance, a considerable amount of literature has been published on the issue of benzene and toluene potential adverse effects on health [13-16]. According to the international agency for research on cancer [17], benzene is categorized as group 1 (carcinogenic to humans) and Toluene as group 2B (quietly carcinogenic to humans). What we know about the adverse effects of benzene and Toluene is largely based on previous studies which have proved that the common adverse effects of these organic compounds is neurotoxicity including drowsiness, headache, tremor, coma and dizziness [16, 18-20]. Benzene exposure has been reported to increase the risk of various cancers including leukemia and hematopoietic cancers

* Corresponding Author: Amir Hessam Hassani
Email: ahh1346@gmail.com
https://doi.org/10.24200/amecj.v3.i02.100

[15, 21]. It has been also recognized that benzene and Toluene affect skin, eyes and respiratory tract by inducing irritation [22-25]. Increased threatening impacts of VOCs increase health and environment concern and therefore, there is a crucial need to develop effective strategies to remove them. Several attempts have been made to eliminate or recover VOCs from wastewater; for example, distillation is commonly used, regardless of azeotropes formation or high energy consumption [6, 7, 10, 12, 26-29]. Hitherto, a number of approaches including adsorption [30-32], condensation [33], incineration [34, 35] and thermal oxidation [36] have been established to eliminate VOCs from the environment. Treatment methods that have been established for VOCs removal are as follows: air stripping, adsorption, advance oxidation, distillation, anaerobic/aerobic biological treatment and the technology of membrane [27, 29, 37-42]. Many researchers have also applied pervaporation with nonporous membranes such as silicon rubber-coated PP to remove aromatic compounds from water sources [43-45]. Moreover, a large body of studies has taken the advantage of membrane-based air stripping (MAS) process by the means of microporous hollow fiber contactors which is very effective in the treatment of aqueous effluents containing VOCs [46-56]. In the context of catalytic oxidation (one of the used techniques for VOCs removal), many researchers have focused on catalysts including noble metals (e.g. Al_2O_3, TiO_2, CeO_2, MnOx), nonmetal oxides (e.g. SiO_2), zeolites (e.g. ZSM, MCM, NaY) [57-62] and carbon derivatives [63, 64]. However, metal oxides that are in charge of VOCs elimination are mostly derivatives of elements distributed in groups III-B through II-B of the periodic table such as Ti, Cu, Mn, Al, Ce, Co, Fe and so on [65-67]. Despite extensive attempts toward VOCs removal, conducted technologies have, to some extent, shortcomings and limitations. This paper aims to review techniques used for VOCs removal and discuss their advantages/disadvantages and finally, focus on introduced solutions to improve the process of VOCs elimination.

2. Data sources

In this review, we used information such as journal articles, statistical data and conferences/seminars papers as our data source. Surfing in scientific websites and databases including Google Scholar and Web of Science was a major way of accessing valuable information and related articles. Therefore, it was important to search at least one of related key words which are included in either titles or abstracts of papers and are as follows: “VOCs removal”, “Catalytic oxidation”, “Adsorbents” and “Nanomaterials”. It was also crucial for papers to contain one or more of the aforementioned keywords to be embodied in this review.

3. Experimental procedures and methods

3.1. Sorbent Methods

The analytical methods for sorbents based on extraction and adsorption (chemical and physical) were used for VOCs removal from water and wastewater samples. Recently, the phenyl sulfonic acid (PhSA) modified carbon nanotubes (CNTs) were presented for benzene removal (BR) from waters. For separation process, the PhSA@CNTs based on the dispersive micro solid phase extraction method (D- μSPE) was used for BR from water. The main mechanism was achieved by the polar–π or π–π electron donor–acceptor interactions between the benzene and SO3H /C6H5 group of CNTs surface (Fig. 1). According to the procedure, 10 mg of CNTs@PhSA nanostructures was added to 5 mL of water samples with different benzene standard solution (0.1--10 mg L^{-1}) in GC vial. After shacking and centrifuging (3500rpm), the CNTs@PhSA sorbent separated from water samples and finally, its concentration was determined by static head space gas chromatography mass spectrometry (SHS-GC-MS) [68]. The mechanism based on CNTs@$PhSO_3H$ was obtained with π–π stacking between aromatic chain and S=O bond of CNTs@$PhSO_3H$ (Fig. 2).

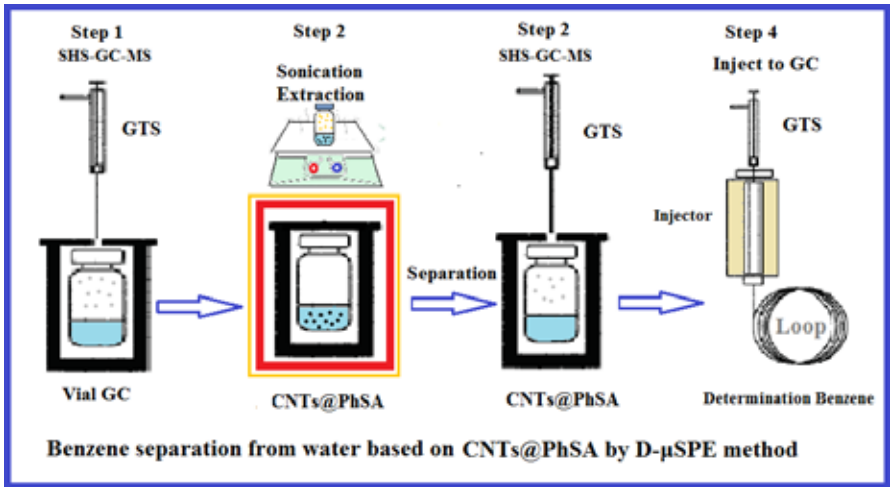

Fig. 1. Benzene extraction from waters based on CNTs@PhSA by D-µ-SPE method

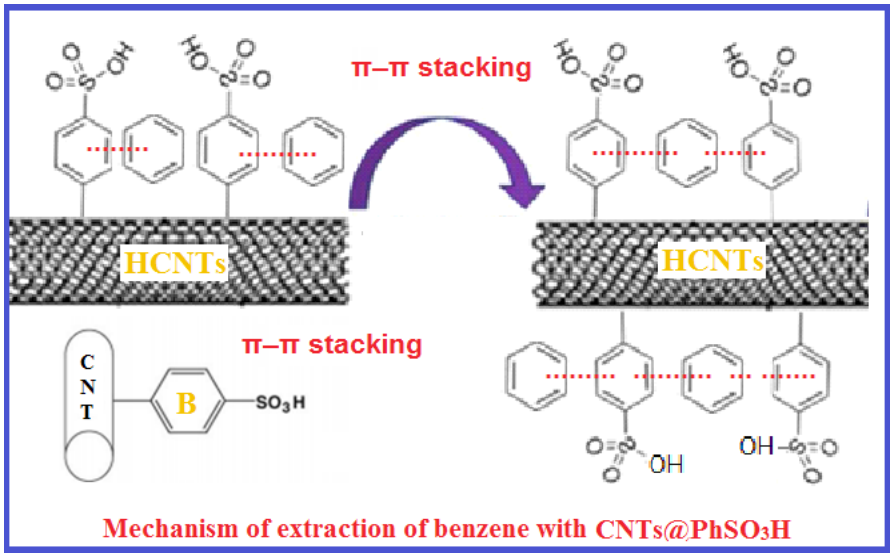

Fig. 2. Mechanism of extraction of benzene with CNTs@PhSO3H

The graphene based materials (GBMs) have been also used as a new technology in different fields of science specially in the environmental chemistry. The GBMs adsorbent was used for the removal of VOCs with high adsorption capacity and cost-effectivity through various functionalization processes on the surface. The intermolecular forces of GBMs with the gaseous pollutants caused gas adsorption. The strength of the interaction of GBMs with VOCs depended on surface area/properties, pore volume/size of the GBMs. The GBMs showed the excellent adsorption for the removal of VOCs. Among the different graphene structures, GO and rGO have mostly used for the VOC removal from waters [69]. The various models of the GO structures are shown in Figure 3 which was used for VOCs removal in different matrices. Hofmann and Holst first introduced graphite oxide and then Ruess et al designed a graphite oxide structure based on a wrinkled carbon sheet. Scholz and Boehm showed that the carbon sheet replaced by carbonyl and hydroxyl. Nakajima and Matsuo used two carbon layers linked to each other by sp_3 CeC bonds with carbonyl and hydroxyl groups. Lerf et al suggested a graphite oxide based on the unoxidized rings of benzene and that a wrinkled region of alicyclic 6- membered ring ethers is distributed randomly in a flat aromatic region. Szabó et al., showed a carbon network structure [70-73].

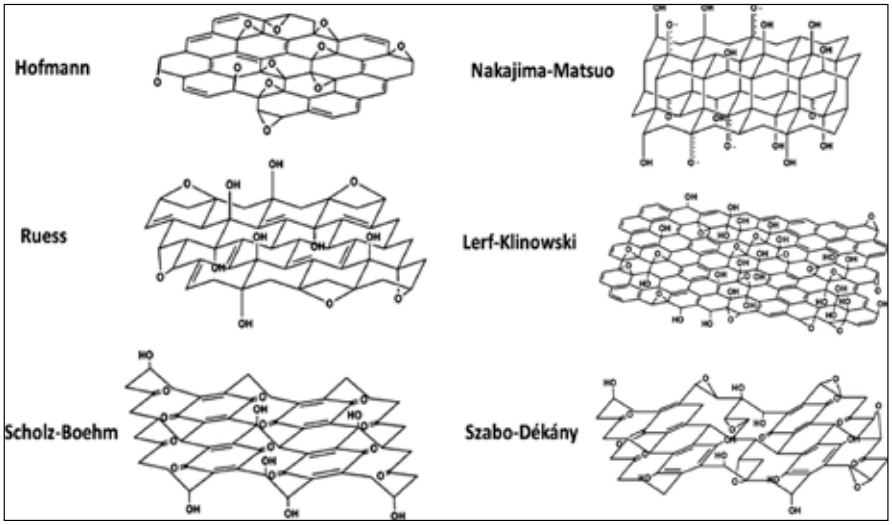

Fig. 3. Various models of the GO structure [70].

benzene, toluene, and xylene (BTX) are the major members of VOCs pollutions. These VOCs are preferably adsorbed on hydrophobic surfaces as compared to hydrophilic surfaces [74-75]. The previously results showed, the GO may exhibit less adsorption capacity for aromatic VOCs. Yu et al showed for 50 ppm benzene, the adsorption capacities for GO and rGO were obtained 216.2 and 276.4 mg g^{-1}, respectively. The rGO sorbent has a hydrophobic property with enhanced tendency (π-π bonds), increasing the adsorption capacity of VOCs relative to GO sorbents. In addition, the surface areas for rGO and GO were achieved 292.6 m^2 g^{-1} and 236.4 m^2 g^{-1}, respectively and due to high surface area of rGO, the adsorption capacity of VOCs was increased [69, 74, 75]. Szczęśniak et al showed that the high surface area of GBMs and GO caused to improve the benzene adsorption capacities for OMC. The incorporation of GO with OMC / KOH increased the surface area from 740 m^2 g^{-1} to 1370 m^2 g^{-1}. Also, the pore volume of OMC from 0.61 increased to 1.06 cm^3 g^{-1} after the formation of GO/OMC. Finally, adsorption capacities for benzene were obtained 633 mg g^{-1} and 750 mg g^{-1} for OMC and GO/OMC, respectively [76-77]. GO - MOF-5 was used for the removal of benzene vapor from air with capacity of 251 mg g^{-1} [78]. Due to high porosity of MOFs, they cannot retain small molecules under ambient conditions. So, the GO/MOF-5 composite was prepared using varying proportions of GO, such as 1.75 wt%, 3.5 wt%, 5.25 wt%, and 7 wt% (Fig 4).

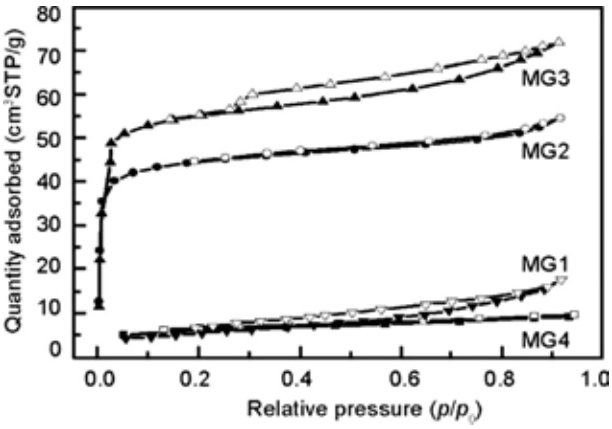

Fig. 4. Adsorption-desorption isotherms for graphene oxide/metal organic framework-5 (GO/MOF-5) for benzene [78]. MG (1–4) represents GO/MOF-5 composite with 1.75%, 3.5%, 5.25%, and 7% of GO in MOF-5.

The GO and rGO was used for the removal of toluene by Kim et al. The π–π bonds, hydrophobic and electrostatic interaction with toluene led to the absorption of toluene on GO / rGO surfaces (Fig. 5). Different types of GBMs such as graphene platelets (GP), rGOMW, and KOH activated rGOMW (rGOMWKOH)) were analyzed for the toluene adsorption [79].

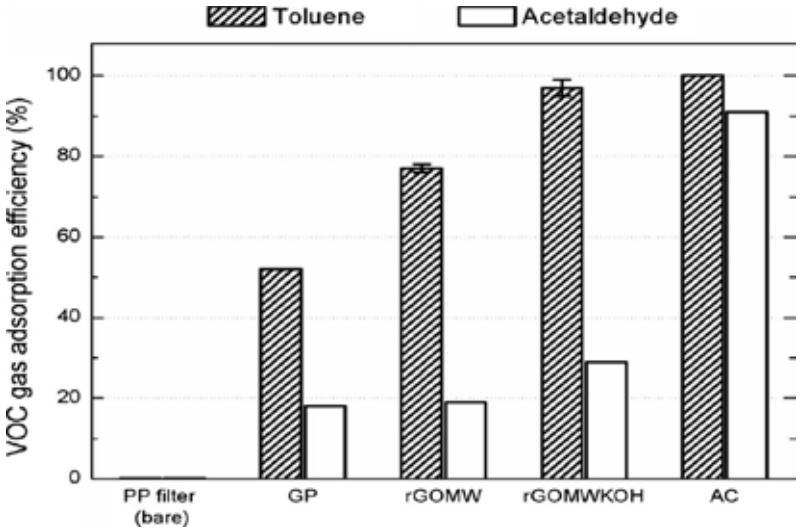

Fig. 5. Toluene and acetaldehyde removal capacity by rGOMWKOH compared to other adsorbents [81].

Aldehyde and ketone compounds are the most carbonyl VOCs which can be considered as sources of the environment contamination. GBMs can efficiently remove the carbonyl compounds from environment. For indoor formaldehyde removal, amino functionalized graphene sponge (G/S) or G/S decorated with graphene nanodots (G-GND/S) were used by Wu et al. G-GND/S with high amine groups on surface as compared to G/S caused a high interaction with formaldehyde molecules (Fig 6). The results showed that the adsorption capacity of GGND/S and G/S were achieved 22.8 mg/g^{-1} and 7.5 mg/g^{-1} for formaldehyde, respectively [80].

Lim et al. prepared mesoporous-structured graphene powder through the method of thermal expansion (Fig. 7) and used them as adsorbents for removing VOCs. According to Figure 8 the characteristics and morphology of the prepared adsorbent was defined through different methods including scanning electron microscopy (SEM), X-ray photoelectron spectroscopy and N_2 isotherms. Adsorption

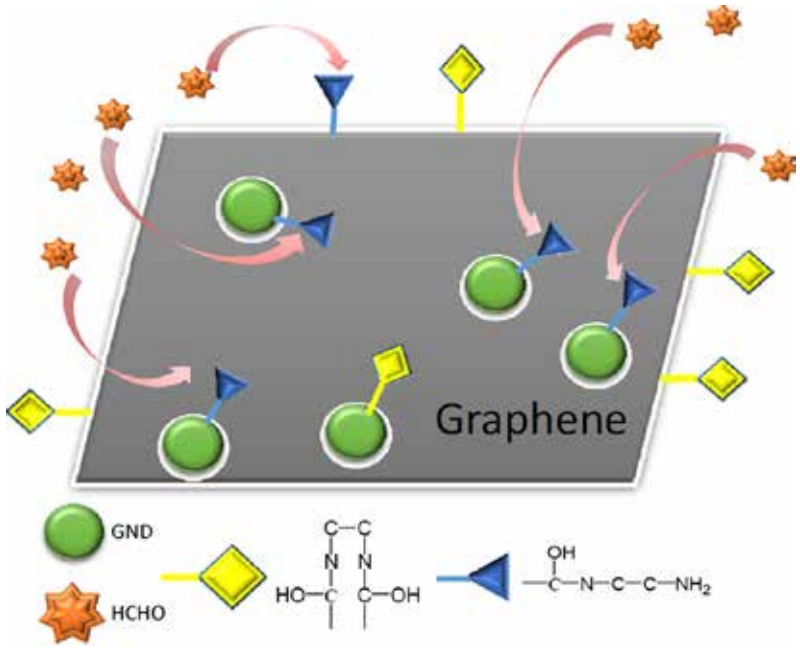

Fig. 6. Interaction of amino graphene nanodots decorated functionalized graphene sponge with formaldehyde molecules

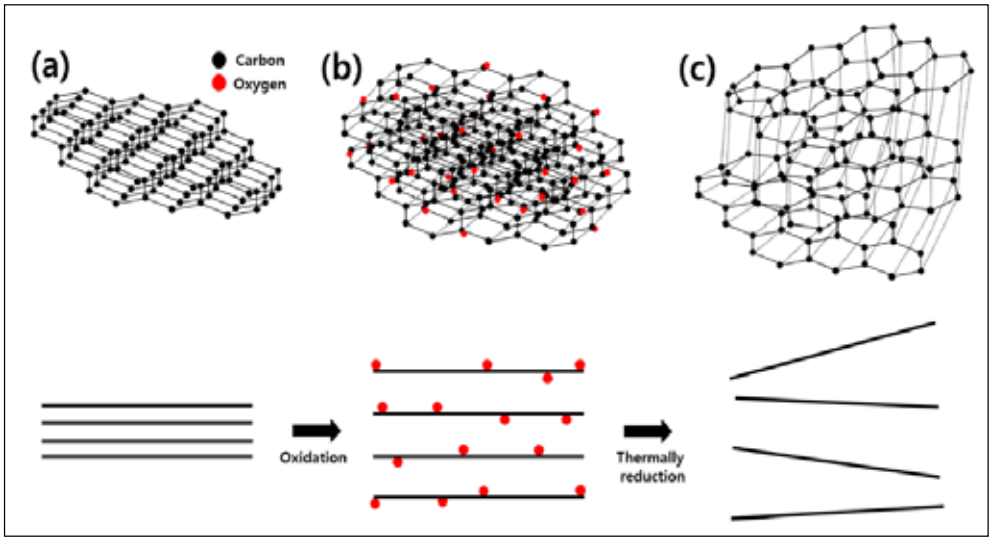

Fig. 7. The scheme of thermal expansion mechanism; a: graphite powder b: GO powder c: TEGP [82].

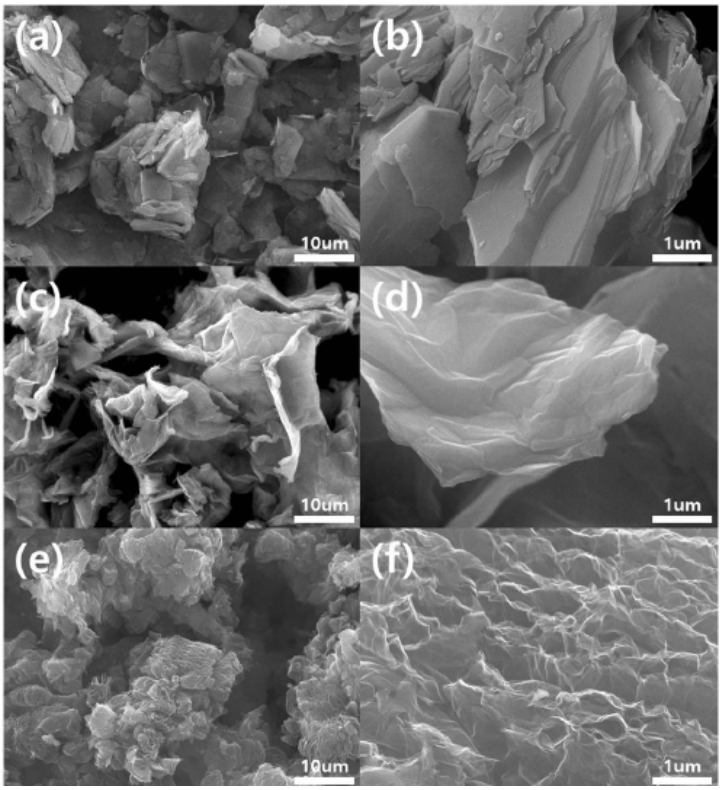

Fig. 8. SEM images of graphite powder (a,b), graphite oxide (GO) (c,d) and TEGP (e,f) [82].

capacity of graphene powder was examined using propylene filter, at a concentration range of VOCs (30, 50, 100 ppm). The results of the study indicated that thermal expanded graphene powder (TEGP) is an effective material for VOCs removal which acts in a proper chemical oxidation using heat energy. It was also reported that TEGP is of economical materials, due to its reusability [82].

3.2. Sole Gel Method

The sole-gel process is a method for producing solid materials from small molecules. As a chemical-wet technique, recently, it has been widely used in the fields of material sciences and ceramic engineering. This kind of methods are employed

primarily for the synthesis of materials (mostly metal oxides) starting with a chemical solution that acts as a precursor for an integrated nexus of both segregated particle and network polymer [83].

Metal alkoxides and metal chlorides, which are considered as frequent precursors, undergo different forms of hydrolysis and poly-condensation reactions. Binding of metal centers with either oxo (M-O-M) or hydroxo (M-OH-M) bridges leads to the formation of metal oxides and generates metal-oxo or metal-hydroxo polymers in solution. Therefore, the sol involves in the formation of a gel-like diphasic system containing both solid and liquid with segregated particles to a continues polymer structure morphologies [83].

The sole-gel method has been increasingly applied for the development of various materials including material for catalysis [84, 85], chemical sensors [86, 87], optical gain media [88], solid state electrochemical devices [88], photochromic and non-linear applications [90-92], membranes [93] and fibers [94]. One of the intriguing applications of the sole-gel technology is photo catalyst preparation. Photo catalysts have been widely used to degenerate VOCs. Common photo catalysts are semiconductors like ZnO, GaP, TiO_2, SiC, CdS and Fe_2O_3 [95]. Among these photo catalysts, TiO_2 is the most applicable photo catalyst in the context of eliminating environmental pollutants because of its chemical stability, high oxidizing potential, low cost, non-toxicity and environmentally friendly properties [96-99]. Parvizi et al. in their study about perovskite nano-catalysts, synthesized a series of La1-x Ax MnO_3 (A: Co, Zn, Mg, Ba) through sol-gel method (Fig. 9) and then evaluated the performance of these catalysts in the elimination process of BTX compounds. After conducting the research, the FTIR results showed that all characteristics related to efficient catalyst was present in synthesized catalyst, indicating acceptable outcomes of sol-gel method [100]. By applying nonhydrolytic sol-gel method, Debecker et al. synthesized V_2O_5-TiO_2 and added Mo and W oxides to promote the catalysis performance of catalyst (Fig. 10). The results of the research indicated a significantly better oxidation performance (93% oxidation) and a highly efficient action for CO_2 selectivity for the purpose of VOCs removal [101]. These results imply the importance of sol-gel method in the process of efficient catalyst synthesis.

Sarafraz Yazdi et al. developed a novel fiber

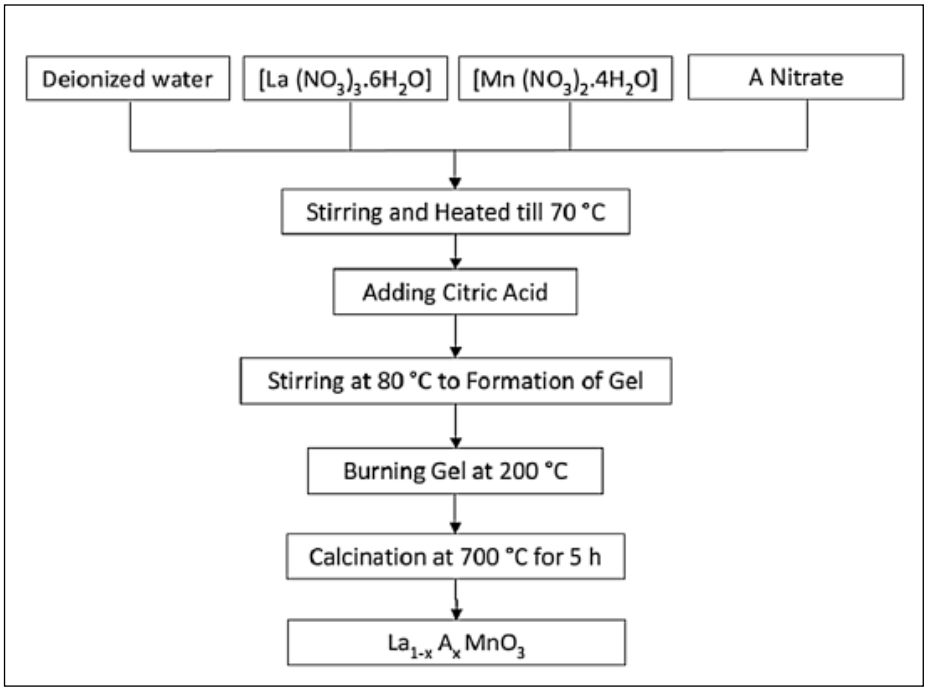

Fig 9. Schematic procedure of La1-x Ax MnO3 (A: Co, Zn, Mg, Ba) perovskite nano-catalyst preparation by sol-gel method [100].

to improve the elimination of trace amounts of BTEX. At first, poly ethylene glycol (PEG) grafted on multi-walled carbon nanotubes (PEG-g-MWCNTs) undergone a chemical bonding with sol-gel to produce the unique fiber, as shown in Figure 11. The results showed that the porous structure, thermal stability, potent selectivity and durability of mentioned fiber lead to a remarkably better performance in the route of removing BTEX. Also, due to porous structure of sol-gel coating, the surface area of fiber, extraction velocity, steps of desorption and capacity of sample loading increase significantly [102].

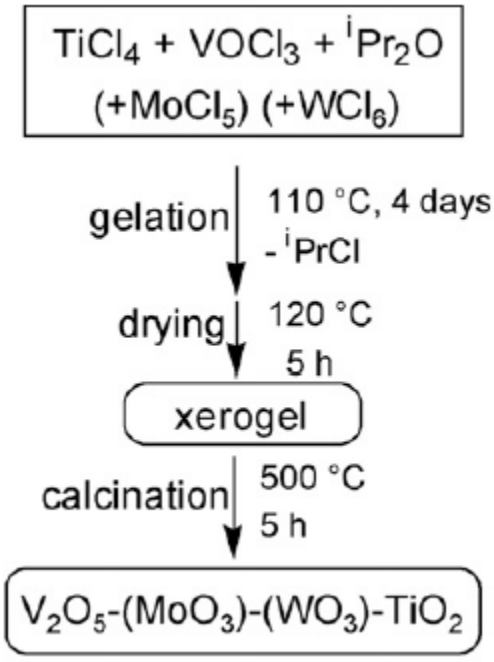

Fig. 10. Nonhydrolytic sol-gel preparation method [101]

3.3. Pervaporation

Membrane-based pervaporation (PV) technology serves as an economical and alternative technique in the organic-organic separation processes. A number of researchers have reported the elimination of VOCs from water sources which has been achieved through various polymeric membranes, using pervaporation technology [103-111]. Uragami et.al prepared a PVC membrane (hydrophobic polymeric membrane) and used an ionic liquid (1-allyl-3-butylimidazolium bis (trifluoromethane sulfonyl) imid ([ABIM]TFIS)) with a remarkable and low affinity for VOCs and water, respectively. Through the process of PV, Uragami and coworkers evaluated the performance of prepared [ABIM] [TFIS] /PVC aqueous solutions of dilute benzene and reported that the combination of PVC membranes with [ABIM] [TFIS] ionic liquid represents higher permeability and benzene/water selectivity in a concentration dependent manner. As shown in Figure 12, it was also revealed that incorporation of PDMS component decreases the density of membrane and induces benzene permeability [112]. Kujawa et al. functionalized and increased the hydrophobicity of two types of ceramic membranes with molecular sizes of 5 kDa and 300 kDa (Fig. 13). They reported that membranes with increased hydrophobicity can efficiently remove VOCs from binary aqueous solutions through vacuum membrane distillation procedure [113].

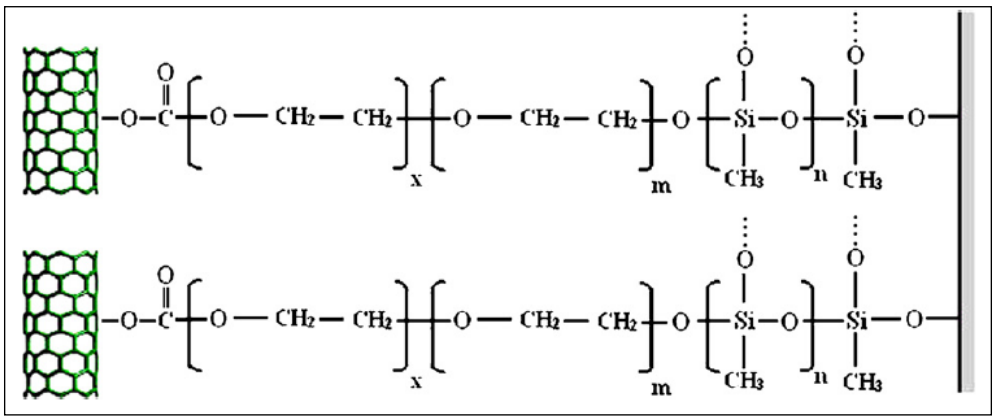

Fig. 11. Sol-gel PEG-g-MWCNTs coating [102]

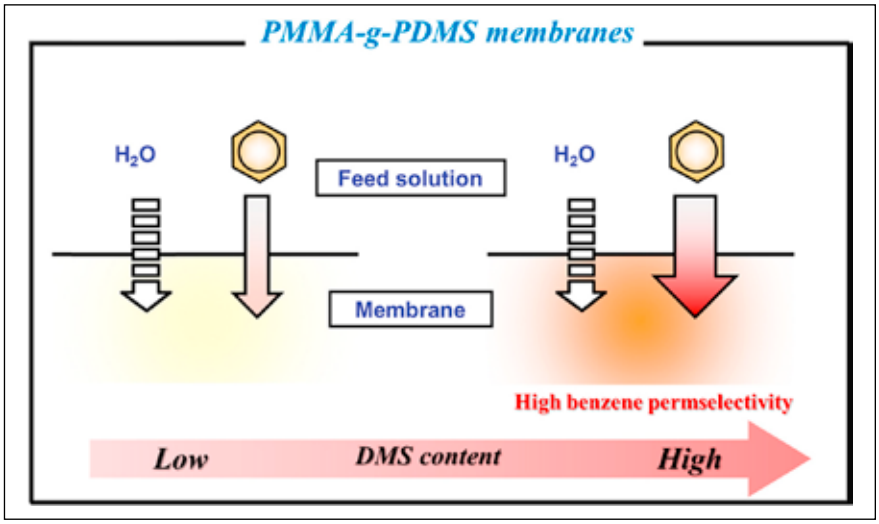

Fig. 12. The illustration of benzene permselectivity and benzene permeability under the effect of PMMA—-PDMS membranes [112].

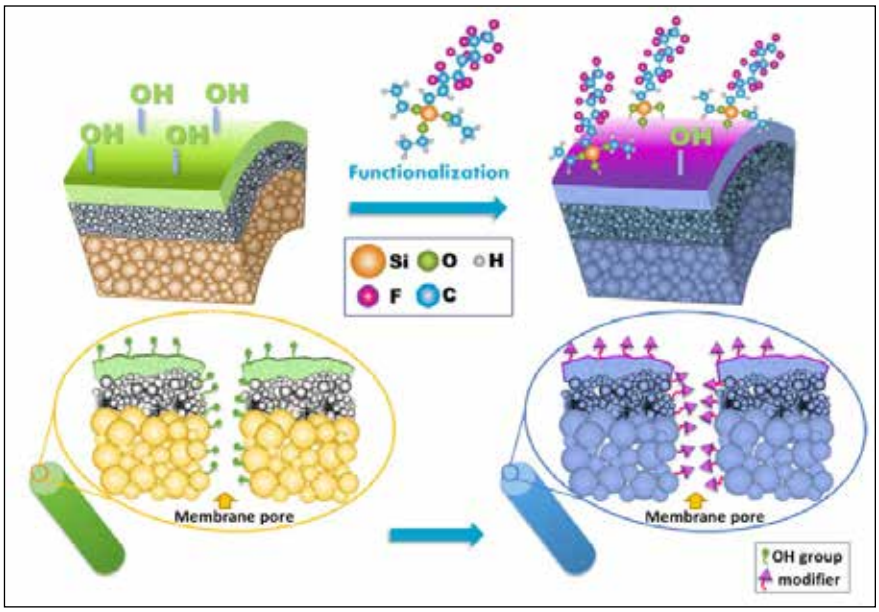

Fig. 13. Ceramic membrane's functionalization by perfluoroalkylsilanes [113].

3.4. Catalytic oxidation

3.4.1.Regenerative catalytic oxidation (RCO)

In parallel with the regenerative thermal oxidation (RTO), RCO is one of the most energy-saving techniques, being as relatively similar working mechanism as RTO. These techniques contain two or more beds with random or structured ceramic packs which are of high specific heat materials (800-1000 J Kg^{-1} K^{-1}) and perform as heat transfer media. As shown in Figure 14, frequently used two bed RCO usually contains ceramic layer, catalyst layer, natural gas burner or electrical heater which plays a role as heat storage, reaction media and heat supply, respectively. Due to its relatively lower price, natural gas is preferred to use rather than electrical heating. The mechanism of VOCs removal in this technique involves passage of VOCs flow from ceramics cabinet A which preheats VOCs, followed by a temperature increase up to 200-300 ^{O}K. When heater keeps the flow temperature of catalyst (i.e., TChamber) higher than the light-off temperature (TC), effective degradation of VOCs occurs. Simultaneously, the releasing heat from VOCs oxidation contributes to Tchamber and even can

serve as a usable heat. In the next step, reacted flow goes down and its heat reserves as a high specific heat, preheating the inlet VOCs flow in the next cabinet B to A cycle. Thermal Recovery Efficiency (η) is a factor evaluating energy-efficiency related properties of oxidizing equipment. Although the η of RTO is up to 90%, the η of RCO can reach 95% or higher [114]. Liu et al. designed a formula of Ru-5M/TiO_2 (M: Mn, Co, Ce, Cu, Fe) for ruthenium-based bimetallic catalyst and examined its effect on benzene oxidation efficiency. After deep examination of different bimetallic species, it was proved that the combination of Ru-5Co/ TiO_2 can be the most effective species for the process of benzene removal. Figure 15 Illustrates the represented mechanism of benzene removal, using combined Ru-5Co/ TiO_2 catalyst [115]. In the study of Zhang et al., nano-crystalline copper-manganese oxides were prepared using sol-gel method. The relativity between Cu and Mn was defined as Cu3x-Mnx (x can be equal to 0, 1, 1.5, 2, 2.5, 3 and is a representation of molar ratio of Cu and Mn); the optimal ratio was also found to be 2. Results showed that $CuMn_2$ with the spinel structure of $CuMn_2O_4$ exhibits a larger surface area, smaller pore size and network oxygen species, leading to enhanced catalytic activity of $CuMn_2$ which can be the result of stabilized $CuMn_2O_4$ active sites and synergistic effect between Cu and Mn (Fig. 16) [116].

3.4.2. Recuperative catalytic oxidation (CO)

Recuperative catalytic oxidation (CO), known as a simplified version of RCO, is a technique consisting of tubular or plate heat exchanger instead of regenerative thermal ceramic layers in RCO. In this technique, at first, a heat exchanger preheats VOCs flow, causing a temperature increase by about 50-200^{O}K. Then, the next heater further heats the flow up to the light-off temperature of catalyst (usually above 573 K). Finally, reinforcement of VOCs oxidation occurs to produce CO_2 and H_2O with a significant amount of heat release. The η of a normal CO is generally lower than 70%, indicating that the costumer should cost more than usual to obtain required energy for keeping the equipment to work

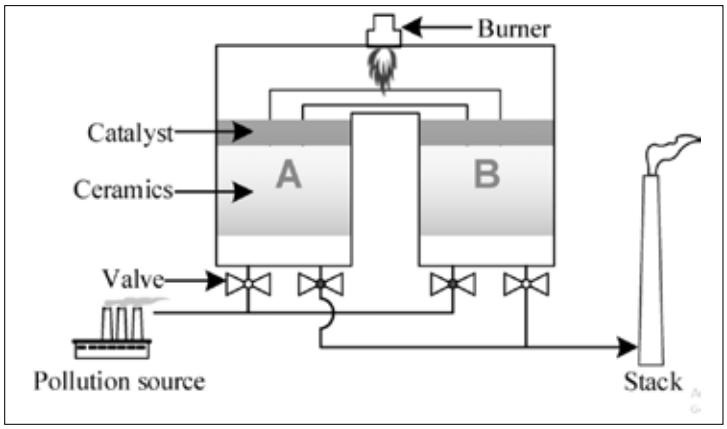

Fig. 14. The schematic diagram of regenerative catalytic oxidizer [114].

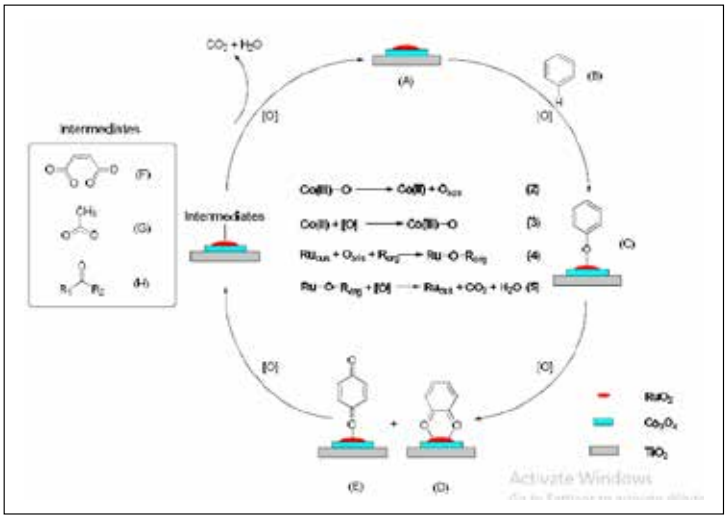

Fig. 15. Presented mechanism of the effect of Ru-5Co/ TiO_2 on the benzene oxidation [115].

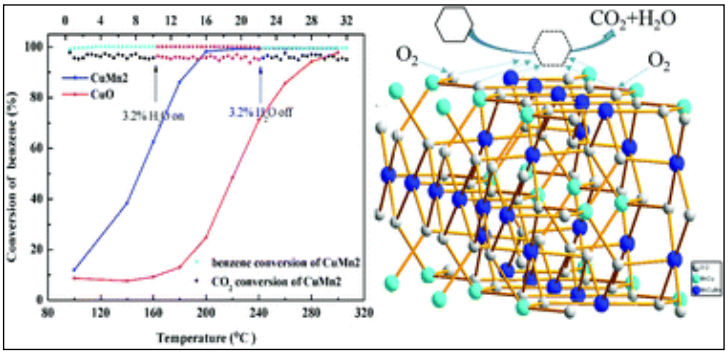

Fig. 16. The sample of $CuMn_2$ and relative spinel structure [116].

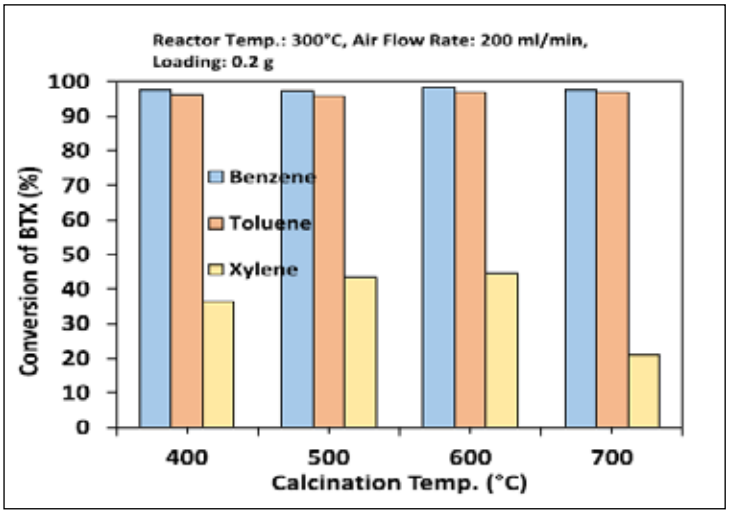

Fig. 17. The effect of manganese oxide calcination temperature on the thermal oxidation of BTX [118].

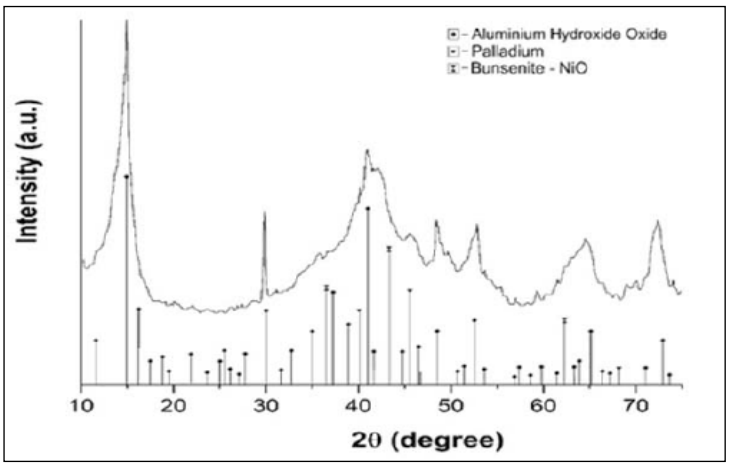

Fig. 18. The XRD pattern of the Ni/Pd/AlOOH [119].

on VOCs elimination. In fact, CO can't be effective for large-scale and low concentrations of VOCs pollutant removal [117]. However, considering low initial investment and high flexibility, the technique of CO can be effective for samples with small flowrate (<5000 m^3 h^{-1}) of VOCs pollutant [114]. Intriguingly, it is important to note that in the case of large-volume and low concentration VOCs emissions, there is an advanced technology named adsorptive concentration-catalytic oxidation which makes it possible to remove such VOCs samples. Hoseini and coworkers aimed to synthesize manganese oxide and impregnate it into different loadings of alumina. They utilized the resulted material in the procedure of BTX oxidation followed by performance analysis. Findings of the study represented the most effective morphology and higher surface area at 10% of alumina loading. Further evaluation highlighted that the best condition for oxidation is 10 kV, 0.2 g Mn10Al in the 200 mL min^{-1} flowrate of pollutant with resulting oxidation of 97, 99 and 74% benzene, toluene and xylene, respectively. The catalytic activity of catalyst was investigated by catalyst calcination at four different temperatures (400, 500, 600, 700 °C). As Figure 17 it can be seen that the highest level of BTX conversion was found to be in Mn600 catalyst [118]. Georgiev in 2019 investigated ozone-assisted catalytic oxidation of benzene through alumina, silica and boehmite-supported Ni/Pd catalysts in 353 K. Three bimetallic Ni/Pd samples in a nano scale were synthesized with loadings of 4.7% Ni, 0.17% Pd supported on SiO_2, AlOOH and Al_2O_3 and by the means of extractive-pyrolytic method. According to the results of the study, the highest steady-state activity of catalysts was attributed to Ni/Pd/AlOOH catalyst (Fig. 18). Georgiev reported that this activity is dependent on the amount of ozone decomposition capacity of catalysts which leads to oxidative species production; a sample with a high ozone decomposition ability (related to surface area of support) is capable of benzene oxidation in a high extent [119].

3.4.3. Photocatalytic oxidation (PCO)

As a different and distinguishable technology, photocatalytic oxidation has received considerable attention, due to its mild reaction condition and non-selectivity. By using UV or visible light in the environment temperature, photocatalytic oxidation works different from thermal catalysis; therefore, compared to RCO and CO, the configuration of PCO is simpler (Fig. 19). Photocatalysis has a wide variety of activities regarding various VOCs at the environment temperature, however, due

to low quantum efficiency and long residence time requirement, it has a limited oxidizing power and load adaptability [114]. Zhang et al. [120] introduced a new modified photocatalyst named TiO_2-UiO-66-NH_2 (constituting from the combination of TiO_2 and UiO-66-NH_2) and reported that the new photocatalyst can significantly improve photocatalytic performance for VOCs oxidation (Fig. 20). According to this study, the TiO_2-UN photocatalytic system, represented good CO_2 selectivity and high photocatalytic activity with 72.70 % of toluene decomposition during 240 min of reaction, which was even higher than single TiO_2 (44.22 %) and UiO-66-NH_2 (7.48 %). In the study of benzene removal by the means of PCO technology, Ji J et al proposed that VUV-PCO technique (Fig. 21) is significantly effective in comparison with the ordinary UV-PCO [121]. In contrast to UV-PCO in which benzene degradation is only attributed to photocatalytic oxidation, VUV-PCO technique consists of several decomposition pathways alongside VUV photolysis and PCO. Benzene degradation hardly occurs under the effect of UV irradiation [122], however, VUV irradiation have a benzene removal efficiency of about 48radiation potency in the process of benzene degradation is related to the formation of hydroxyl radicals (ŸOH) and oxygen species such as O(1D), O(3P) and O_3 [123].

3.5. Ozonation-catalytic oxidation

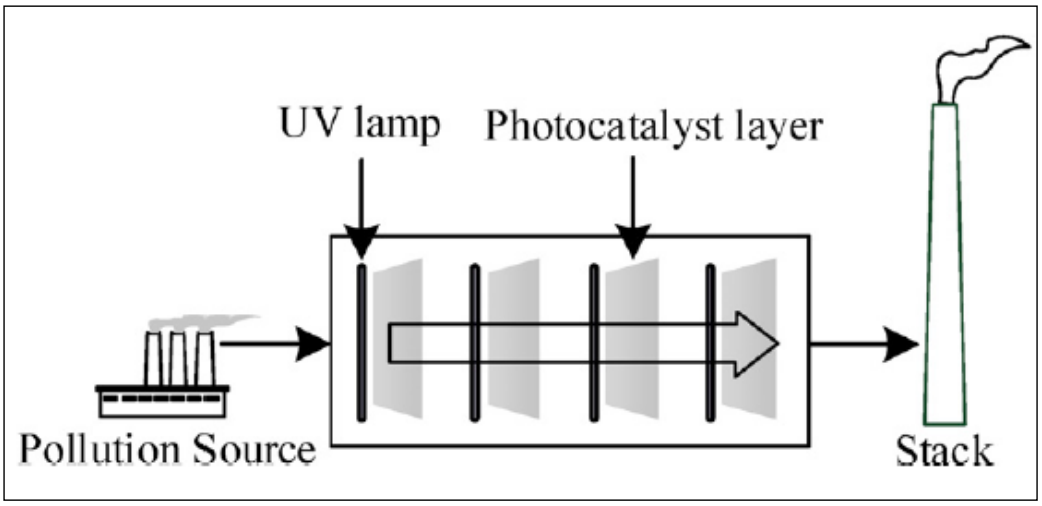

Fig. 19. Schematic configuration of PCO [114].

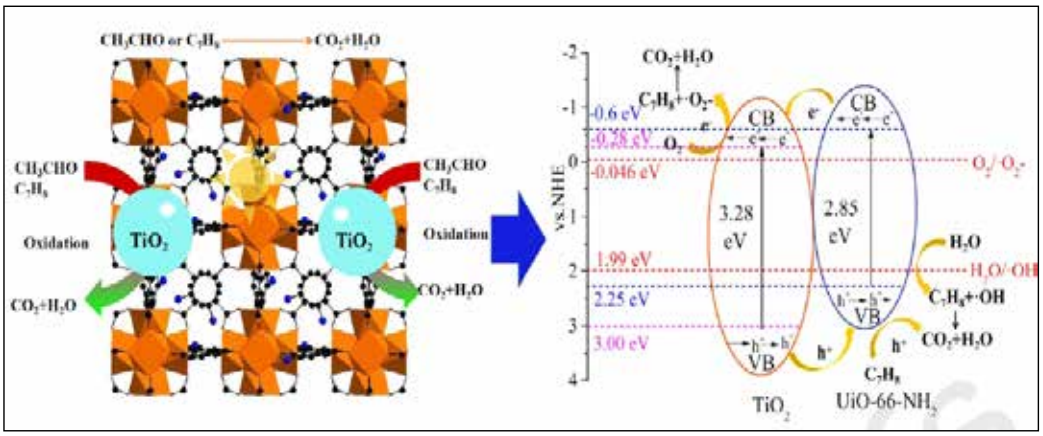

Fig. 20. Hypothesized pathways for photocatalytic oxidation of VOCs by TiO2-UiO-66-NH_2 [120].

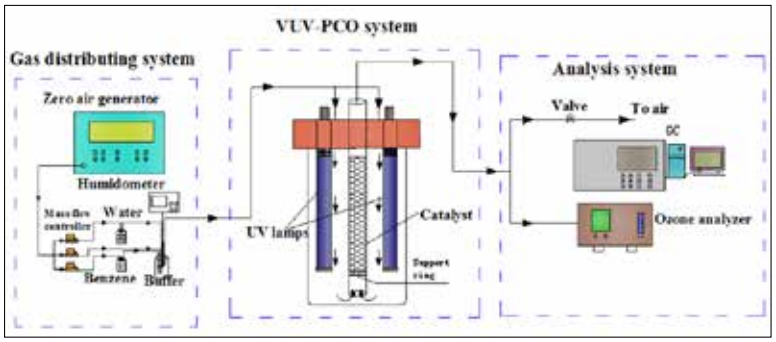

Fig. 21. The schematic diagram of VUV-PCO system [121].

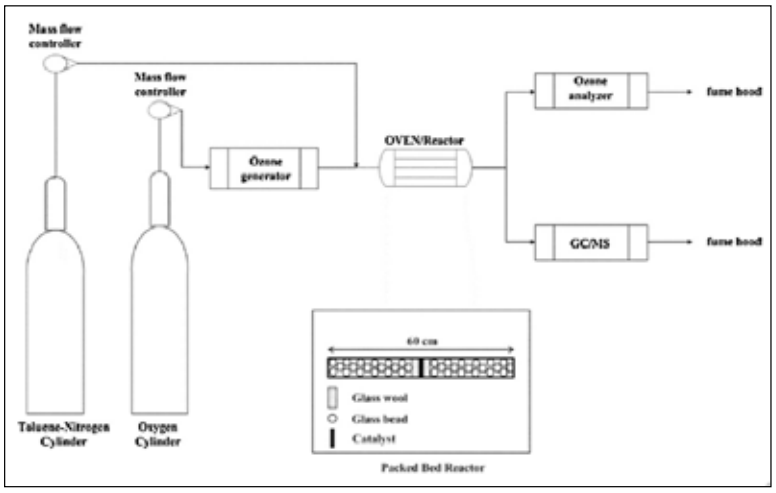

Fig. 22. The scheam of experimental procedure [126].

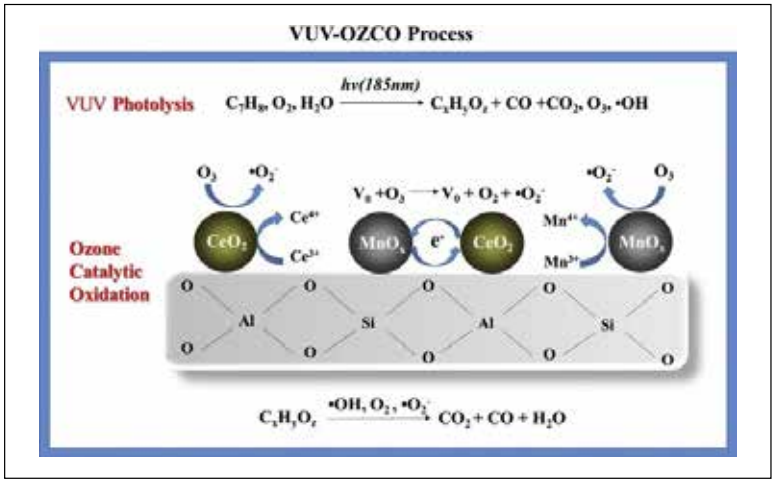

Fig. 23. VUV-OZCO process [125].

In the technology of ozonation-catalytic oxidation, Ozone (O_3), a strong oxidant with a standard redox potential at 2.07 eV, is used. Water sterilization and wastewater treatment procedures have extensively taken the advantages of ozone oxidation. Ozone oxidation has been extensively applied in water sterilization and wastewater treatment procedures. Since ozone isn't very stable in gas environment, as a single technique, it can't be so effective in the oxidation of VOCs to CO_2 and H_2O. However, ozone oxidation has the capability of being used as a pre-treatment step before common catalytic techniques (e.g. thermal catalysis and photocatalysis) and promotes a synergistic effect alongside these technologies. Rezaei et al. in their 2013 study indicated that transition metal oxide-based catalysts propose efficient VOCs removal by catalytic ozonation, obviating the need for costly noble metals which are frequently used in the VOCs catalytic combustion with oxygen. The mentioned study investigated different loadings of Mn in a temperature range and reported that increased temperature leads to better activity of catalyst and lower loadings of Mn resulting in surged and efficient toluene oxidation (analyzed by GC-MASS) and ensuing ozone decomposition (measured by ozone analyzer) (Fig. 22) [124]. Shu et al. designed a novel process which was a combination of VUV photolysis and O_3 catalytic oxidation (VUV-OZCO). In this system, VOCs are firstly destructed by VUV and then are oxidized through VUV-generated O_3 in the presence of catalyst. O_3 by-product is also eliminated simultaneously. In the study of Shu et al. it was revealed that the novel Mn-xCe-ZSM-5 catalyst along with VUV-OZCO system (Fig. 23) can have the capacity to simultaneously decompose O_3 by-product and improve toluene removal efficiency [125].

3.6. Non-thermal plasma-catalytic oxidation

Non-thermal plasma (NTP) which has been introduced as green technology for elimination of VOCs from indoor and industrial gas streams, is a superior source of chemically active species (OH and O^{2-} radicals, ions, excited species, etc). This property leads non-thermal plasma to provide a highly reactive environment (caused by electron's acceleration, dissociation and ionization); without any energy consumption on heating the entire gas stream, in which reactive species oxidize various VOCs molecules and consequently degrade them. Besides low energy efficiency and inferior CO_2 selectivity, a major difficulty with non-thermal plasma is production of by-products including NOX, O_3 and other intermediates relating to the fact that electrons do not have enough energy to mineralize BTX molecules [127]. Thus, non-thermal plasma oxidation can't be considered as a single technique to deal with VOCs pollution, because products of uncompleted reactions in this technique can act as secondary pollutions on their own.

A great solution for the aforementioned problem is combining the non-thermal plasma oxidation with catalysis (Fig. 24). This combination has been extensively investigated during the last decade, indicating that the system of non-thermal plasma-catalysis is obviously capable of improving energy efficiency and suppressing unwanted by-products in the process of VOCs degradation [128]. Non-thermal plasma catalysis system consists of two configurations: in-plasma catalysis (IPC) and post-plasma catalysis (PPC). Guo et al. investigated the efficiency of NTP+ MnOx catalyst in the elimination of benzene and showed that this combination can significantly improve benzene removal efficiency and promote CO_2 formation, with a simultaneously suppression of CO [129].

In the study of Jiang et al. both IPC and PPC

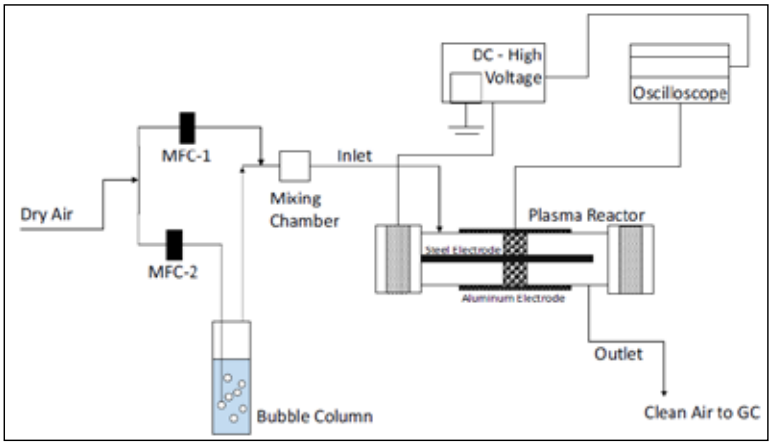

Fig. 24. Experimental setup of hybrid plasma-catalytic system for oxidation of VOCs [115].

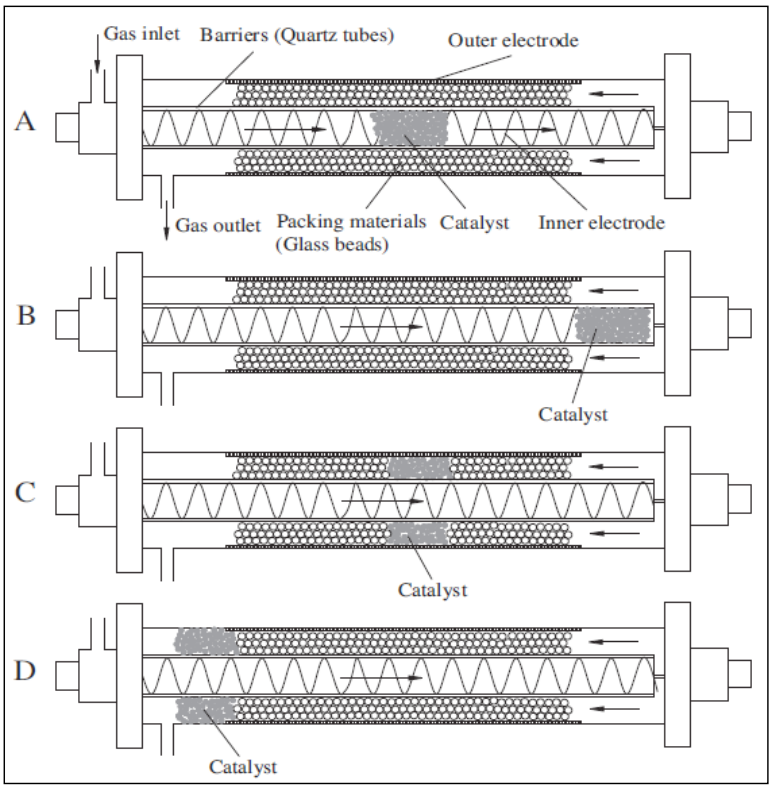

Fig. 25. Different plasma-catalysis systems in IPC and PPC configurations: (a) catalysts in the region I, (b) catalysts in the downstream of region I, (c) catalysts in the region II, (d) catalysts in the downstream of region II [130].

configurations of NTP (Fig. 25) constituted from a hybrid surface/packed bed discharge (HSPBD) with different catalysts including Agx Ce1-x/ɣ-Al_2O_3 was applied. From the result of the study, it was revealed that through the plasma-catalysis system and present of Agx Ce1-x/ɣ-Al_2O_3 catalyst significantly enhance benzene degradation and improve COx selectivity. The study of Jiang also showed that the PPC process has a better effect on the decomposition of O_3 and benzene [130].

3.7. Nanotechnology

Nanotechnology is an increasingly important area of the recent technology, playing a cardinal role in a bunch of fields. Among the various subtypes of this technology, carbon nanotubes (CNTs) has attracted a great deal of interest in the context of industrial applications and implementations. As shown in Figure 26 and based on the number of the structure layers, CNTs are classified as single walled carbon nanotubes (SWCNTs) and multi walled carbon nanotubes (MWCNTs).

Pourfayaz et al. evaluated the adsorption capacity of two types of multi walled carbon nanotubes (MWCNTs) (Fig. 27) with different functional groups and analyzed them using gas chromatography (GC). Confirmation of functionalization was performed through fourier transform infrared (FTIR). The observed findings demonstrated that the MWCNTs with a larger surface area and higher crystallinity have a significant adsorption capacity for both benzene and toluene [132].

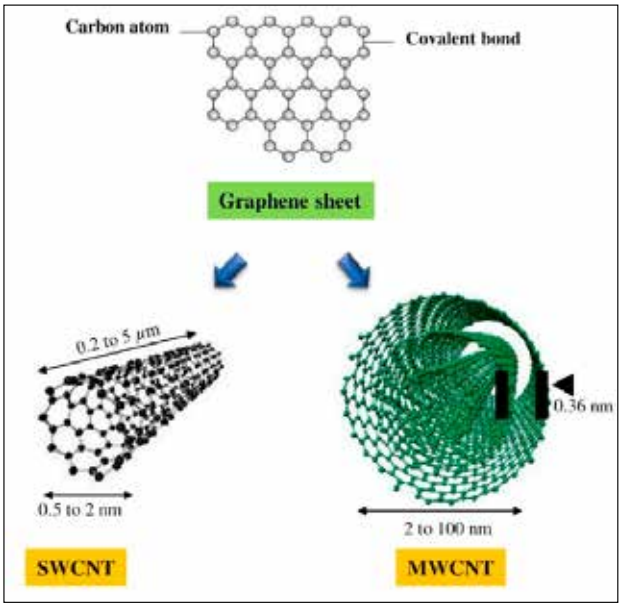

Fig. 26. The conceptual scheme representing general dimensions of the length and width of single walled carbon nanotubes (SWCNTs) and multi walled carbon nanotubes (MWCNTs) [131].

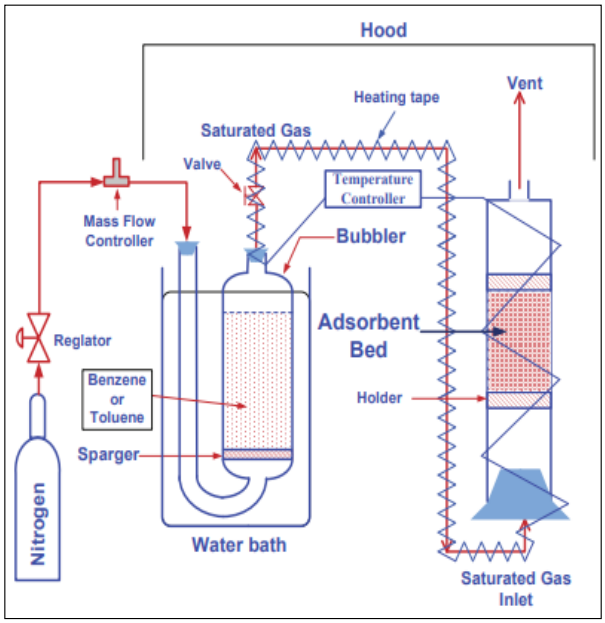

Fig. 27. Schematic diagram of experiment setup toward measurement of adsorption capacity of MWCNTs [132].

4. Comparing of diriment sorbent for removal VOCs from waters/gas

The removal procedure for VOCs from waters was compared by different analyzer such as GC-MS,GC-FID, HS-GC-MS, GC-FID/ HPLC-UV, SWV and HPLC which was shown in Table 1.

Due to Table 1, the different sorbents and techniques compared as detection limit (LOD), recovery(R), relative standard deviation(RSD%), adsorption/ desorption, temperature(T) and absorption capacity(AC) in water samples.

Table1. Determination and separation VOCs from water/gas by different sorbents and methods

VOCs	Method	Analyzer	Analytical Features	Matrix	Ref.
BTEX	ASTM	GC-MS	**LOD**: 0.11–0.48 **Recovery**: 94–107%	Water	[133]
BTEX	DAI	GC-FID	**LOD**: 0.61–1.11 **Recovery**: 95-99%	Water	[134]
BTEX	Sorbent	HS-GC-MS	**LOD**: 0.001–0.05 **RSD:** <4.2%	Water	[135]
BTX	LV-LLE	GC-FID HPLC-UV	**RSD**: 2.4-11.9 **R:** 0.8452-0.9999 **Permenkes**:0.01-0.7 **Deviation**: 2.13-10.96 **LOD**:0.1-0.3	Water	[136]
BTEX	CBD-DE	SWV	**LOD B**:3.0×10^{-7} mol L^{-1} **LODT**:8.0×10^{-7} mol L^{-1} **LOD X**: 9.1×10^{-7} mol L^{-1} **Recovery:** 98.9-99.4	Water	[137]
ROS	SE-UOOG	GC	**LOD**: 0.023 mg/g **RSD**: <2% **Recovery**: 95.4-102%	Water	[138]
p-xylene	SLS-MOF/ zeolites	SOM	**Recovery**: more than 95% **Selectivity values** of 24.0, 10.4 and 6.2 *vs. o*X, *e*B and *m*X	Water / Gas	[139]
Benzene	D – μ-SPE	SHS-GC-MS	**AC:** CNTs@PhSA,157.34 mg g^{-1} **AC:** CNTs, 157.34 mg g^{-1} **Recovery:** 96.8-102	Water	[140]
Toluene	G-PhAPTMS,- SGEP	GC-FID GC-MS	**Removal efficiency**:> 95% **Adsorption**: Chemical and physical **Flow rate** : 200 ml min^{-1} **Temperature**: 40°C	Air	[140]
benzene toluene	copper oxide nanoparticles (CuO-NPs)	HS-GC	**AC for benzene**: 100.24 mg g^{-1} **AC for toluene**: 111.31 mg g^{-1} **Adsorption efficiency** : 98.7% for benzene **Adsorption efficiency** : 92.5% for toluene	Water	[142]
VOCs	SPME-sol-gel SWCNT / silica	GC-MS	**LOD:** 0.09–0.2 ng mL^{-1} **Adsorption**: 15 min for 25°C **Desorption**: 3 min for 280 °C	air	[143]
Formaldehyde	SPME PDMS-DVB	GC-MS	**LOD:** 0.002–0.032 μg m^{-3} **Adsorption**: 15 min for 25°C **Desorption**: 4 min for 250 °C	Air water	[144]
phenol	HS-SPME CW-DVB	GC-MS	**LOD:** 1.13–4.60 ngmL^{-1}	water	[145]
Alkyl PAH	HS-SPME- PDMS	GC-MS	**LOD**: 0.002–0.6 ng mL^{-1}	water	[146]
Volatile sulfur	HS-SPME-PDMS-CAR	GC-FPD	**LOD**: 1.6–93.5 ng L^{-1}	water lakes	[147]
PBDE	DI-SPME MWCNT	GCECD	**LOD:** 3.6–8.6 ng L^{-1} **Recovery**: 90–119%	river water	[148]
OCP	HS-SPME	GCμECD	**LOD:** 0.16–0.84 ng L^{-1} **Recovery**: 63–127%	Sea water	[149]
VOCs	3D-SPE-CB-PLA)	HPLC	r^2=0.96 **Infill print densities**: 15 - 50%. **Ambient temperatures** : 19.0±0.5 °C	water	[150]

AC: Absorption Capacity
GC-MS: Gas chromatography mass spectrometry
GC-FID: Gas chromatography equipped with flame ionization detector
SWV: Square wave voltammetry
SHS-GC-MS: Head space gas chromatography mass spectrometry
GC: Gas Chromatography
SOM: Sized Organic Molecules
ROS: Residual organic solvent (ethanol, tetrahydrofuran, cyclohexane, n-heptane)
D- μ-SPE: Dispersive micro solid phase extraction method
SLS: Solid liquid separation
SE-UOOG: Solvent extraction-Unconventional oil ore Gangues
CBD-DE: Cathodically pretreated boron doped diamond electrode
LV-LLE: Low volume liquid-liquid extraction
DAI: Direct aqueous injection
ASTM: ASTM D-5790 Purge and trap
G-PhAPTMS- SGEP: Functionalizing graphene with N-Phenyl-3-aminopropyl trimethoxy -sorbent gas extraction
HS-GC: Headspace gas chromatograph
3D-SPE-CB-PLA: 3D printed solid-phase extraction carbon black modified polylactic acid (PLA)
OCP: Organo chlorine pesticides
PBDE: Polybrominated diphenyl ethers ACN: acetonitrile
BTEX: benzene, toluene, ethyl benzene, ortho-xylene and meta- and para-xylene
BTX: benzene, toluene and xylene
DAD: diode array detector
DI: direct immersion
ECD: electron capture detector
FID: flame ionization detector
FPD: flame photometric detector
FD: fluorescence detection
LOD: limit of detection (μg L^{-1})
LOQ: limit of quantification (μg L^{-1})
MA: microwave assisted
MAE: microwave assisted extraction
MW: multiwalled; PAHs: polycyclic aromatic hydrocarbons
PDMSAC: PDMS mixed with activated C
TSD: thermoionic specific detection

5. Conclusions

Through entering from different sources such as water, air and foods, the VOCs cause several diseases in humans. So, the environmental samples such as water, wastewater and air must be controlled and determined by applied methodologies. The human life depends on water future and elimination of pollutions such as VOCs in waters. By growing economy and increasing population, the main theme is water supplies without any contaminations. Quantity and quality of water must be checked daily and main parameters of waters should be controlled. So, the water, especially drinking water conservation is extremely important, and contaminations such as BTEX, VOCs and other organic pollutions in waters should be removed by new technologies. The technologies based on sorbents depend on water characteristics, affordability, acceptability and level of application. Every methodology for VOCs removal from waters have many advantages and disadvantages for water treatment. Therefore, the important parameters for any methodology such as speed, simplicity and selectivity must be studied. The vary methodology such as, solid phase extraction, liquid phase extraction, the adsorption/ desorption, the sole gel technology, RCO, CO and PCO have been used for VOCs removal from waters. In this review the recent technologies based on sorbents or catalysts are introduced for VOCs removal from water samples.

6. Acknowledgement

This review was supported by the Science and Research Branch, Islamic Azad University and Dr. Hamid Shirkhanloo in Research Institute of Petroleum Industry of Iran.

7. References

[1] K. Tzortzatou, E. Grigoropoulou, Catalytic oxidation of industrial organic solvent vapors, J. Environ. Sci. Health Part A, 45 (2010) 534-541.
[2] I. Rutkiewicz, W. Kujawski, J. Namieśnik, Pervaporation of volatile organohalogen compounds through polydimethylsiloxane membrane, Desalination, 264 (2010) 160-164.
[3] W.S. Backer, WITHDRAWN: The impact of methyl tertiary-butyl ether (MTBE) on contaminated drinking water in organic

blood chemistry, Elsevier. 2013.
[4] I. Levchuk, A. Bhatnagar, M. Sillanpää, Overview of technologies for removal of methyl tert-butyl ether (MTBE) from water, Sci. Total Environ., 476 (2014).415-433.
[5] C. Perego, R. Bagatin, M. Tagliabue, R. Vignol, et al., Zeolites and related mesoporous materials for multi-talented environmental solutions, Micropor. Mesopor. Mater., 166 (2013) 37-49.
[6] S. Xia, X. Dong, Y. ZHU, W. Wei, F. Xiangli, W. Jin, Dehydration of ethyl acetate–water mixtures using PVA/ceramic composite pervaporation membrane, Sep. Purif. Technol., 77 (2011) 53-59.
[7] U. Hömmerich, R. Rautenbach, Design and optimization of combined pervaporation/ distillation processes for the production of MTBE, J. Membrane Sci., 146 (1998) 53-64.
[8] W. Kujawski, Application of pervaporation and vapor permeation in environmental protection, Polish J. Environ. Studies, 9 (2000)13-26.
[9] P. Sampranpiboon, R. Jiraratananon, D. Uttapap, X. Feng, RY. Huang., Pervaporation separation of ethyl butyrate and isopropanol with polyether block amide (PEBA) membranes, J. Membrane Sci., 173 (2000) 53-59.
[10] W. Yoshida, Y. Cohen, Removal of methyl tert-butyl ether from water by pervaporation using ceramic-supported polymer membranes, J. Membrane Sci., 229 (2004) 27-32.
[11] D. Zadaka-Amir, A. Nasser, S. Nir, YG. Mishael, Removal of methyl tertiary-butyl ether (MTBE) from water by polymer–zeolite composites, Micropor. Mesopor. Mater., 151(2012) 216-222.
[12] K. Zhou, QG. Zhang, GL. Han, AM. Zhu, QL. Liu, Pervaporation of water–ethanol and methanol–MTBE mixtures using poly (vinyl alcohol)/cellulose acetate blended membranes, J. Membrane Sci., 448 (2013) 93-101.
[13] A. Kumar, BP. Singh, M. Punia, D. Singh, K. Kumar, VK. Jain, Assessment of indoor air concentrations of VOCs and their associated health risks in the library of Jawaharlal Nehru University, New Delhi, Environ. Sci. Pollut. Res., 21 (2014)2240-2248.
[14] P. Saxena, C. Ghosh, A review of assessment of benzene, toluene, ethylbenzene and xylene (BTEX) concentration in urban atmosphere of Delhi, Int. J. Phys. Sci., 7 (2012) 850-860.
[15] A.R. Schnatter, DC. Glass, G. Tang, RD. Irons, L. Rushton, Myelodysplastic syndrome and benzene exposure among petroleum workers: an international pooled analysis, J. Natl. Cancer Inst., 104 (2012) 1724-1737.
[16] T. Tunsaringkarn, W. Siriwong, A. Rungsiyothin, S. Nopparatbundit, Occupational exposure of gasoline station workers to BTEX compounds in Bangkok, Thailand, Int. J. Occup. Environ. Med., 3 (2012) 117-125.
[17] Cancer, I.A.f.R.o. Agents classified by the IARC Monographs. International Agency for Research on Cancer, pp1-109, 2014. http://monographs.iarc.fr/ENG/Classification/ClassificationsAlphaOrder.pdf
[18] S. Garte, E. Taioli, T. Popov, C. Bolognesi, P. Farmer, F. Merlo, Genetic susceptibility to benzene toxicity in humans, J. Toxicol. Environ. Health Part A, 71 (2008)1482-1489.
[19] C. Abbate, C. Giorgianni, F. Munao, R. Brecciaroli, Neurotoxicity induced by exposure to toluene, Int. Arch. Occup. Environ. Health, 64 (1993) 389-392.
[20] L. Ernstgård, E. Gullstrand, A. Löf, G. Johanson, Are women more sensitive than men to 2-propanol and m-xylene vapors, Occup. Environ. Med., 59 (2002) 759-767.
[21] GG. Bond, EA. McLaren, CL. Baldwin, RR. Cook, An update of mortality among chemical workers exposed to benzene, Occup. Environ. Med., 43 (1986) 685-691.
[22] MA. Midzenski, MA. McDiarmid, N. Rothman, K. Kolodner, Acute high dose exposure to benzene in shipyard workers.

Am. J. Ind. Med., 22 (1992) 553-565.

[23] K. Murata, S. Araki, K. Yokoyama, T. Tanigawa, K. Yamashita, F. Okajima, T. Sakai, C. Matsunaga, K. Suwa, Cardiac autonomic dysfunction in rotogravure printers exposed to toluene in relation to peripheral nerve conduction, Ind. health, 31(1993) 79-90.

[24] JE. Cometto-Mu, WS. Cain, Relative sensitivity of the ocular trigeminal, nasal trigeminal and olfactory systems to airborne chemicals, Chem. Senses., 20 (1995) 191-198.

[25] E. Ahaghotu, RJ. Babu, A. Chatterjee, M. Singh, Effect of methyl substitution of benzene on the percutaneous absorption and skin irritation in hairless rats, Toxicol. lett., 159 (2005) 261-271.

[26] F. Doghieri, A. Nardella, GC. Sarti, C. Valentini, Pervaporation of methanol-MTBE mixtures through modified poly (phenylene oxide) membranes, J. Membrane Sci., 91(1994) 283-291.

[27] L. Gales, A. Mendes, C. Costa, Removal of acetone, ethyl acetate and ethanol vapors from air using a hollow fiber PDMS membrane module, J. Membrane Sci., 197(2002)211-222.

[28] W. Kujawski, S. Krajewska, M. Kujawski, L. Gazagnes, A. Larbot, M. Persin, Pervaporation properties of fluoroalkylsilane (FAS) grafted ceramic membranes, Desalination., 205 (2007) 75-86.

[29] A. Urkiaga, N. Bolano, L. De Las Fuentes, Removal of micropollutants in aqueous streams by organophilic pervaporation, Desalination.,149 (2002) 55-60.

[30] J. Cheng, L. Li, Y. Li, Q. Wang, C. He, Fabrication of pillar [5] arene-polymer-functionalized cotton fibers as adsorbents for adsorption of organic pollutants in water and volatile organic compounds in air, Cellulose, 26 (2019) 3299-3312.

[31] V. Kumar, S. Kumar, KH. Kim, DC. Tsang, SS. Lee, Metal organic frameworks as potent treatment media for odorants and volatiles in air, Environ. Res. Lett., 168 (2019)336-356.

[32] S. KP Veerapandian, N. De Geyter, JM. Giraudon, JF. Lamonier, R. Morent, The use of zeolites for VOCs abatement by combining non-thermal plasma, adsorption, and/or catalysis: a review, Catalysts, 9 (2019) 98.

[33] J. Hou, Z. Xia, S. Li, K. Zhou, N. Lu, Operation parameter optimization of a gas hydrate reservoir developed by cyclic hot water stimulation with a separated-zone horizontal well based on particle swarm algorithm, Energy J., 96 (2016) 581-591.

[34] MA. Campesi, CD. Luzi, GF. Barreto, OM. Martínez, Evaluation of an adsorption system to concentrate VOC in air streams prior to catalytic incineration, J. Environ. Manage., 154 (2015) 216-224.

[35] F. Chu, Y. Zheng, B. Wen, L. Zhou, J. Yan, Y. Chen, Adsorption of toluene with water on zeolitic imidazolate framework-8/graphene oxide hybrid nanocomposites in a humid atmospherem, RSC Adv., 8 (2018) 2426-2432.

[36] M. Mao, Y. Li, J. Hou, M. Zeng, X. Zhao. Extremely efficient full solar spectrum light driven thermocatalytic activity for the oxidation of VOCs on OMS-2 nanorod catalyst, Appl. Catal. B., 174 (2015) 496-503.

[37] W. Jianping, C. Yu, J. Xiaoqiang, C. Dongyan, Simultaneous removal of ethyl acetate and ethanol in air streams using a gas–liquid–solid three-phase flow airlift loop bioreactor, Chem. Eng. J., 106 (2005) 171-175.

[38] LM. Vane, FR. Alvarez, Full-scale vibrating pervaporation membrane unit: VOC removal from water and surfactant solutions, J. Membrane Sci., 202 (2002) 177-193.

[39] LM. Vane, FR. Alvarez, B. Mullins, Removal of methyl tert-butyl ether from water by pervaporation: bench-and pilot-scale evaluations, Environ. Sci. Technol., 35 (2001) 391-397.

[40] S. Zheng, C. Shen, M. Alunbate, J. Deng, L. Wang, Z. Han, H. Tang, Discovery of VOC-compliant TEOS sol and its application to SiO_2/novolac hybrid coatings, Prog. Org.

Coat., 76 (2013) 425-431.
[41] D. Delimaris, T. Ioannides, VOC oxidation over MnOx–CeO_2 catalysts prepared by a combustion method, Appl. Catal. B., 84 (2008) 303-312.
[42] E. Gallego, JF. Perales, FJ. Roca, X. Guardino, Surface emission determination of volatile organic compounds (VOC) from a closed industrial waste landfill using a self-designed static flux chamber, Sci. Total Environ., 470 (2014) 587-599.
[43] HO. Karlsson, G. Trägårdh, Aroma compound recovery with pervaporation-feed flow effects, J. Membrane Sci., 81 (1993) 163-171.
[44] T. Masuda, M. Takatsuka, BZ. Tang, T. Higashimura, Pervaporation of organic liquid-water mixtures through substituted polyacetylene membranes, J. Membrane Sci., 49 (1990) 69-83.
[45] HC. Park, NE. Ramaker, MH. Mulder, CA. Smolders, Separation of MTBE-methanol mixtures by pervaporation, Sep. Sci. Technol., 30 (1995) 419-433.
[46] Z. Qi, EL. Cussler, Microporous hollow fibers for gas absorption: I. Mass transfer in the liquid, J. Membrane Sci., 23 (1985) 321-332.
[47] M. Bhowmick, MJ. Semmens, Batch studies on a closed loop air stripping process, Water Res., 28 (1994) 2011-2019.
[48] MJ. Semmens, R. Qin, A. Zander. Using a microporous hollow-fiber membrane to separate VOCs from water, J. AM. Water Works ASS., 81 (1989) 162-167.
[49] AK. Zander, MJ. Semmens, RM. Narbaitz, Removing VOCs by membrane stripping. J. AM. Water Works ASS., 81 (1989) 76-81.
[50] K. Castro, AK. Zander, Membrane air-stripping: effects of pretreatment, J. AM. Water Works ASS., 87 (1995) 50-61.
[51] A. Das, I. Abou-Nemeh, S. Chandra, KK. Sirkar, Membrane-moderated stripping process for removing VOCs from water in a composite hollow fiber module, J. Membrane Sci., 148 (1998) 257-271.
[52] H. Mahmud, A. Kumar, Rm. Narbaitz, T. Matsuura, Membrane air stripping: a process for removal of organics from aqueous solutions. 1998.
[53] H. Mahmud, A. Kumar, RM. Narbaitz, T. Matsuura, A study of mass transfer in the membrane air-stripping process using microporous polyproplylene hollow fibers, J. Membrane Sci., 179 (2000) 29-41.
[54] H. Mahmud, A. Kumar, RM. Narbaitz, T. Matsuura, Mass transport in the membrane air-stripping process using microporous polypropylene hollow fibers: effect of toluene in aqueous feed, J. Membrane Sci., 209 (2002) 207-219.
[55] A. Malek, K. Li, WK. Teo, Modeling of microporous hollow fiber membrane modules operated under partially wetted conditions, Ind. Eng. Chem. Res., 36 (1997) 784-793.
[56] A. Gabelman, ST. Hwang, Hollow fiber membrane contactors, J. Membrane Sci., 159 (1999) 61-106.
[57] M. Jabłońska, A. Król, E. Kukulska-Zając, K. Tarach, V. Girman, L. Chmielarz, K. Góra-Marek, Zeolites Y modified with palladium as effective catalysts for low-temperature methanol incineration, Appl. Catal. B., 166 (2015) 353-365.
[58] SC. Kim, WG. Shim, Properties and performance of Pd based catalysts for catalytic oxidation of volatile organic compounds, Appl. Catal. B., 92 (2009) 429-436.
[59] ME. Jenkin, SM. Saunders, RG. Derwent, MJ. Pilling, Development of a reduced speciated VOC degradation mechanism for use in ozone models, Atmos. Environ., 36 (2002) 4725-4734.
[60] JY. Jeon, HY. Kim, SL. Woo, Mechanistic study on the SCR of NO by C3H6 over Pt/V/MCM-41. Appl. Catal. B., 44 (2003) 301-310.
[61] DP. Debecker, B. Farin, EM. Gaigneaux, C. Sanchez, C. Sassoye, Total oxidation of propane with a nano-RuO2/TiO2 catalyst, Appl. Catal. A-gen., 481 (2014) 11-18.
[62] MP. Pina, S. Irusta, M. Menéndez, J. Santamaria, R. Hughes, N. Boag, Combustion of volatile organic compounds over platinum-based catalytic membranes, Ind. Eng. Chem. Res., 36 (1997) 4557-4566.
[63] HJ. Joung, JH. Kim, JS. Oh, DW You, HO. Park,

KW. Jung, Catalytic oxidation of VOCs over CNT-supported platinum nanoparticles, Appl. Surf. Sci., 290 (2014) 267-273.

[64] Z. Abdelouahab-Reddam, R. El Mail, F. Coloma, A. Sepúlveda-Escribano, Platinum supported on highly-dispersed ceria on activated carbon for the total oxidation of VOCs, Appl. Catal. A-Gen., 494 (2015) 87-94.

[65] M. Konsolakis, SA. Carabineiro, PB. Tavares, JL. Figueiredo, Redox properties and VOC oxidation activity of Cu catalysts supported on Ce1−xSmxOδ mixed oxides, J. Hazard. Mater., 261 (2013) 512-521.

[66] M. Piumetti, D. Fino, N. Russo, Mesoporous manganese oxides prepared by solution combustion synthesis as catalysts for the total oxidation of VOCs, Appl. Catal. B., 163 (2015) 277-287.

[67] S. Scirè, RM. Riccobene, C. Crisafulli, Ceria supported group IB metal catalysts for the combustion of volatile organic compounds and the preferential oxidation of CO, Appl. Catal. B., 101 (2010) 109-117.

[68] SH. Teimoori, AH. Hassani, M. Panaahie, Extraction and determination of benzene from waters and wastewater samples based on functionalized carbon nanotubes by static head space gas chromatography mass spectrometry Anal. Method Environ. Chem. J., 3 (2020) 17-26

[69] V. Kumar, YS. Lee, JW Shin, KH. Kim, D. Kukkar, YF. Tsang, Potential applications of graphene-based nanomaterials as adsorbent for removal of volatile organic compounds Vanish Kumara,1, Yoon-Seo Lee, Environ. Int., 135 (2020) 105356.

[70] DR. Dreyer, S. Park, CW. Bielawski, RS. Ruoff. The chemistry of GO, Chem. Soc. Rev., 39 (2010) 228-40.

[71] G. Ruess, Über das Graphitoxyhydroxyd (Graphitoxyd). Monatshe. Chem. Verwandte Teile Wissenschaft., 76 (1974) 381–417.

[72] W. Scholz, HP. Boehm, Untersuchungen am graphitoxid. VI. Betrachtungen zur struktur des graphitoxids, Z Anorg Allg Chem., 369 (1969) 327–340.

[73] T. Szabó, O. Berkesi, P. Forgó, K. Josepovits, Y. Sanakis, D. Petridis, I. Dékány, Evolution of surface functional groups in a series of progressively oxidized graphite oxides, Chem. Mater., 18 (2006) 2740-2749.

[74] F. Chu, Y. Zheng, B. Wen, L. Zhou, J. Yan, Y. Chen, Adsorption of toluene with water on zeolitic imidazolate framework-8/graphene oxide hybrid nanocomposites in a humi atmosphere, RSC Adv., 8 (2018) 2426-2432.

[75] L. Yu, L. Wang, W. Xu, L. Chen, M. Fu, J. Wu, D. Ye. Adsorption of VOCs on reduced graphene oxide, J. Environ. Sci., 67 (2018) 171-8.

[76] B. Szczęśniak, J. Choma, m. Jaroniec, Effect of graphene oxide on the adsorption properties of ordered mesoporous carbons toward H2, C6H6, CH4 and CO2, Micropor. Mesopor. Mater., 261 (2018) 105-110.

[77] B. Szczęśniak, L. Osuchowski, J. Choma, M. Jaroniec. Highly porous carbons obtained by activation of polypyrrole/reduced graphene oxide as effective adsorbents for CO_2, H 2 and C_6H_6, J. Porous Mater., 25 (2018) 621-627.

[78] GQ. Liu, MX. Wan, ZH. Huang, FY. Kang, Preparation of graphene/metal-organic composites and their adsorption performance for benzene and ethanol, New Carbon Mater., 30 (2015) 566-571.

[79] JM. Kim, JH. Kim, CY. Lee, DW. Jerng, HS. Ahn, Toluene and acetaldehyde removal from air on to graphene-based adsorbents with microsized pores, J. Hazard. Mater., 344 (2018) 458-65.

[80] L. Wu, l. Zhang, T. Meng, F. Yu, J. Chen, J. Ma, Facile synthesis of 3D amino-functional graphene-sponge composites decorated by graphene nanodots with enhanced removal of indoor formaldehyde, Aerosol Air Qual Res., 15 (2015) 1028-34.

[81] V. Kumar, YS. Lee, JW. Shin, KH. Kim,D. Kukkar, YF. Tsang, Potential applications of graphene-based nanomaterials as adsorbent for removal of volatile organic compounds, Environ. Int., 135 (2020) 105356.

[82] ST. Lim, JH. Kim, CY. Lee, S. Koo, DW. Jerng, S. Wongwises, HS. Ahn, Mesoporous graphene adsorbents for the removal of toluene and xylene

at various concentrations and its reusability, Sci. Rep., 9 (2019) 1-12.

[83] TK. Tseng, YS. Lin, YJ. Chen, H. Chu, A review of photocatalysts prepared by sol-gel method for VOCs removal, Int. J. Mol. Sci., 11 (2010) 2336-2361.

[84] U. Schubert, Catalysts made of organic-inorganic hybrid materials, New J. Chem., 18 (1994) 1049-1058.

[85] J. Blum, A. Rosenfeld, F. Gelman, H. Schumann, D. Avnir, Hydrogenation and dehalogenation of aryl chlorides and fluorides by the sol–gel entrapped RhCl3–Aliquat 336 ion pair catalyst, J. Mol. Catal. A Chem., 146 (1999) 117-122.

[86] P. Banet, C. Cantau, C. Rivron, TH. Tran-Thi, Nano-porous sponges and proven chemical reactions for the trapping and sensing of halogenated gaseous compounds, Actual. Chim., (2009) 30-35.

[87] J. Lin, CW. Brown, Sol-gel glass as a matrix for chemical and biochemical sensing. Trac-Trend Anal. Chem., 16 (1997) 200-211.

[88] R. Gvishi, U. Narang, G. Ruland, DN. Kumar, PN. Prasad, Novel, Organically Doped, Sol–Gel-Derived Materials for Photonics: Multiphasic Nanostructured Composite Monoliths and Optical Fibers, Appl. Organomet. Chem., 11 (1997) 107-127.

[89] B. Dunn, GC. Farrington, B. Katz, Sol-gel approaches for solid electrolytes and electrode materials, Solid State Ion., 70 (1994) 3-10.

[90] D. Levy, L. Esquivias, Sol–gel processing of optical and electrooptical materials, Adv. Mater., 7 (1995) 120-129.

[91] B. Dunn, JI. Zink, Optical properties of sol–gel glasses doped with organic molecules. J. Mater. Chem., 1 (1991) 903-913.

[92] D. Levy, Recent applications of photochromic sol-gel materials. molecular crystals and liquid crystals science and technology, section A, Mol. Cryst. Liq. Cryst., 297 (1997) 31-39.

[93] G. Xomeritakis, CY. Tsai, YB. Jiang, CJ. Brinker, Tubular ceramic-supported sol–gel silica-based membranes for flue gas carbon dioxide capture and sequestration, J. Membr. Sci., 341 (2009) 30-36.

[94] Z. Zeng, W. Qiu, M. Yang, X. Wei, Z. Huang, F. Li, Solid-phase microextraction of monocyclic aromatic amines using novel fibers coated with crown ether, J. Chromatogr. A., 934 (2001) 51-57.

[95] MR. Hoffmann, ST. Martin, W. Choi, DW. Bahnemann, Environmental applications of semiconductor photocatalysis, Chem. Rev., 95 (1995) 69-96.

[96] L. Cao, Z. Gao, SL. Suib, TN. Obee, SO. Hay, JD. Freihaut, Photocatalytic oxidation of toluene on nanoscale TiO2 catalysts: studies of deactivation and regeneration, J. Catal., 196 (2000) 253-261.

[97] S. Yamazaki, H. Abe, T. Tanimura, Y. Yamasaki, K. Kanaori, K. Tajima, Effect of thermal treatment on the photocatalytic degradation of ethylene, trichloroethylene, and chloroform, Res. Chem. Intermed., 35 (2009) 91-101.

[98] WH. Ching, M. Leung, DY. Leung, Solar photocatalytic degradation of gaseous formaldehyde by sol–gel TiO2 thin film for enhancement of indoor air quality, Sol. Energy., 77 (2004) 129-135.

[99] BY. Lee, SW. Kim, SC. Lee, HH. Lee, SJ. Choung, Photocatalytic decomposition of gaseous formaldehyde using TiO_2, SiO_2− TiO_2 and Pt−TiO_2, Int. J. Photoenergy, 5 (2002) 463920.

[100] N. Parvizi, N. Rahemi, S. Allahyari, M. Tasbihi, Plasma-catalytic degradation of BTX over ternary perovskite-type La1-x (Co, Zn, Mg, Ba) xMnO3 nanocatalysts, J. Ind. Eng. Chem., 84 (2020) 167-178.

[101] DP. Debecker, R. Delaigle, K. Bouchmella, P. Eloy, EM. Gaigneaux, PH. Mutin, Total oxidation of benzene and chlorobenzene with MoO3-and WO3-promoted V2O5/TiO2 catalysts prepared by a nonhydrolytic sol–gel route, Catal. Today, 157 (2010) 125-130.

[102] A. Sarafraz-Yazdi, A. Amiri, G. Rounaghi, HE. Hosseini, A novel solid-phase microextraction using coated fiber based sol–gel technique using poly (ethylene glycol) grafted multi-walled carbon nanotubes for determination of benzene, toluene, ethylbenzene and o-xylene in water samples with gas chromatography-flam ionization detector, J.

Chromatogr. A, 1218 (2011) 5757-5764.

[103] T. Uragami, H. Yamada, T. Miyata, Removal of dilute volatile organic compounds in water through graft copolymer membranes consisting of poly (alkylmethacrylate) and poly (dimethylsiloxane) by pervaporation and their membrane morphology, J. Membr. Sci., 187 (2001) 255-269.

[104] T. Uragami, T. Ohshima, T. Miyata, Removal of benzene from an aqueous solution of dilute benzene by various cross-linked poly (dimethylsiloxane) membranes during pervaporation, Macromolecules, 36 (2003) 9430-9436.

[105] T. Ohshima, T. Miyata, T. Uragami, H. Berghmens, Cross-linked smart poly (dimethylsiloxane) membranes for removal of volatile organic compounds in water, J. Mol. Struc., 739 (2005) 47-55.

[106] T. Ohshima, Y. Kogami, T. Miyata, T. Uragami, Pervaporation characteristics of cross-linked poly (dimethylsiloxane) membranes for removal of various volatile organic compounds from water, J. Membrane Sci., 260 (2005) 156-163.

[107] H. Zhen, SM. Jang, WK. Teo, K. Li, Modified silicone–PVDF composite hollow fiber membrane preparation and its application in VOC separation, J. Appl. Polym. Sci., 99 (2006) 2497-2503.

[108] H. Wu, L. Liu, F. Pan, C. Hu, Z. Jiang, Pervaporative removal of benzene from aqueous solution through supramolecule calixarene filled PDMS composite membranes, Sep. Purif. Technol., 51 (2006) 352-358.

[109] S. Chovau, A. Dobrak, A. Figoli, F. Galiano, S. Simone, E. Drioli, SK. Sikdar, B. Van der Bruggen, Pervaporation performance of unfilled and filled PDMS membranes and novel SBS membranes for the removal of toluene from diluted aqueous solutions, Chem. Eng. J., 159 (2010) 37-46.

[110] J. Xu, A. Ito, Removal of VOC from water by pervaporation with hollow-fiber silicone rubber membrane module, Desalination Water Treat., 17 (2010) 135-42.

[111] T. Uragami, I. Sumida, T. Miyata, T. Shiraiwa, H. Tamura, T. Yajima, Pervaporation characteristics in removal of benzene from water through polystyrene-poly (dimethylsiloxane) IPN membranes, Mater. Sci. Appl., 2 (2011)169.

[112] T. Uragami, Y. Matsuoka, T. Miyata. Removal of dilute benzene in water through ionic liquid/poly (vinyl chloride) membranes by pervaporation, J. Membrane Sci. Res., 2 (2016) 20-5.

[113] J. Kujawa, S. Al-Gharabli, W. Kujawski, K. Knozowska. Molecular grafting of fluorinated and nonfluorinated alkylsiloxanes on various ceramic membrane surfaces for the removal of volatile organic compounds applying vacuum membrane distillation, ACS Appl. Mater. Inter., 9 (2017) 6571-90.

[114] Z. Zhang, Z. Jiang, W. Shangguan. Low-temperature catalysis for VOCs removal in technology and application: A state-of-the-art review, Catal. Today, 264 (2016) 270-8.

[115] X. Liu, J. Zeng, W. Shi, J. Wang, T. Zhu, Y. Chen. Catalytic oxidation of benzene over ruthenium–cobalt bimetallic catalysts and study of its mechanism, Catal, Sci, Technol., 7 (2017) 213-21.

[116] M. Zhang, W. Li, X. Wu, F. Zhao, D. Wang, X, Zha, S. Li, H. Liu, Y. Chen. Low-temperature catalytic oxidation of benzene over nanocrystalline Cu–Mn composite oxides by facile sol–gel synthesis, New J. Chem., 44 (2020) 2442-51.

[117] P. Marín, FV. Díez, S. Ordóñez. A new method for controlling the ignition state of a regenerative combustor using a heat storage device, Appl. Energy, 116 (2014) 322-32.

[118] S. Hoseini, N. Rahemi, S. Allahyari, M. Tasbihi. Application of plasma technology in the removal of volatile organic compounds (BTX) using manganese oxide nano-catalysts synthesized from spent batteries, J. Clean. Prod., 232 (2019) 1134-47.

[119] V. Georgiev. Ozone Assisted Low Temperature Catalytic Benzene Oxidation over Al2O3, SiO2, AlOOH Supported Ni/Pd Catalytic, Int. J. Chem. Mater. Eng., 14 (2020) 168-73.

[120] J. Zhang, Y. Hu, J. Qin, Z. Yang, M. Fu. TiO_2-UiO-66-NH_2 nanocomposites as efficient photocatalysts for the oxidation of VOCs, Chem. Eng. J., 385 (2020) 123814.

[121] J. Ji, Y. Xu, H. Huang, M. He, S. Liu, G. Liu, R. Xie, Q. Feng, Y. Shu, Y. Zhan, R. Fang. Mesoporous TiO_2 under VUV irradiation: Enhanced photocatalytic oxidation for VOCs degradation at room temperature, Chem. Eng. J., 327 (2017) 490-9.

[122] H. Huang, G. Liu, Y. Zhan, Y. Xu, Lu H, H. Huang, Q. Feng, M. Wu. Photocatalytic oxidation of gaseous benzene under VUV irradiation over TiO_2/zeolites catalysts, Catal. Today, 281 (2017) 649-55.

[123] P. Fu, P. Zhang, J. Li. Photocatalytic degradation of low concentration formaldehyde and simultaneous elimination of ozone by-product using palladium modified TiO_2 films under UV irradiation. Appl. Catal. B: Environ., 105 (2011) 220-8.

[124] E. Rezaei, J. Soltan, N. Chen. Catalytic oxidation of toluene by ozone over alumina supported manganese oxides. Effect of catalyst loading, Appl. Catal. B: Environ., 136 (2013) 239-47.

[125] Y. Shu, M. He, J. Ji, H. Huang, S. Liu, DY. Leung. Synergetic degradation of VOCs by vacuum ultraviolet photolysis and catalytic ozonation over Mn-xCe/ZSM-5, J. Hazard. Mater., 364 (2019) 770-9.

[126] E. Rezaei, J. Soltan. Low temperature oxidation of toluene by ozone over MnOx/γ-alumina and MnOx/MCM-41 catalysts, Chem. Eng. j., 198 (2012) 482-90.

[127] AM. Vandenbroucke, R. Morent, N. De Geyter, C. Leys. Non-thermal plasmas for non-catalytic and catalytic VOC abatement, J. Hazard. Mater., 195 (2011) 30-54.

[128] HH. Kim, Y. Teramoto, N. Negishi, A. Ogata. A multidisciplinary approach to understand the interactions of nonthermal plasma and catalyst: A review, Catal. Today, 256 (2015) 13-22.

[129] H. Guo, X. Liu, H. Hojo, X. Yao, H. Einaga, W. Shangguan. Removal of benzene by non-thermal plasma catalysis over manganese oxides through a facile synthesis method, Environ. Sci. Pollut. Res., 26 (2019) 8237-47.

[130] N. Jiang, J. Hu, J. Li, K. Shang, N. Lu, Y. Wu. Plasma-catalytic degradation of benzene over Ag–Ce bimetallic oxide catalysts using hybrid surface/packed-bed discharge plasmas, Appl. Catal. B: Environ., 184 (2016) 355-63.

[131] DK. Patel, HB. Kim, SD. Dutta, K. Ganguly, KT. Lim. Carbon nanotubes-based nanomaterials and their agricultural and biotechnological applications, Mater., 13 (2020) 1679.

[132] F. Pourfayaz, S. Boroun, J. Babaei, B. Ebrahimi Hoseinzadeh. An evaluation of the adsorption potential of MWCNTs for benzene and toluene removal, Int. J. Nanosci. Nanotechnol., 10 (2014) 27-34.

[133] LH. Keith, H. Lawrence, HJ. Brass, DJ. Sullivan, JA. Boiani, KT. Alben, An introduction to the national environmental methods index, Environ. Sci. Technol., 6 (2005) 173A-176A.

[134] R. Kubinec, J. Adamuščin, H. Jurdáková, M. Foltin, I. Ostrovský, A. Kraus, L. Soják, Gas chromatographic determination of benzene, toluene, ethylbenzene and xylenes using flame ionization detector in water samples with direct aqueous injection up to 250 µl, J. Chromatogr. A, 1084 (2005) 90-4.

[135] V. López Grimau, MC. Gutiérrez Bouzán, J. Griera, JM. Guadayol Cunill. Determination of non halogenated solvents in industrial wastewater using solid phase microextraction (SPME) and GC-MS, Latin Am. Appl. Res., 36 (2006) 49-55.

[136] R. Yusiasih, R. Marvalosha, SD. Suci, E. Yuliani, MM. Pitoi, Low volume liquid-liquid

extraction for the determination of benzene, toluene, and xylene in water by GC-FID and HPLC-UV, IOP Conf. Ser.: Earth Environ. Sci., 277 (2019) 012019.

[137] G. Garcia de Freitas Junior, TM. Florêncio, RJ.Mendonça, GR. Salazar-Banda, Rt. Oliveira, Simultaneous Voltammetric Determination of Benzene, Toluene and Xylenes (BTX) in Water Using a Cathodically Pre-Treated Boron-Doped Diamond Electrode, Electroanal., 31 (2019) 554-559.

[138] X. Li, Z. Jia, J. Wang, H. Sui, L. He, OA.Volodin, Detection of Residual Solvent in Solvent-Extracted Unconventional Oil Ore Gangues. J. Eng. Thermophys., 28 (2019) 499-506.

[139] N. Sun, SQ. Wang, R. Zou ,WG. Cui,A Zhang , T. Zhang, Q. Li, ZZ. Zhuang, YH. Zhang,J. Xu, MJ. Zaworotko, Benchmark selectivity p-xylene separation by a non-porous molecular solid through liquid or vapor extraction, Chem. sci.,10 (2019) 8850-8854.

[140] S. Teimoori, AH.Hassani , M. Panaahie, The Extraction and determination of benzene from waters and wastewater samples based on functionalized carbon nanotubes by static head space gas chromatography mass spectrometry, Anal. Method Environ. Chem. J., 3 (2020) 17-26.

[141] MB. Hosseinabadi, AF. Zarandi, Functionalized graphene-trimethoxyphenyl silane for toluene removal from workplace air by sorbent gas extraction method, Anal. Method. Environ. Chem. J., 2 (2019) 45-54.

[142] L. Mohammadi, E. Bazrafshan, M. Noroozifar, A. Ansari-Moghaddam, F. Barahuie, D. Balarak , Adsorptive removal of Benzene and Toluene from aqueous environments by cupric oxide nanoparticles: kinetics and isotherm studies, J. Chem., 2017 (2017) 2069519.

[143] SG. Attari, A. Bahrami, FG. Shahna, M. Heidari, Solid-phase microextraction fiber development for sampling and analysis of volatile organohalogen compounds in air, J. Environ. Health Sci. Eng., 12 (2014) 123-130.

[144] C. Nerın, MR. Philo, J. Salafranca, L.Castle, Determination of bisphenol-type contaminants from food packaging materials in aqueous foods by solid-phase microextraction–high-performance liquid chromatography, J. Chromatogr., 963 (2002) 375-380.

[145]FJ. Conde, Am. Afonso, V.González, JH. Ayala, Optimization of an analytical methodology for the determination of alkyl-and methoxy-phenolic compounds by HS-SPME in biomass smoke, Anal. Bioanal. chem., 385 (2006) 1162-1171.

[146] SB.Hawthorne, CB. Grabanski, DJ. Miller, JP. Kreitinger, Solid-phase microextraction measurement of parent and alkyl polycyclic aromatic hydrocarbons in milliliter sediment pore water samples and determination of K DOC values, Environ. Sci. Technol., 39 (2005) 2795-2803.

[147] X. Lu, C.Fan, J. Shang, J. Deng, H. Yin, Headspace solid-phase microextraction for the determination of volatile sulfur compounds in odorous hyper-eutrophic freshwater lakes using gas chromatography with flame photometric detection, Microchem. J., 104 (2012) 26–32.

[148] JX. Wang, DQ. Jiang, ZY. Gu, XP.Yan, Multiwalled carbon nanotubes coated fibers for solid-phase microextraction of polybrominated diphenyl ethers in water and milk samples before gas chromatography with electron-capture detection, J. Chromatogr. A, 1137 (2006) 8-14.

[149]MH. Banitaba, AA. Mohammadi, SS. Davarani, A. Mehdinia, Preparation and evaluation of a novel solid-phase microextraction fiber based on poly(3,4-ethylenedioxythiophene) for the analysis of OCPs in water, Anal. Methods, 3 (2011) 2061–2067.

[150] LA. Lagalante, AJ. Lagalante,AF. Lagalante. 3D printed solid-phase extraction sorbents for removal of volatile organic compounds from water, J. Water Process Eng., 35 (2020)101194.

Anal. Method Environ. Chem. J. 3 (2) (2020) 59-73

AMECJ

Research Article, Issue 2
Analytical Methods in Environmental Chemistry Journal
Journal home page: www.amecj.com/ir

Facile synthesis of a modified HF-free MIL-101(Cr) nanoadsorbent for extraction nickel in water and wastewater samples

Saeed Fakhraie [a,*] and Ali Ebrahimi [b]

[a]*Chemistry Department, Yasouj University, P.O. Box 74831-75918, Yasouj, Iran*
[b]*Occupational Health Engineering Department, School of Public Health, Qom University of Medical Sciences, Qom, Iran*

ARTICLE INFO:

Received 16 Feb 2020
Revised form 12 Apr 2020
Accepted 8 May 2020
Available online 28 Jun 2020

Keywords:
MIL-101(Cr) nanoadsorbent,
Nickel,
Water and wastewaters,
Dispersive suspension micro solid phase extraction,
Atom trap-flame atomic absorption spectrometry

ABSTRACT

A novel sorbent based on MIL-101(Cr) nanoadsorbent as a MOF structure was used for nickel extraction from water and wastewater samples. In this study, 30 mg of MIL-101(Cr) nanoadsorbent dispersed in 50 mL of water or wastewater samples, after sonication and adjusting pH =8.5, the nickel ions was extracted by carboxyl groups of terephthalic acid (MOF─(C_6H_4 $(COO)^{2-}$…. Ni^{2+}) by dispersive suspension-micro solid-phase extraction (DS-µ-SPE). The MOF was separated from liquid phase with filter membrane (0.2 µm), eluted with 0.5 mL of nitric acid as back-extraction solution and finally, the nickel concentration in elution was determined by atom trap-flame atomic absorption spectrometry (AT-FAAS) after dilution with DW up to 1 mL. The LOD, the linear range and preconcentration factor were achieved 1.5 µg L^{-1}, 5-160 µg L^{-1} and 49.7, respectively. The absorption capacity of MOF for nickel was obtained 136.8 mg g^{-1}. The results of procedure were validated by spiking of samples and ET-AAS analyzer.

1. Introduction

Nickel is the 28th element of Periodic table that found in abundance the earth's crust [1-4]. Pure nickel is a hard, silvery white, lustrous, malleable, ductile, shining metal with high electrical and thermal conductivity [2,5]. The soluble nickel salts and metallic nickel, nickel sulphides and nickel oxides are poorly water soluble [2]. Nickel as a heavy metal, nonessential great environmental concern because widely occurring in the environment from various natural sources including emissions from fossil fuel consumption and anthropogenic processes including modern technologies and production of products such as coins, jewelry, stainless steel, batteries, medical devices, plating and welding [6-9]. In 2008, nickel received the shameful name of the "Allergen of the Year" [8]. Humans are exposed to nickel in both occupational and Non-occupational forms. Occupational exposure to Nickel is primarily associated with workers in the producing and using of Nickel in industry sectors. Non-occupational sources of nickel exposure include is food, air and water. Human exposure to nickel occurs of inhalation, dermal contact, and gastrointestinal primary routes. Some specific aspects of nickel toxicities include Genotoxicity, Developmental toxicity, Neurotoxicity, Haematotoxicity, Immunotoxicity, Neurotoxicity

* Corresponding Author: Saeed Fakhraie
Email: saeedfakhraie@yahoo.com
https://doi.org/10.24200/amecj.v3.i02.103

and Carcinogenicity is [2, 4, 5, 8-11]. The adverse health effects of nickel for humans depend on the route of exposure, water solubility of nickel compounds, dose, bodyweight, sensitivity and exposure periods [10]. Exposure to nickel causes irritation of the nose, vertigo, insomnia, sinuses and loss of sense of smell, headache, nausea, vomiting, chest pain, nonproductive cough, dyspnoea, cyanosis, abdominal pain, diarrhea, tachycardia, palpitations, sweating, visual disturbances, weakness, lassitude and shortness of breath, giddiness and it could also lead to asthma, bronchitis and other respiratory diseases, eventually causing lung cancer [4,8,12]. According to the Research on Cancer (IARC) and the U.S. Department of Health nickel sulfate, sulfides and oxides combinations of nickel are be classified in Group 1, (i.e. cancerogenic to humans) and metallic nickel in Group 2B, (i.e. Possibly carcinogenic to humans [2,5,8,13]. The Permissible Exposure Limit (PEL) by Occupational Safety and Health Administration (OSHA) for dust, fume and metal of nickel and Recommended Exposure Limit (REL) by National Institute of Occupational Safety and Health (NIOSH) for metal and soluble of nickel are 1and 0.015 mg m^3 respectively. In addition, World Health Organization (WHO) has proposed a guideline value of 20 µg L^{-1} for the maximum permissible concentration of nickel in drinking water [14, 15]. A variety of methods such as cloud point extraction (CPE) [16-20], ionic liquid dispersive liquid-liquid micro extraction (IL-DLLME) [18,21], liquid–liquid extraction, cold induced aggregation microextraction (CIAME) [15], Solid phase extraction (SPE) [22-26], ligandless-ultrasound-assisted emulsification microextraction (USAEME) [27], coupled to various instrumental techniques like flame atomic absorption spectrometry (FAAS) [16,23,28,29,30-32] graphite furnace atomic absorption spectrometry (GFAAS) [33-34], ultrasonic nebulizer and inductively coupled plasma optic emission spectrometry (USN-ICP-OES) [17], inductively coupled plasma atomic emission (ICP AES) [35], UV spectrometry [36], X-ray fluorescence spectrometry [37], inductively coupled plasma optic emission spectrometry (ICP-OES) [21], high performance liquid chromatography (HPLC) [38], inductively coupled plasma optic emission spectrometry (ICP-OES), have been developed for the for preconcentration and determination of nickel at low concentrations [39]. During the last decade, metal-organic frameworks (MOFs) have widely attracted international attention due to their high thermal stability, large surface area, and pore volume. Although a variety of MOFs has been developed, having their own particular properties, MIL (standing for materials of institute Lavoisier) structures have been more intriguing than other constituents owing to their extra-large cavities, high moisture stability, and lower production cost. For the first time, Ferey and his colleagues succeeded to synthesize nanoporous chromium terephthalate MIL-101(Cr) with a 3D structure by incorporating ter- ephthalic acid (benzene-1,4-dicarboxylic acid), chromium salt ($Cr(NO_3)_3 \cdot 9H_2O$) and hydrofluoric acid (HF), as a modulator, in an aqueous medium [40]. In addition to the substantially large surface area and pore volume, they displayed that MIL-101(Cr) has an exclusive pore size distribution with two types of inner cages (29 Å and 34 Å) and windows (12*12 Å and 14.7*16 Å). These promising features have unprecedentedly boosted the role of MIL-101(Cr) and its derivatives in the gas storage (CO_2 [43–44], CH_4 [45–49] and H_2 [50–53]), gas separation (CO_2/CH_4 [54–56] and CO_2/N_2 [57–59]) and catalytic applications [60–63].

2. Material and Methods

2.1. Instrumental

The nickel concentration was determination by spectra GBC 906 double beam atom trap flame atomic absorption spectrophotometer with deuterium lamp as a background correction (AT-F AAS, GBC, Aus). The atom trap was installed on an air-acetylene burner. The operating software of

AVANTA was utilized for collecting and storing data. A HCL of nickel adjusted at a current of 4.0 mA and a wavelength of 232.0 nm with a spectral bandwidth of 0.2 nm. The working range for nickel was obtained 0.5 -8 mg L^{-1}. The pH-meter (Metrohm 744 Switzerland), centrifuge (EBA, Germany) and ultrasonic bath (Kunshan) were used.

2.2. Reagents and Materials

In the synthesis procedure, chemicals including Chromium nitrate nonahydrate ($Cr(NO_3)3.9H_2O$, 97%), 1, 4-benzene dicarboxylic acid (H_2BDC), Methanol (MeOH, Merck, 99.9%), ethanol (EtOH, Merck, 99.9%), N, N-dimethylformamide (DMF, Merck, 99.8%) and Acetone were purchased from commercial vendors and utilized as received. (DI) water was employed as solvents. All reagents with analytical grade purchased from Merck (Darmstadt, Germany). Stock solutions of Ni(II) were prepared by dissolving powder amounts of $Ni(NO_3)_2$ in deionized water (DW). The standard solutions were prepared daily by diluting with deionized water. Deionized water prepared from Milli-Q plus water from Millipore, USA. The pH of solutions was adjusted by ammonium chloride (NH_3/NH_4Cl) for pH 8–10. All the laboratory glasses were cleaned by 10% (v/v) nitric acid for 24 h and washed with DW 10 times.

2.3. Preparation of MIL-101(Cr) nanoparticles

In a typical procedure, 16 g of $Cr(NO_3)_3.9H_2O$ and 6.56 g of terephthalic acid were separately added to deionized water (200 mL) and mixture was intensively stirred for 30 min with a magnetic stirrer. The resulting mixture was transferred to a stainless steel autoclave and heated at 220 °C for 18 h. Upon heating, the mixture became as a soft green powder which was washed five times with boiling deionized water, three times with MeOH and three times with acetone in order to remove impurities and unreacted materials. In addition, to separate the remained terephthalic acid, the resulting solid was suspended in 50 mL of dimethylformamide and kept at 70°C overnight. After cooling, the sample was washed by pure ethanol for three times and the resulting powder was dried at 100 °C for 24 h to obtain the final product.

2.4. Characterization

To investigate the crystallinity and phase structure of the samples, powder X-ray diraction (PXRD) method was considered by using Philips PW-1730 instrument with Cu-Kα radiation (λ = 1.5406 Å). The scanning rate was 1 deg/min and operating power was 40 kV and 40 mA. To determine the functional groups, Fourier transform infrared spectroscopy (FT-IR) was performed using Bruker (VERTEX 70) spectrum from 400 to 4000 cm^{-1}. Field Emission Scanning Electron Microscopy (FE-SEM) studies were carried out with a JEOL JEM 3010 instrument under 15 kV voltage and 50 kx and 100 kx magnifications. The specific surface area, total pore volume, average pore width and pore size distribution measurements was performed with a Micrometrics ASAP-2010 instrument by adsorption of nitrogen at 77 K. Before analysis, the sample was degassed at 175°C and vacuum pressure for 2 h to remove moisture, solvents and other unwelcome molecules from pores.

2.5. Analytical Procedure

By DS-μ-SPE procedure, the nickel ions were separated/preconcentrated from 50 mL of wastewater based on MIL-101(Cr) as MOF nanoadsorbent. First, the pH of wastewater samples and standard nickel solution containing 1-400 μg L^{-1} was adjusted up to 8.5 with phosphate or ammonium chloride buffer before adding 30 mg of MIL-101(Cr). After shaking in ultrasonic bath for 5 min at room temperature (50 kHz, 100 W), the nickel ions was extracted by carboxyl groups of MIL-101(Cr). Then the MIL-101 sorbent was separated from liquid phase with filter membrane (0.2 μm) based on vacuum accessory and eluted with 0.5 mL of nitric acid as back-extraction solution. Finally, the nickel concentration in eluent was determined by atom trap-flame atomic absorption spectrometry (AT-FAAS) after dilution with DW up to 1 mL(Fig. 1).

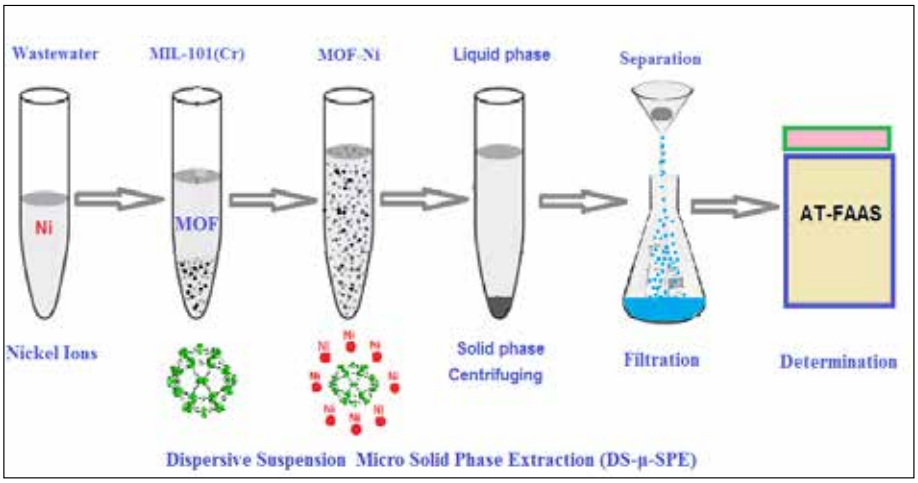

Fig.1. Nickel extraction based on MIL-101(Cr) from wastewater samples by DS-μ-SPE procedure

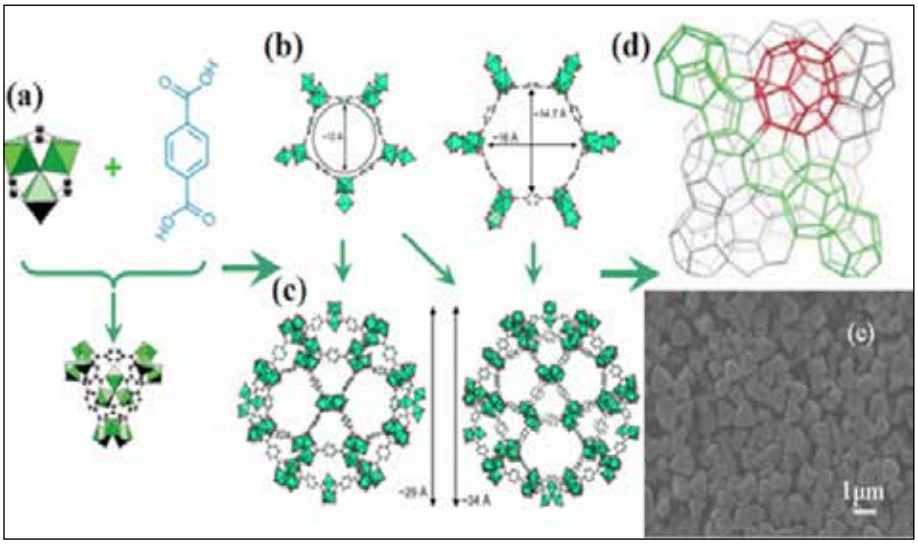

Fig.2. The robust framework of MIL-101 based on chromium (III) octahedral clusters

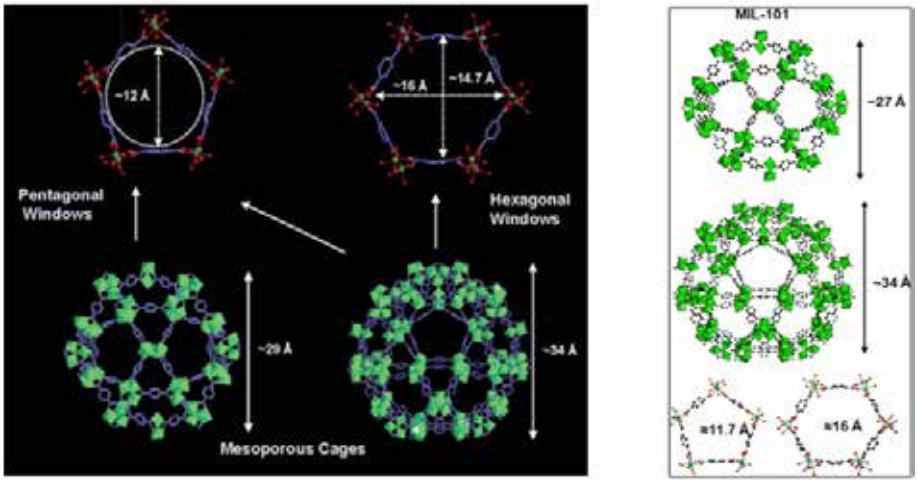

Fig.3. The structure of two types of mesoporous cages in MIL-101 with pentagonal forms

3. Results and discussion

F´erey et al. prepared MIL-101 (MIL, Mat´erial Institut Lavoisier) with a chemical composition of {Cr_3F (H_2O) 2O (BDC) 3. nH_2O} (n 25; 1, 4-benzenedicarboxylate (BDC) and superior physicochemical properties. The robust framework of MIL-101 was comprised of trimeric chromium (III) octahedral clusters interconnected by BDC molecules resulting in an augmented MTN zeotype structure (Fig. 2).

This structure was comprised of two types of mesoporous cages with diameters of ~29 and 34 Å accessible through two types of microporous windows (the smaller cages have pentagonal windows with a free opening of ~12 Å, while the larger cages possess both pentagonal and hexagonal windows with a ~14.7 Å by 16 Å free aperture) (Fig. 3).

3.1. Extraction Mechanism

The material exhibits excellent stability against moisture and other chemicals, and the terminal water molecules in MIL-101 can be removed by heating in air or under vacuum at 423 K, which generates two coordinatively unsaturated open metal sites (CUS) per trimeric Cr(III) octahedral cluster. In addition to its highly porous nature, MIL-101 has attracted considerable attention because functional modifications on MIL-101 can be achieved easily either directly using a functionalized ligand during the synthesis or indirectly via the diverse post-synthesis chemical treatment on the CUS or on the organic linkers. Among the MOFs known, MIL-101 is one of the most promising porous materials for future energy and environmental applications, surpassing MOF-5 or HKUST-1, owing to its superior physicochemical properties including high hydrothermal/chemical stability and desirable textural properties. Due to MIL-101 Structure nickel was physically and chemically extracted based on porous materials in MIL-101 nanostructure and covalence bonding by carboxyl groups of terephthalic acid (MOF-(C_6H_4 $(COO)^{2-}$ ….Ni^{2+}) , respectively (Fig. 4).

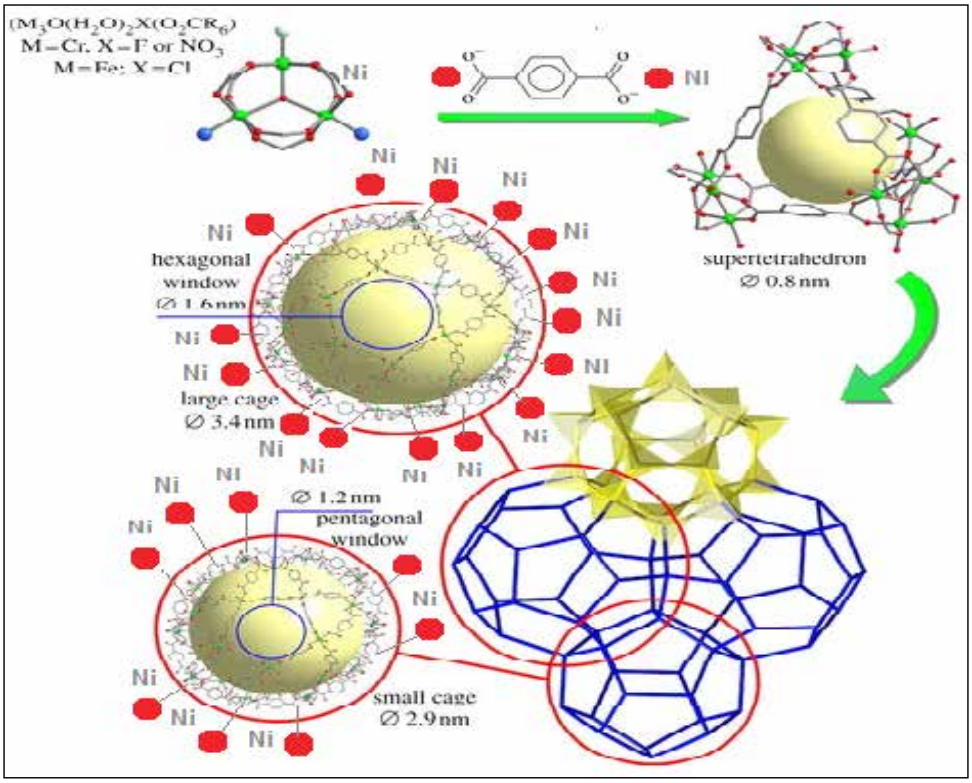

Fig. 4. The extraction mechanism of nickel by MIL-101 nanostructure

3.2. PXRD patterns

PXRD pattern of the MIL-101(Cr) sample, prepared without modulators, is depicted in Figure 5. As it stated, MIL-101(Cr) possessed the most intensive peaks, as an indicator of the most crystallinity. The negligible peaks at around 2θ = 17.4°, 25.2° or 27.9° affirmed successful removal of unreacted H_2BDC crystals from the sample framework [36]. Moreover, the main diraction peaks of MIL-101(Cr) (2θ ≈ 5.25°, 8.55°, 9.15°, and 16.58°) was thoroughly compatible with the MIL-101-HF-1, as a general reference for MIL-101(Cr).

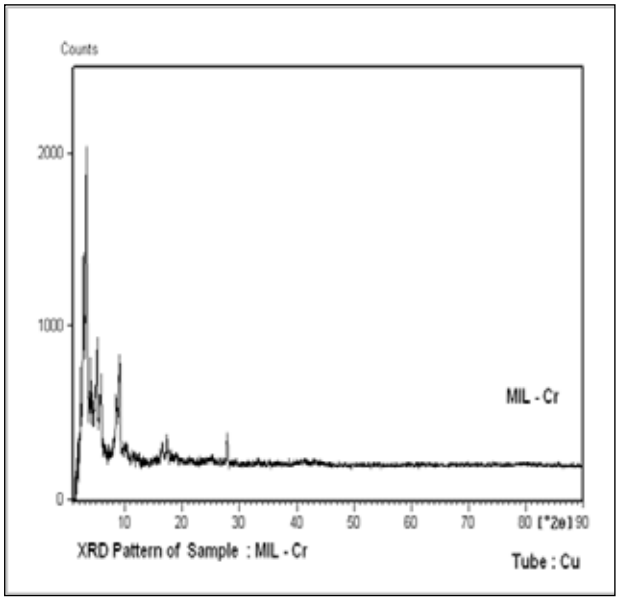

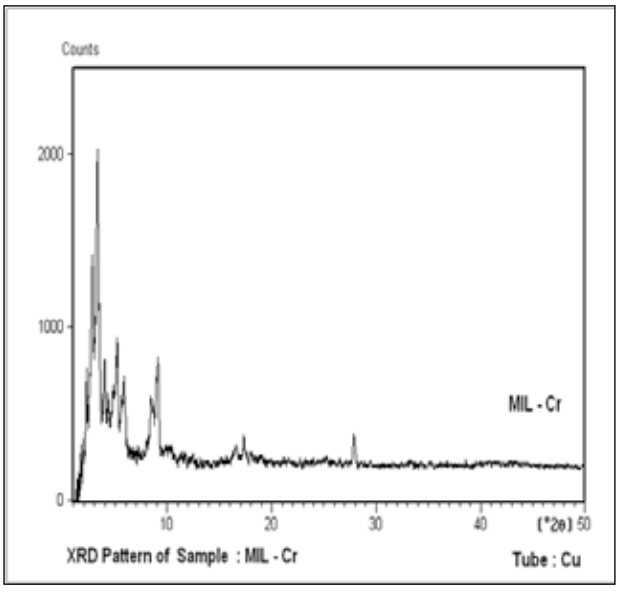

Fig. 5. The PXRD pattern of the MIL-101(Cr) sample

3.3. FE-SEM

The morphology of the prepared MIL-101(Cr) sample was characterized by field emission scanning electron microscope (FE-SEM) analysis. As it is seen in Figure 6, the image of MIL-101(Cr) shows highly crystalline octahedral morphology for this material which was compatible with the reported MIL-101(Cr) structures. In addition, there were no needle-shaped crystals in the images representing the complete removal of H_2BDC crystals by the post-purification process.

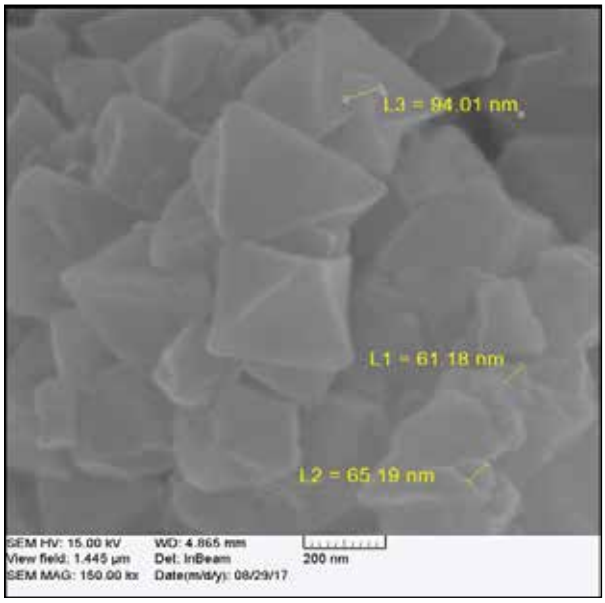

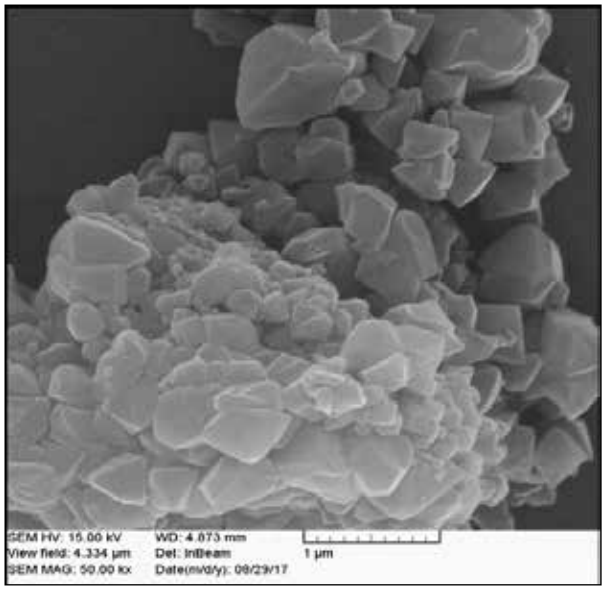

Fig. 6. The morphology of MIL-101(Cr) by field emission scanning electron microscope (FE-SEM)

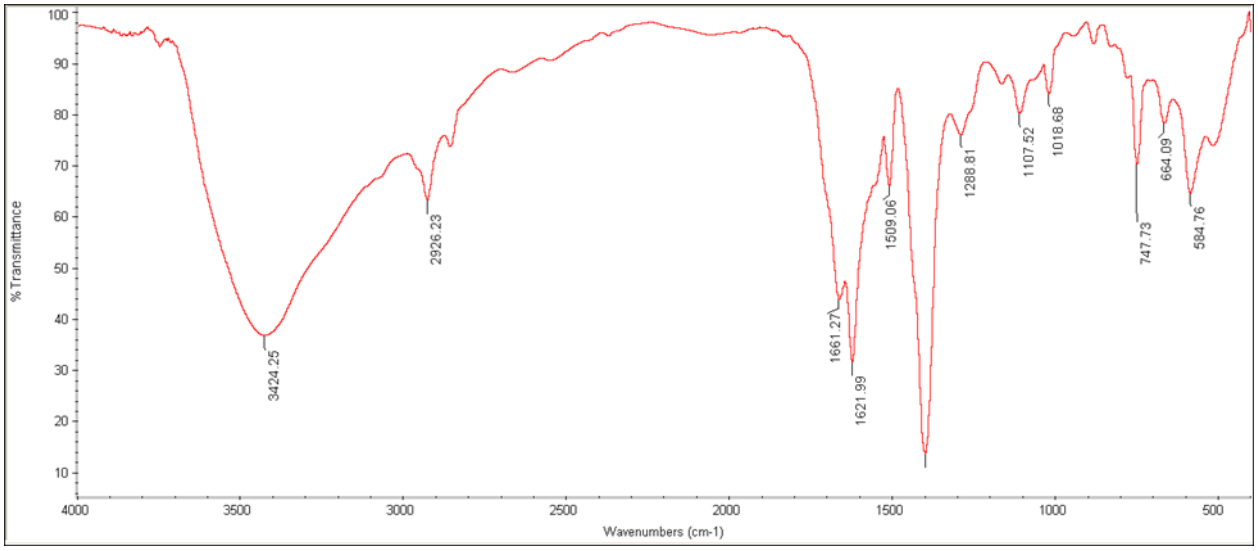

Fig. 7. FT-IR spectra of the synthesized MIL-101(Cr)

3.4. FT-IR

FT-IR spectra of the synthesized MIL-101(Cr) illustrated in Figure 7. In this spectrum the peak around of 570 cm^{-1} was assigned to the Cr–O stretching vibration, reflecting the formation of MIL-101(Cr) structure. The peaks of between 600 and 1600 cm^{-1} were indicated to H_2BDC and its aromatic rings. The bands at 750, 884, 1160 cm^{-1} were attributed to the C–H bond in CH_3 group and the peak observed at 1508 cm^{-1} indicates the C=C stretching. A strong band at 1404 cm^{-1} is related to O–C–O symmetric vibrations and showing the dicarboxylate moiety in the sample. The typical bands located at 1625 and 3400 cm^{-1} confirmed the presence of hydroxyl groups or moisture in the sample. The FT-IR results were in accordance to the previous reports FT-IR patterns which could be an evidence for the formation of MIL-101(Cr) structures (Fig. 7).

3.5. Physical properties

To determine physical properties of synthesized MIL-101(Cr) sample, the N_2 sorption test at 77 K was carried out. The related N_2 sorption isotherms along with the pore size distribution graphs are depicted in Figure 8. According to Figure 9-11, the N_2 sorption isotherms exhibit the typical type I curve with sharp N_2 adsorption at low partial pressures (P/P0 < 0.01) and a H_2 hysteresis loop. In addition, the adsorbents have conical pores and crystals were composed of the microporous structure. The specific surface area and pore volume of MIL-101(Cr) were calculated and summarized in Table 1. The results indicated that MIL-101(Cr) possessed the BET surface area (2155 m^2g^{-1}) and the Barrett–Joyner–Halenda (BJH) pore size distribution curve (b) derived from adsorption data of the isotherms indicates a main peak with average pore width of 2.1 for MIL-101(Cr). The result implies the microporous nature of samples and is in agreement with the results deduced from nitrogen adsorption-desorption isotherms and pore size distribution.

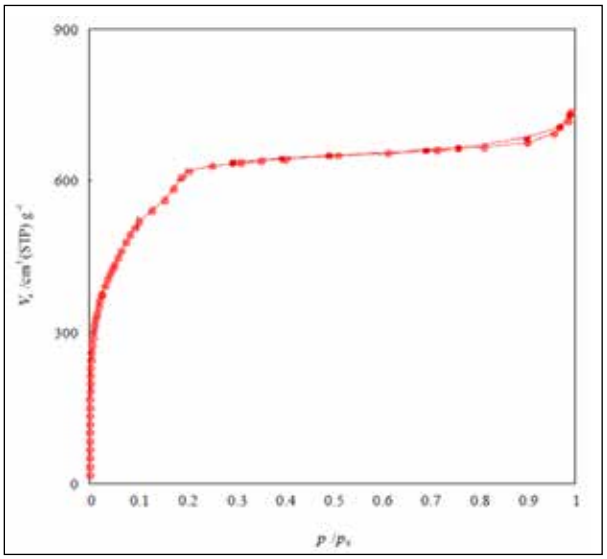

Fig. 8. Adsorption/desorption isotherm of Cr-MOF adsorbent with adsorptive of N_2 at 77oK

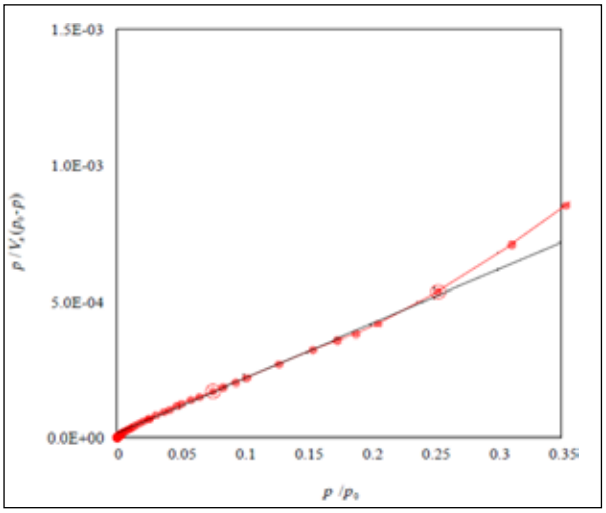

Fig. 9. BET plot of Cr-MOF adsorbent with adsorptive of N_2 at 77°K

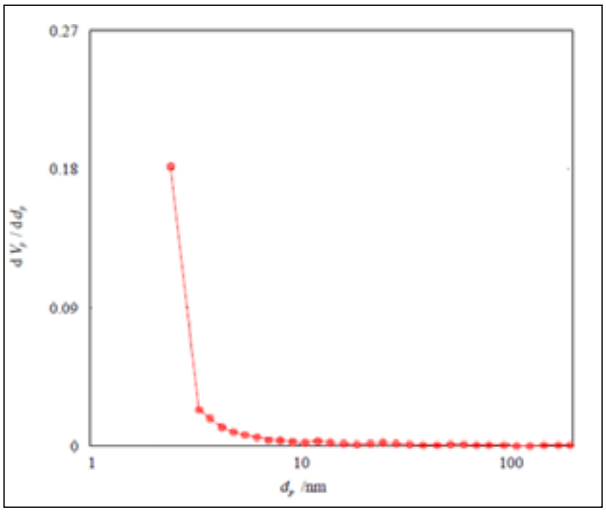

Fig. 10. BJH plot of Cr-MOF adsorbent for absorption branch at 77°K

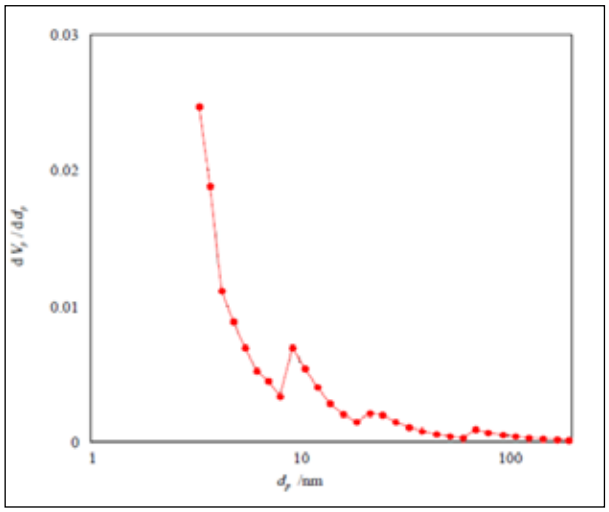

Fig. 11. BJH-plot of Cr-MOF adsorbent for desorption branch at 77°k

Table 1. Physical properties of Cr-MOF (MIL-101(Cr)) adsorbent

Product	BET Surface area (m^2 g^{-1})	Average pore width (nm)	Vm (cm^3 g^{-1})	Total pore volume (cm^3 g^{-1})
MOF	2155	2.1	495	1.13

3.6. Optimization

The DS-µ-SPE procedure based on Cr-MOF adsorbent was applied for speciation and preconcentration of nickel in water samples. For optimization many parameters such as amount of sorbent, volume of samples, shaking time, interference Ions and pH were optimized.

3.6.1. Amount of sorbent

For efficient extraction of nickel, the amount of MIL-101(Cr) nanoadsorbent was studied. For this purpose, the amounts of 5 - 50 mg of MIL-101(Cr) were used for nickel extraction by the DS-µ-SPE method. The results showed, the high recoveries between 95-105% were obtained in wastewater samples with 28 mg of MIL-101(Cr) for Ni extraction. Therefore, 30 mg of MOF was used as optimum mass for Ni extraction at pH=8.5 (Fig. 12).

3.6.2. Volume of samples

The sample volume for nickel extraction based on MOF was evaluated by DS-µ-SPE method. In this study the vary volume of wastewater samples between 5-100 mL was studied and optimized for 5-160 µg L^{-1} of nickel concentration. Based on results, the efficient extractions were achieved for 55 mL of wastewater samples. Therefore, 50 mL blood sample was selected as the optimal sample volume for further study (Fig. 13).

3.6.3. The Shaking time

The time of extraction depended on the sonication of MIL-101(Cr) nanoadsorbent in the wastewater samples, which was increased interaction between carboxyl group of MIL-101(Cr) with Ni(II) at

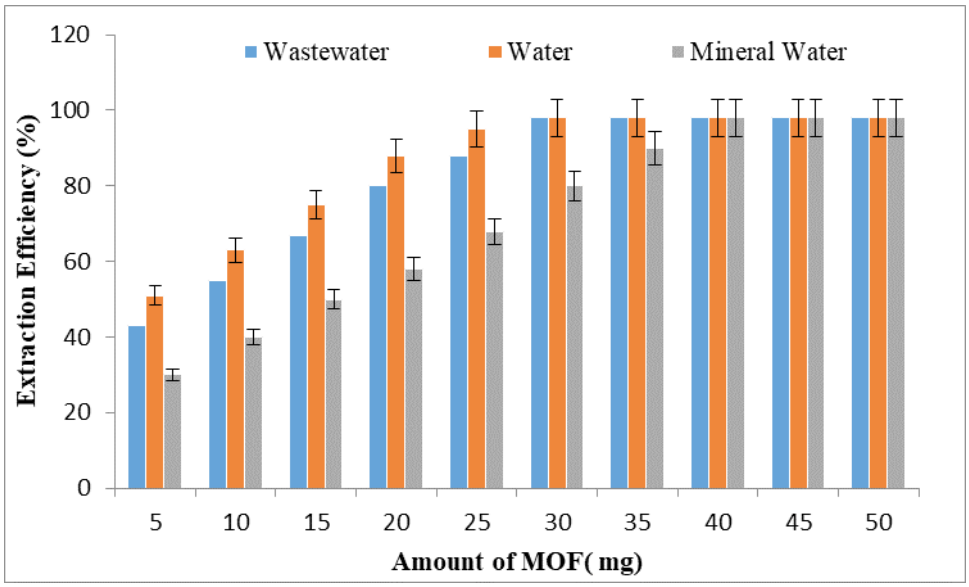

Fig. 12. The effect of MOF amount for Ni(II) extraction from water samples

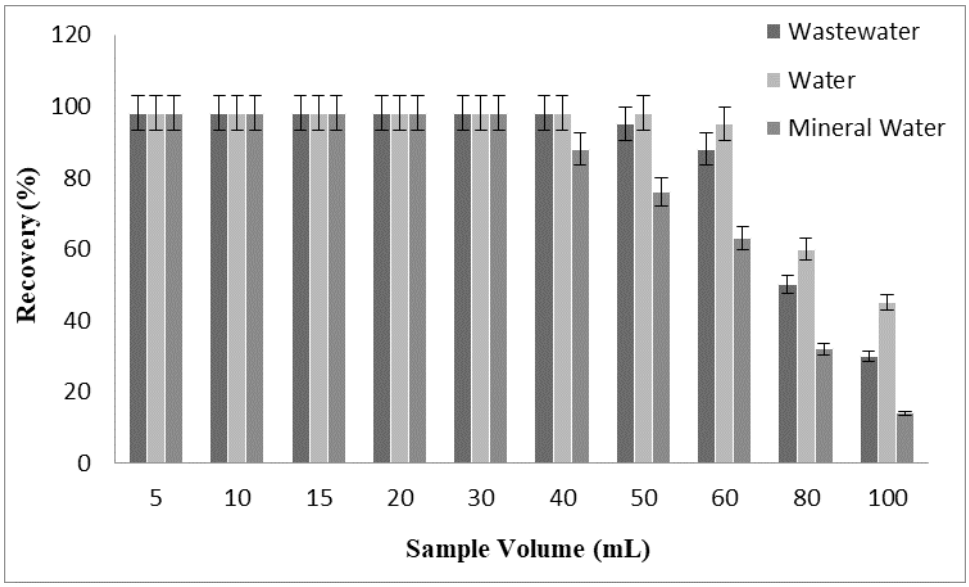

Fig.13. The effect of sample volume for Ni(II) extraction from water samples

pH=8.5. By dispersion of the MIL-101(Cr), the mass-transference and extraction was performed. So, the effect of shaking time was studied for 1-20 min. By results, the sonication of 5.0 min had efficient extraction for Ni ions in wastewater samples for 30 mg of sorbent. Therefore, 5.0 minute was used as the optimum shaking time by DS-µ-SPE procedure.

3.6.4. The pH effect

The pH has main role for nickel extraction by MIL-101(Cr) nanoadsorbent. So, the effect of different pH (2-11) for extraction of Ni (II) in wastewater samples were investigated by DS-µ-SPE procedure. The results demonstrated that the MIL-101(Cr) as MOF sorbent could be efficiently captured Ni (II) in pH of 8-8.5. Also, the recoveries

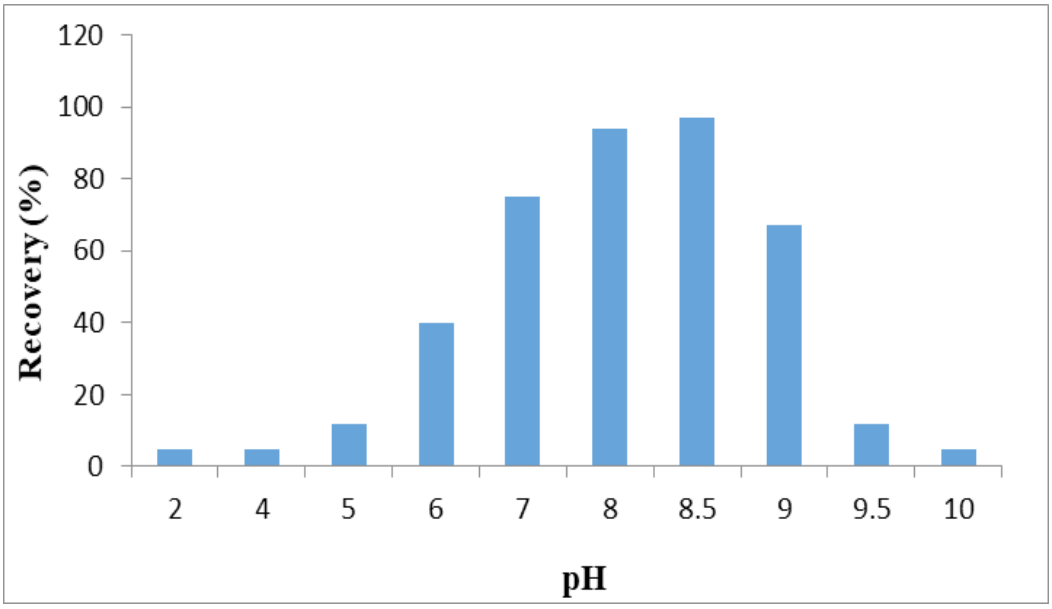

Fig. 14. The effect of pH for Ni(II) extraction based on MOF from water samples

for Ni (II) based on Cr-MOF were obtained more than 95% in pH 8.5 and the decreased at lower and higher pH (7.5>pH>9). So, pH=8.5 was selected for further experiments (Fig. 14). The mechanism of nickel extraction depend on the coordination of covalent bond of sorbent [Ni^{2+}→ $(COO)^{2-}$] with the positively charged of nickel.

3.6.5. Validation

The validation of DS-µ-SPE procedure based on MOF was obtained by spiking samples. The different concentration of nickel added to real samples as lower and upper ranges in wastewater and water samples. The results showed a good recovery between 95%-106% which was shown in Table 2. Also, the validation was confirmed with electrothermal atomic absorption spectrometry (ET-AAS) coupled with microwave digestion process (Table 3). Based on results in Tables 2 and 3, the nickel ions were efficiently extracted by Cr-MOF adsorbent in optimized conditions.

Table 2. The validation of DS-µ-SPE procedure based on MOF for nickel(II) extraction from water samples

Samples	Added (µg L^{-1})	*Found (µg L^{-1})	Recovery (%)
Water	------	86.75 ± 3.55	------
	100	185.63 ± 8.73	98.8
Tab water	------	6.22 ± 0.34	------
	5	11.53 ± 0.48	106.2
[a]Wastewater	------	144.62 ± 6.13	------
	150	288.49 ± 13.26	95.9
Well water	------	38.54 ± 2.05	------
	40	77.68 ± 3.06	97.8

* Mean of three determinations ± cconfidence interval (P= 0.95, n=8)

[a] Wastewater samples diluted with DW (1:1)

Table 3. Validation of methodology for nickel extraction from water samples by comparing to ET-AAS coupled with microwave digestion process

Samples	Added (µg L^{-1})	*Found ETAAS (µg L^{-1})	*Found AT-FAAS (µg L^{-1})	Recovery ETAAS (%)	Recovery AT-FAAS (%)
Water 1	------	10.56± 0.43	10.18± 0.52	------	------
	10	20.31 ± 0.86	19.87 ± 0.93	97.5	96.9
Water 2	------	33.82 ± 1.57	31.95 ± 1.63	------	------
	30	62.98 ± 2.78	60.88 ± 3.02	97.2	96.4
Water 3	------	75.21 ± 3.26	73.93 ± 3.39	------	------
	50	125.73 ± 6.03	122.86 ± 6.24	101.1	97.8
Water 4	------	93.12 ± 4.16	94.27 ± 4.43	------	------
	100	191.62 ± 8.94	194.77 ± 9.24	98.5	100.5

*Mean of three determinations ± cconfidence interval (P= 0.95, n=8)

Water1: Darband River,

Water 2: Hesarak River

Water 3: DarAbad River

Water 4: Zaferaniyeh and Velenjak River

3.6.6. Discussions

For metal determination with the DS-µ-SPE procedure based on Cr-MOF adsorbent, the effect of the main parameters, such as amount of sorbent, volume of samples, shaking time, interference Ions and pH were optimized thoroughly. Results this study revealed that MIL-101(Cr) nanoadsorbent was used as a novel sorbent for dispersive suspension micro solid phase extraction (DS-µ-SPE) nickel from environmental waters. In in study highly crystalline octahedral morphology of MIL-101(Cr) sample as reported MIL-101(Cr) structures in other studies was characterized by field emission scanning electron microscope (FE-SEM) analysis [64,65]. FT-IR characterization was conducted to detect the identity of the MIL-101(Cr) functional groups that the FT-IR results were in accordance to the previous reports [59, 64-66]. In this study, optimum mass of MOF, pH and time for Ni extraction 30 mg, 7.5 and 5 minute at pH: 7.5, 30 respectively were obtained in wastewater samples so that Behbahani, M., et al. this parameters for Modification of magnetized MCM-41 by pyridine groups for ultrasonic-assisted dispersive micro-solid-phase extraction of nickel ions 24 mg, 7.5 and 8 minute has been reported [67]. Based on results, under optimized conditions detection limit, the linear range were achieved of 1.5 µg L^{-1}, 5-160 µg L^{-1}. In study safavi et al. linear range for 2-amino-cyclopentene-1-dithiocarboxylicacid absorbent and Cloud point extraction method linear in the range of 20–500 µg L^{-1} Obtained [22]. The findings of this study showed that MIL-101(Cr) as a valid procedure for extraction nickel in water samples can be used.

4. Conclusions

The MIL-101(Cr) as a MOF nanoadsorbent was synthesized and used for nickel extraction from water samples by DS-µ-SPE procedure. After extraction nickel ions with MOF adsorbent at pH=8.5, it was back-extracted from adsorbent and finally, the concentration was determined by AT-FAAS. The low LOD of 1.5 µg L^{-1} and the favorite linear range 5-160 µg L^{-1} was achieved. The high absorption capacity of 136.8 mg g^{-1} was obtained by MIL-101(Cr). The efficient, simple and fast extraction was achieved in low time by DS-µ-SPE procedure. The MIL-101(Cr) as solid-phase had high recovery more than 97% for Ni(II) extraction from waters without any chelating agents. Therefore, extraction of nickel based on

MIL-101(Cr) can be used as efficient procedure for determination and separation of Ni(II) in water samples by AT-FAAS

5. Acknowledgements

The authors wish to thank Qom University of Medical Sciences, Qom, Iran, Iranian Petroleum Industry Health Research Institute (IPIHRI), and the Iranian Research Institute of Petroleum Industry (RIPI) for supporting of this work.

6. References

[1] E. Nieboer, J.O. Nriagu, Nickel and human health, International Conference on nickel metabolism and toxicology, Espoo, Finland. Wiley, 1992.

[2] K.K. Das, S.N. Das, S. A. Dhundasi, Nickel: molecular diversity, application, essentiality and toxicity in human health, Biometals: molecular structures, binding properties and applications, Nova Sci. Publishers, (2010) 33-58.

[3] A. Arita, M. Costa, Epigenetics in metal carcinogenesis: nickel, arsenic, chromium and cadmium, Metallomics, 3 (2009) 222-228.

[4] K.S. Cameron, B. Virginia, B.T. Paul, Exploring the molecular mechanisms of nickel-induced genotoxicity and carcinogenicity: a literature review, Rev. Environ. Health, 2 (2011) 81-92.

[5] K.K. Das, S.N. Das, S. A. Dhundasi, Nickel, its adverse health effects & oxidative stress, Indian J. Med. Res., 4 (2008) 412.

[6] A. Arita, M. Costa, Epigenetics in metal carcinogenesis: nickel, arsenic, chromium and cadmium, Metallomics, 3 (2009) 222-228.

[7] P.C. Nagajyoti, K.D. Lee, T.V.M. Sreekanth. Heavy metals, occurrence and toxicity for plants: a review, Environ. Chem. lett., 3 (2010) 199-216.

[8] A. Duda-Chodak, U. Blaszczyk, The impact of nickel on human health, J. Elem., 4 (2008) 685-693.

[9] S. Buxton, E. Garman, K.E. Heim, T. Lyons-Darden, C. E. Schlekat, M. D. Taylor, A.R. Oller, Concise review of nickel human health toxicology and ecotoxicology, Inorganics, 7 (2019) 89.

[10] N. Alam, S.J. Corbett, H.C. Ptolemy, Environmental health risk assessment of nickel contamination of drinking water in a country town in NSW, New South Wales Public Health bull., 10 (2008) 170-173.

[11] M.G. Permenter, J.A. Lewis, D.A. Jackson, Exposure to nickel, chromium, or cadmium causes distinct changes in the gene expression patterns of a rat liver derived cell line, PLOS one, 11 (2011) e27730.

[12] F. Akbal, S. Camcı, Copper, chromium and nickel removal from metal plating wastewater by electrocoagulation, Desalination, 3 (2011) 214-222.

[13] K. Bhupander, D.P. Mukherjee, Assessment of human health risk for arsenic, copper, nickel, mercury and zinc in fish collected from tropical wetlands in India, Adv. Life Sci. Technol., 2 (2011) 13-24.

[14] NIOSH Manual of analytical methods (NMAM, 5 Edition), U.S. department of health and human services, 2015.

[15] H. Abdolmohammad-Zadeh, E. Ebrahimzadeh. Ligandless cloud point extraction for trace nickel determination in water samples by flame atomic absorption spectrometry, J. Brazilian Chem. Soc., 3 (2011) 517-524.

[16] C.A. Şahin, M. Efeçınar, N. Şatıroğlu. Combination of cloud point extraction and flame atomic absorption spectrometry for preconcentration and determination of nickel and manganese ions in water and food samples, J. Hazard. Mater., 3 (2010) 672-677.

[17] A. Safavi, H. Abdollahi, M.R. Hormozi Nezhad, R. Kamali, Cloud point extraction, preconcentration and simultaneous spectrophotometric determination of nickel and cobalt in water samples, Spectrochim. Acta Part A: Mol. Biomol. Spec., 12 (2004) 2897-2901.

[18] J. Chen, K.C. Teo, Determination of cobalt and nickel in water samples by flame atomic absorption spectrometry after cloud point

extraction, Anal. Chim. Acta, 2 (2001) 325-330.
[19] J.L. Manzoori, G. Karim-Nezhad, Development of a cloud point extraction and preconcentration method for Cd and Ni prior to flame atomic absorption spectrometric determination, Anal. Chim. Acta, 2 (2004) 173-177.
[20] C. Fan, Q. Pan, Q. Li, L. Wang, Cloud point-TiO 2/sepiolite composites extraction for simultaneous preconcentration and determination of nickel in green tea and coconut water, J. Iran. Chem. Soc., 2 (2016) 331-337.
[21] S.M.N. Moalla, A.S. Amin. An ionic liquid-based microextraction method for highly selective and sensitive trace determination of nickel in environmental and biological samples, Anal. Method., 24 (2015) 10229-10237.
[22] A. Moghimi, M.J. Poursharifi, Perconcentration of Ni (II) from sample water by modified nano fiber, Oriental J. Chem., 1 (2012) 353.
[23] S.Z. Mohammadi, D. Afzali, Y.M. Baghelani. Flame atomic absorption spectrometry determination of trace amounts of nickel ions in water samples after ligandless ultrasound-assisted emulsification microextraction, Anal. Sci., 9 (2010) 973-977.
[24] V.A. Lemos, G.S. Do Nascimento, L.S. Nunes, A new functionalized resin for preconcentration and determination of cadmium, cobalt, and nickel in sediment samples, Water, Air, Soil Pollut., 2 (2015) 2.
[25] H. Shirkhanloo, M. Falahnejad, H. Zavvar Mousavi, Mesoporous silica nanoparticles as an adsorbent for preconcentration and determination of trace amount of nickel in environmental samples by atom trap flame atomic absorption spectrometry, J. Appl. Spec., 6 (2016) 1072-1077.
[26] H. Sereshti, V. Khojeh, M. Karimi, S. Samadi, Ligandless-ultrasound-assisted emulsification-microextraction combined with inductively coupled plasma-optical emission spectrometry for simultaneous determination of heavy metals in water samples, Anal. Method., 1 (2012) 236-241.
[27] V.A. Lemos, V.J. Ferreira, J.A. Barreto, L.A. Meira, Development of a method using ultrasound-assisted emulsification microextraction for the determination of nickel in water samples, Water, Air, Soil Pollut., 5 (2015) 141.
[28] M. Karimi, S. Dadfarnia, A.M.H. Shabani, Application of deep eutectic solvent modified cotton as a sorbent for online solid-phase extraction and determination of trace amounts of copper and nickel in water and biological samples, Biol. Trace Elem. Res., 1 (2017) 207-215.
[29] M.R. Jamali, A. Madadjo, R. Rahnama. Determination of nickel using cold-induced aggregation microextraction based on ionic liquid followed by flame atomic absorption spectrometry, J. Anal. Chem., 5 (2014) 426-431.
[30] J.L. Manzoori, G. Karim-Nezhad, Development of a cloud point extraction and preconcentration method for Cd and Ni prior to flame atomic absorption spectrometric determination, Anal. Chim. Acta, 2 (2004) 173-177.
[31] A.A. Gouda, A.M. Summan, A.H. Amin, Development of cloud-point extraction method for preconcentration of trace quantities of cobalt and nickel in water and food samples, RSC Adv., 96 (2016) 94048-94057.
[32] T.G. Kazi, H.I. Afridi, N. Kazi, M.K. Jamali, M.B. Arain. Copper, chromium, manganese, iron, nickel, and zinc levels in biological samples of diabetes mellitus patients, Biol. Trace Elem. Res., 1 (2008) 1-18.
[33] F.A. Lobo, D. Goveia, A.P. Oliveira, L.P.C. Romão, Development of a method to determine Ni and Cd in biodiesel by graphite furnace atomic absorption spectrometry, Fuels, 1 (2011) 142-146.
[34] P. Liang, L. Peng, "Determination of nickel in water samples by graphite furnace atomic absorption spectrometry after ionic liquid-based dispersive liquid-liquid microextraction preconcentration, Atom. Spec., 2 (2012) 53-58.
[35] Y Xu, J Zhou, G Wang, J Zhou, G Tao, Determination of trace amounts of lead,

arsenic, nickel and cobalt in high-purity iron oxide pigment by inductively coupled plasma atomic emission spectrometry after iron matrix removal with extractant-contained resin, Anal. Chim. Acta, 1 (2007) 204-209.

[36] F. Zhou, C. Li, H. Zhu, Y. Li, A novel method for simultaneous determination of zinc, nickel, cobalt and copper based on UV–VIS spectrometry, Optik, 182 (2019) 58-64.

[37] X. Lu, L. Wang, K. Lei, J. Huang, Y. Zhai, Contamination assessment of copper, lead, inc, manganese and nickel in street dust of Baoji, NW China, J. Hazard. Mater., 3 (2009) 1058-1062.

[38] Q. Zhou, A. Xing, K. Zhao, Simultaneous determination of nickel, cobalt and mercury ions in water samples by solid phase extraction using multiwalled carbon nanotubes as adsorbent after chelating with sodium diethyldithiocarbamate prior to high performance liquid chromatography, J. Chromatogr. A, 1360 (2014) 76-81.

[39] Q. Han, Y. Huo, L. Yang, X. Yang, Y. He, J. Wu, Determination of trace nickel in water samples by graphite furnace atomic absorption spectrometry after mixed micelle-mediated cloud point extraction, Molecules, 10 (2018) 2597.

[40] G. Férey, C. Mellot-Draznieks, C. Serre, F. Millange, J. Dutour, S. Surble, I. Margiolaki, A chromium terephthalate-based solid with unusually large pore volumes and surface area, Sci., 309 (2005) 2040–2042.

[41] M.S. Alivand, M. Shafiei-Alavijeh, Tehrani NHMH, E. Ghasemy, A. Rashidi, S. Fakhraie, Facile and high-yield synthesis of improved MIL-101(Cr) metal-organic framework with exceptional CO2 and H_2S uptake; the impact of excess ligand- cluster, Micropor. Mesopor. Mater., 279 (2019) 153–164.

[42] M. Montazerolghaema, S.F. Aghamiri, S. Tangestaninejad, M.R. Talaie, Metal-organic framework MIL-101 doped with metal nanoparticles (Ni & Cu) and its e□ect on CO2 adsorption properties, RSC Adv., 6 (2016) 632–640.

[43] S. Pourebrahimi, M. Kazemeini, L. Vafajoo, Embedding graphene nanoplates into MIL-101(Cr) pores: synthesis, characterization, and CO2 adsorption studies, Ind. Eng. Chem. Res., 56 (2017) 3895–3904.

[44] N.A.A. Qasem, N.U. Qadir, R. Ben-Mansour, S.A.M. Said, Synthesis, characteriza- tion, and CO2 breakthrough adsorption of a novel MWCNT/MIL-101(Cr) composite, J. CO2 Util. 22 (2017) 238–249.

[45] P.L. Llewellyn, S. Bourrelly, C. Serre, A. Vimont, M. Daturi, L. Hamon, G.D. Weireld, J.S. Chang, D.Y. Hong, Y.K. Hwang, S.H. Jhung, G. Fe´rey, High uptakes of CO2 and CH4 in mesoporous metals organic frameworks MIL-100 and MIL-101, Langmuir J., 24 (2008) 7245–7250.

[46] S. Kayal, B. Sun, A. Chakraborty, Study of metal-organic framework MIL-101(Cr) for natural gas (methane) storage and compare with other MOFs (metal-organic frameworks), Energ., 91 (2015) 772–781.

[47] K. Munusamy, G. Sethia, D.V. Patil, P.B.S. Rallapalli, R.S. Somani, H.C. Bajaj, Sorption of carbon dioxide, methane, nitrogen and carbon monoxide on MIL- 101(Cr): volumetric measurements and dynamic adsorption studies, Chem. Eng. J., 195 (2012) 359-68.

[48] P. Chowdhury, S. Mekala, F. Dreisbach, S. Gumma, Adsorption of CO, CO2 and CH4 on Cu-BTC and MIL-101 metal organic frameworks: effect of open metal sites and adsorbate polarity, Mesopor. Mater., 152 (2012) 246–252.

[49] P.Á Szilágyi, P. Serra-Crespo, J. Gascon, H. Geerlings, B. Dam, The impact of post-synthetic linker functionalization of MOFs on methane storage: the role of defects, Front. Energ. Res., 4 (2016) 9.

[50] Z. Yu, J. Deschamps, L. Hamon, P.K. Prabhakaran, P. Pre, Hydrogen adsorption and kinetics in MIL-101(Cr) and hybrid activated carbon-MIL-101(Cr) materials, Int. J. Hydrogen Energ., 45 (2017) 8021–8031.

[51] A. Malouche, G. Blanita, D. Lupu, J. Bourgon, J. Nelayah, C. Zlotea, Hydrogen absorption in 1 nm Pd clusters confined in MIL-101(Cr), J. Mater. Chem., 44 (2017) 23043–23052.

[52] N. Bimbo, W. Xu, J.E. Sharpe, V.P. Ting, T.J. Mays, High-pressure adsorptive sto- rage of hydrogen in MIL-101 (Cr) and AX-21 for mobile applications: Cryocharging and cryokinetics, Mater. Design., 89 (2016) 1086–1094.

[53] G. Blăniţă, M. Streza, M.D. Lazăr, D. Lupu, Kinetics of hydrogen adsorption in MIL- 101 single pellets, Int. J. Hydrogen Energ., 42 (2017) 3064–3077.

[54] X. Zhou, W. Huang, J. Miao, Q. Xia, Z. Zhang, H. Wang, Z. Li, Enhanced separation performance of a novel composite material GrO@MIL-101 for CO2/CH4 binary mixture, Chem. Eng. J., 266 (2015) 339–344.

[55] M.S. Alivand, F. Farhadi, Multi-objective optimization of a multi-layer PTSA for LNG production, J. Nat. Gas Sci. Eng., 49 (2018) 435–446.

[56] Q. Yan, Y. Lin, C. Kong, L. Chen, Remarkable CO2/CH4 selectivity and CO2 ad- sorption capacity exhibited by polyamine-decorated metal-organic framework ad- sorbents, Chem. Commun., 49 (2013) 6873–6875.

[57] Y. Lin, H. Lin, H. Wang, Y. Suo, B. Li, C. Kong, L. Chen, Enhanced selective CO2 adsorption on polyamine/MIL-101(Cr) composites, J. Mater. Chem. A., 2 (2014) 14658–14665.

[58] Z. Zhou, L. Mei, C. Ma, F. Xu, J. Xiao, Q. Xia, Z. Li, A novel bimetallic MIL-101(Cr, Mg) with high CO2 adsorption capacity and CO2/N2 selectivity, Chem. Eng. Sci., 147 (2016) 109–117.

[59] Q. Liu, L. Ning, S. Zheng, M. Tao, Y. Shi, Y. He, Adsorption of carbon dioxide by MIL-101(Cr): regeneration conditions and influence of flue gas contaminants, Sci. Rep., 3 (2013) 2916.

[60] Y. Wang, Y. Zhang, Z. Jiang, G. Jiang, Z. Zhao, Q. Wu, Y. Liu, Q. Xu, A. Duan, C. Xu, Controlled fabrication and enhanced visible-light photocatalytic hydrogen pro- duction of Au@CdS/MIL-101 heterostructure, Appl. Catal. B: Environ., 185 (2016) 307–314.

[61] X. Li, Y. Pi, Q. Xia, Z. Li, J. Xiao, TiO2 encapsulated in Salicylaldehyde-NH2-MIL-101(Cr) for enhanced visible light-driven photodegradation of MB, Appl. Catal. B: Environ., 191 (2016) 192–201.

[62] M.L. Hu, V. Safarifard, E. Doustkhah, S. Rostamnia, A. Morsali, N. Nouruzi, S. Beheshti, K. Akhbari, Taking organic reactions over metal-organic frameworks as heterogeneous catalysis, Micropor. Mesopor. Mater., 256 (2018) 111–127.

[63] L. Qin, Z. Li, Z. Xu, X. Guo, G. Zhang, Organic-acid-directed assembly of iron-carbon oxides nanoparticles on coordinatively unsaturated metal sites of MIL-101 for green photochemical oxidation, Appl. Catal. B: Environ., 179 (2015) 500–508.

[64] M. Shafiei, M.S. Alivand, A. Rashidi, A. Samimi, D. Mohebbi-Kalhori, Synthesis and adsorption performance of a modified micro-mesoporous MIL-101 (Cr) for VOCs removal at ambient conditions, Chem. Eng. J., 341 (2018) 164-174.

[65] P.B. Rallapalli, M.C. Raj, S. Senthilkumar, R.S. Somani, H.C. Bajaj, HFfree synthesis of MIL101 (Cr) and its hydrogen adsorption studies, Environ. Prog. Sustain. Energ., 2 (2016) 461-468.

[66] N. Tian, The synthesis of mesostructured NH 2-MIL-101 (Cr) and kinetic and thermodynamic study in tetracycline aqueous solutions, J. Porous Mater., 5 (2016) 1269-1278.

[67] M. Behbahani, V. Zarezade, A. Veisi, F. Omidi, S. Bagheri, Modification of magnetized MCM-41 by pyridine groups for ultrasonic-assisted dispersive micro-solid-phase extraction of nickel ions, Int. J. Environ. Sci. Technol., 10 (2019) 6431-6440.

Anal. Method Environ. Chem. J. 3 (2) (2020) 74-81

AMECJ

Research Article, Issue 2
Analytical Methods in Environmental Chemistry Journal
Journal home page: www.amecj.com/ir

One-step synthesis of zinc-encapsulated MCM-41 as H_2S adsorbent and optimization of adsorption parameters

Nastaran Hazrati [a], Ali Akbar Miran Beigi [*,b], Majid Abdouss [a] and Amir Vahid [b]

[a] *Department of Chemistry, Amirkabir University of Technology, Tehran, Iran.*
[b] *Oil Refining Research Division, Research Institute of Petroleum Industry, Tehran, Iran.*

ARTICLE INFO:

Received 20 Feb 2020
Revised form 19 Apr 2020
Accepted 10 May 2020
Available online 29 Jun 2020

Keywords:
Zinc encapsulated MCM-41,
H_2S gas,
Adsorption,
Extraction,
UOP163 method

ABSTRACT

The nano-sized structure of well-ordered Zn@MCM-41 adsorbent was synthesized through a direct hydrothermal method using CTAB as a structure-directing agent in an ammonia aqueous solution with different amounts of zinc acetylacetonate which were inserted into the structure-directing agent's loop during the synthesis. The XRD, HRTEM, and N_2 adsorption-desorption isotherms were used to characterize the prepared ZnO functionalized mesoporous silica samples. As a result, the presence of ZnO in highly-ordered MCM-41's pore was proved as well as maintenance of the ordered meso-structure of MCM-41. The materials were possessed with a high specific surface area (1114-509 m^2 g^{-1}) and a large pore diameter (4.03-3.27 nm). Based on the obtained results from the adsorption of H_2S gas in a lab-made setup, the Znx@MCM-41 showed the superior ability to increase of ZnO amount up to 7 hours as a breakthrough point. A two factor (zinc percent and temperature) experimental design with three levels was accomplished to optimize the adsorption parameters. The influence of parameters and the interactions on the adsorption of H_2S were studied and optimized. Also, the H_2S breakpoint curves carried on by UOP163 method.

1. Introduction

In recent years, the preparation and application of nano-sized materials due to their large surface areas have received by increasing attention in various areas of research [1-5]. Nano-ordered MCM-41 is a mesoporous well-ordered structure with a narrow pore size between 1.5 and 10 nm and a high surface area up to 1500 m^2 g^{1-} [6-8]. MCM-41 is a net silica network possessing, the slight acidity and low-capacity ion-exchange [9] which has great uses in many fields such as catalysis [10, 11], separation [12], medicine [13], and hydrogen sulfide removal [5, 14-16]. Giving in hand that pure siliceous MCM-41 may have limited applications [17], setting chemical-bonded functional groups in the MCM-41 channels [18], make it as a well-heterogeneous reusable catalyst in most of the reactions. Therefore, much of the research has been done to prepare the active substance through the modification of the silicate framework of MCM-41 by inorganic elements or organic functional groups [19]. Different methods for inorganic functionalization of mesoporous silica have been considered like the addition of inorganic compounds to the sol-gel mixture [20], template ion-exchange

* Corresponding Author: Ali Akbar Miran Beigi
Email: miranbeigiaa@ripi.ir
https://doi.org/10.24200/amecj.v3.i02.104

method [21], impregnation of calcined silica [22, 23, 5], chemical vapor decomposition [24, 19], and using metal-containing templates [25]. Desulfurization process, as one of the main applications of metal-containing mesoporous silica, is the most interesting area of research for lowering the sulfur-containing material, especially in oil industry [16, 26]. Hydrogen sulfide (H_2S) is a naturally occurring toxic and malodorous gas contained in most of the world's crude oils. Not only it may harm product value, but also it compromises environmental and safety compliance, such as infrastructure damages from corrosion attack, producing odors, and more. The environmental impacts on the sulfur content have forced on refiners to produce the clean petrochemical products. That is why managing hydrogen sulfide content is one of the every-stage challenges hydrocarbon processing, refining, and transportation [27]. In different industries, the H_2S can be removed using a variety of the physical-chemical and the biological methods. These methods include the Claus process, the chemical oxidants, the caustic scrubbers, H_2S scavengers, the liquid amine absorption, the liquid-phase oxidation, the physical solvents, as membrane-based processes, biological procedure, and the adsorptive methods [27, 19]. After the studies of Westmoreland et al., the H_2S adsorbents were applied based on zinc, copper, iron, and calcium oxides as proper elements due to their thermal stabilities as well as sulfur removal efficiencies. However, based on thermodynamic point of view, it can be indicated that the ZnO is an outstanding adsorbent with high efficiency for sulfur removal because of the high equilibrium constant. Furthermore, the ZnO is considered as a profitable stable sorbent as compared to many other metal oxides [28]. Herein, we described the characterization and the synthesis of zinc-incorporated MCM-41 through in-situ insertion of zinc complexes into the hydrophobic loops of micelles of structure directing agent. Therefore, the H_2S was efficiently adsorbed on zinc-incorporated MCM-41.

2. Experimental

2.1. Reagents and Materials

Tetraethylorthosilicate (TEOS), cetyltrimethylammonium bromide (CTAB), sodium acetate, zinc acetylacetonate ($Zn(acac)_2$), ethanol, ammonia and acetone were purchased from Merck company and used as received without any further purification. All of reagents were purchased from Merck. Germany.

2.2. Preparation of Zinc-incorporated MCM-41

A mixture of TEOS, cetyltrimethylammonium bromide CTAB, sodium acetate, ethanol, ammonia, deionized water (DW) and $Zn(acac)_2$ with the following molar composition (1+5x), 0.3, 1.5, 1, 14, 20 and x was used for the synthesis of Zinc-incorporated MCM-41. To start the synthesis, the proper amount of CTAB and sodium acetate was dissolved in water. Next, the dissolved $Zn(acac)_2$ (in ethanol and ammonia) were added to the solution. While stirring, TEOS was added, and after 70 minutes of stirring in 35°C, the suspension was poured into the stainless steel autoclave and heated at 70 °C for 24 hours. The obtained precipitate was filtered and then, washed with the applicable amount of acetone and DW, respectively. The prepared samples were calcined in 550 °C for 5 hours (1 °C min^{-1}). The prepared sample of Znx@MCM, where x indicates the percent of zinc (%) in the product were characterized by angle X-ray diffraction, nitrogen physisorption and high-resolution transmission electron microscopy. Also, the ability of Znx@MCM for H_2S adsorption was investigated.

2.3. Characterization

X-ray diffraction patterns were recorded on a Philips 1840 diffractometer with a Nickel-filtered Cu Kα anode (1.5418˚ A). Textural analyses were carried out on a Micromeritics Tristar 3020 system by determining the nitrogen adsorption–desorption isotherms at -196 °C. Before the analysis, the samples were degassed in vacuum for 5 hours at 300 °C until a stable vacuum of 0.1 Pa was reached. The Brunauer–Emmett–Teller (BET)

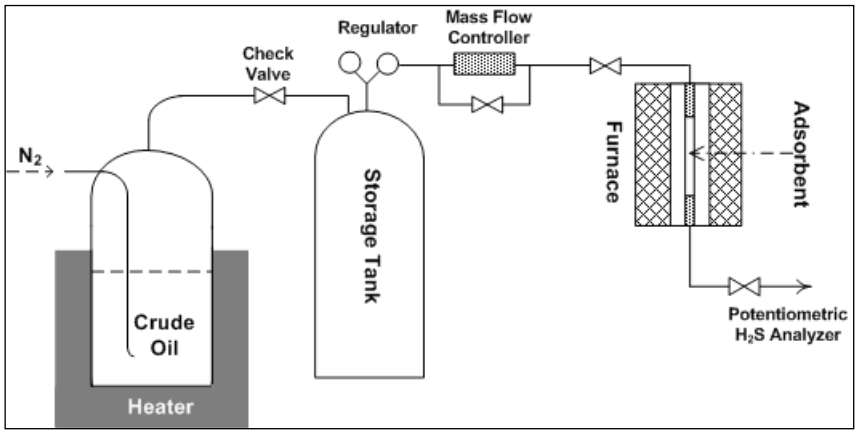

Fig. 1. Schematic plan of experimental set-up

specific surface area and the total pore volume was calculated for all of the samples. The mean pore diameter was determined by applying the Barrett–Joyner–Halenda (BJH) model. The wall thickness was calculated as the difference between the lattice parameter (a0) and the pore diameter. Transmission electron microscopy (TEM) images were obtained by a 200 kV Schottky field emitter high resolution transmission electron microscopy equipped with TEM.

2.4. Desulfurization process

H_2S of Naftshahr crude oil of Iran was extracted by cold stripping and collecting in a cylinder. The concentration of hydrogen sulfide in LPG was 5000 ppm (mg L^{-1}) as the final criterion for the H_2S breakthrough. Adsorption measurements for H_2S were accomplished using a lab-made setup (Fig. 1). The reactor effluent stream was analyzed by UOP163 method which gave the H_2S breakpoint curves.

3. Results and Discussion

3.1. X-ray diffraction

All of the samples were characterized by X-ray diffraction (XRD) to get structural confirmations about the porosity and structure of the materials. XRD patterns of the synthesized samples are given in Figure 2. The low angle patterns of prepared samples illustrated an intense peak at about 2.10 ° 2θ assigned to d100 reflection which is the typical sign of hexagonal mesoporous arrangement. The more amounts of zinc, the lower intensity of all reflections, especially in d100 plan can be observed. Consequently, the distinct decrease of structural order is caused by high metal loading and pore fouling. Then, the less intense reflection caused to the more zinc loading. On the other hand, the high angle XRD patterns of zinc incorporated MCM-41 samples (Fig. 3) indicate a peak on 36.0° 2θ assigned to d101 reflection which identifies hexagonal zinc oxide crystals is indeed present inside the pores of the MCM-41.

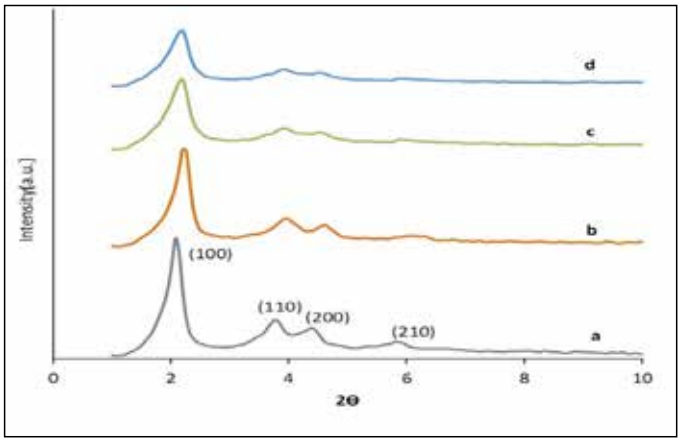

Fig. 2. X-ray diffraction patterns of a) MCM-41 b) Zn3@MCM-41 c) Zn6@MCM-41 d)Zn9@MCM-41

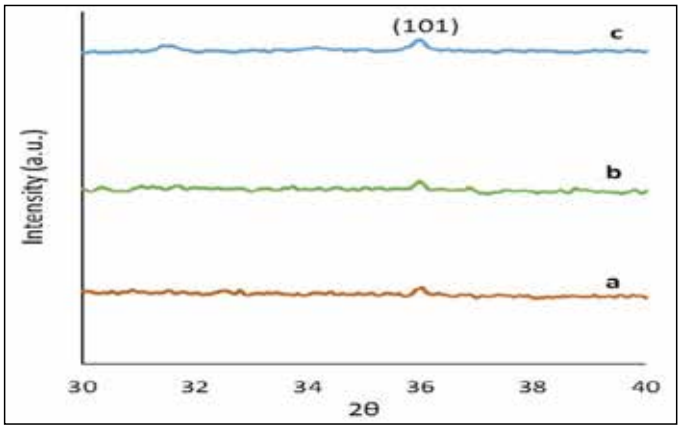

Fig. 3. High angle X-ray diffraction patterns of a) Zn3@MCM-41 b) Zn6@MCM-41 c) Zn9@MCM-41.

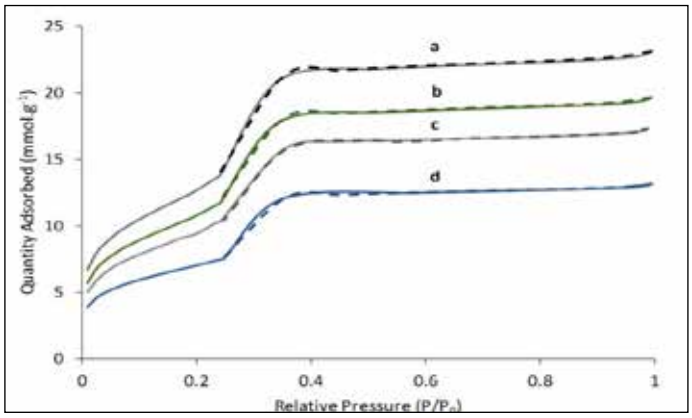

Fig. 4. Nitrogen adsorption isotherms of a) MCM-41 b) Zn3@MCM-41 c) Zn6@MCM-41

Table 1. Textural properties of Znx@MCM-41 zinc-containing samples (x = 0, 3, 6 and 9). a) Volume of mesopores b) d-spacing from XRD (nm) c) Unit cell parameter (nm) d) Pore diameter (nm) e) wall thickness from [a - (Wd/1.050)] equation (nm).

Sample name	S_{BET} (m^2g^{-1})	V_P (cm^3g^{-1})[a]	d (nm)[b]	a (nm)[c]	W_d (nm)[d]	b_d (nm)[e]
MCM-41	1114	0.85	4.01	4.63	3.93	0.89
Zn3@MCM-41	891	0.72	4.24	4.89	4.03	1.06
Zn6@MCM-41	571	0.55	4.05	4.67	3.63	1.21
Zn9@MCM-41	509	0.34	4.12	4.76	3.27	1.65

3.2. N_2 Adsorption.

The well-known, nitrogen physisorption technique was used for determination of the textural properties of prepared porous materials. The N_2 adsorption isotherms of all of the samples are shown in Figure 4. MCM-41 (Fig. 4a) shows a type-IV isotherm, which is a sign to have mesopores. At lower relative pressure (0.2 to 0.3), the adsorption branch of isotherm is expected to be the filling of mesopores stage with liquid nitrogen through capillary condensation. In this stage the sharpness is a sign of size uniformity and structural order of mesopores.

Desorption branch of isotherms accords with the adsorption which is an additional sign of high uniformity of mesopores. Textural properties of Znx@MCM-41 samples obtained from XRD and N_2 adsorption isotherms are tabulated in Table 1. From the table it is observed that the pore volume of the MCM-41 sample is decreased after loading inside the pores and the pores are not completely blocked. Decreasing of specific surface area by more loading indicates insertion of ZnO inside of the mesopores.

3.3. High Resolution TEM (HRTEM)

HRTEM images of Znx@MCM-41 (x=3, 6 and 9) are shown in Figure 5. Based on the obtained results, the high ordered array of the sample shows that the hexagonal structure of mesopores didn't damage in the in-situ loading of zinc.

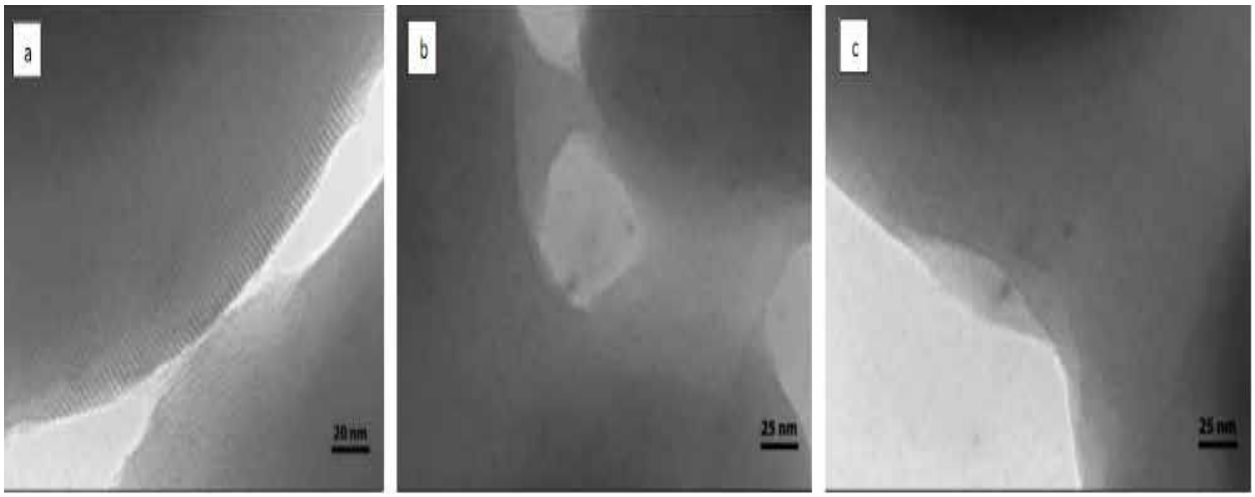

Fig. 5. HR-TEM images of zinc containing MCM-41. a) Zn3@MCM-41 b) Zn6@MCM-41 c) Zn9@MCM-41.

3.4. H_2S Adsorption

Synthesized samples showed great ability to remove H_2S at standard temperatures. As presented in Table 2, the changes of operating conditions were resulted by variation in practical temperature (50, 175 and 300°C), while space velocity in all the experiments was fixed on 3000 h^{-1}. Nine different experiments, designed based on two factors (A: zinc percentage and B: temperature), are shown in Table 2, which also contains the responses in the last column (tbp). The responses define hydrogen sulfide breakpoint in the carrier gas, the minute that H_2S concentration in the outlet gas becomes 5000 ppm.

Table 2. The experimental data of the breakpoints for experiments. (A: Zinc mole percentage B: Temperature tbp: Breakthrough time)

Run	Independent Variables		
	A	B	t_{bp} (min)
Blank	0	50	40.0
1	3	50	135.2
2	3	175	163.1
3	3	300	192.0
4	6	50	171.3
5	6	175	250.2
6	6	300	328.1
7	9	50	232.5
8	9	175	363.4
9	9	300	411.0

3.5. Effect of ZnO content and temperature

In this work, different amounts of zinc oxide were incorporated into the pores of MCM-41 by an in situ approach. It is clear that increasing zinc content at same operating condition (T: 175°C and space velocity: 3000 h^{-1}) caused noticeable increasing of adsorption (Fig. 6). This is attributed to increase in the active sites by rising zinc oxide loading which improves the chemical adsorption of hydrogen sulfide on the materials.

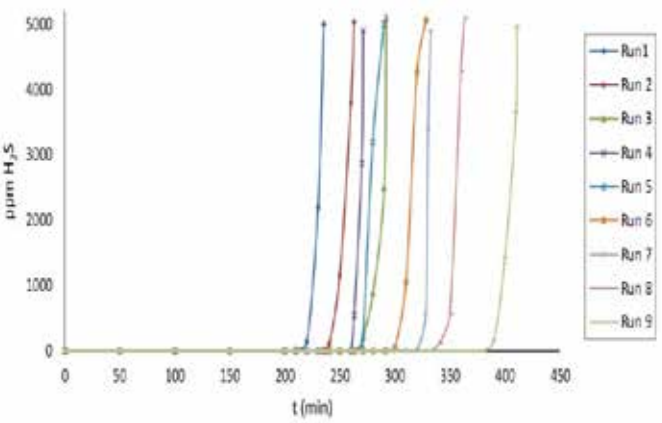

Fig. 6. Breakthrough curves of H_2S adsorption on Znx@MCM-41. The box at the right side of the figure indicates the run number (Table 1).

The effect of temperature was also investigated. With the increase in the temperature of absorption, the H_2S breakthrough was occurred later. Moreover increasing the temperature speeds up the adsorption by strengthening chemisorption of H_2S on ZnO [15], tbp increases as a consequence.

3.6. Effect of metal modification method

The selection of a hydrophobic zinc precursor ($Zn(acac)_2$) is the main reason to lead the zinc particles inside of the mesopores of MCM-41 by the influence of solvent-solute interactions in synthesis process. As comparing to the previous work based on wet impregnation for synthesis of ZnO containing MCM-41 [15], the pore volume and surface area of Zn@MCM-41 by proposed method was higher than previous work. Besides the values of H_2S breakthrough in the same operational condition is considerable. This might be because of the high dispersion and accessibility of zinc nanoparticles inside of the mesopores. Furthermore the smaller size of zinc nanoparticles improves the selectivity and effectiveness of them in the adsorption of H_2S.

3.7. Analysis of variance

The analysis of variance (ANOVA) on tbp is given in Table 3. If the value of F is more than that of the F-table at a similar probability level, the factor or

the interaction is statistically significant. The factors A, B and interaction AB verified to be statistically effective on tbp. The greater F the more significant effects on the response. The level of adsorption is given by regression equation of analysis of variance. It is consist of the linear relationship among all of the effects, and the response of the final equations in terms of effective variables is presented in equation 1:

$$T = +71.14 + 14.43\,A + 0.036\,B + 0.081\,AB \quad \text{(EQ.1)}$$

According to Figure 7, the interaction between two factors may be obtainable which influences on the response (tbp) with the confidence level of 95%. Figure 8 also shows the three-dimensional curves presenting the impact of temperature and zinc percentage on the breakpoints. The slope increase in response, observed on each curve, indicates that the effect of zinc percentage (factor A) on the response is greater than the effect of absorption temperature (factor B).

Table 3. Analysis of variance (ANOVA)

Source	Sum of Square	Degree of freedom	Mean Square	F-value	P-value (Prob>F)	Remark
Model	73838.5	3	24612.8	74.33	<0.0001	significant
A-Zn %	44376.0	1	44376.0	134.01	<0.0001	significant
B-Temp	25741.5	1	25741.5	77.73	0.0003	significant
AB	3721.0	1	3721.0	11.24	0.0203	significant
R-Error	1655.5	5	331.1	-	-	-
C-Total	75494.2	8	-	-	-	-

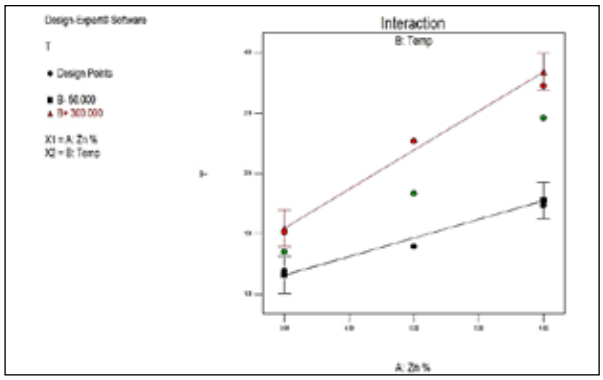

Fig. 7. Interaction between factors and their effect on breakpoint

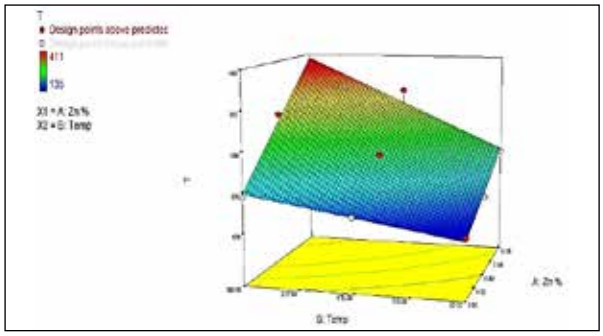

Fig. 8. Three-dimensional curves presenting the impact of factors on response

4. Conclusions

Herein nanoparticles of zinc were successfully immobilized into the mesopores of MCM-41. A significant difference between the presented approach and the typical in-situ pathways is based on the precursor's behavior in the solution. In this process, $Zn(acac)_2$ was located inside the hydrophobic micelles at which they were arranged by surfactant (before adding silica source) and after that, the zinc oxide nanopaticles were anchored onto silica walls. Although the metal precursor was added in the synthesis medium, the introduced metal in silica's walls is less than other in-situ methods. Notably, the characterization techniques showed considerably high specification for all of the samples as mentioned above. The results showed the high capacity of materials to adsorb H_2S. H_2S removal from LPG cut of the studied crude oil in the point of Zn= 9 wt. % and T = 300°C was adsorbed for about 7 hours in space velocity of 3000 h^{-1}. Additionally, the comparison between this work with the other published method showed, the more ability and efficienty extraction of H_2S gas.

5. Acknowledgements

The authors wish to thank from Amirkabir University of Technology, Tehran, Iran, Iranian Research Institute of Petroleum Industry (RIPI) for supporting of this work.

6. References

[1] C. Bensing, M. Mojić, S. Gómez-Ruiz, S. Carralero, B. Dojčinović, D. Maksimović-Ivanić, S. Mijatović, G.N. Kaluderović, Evaluation of functionalized mesoporous silica SBA-15 as a carrier system for Ph3Sn(CH2)3OH against the A2780 ovarian carcinoma cell line, Dalton Trans., 45 (2016) 18984-18993.

[2] Y. Wan, D. Zhao, On teh controllable soft-templating approach to mesoporous silicates, Chem. Rev., 107 (2007) 2821–2860.

[3] A. Sterczynska, A. Derylo-Marczewska, M. Zienkiewicz-Strzalka, M. Sliwinska-Bartkowiak, K. Domin, Surface properties of Al-functionalized mesoporous MCM-41 and teh melting behavior of water in Al-MCM-41 nanopores, Langmuir, 33 (2017) 11203–11216.

[4] F.J. Carmona, I. Jimenez-Amezcua, S. Rojas, C.C. Romao, J.A. Navarro, C.R. Maldonado, E. Barea, Aluminum doped MCM-41 nanoparticles as platforms for the dual encapsulation of a CO-releasing molecule and cisplatin, Inorg. Chem., 56 (2017) 10474-10480.

[5] M. Abdouss, N. Hazrati, A.A. Miran-Beigi, A. Vahid, A. Mohammadalizadeh, Effect of the structure of the support and the aminosilane type on the adsorption of H_2S from model gas, RSC Adv., 4 (2014) 6337-6345.

[6] M. Thommes, K. Kaneko, A.V. Neimark, J.P. Olivier, F. Rodriguez-Reinoso, J. Rouquerol, K.S. Sing, Physisorption of gases, with special reference to the evaluation of surface area and pore size distribution (IUPAC Technical Report), Pure Appl. Chem., 87 (2015) 1051-1069.

[7] V.B. Cashin, D.S. Eldridge, A. Yu, D. Zhao, Surface functionalization and manipulation of mesoporous silica adsorbents for improved removal of pollutants: a review, Environ. Sci. Water Res. Technol., 4 (2018) 110-118.

[8] E. Dündar-Tekkaya, Y. Yürüm, Int. J. Hydrog, Mesoporous MCM-41 material for hydrogen storage: A short review, Int. J. Hydrog. Energ., 41 (2016) 9789-9795.

[9] E. Lovell, Y. Jiang, J. Scott, F. Wang, Y. Suhardja, M. Chen, J. Huang, R. Amal, CO2 reforming of methane over MCM-41-supported nickel catalysts: altering support acidity by one-pot synthesis at room temperature, App. Catal. A: General, 473 (2014) 51-58.

[10] B.S. Kim, C.S. Jeong, J. M. Kim, S.B. Park, S.H. Park, J.K. Jeon, S.C. Jung, S.C. Kim, Y.K. Ex Situ, Catalytic upgrading of lignocellulosic biomass components over vanadium contained H-MCM-41 catalysts, Catal. Today, 265 (2016) 184-191.

[11] M. Fadhli, I. Khedher, J.M. Fraile, J. Mol. Catal, Modified Ti/MCM-41 catalysts for enantioselective epoxidation of styrene, J. Mol.

Catal. A Chem., 420 (2016) 282-289.

[12] WY. Sang, OP. Ching, Tailoring MCM-41 mesoporous silica particles through modified sol-gel process for gas separation, AIP Conf. Proc., 1891 (2017) 020147.

[13] E. Beňová, V. Zeleňák, D. Halamová, M. Almáši, V. Petrul'ová, M. Psotka, A. Zeleňáková, M. Bačkor, V. Hornebecq, A drug delivery system based on switchable photo-controlled p-coumaric acid derivatives anchored on mesoporous silica, J. Mater. Chem. B, 5 (2017) 817-825.

[14] JJ. Zhang, WY. Wang, GJ. Wang, C. Kai, H. Song, L. Wang, Equilibrium, kinetic and thermodynamic studies on adsorptive removal of H_2S from natural gas by amine functionalisation of MCM-41. Prog. React. Kinet. Mec., 42 (2017) 221-234.

[15] N. Hazrati, M. Abdouss, A. Vahid, A. A. Miran Beigi, A. Mohammadalizadeh, Removal of H 2 S from crude oil via stripping followed by adsorption using ZnO/MCM-41 and optimization of parameters, Environ. Sci. Technol., (2014) 997-1006.

[16] Y.S. Hong, Z.F. Zhang, Z.P. Cai, X.H. Zhao,B.S. Liu, Deactivation kinetics model of H_2S removal over mesoporous LaFeO3/MCM-41 sorbent during hot coal gas desulfurization. Sustain, Energ. Fuels, 28 (2014) 6012-6018.

[17] X. Feng, Z. Yan, N. Chen, Y. Zhang, X. Liu, Y. Ma, X. Yang, W. Hou, Synthesis of a graphene/ polyaniline/MCM-41 nanocomposite and its application as a supercapacitor. New J. Chem., 37 (2013) 2203-2209.

[18] Y. Bao, X. Yan, W. Du, X. Xie, X. Pan, J. Zhou, L. Li, Application of amine-functionalized MCM-41 modified ultrafiltration membrane to remove chromium (VI) and copper (II), Chem. Eng. J., 281 (2015) 460-4607.

[19] D.P. Sahoo, D. Rath, B. Nanda, K. Parida, Transition metal/metal oxide modified MCM-41 for pollutant degradation and hydrogen energy production: a review, RSC Adv., 5(2015) 83707-83724.

[20] E.P. Baston, A.B. Franca, A.V. da Silva Neto, E.A. Urquieta-Gonzalez, Incorporation of the precursors of Mo and Ni oxides directly into the reaction mixture of sol–gel prepared γ-Al2O3-ZrO2 supports evaluation of the sulfided catalysts in the thiophene hydrodesulfurization, Catal. Today, 246 (2015) 184-190.

[21] A. Kowalczyk, A. Borcuch, M. Michalik, M. Rutkowska, B. Gil, Z. Sojka, P. Indyka, L. Chmielarz, MCM-41 modified with transition metals by template ion-exchange method as catalysts for selective catalytic oxidation of ammonia to dinitrogen, Micropor. Mesopor. Mater., 240 (2017) 9-21.

[22] KS. Kamarudin, NO. Alias, Adsorption performance of MCM-41 impregnated with amine for CO2 removal, Fuel Process. Technol., 106 (2013) 332-337.

[23] S. Qiu, X. Zhang, Q. Liu, T. Wang, Q. Zhang, L. Ma, A simple method to prepare highly active and dispersed Ni/MCM-41 catalysts by co-impregnation, Catal. Commun., 42 (2013) 73-78.

[24] R. Atchudan, S. Perumal, TN. Edison, YR. Lee, Highly graphitic carbon nanosheets synthesized over tailored mesoporous molecular sieves using acetylene by chemical vapor deposition method, RSC adv., 5 (2015) 93364-93373.

[25] AA. Gewirth, JA. Varnell, AM. Di Ascro. Nonprecious metal catalysts for oxygen reduction in heterogeneous aqueous systems, Chem. Rev., 118 (2018) 2313-2339.

[26] B. Elyassi, Y. Al Wahedi, N. Rajabbeigi, P. Kumar, J.S. Jeong, X. Zhang, P. Kumar, V.V. Balasubramanian, M.S. Katsiotis, K.A. Mkhoyan, N. Boukos. A high-performance adsorbent for hydrogen sulfide removal, Micropor. Mesopor. Mater., 190 (2014) 152-155.

[27] S. Jafarinejad, Control and treatment of sulfur compounds specially sulfur oxides (SOx) emissions from the petroleum industry: a review, Chem. Int., 2 (2016) 242-253.

[28] P.R. Westmoreland, D.P. Harrison, Evaluation of candidate solids for high-temperature desulfurization of low-Btu gases, Environ. Sci. Technol., 10 (1976) 659-661.

Anal. Method Environ. Chem. J. 3 (2) (2020) 82-91

AMECJ

Research Article, Issue 2
Analytical Methods in Environmental Chemistry Journal
Journal home page: www.amecj.com/ir

Aluminum separation from drinking water and serum samples based on djenkolic acid immobilized on the multi walled carbon nanotubes by ultrasound-assisted dispersive micro solid phase extraction

Farnaz Hosseini[*, a] **and Sara Davari** [b]

[a] *Islamic Azad University, Tehran Medical Branch, Iran*
[b] *Islamic Azad University, Tehran Medical Branch, Iran*

ARTICLE INFO:

Received 2 Mar 2020
Revised form 30 Apr 2020
Accepted 21 May 2020
Available online 29 Jun 2020

Keywords:
Aluminum,
Poly methyl ether thiol sorbent,
Dispersive micro solid phase extraction,
Waters,
Human serum,
Electrothermal atomic absorption spectrometry

ABSTRACT

A new method for aluminum extraction from drinking water and human serum samples was used by djenkolic acid (DJKA) immobilized on multi walled carbon nanotubes (MWCNTs-DJKA). By procedure, the mixture of 25 mg of MWCNTs-DJKA sorbent and hydrophobic ionic liquid ([OMIM][PF6]) were dispersed with ultrasonic bath in 10 mL of drinking water and serum samples for 10 min at pH=5. The aluminum ions were extracted based on MWCNTs-DJKA sorbent in liquid phase by ultrasound-assisted dispersive micro solid phase extraction (USA-D-μ-SPE). After centrifuging, the Al (III) was separated from liquid phase by ionic liquid phase in bottom of centrifuge PVC tube. Finally, the Al (III) were back-extracted from sorbent/IL in acidic pH and measured by electrothermal atomic absorption spectrometry (ET-AAS). In optimized study, LOD, LOQ, the linear range, the working range and the enrichment factor were obtained 0.1 μg L^{-1}, 0.3 μg L^{-1}, 0.3-12.8 μg L^{-1}, 0.3-30.7 μg L^{-1} and 9.92, respectively (RSD< 5%). The adsorption capacity of the MWCNTs-DJKA sorbent was obtained in batch system. Based on proposed procedure, the mean concentrations of aluminum in drinking waters and serum samples were lower than world health organization (WHO) and American conference of governmental industrial hygienists (ACGIH) references. The method was validated by spiking samples and standard reference materials (SRM) in water and human biological samples.

1. Introduction

Aluminum used in different products such as pharmaceuticals (Al-Mg/S), cover or additives for foods, plates, cars and airplanes. The aluminium compounds have solid forms with high melting points and solubility in water in low pH. The aluminium cation (Al^{3+}) has a strong affinity to hydroxide form [$Al(OH)_3$] as precipitation. Aluminium production" has been classified as carcinogenic to humans by the International Agency for Research on Cancer (IARC). Aluminium in the diet has ranges between 0.1 to 0.3% based on aluminium intake and urinary elimination. Over dose of aluminum caused to Alzheimer's disease (AD). Aluminium is the most

* Corresponding Author: Farnaz Hosseini
Email: hfarnaz.1990@gmail.com
https://doi.org/10.24200/amecj.v3.i02.105

abundant metal and the third most abundant element in the Earth's crust. This metal separated from its ores by industrial scale and caused to change from decorative metal to the most widely used metal in different industries [1]. WHO reported that aluminum salts can be absorbed by the gut and concentrated in various human tissues including bone, parathyroid, and brain. Aluminum concentrations in brain tissue should be lower than 2 μg g^{-1}. The daily dietary intake of aluminum (510 mg) is completely eliminated. On the other hand, the pervious works showed that the high aluminum intake may be harmful to some patients with bone or renal diseases [2]. Also, the aluminum can be detected in brain tissues of patients with Alzheimer's disease [3] and the pulmonary fibrosis have been evident under high-dose aluminum exposure [4]. The neurotoxicity of aluminium has been demonstrated in humans, animal models and in tissue and cell culture. The neurotoxicity of aluminum is indisputable and it is difficult to understand the mechanism of neurotoxin in human body [5].Aluminium toxicity created from the interaction between aluminum and plasma membrane and in humans Mg^{2+} and Fe^{3+} are replaced by Al^{3+}, which causes many disturbances associated with intercellular interaction [6]. Workers are exposed to various occupational hazardous factors such as fumes and gases, mineral dusts, and VOCs. Workers in aluminum factory were shown the respiratory symptoms, phlegm, dyspnea, wheezing and chest tightness [7].Also, it has been shown that Bauxite mining causes respiratory and skin problems, in addition to other injuries consistent with mining and heavy industries. Workers in alumina refineries have symptoms include osteosclerosis, sinus trouble, chest pains, coughs, thyroid disorders, anemia, dizziness, weakness and nausea. As hazards of aluminium in environment and humans, determination and separation aluminum in human body and waters is very necessary. Many analytical techniques was used for determination of aluminum in different matrix such as flame atomic absorption spectrometry (F-AAS) [9], stripping Voltammetry (SV) [10], inductively coupled plasma-atomic emission spectrometry (ICP-AES) [11], High performance liquid chromatography/ inductively coupled plasma mass spectrometry (HPLC/ICPMS) [12,13], electrothermal atomic absorption spectrometry (ETAAS) [14] and inductively coupled plasma mass spectrometry (ICP-MS) [15]. Also, sample preparation was needed for separating of contaminations from water and biological samples. For this purpose, the vary preconcentration/separation techniques such as liquid–liquid extraction (LLE), dispersive liquid–liquid microextraction (DLLME) [16, 17], and solid phase extraction (SPE) [18] was applied. Recently, the SPE methods were used as a suitable technique for extraction aluminum as compared to others. The SPE have some advantages including simplicity, lower cost, higher enrichment factor, less lower LOD, and the ability to combine with different detection techniques such as ICP-MS [19, 20]. The aim of this study is to develop a novel technique based on MWCNTs-DJKA sorbent for separation and determination of aluminum from drinking water and human serum samples by USA-D-μ-SPE procedure coupled to ET-AAS.

2. Experimental

2.1. Instrumental

The spectra GBC atomic absorption spectrometer (AAS, Plus 932, Australia) using a electrothermal module (ET-AAS) was used for determination aluminum in different samples. The parameters of alminum of were adjusted by recommended of the manufacturer. A multi cathode lamp for Al (MCL) with the current lamp (6 mA), the wavelength (396.2 nm) and spectral bandwidth (0.5 nm) was applied. All results were performed by auto injection of samples (1-100μL) and ANANTA software. The pH in water and serum samples were determined and adjusted by a pH-meter of Metrohm (744, Switzerland) which was with a glassy electrode. The samples were separated using a centrifuge accessory (Eppendorf, 5702 Series Centrifuge, 022629905, 4,400rpm) with rotor (A-4-38) and round bucket(4 × 85 mL), rotary knobs. An ultrasonic bath (100DE, China) with temperature control was used in this study.

Table 1. Comparind of the structure of MWCNTs and MWCNTs-DJKA

Carbon Nano Structure	Diameter (nm)	Length (um)	Surface Area (m^2/gr)
MWCNT	14-30	11-24	375
MWCNTs-DJKA	15-38	13-30	345

2.2. Material and Reagents

The reagents such as acids, bases and organic and inorganic solvents were purchased from Merck Company (Germany, ultra-trace grade). MWCNTs (particle size <100 µm) was prepared from RIPI, Iran. DL-djenkolic acid ($C_7H_{14}N_2O_4S_2$, DJKA, CAS N.: 28052-93-9) was purchased fron sigma Aldrich, Germany. 1-methyl-3-octylimidazolium hexafluorophosphate ([OMIM] PF6]), CAS N: 304680-36-2, Purity > 99.0). Standard stock solutions (1000 ppm) of Al (III) purchased from Merck, Darmstadt, Germany. Deionized water (DW) prepared from Milli-Q plus water purification system (Millipore, Bedford, MA, USA). The all solutions of procedure were daily prepared by diluting of standard solutions with DW. The eight point of calibration curve for aluminum were prepared daily by diluting the stock solutions of alminum ions with DW prior to analysis. The pH adjustments were made using appropriate buffer solutions including ammonium acetate (CH_3COOH/ $CHCOONH_4$, 0.2 Mol) for pH 4-6 in this study.

2.3. Sampling

All glasses and PVC tubes were cleaned with a mixture of 0.1 M of HNO_3/H_2SO_4 solution for 12 h and washed for 10 times with DW before using. As trace concentrations of Al in serum and drinking water, even low contamination at any step of sample storage, preparation, and analysis can be effected on the accuracy of the results. Human serum samples collected into 2 mL of Eppendorf tube tubes and kept at -20^{O}C. Serum and wastewater samples were collected from aluminum factories, Iran. The water prepared and stored by standard method for sampling from water by adding HNO_3 (2%) to waters. In this study, the world medical association declaration of Helsinki (WMADH) based on guiding physicians in human body research was considered.

2.4. Characterization

The Brunauer-Emmett-Teller (BET) method was used for studying the microstructure (surface area and pore size) of nanostructure. The surface area and porosity of the MWCNTs and MWCNTs-DJKA, before and after heat treatment in 350^{O}C were almost similar. The structure of MWCNTs and MWCNTs-DJKA including length, diameter and surface area were provided in **Table 1**. In this study, the surface area of MWCNTs was found 375 m^2 g^{-1}, which was similar to previous literature for MWCNT. The low specific surface area in CNTs depended on the large diameters and many walls**.** The surface area of MWCNTs-DJKA (345 m^2 g^{-1}) is little lower than simple MWCNT (375 m^2 g^{-1}) because of MWCNTs functionalized with DJKA.

2.5. Procedure of aluminum extraction

By procedure, the aluminum ions were extracted from drinking water and human serum samples by MWCNTs-DJKA. In this work, the mixture of 25 mg of MWCNTs-DJKA adsorbent and [OMIM][PF6] were added to 10 mL of samples and dispersed with ultrasonic bath for 10 min at pH=5. The aluminum ions were extracted based on MWCNTs-DJKA sorbent by ultrasound-assisted dispersive micro solid phase extraction (USA-D-µ-SPE). After centrifuging at 4000 rpm, the Al (III) ions were separated from liquid phase by hydrophobic ionic liquid phase in bottom of centrifuge PVC tube. Finally, the Al (III) were back-extracted from sorbent/IL with 0.5 mL of HNO3 (0.1 M) and measured by ET-AAS after dilution up to 1 mL with DW **(Fig.1)**.

3. Results and Discussions

3.1. Synthesis of MWCNT

High-purity MWCNTs were synthesized by use of camphor, an environment-friendly hydrocarbon as a carbon source using chemical vapor deposition

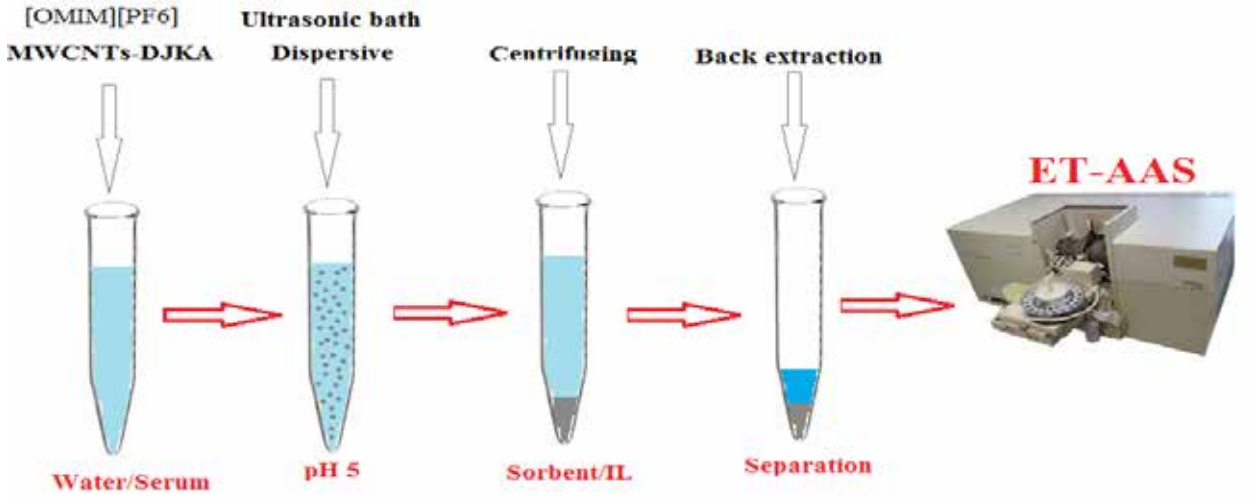

Fig. 1. Procedure of aluminum extraction based on MWCNTs-DJKA by USA-D-μ-SPE

(CVD) method on Co-Mo/MgO Nano-catalysts. The Nano-catalyst synthesized by sol-gel method. MWCNTs growth at temperatures of about 900-1000 °C in 45-60 minutes was conducted. Concentration of active metals was 5-10%. The Nano-catalyst (Co-Mo/MgO) was prepared by our special sol-gel method (Sayes et al., 2006, Rashidi et al., 2007). The composition of Co: Mo: Mgo for MWCNTs was 2.5:2.5:95 molar ratio. In chemical vapor deposition method, generally a precursor gas as a carbon source enters the furnace. In this study, the used experimental setup for CNTs production consisted of a quartz tube reactor with a length of 150 and 7 cm in diameter. It was heated in a resistive furnace in the temperature range from 900 to 1000 °C and at ambient pressure. The camphor was used as the carbon precursor and placed in the early part of the reactor and copper Nano-catalyst was placed in the middle of the reactor. The reactor was then put in a three thermal zone furnace, the first part for the evaporation of camphor, Part II for the reaction zone and Part III for cooling of the exhaust vapors. Before using MWCNT as adsorbent, purification process and meshing were performed.

3.2. Synthesis of Djenkolic on MWCNTs

The immobilization of 3,3′-(Methylenedithio) dialanine (djenkolic acid, DJKA) on multi-wall carbon nanotubes was obtained. The pure MWCNTs (0.5 g) were mixed with H_2SO_4 and HNO_3 solutions and chaked with 300 rms for 2 h. The MWCNTs were oxidized based on carboxyl groups (MWCNTs-COOH). Then, the MWCNTs-COOH were washed with DW many times before it filtered with Watman filter (0.2 nm) based on vacuum accessory. Them, the carboxyl groups on MWCNTs (COOH) convert to hydroxil group (OH) by reducing agent and washed and dried before using. The 0.5 g of MWCNTs-OH were dispersed in 10 mL of toluene and 1 mL of 3-(trimethoxysilyl)propyl chloride added drop by drop very quickly. The chloro silica on MWCNTs prepared by refluxing, washing and driing at 70 °C. Finally, the cholor functionized on MWCNTs was used by djenkolic acid in ethanolic solution which was shaked with 20 micro liter of N,N-diethylethanamine for 20 min before refluxed at 70 °C for 2 h. Finally the product of MWCNTs-DJKA was synteszed. The sulfur groups of this molecule act as chelation sites to which divalent metal ions coordinate. In addition to these groups, the formation of a stable ring with metal ions is a factor of increasing efficiency on the trapping process in the variable conditions (**Fig. 2**).

3.3. FTIR Analysis

The appearance of a broad peak in the range 2500–3600 cm^{-1} in the FTIR spectra of these compounds is due to the characteristic O–H and NH stretching vibration of enolic, carboxylic, and

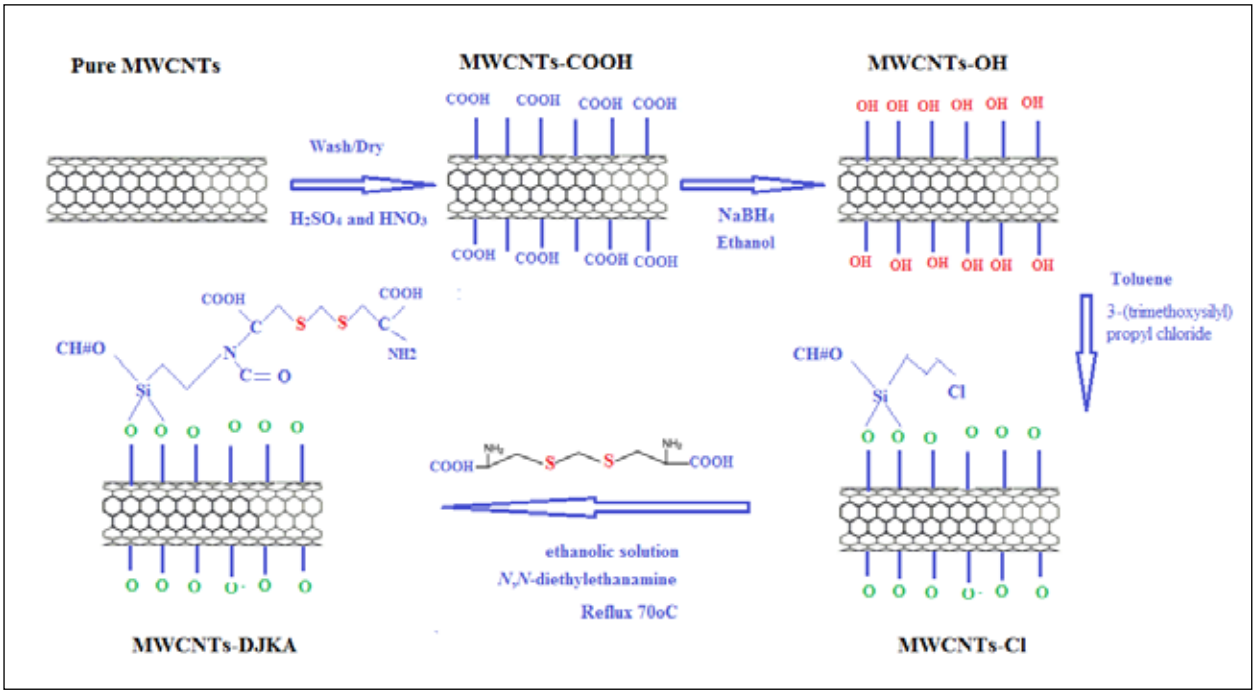

Fig. 2. Synthesis of Djenkolic on MWCNTs

Amine functionalities. As **Figure 3**, The absorption bands at 3420, 1718, 1623, and 1060 cm^{-1} shown in the spectra of MWCNT and MWCNTs-DJKA are ascribed to the stretching bands ν(O–H), ν(C=O), ν(C=C), and ν(C–O) respectively. Moreover, the peak at 1410 cm^{-1} may be attributed to tertiary OH groups [53,54]. Also, the characteristic bands observed at around 1062 and 1169–1218 cm^{-1} in the spectra of the MWCNTs-DJKA and GO correspond to the vibration bands of ν(S=O) derived from SO3H groups. The presence of SO3 group is also confirmed by the presence of the peak at 1221 cm^{-1}.

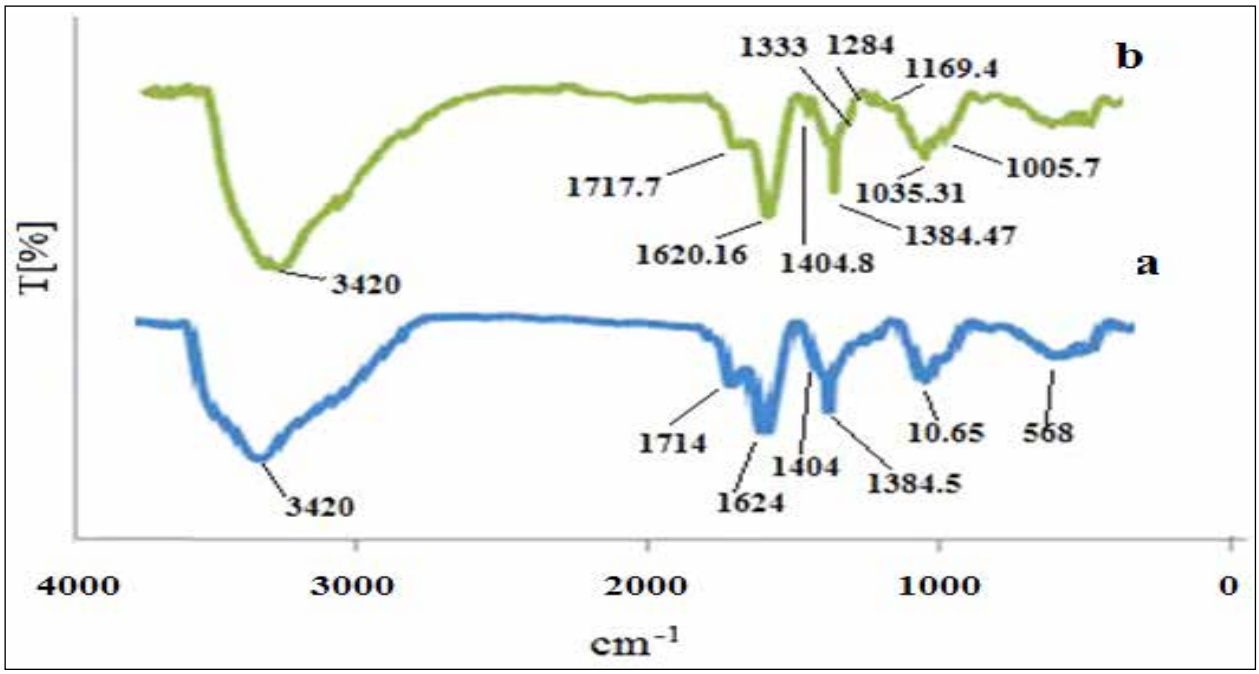

Fig. 3. FTIR spectra of a) MWCNT and b) MWCNTs-DJKA

3.4. SEM and XRD Analysis

After synthesis, the SEM images of MWCNTs and MWCNTs-DJKA were obtained which was shown in **Figure 4a and 4b**. Nitrogen adsorption The X-ray diffraction (XRD) spectrum of MWCNTs and MWCNTs-DJKA was shown in **Figure 5**. The XRD of MWCNTs-DJKA is similar to MWCNTs and the crystallinity /morphology of MWCNTs were preserved during synthesis of MWCNTs-DJKA. The MWCNTs-DJKA showed typical peak of (002), (110), and (400) at 2θ = 26.5, 42.4, and 52.7°, respectively.

3.5. Optimization of pH

The main factor for extraction aluminum from serum and water samples is pH. So, the effect of different pH from 2 to 10 was investigated by USA-D-μ-SPE procedure. The results showed that the MWCNTs-DJKA could be simply extracted alminum in a pH of 4-6. Therefore, the efficient extraction for Al(III) were achieved more than 97% at optimized pH and the recoveries were decreased at pH more than 6 and less than 4. So, pH=5 was used for further works in this study **(Fig. 6)**. The results showed that, aluminum can

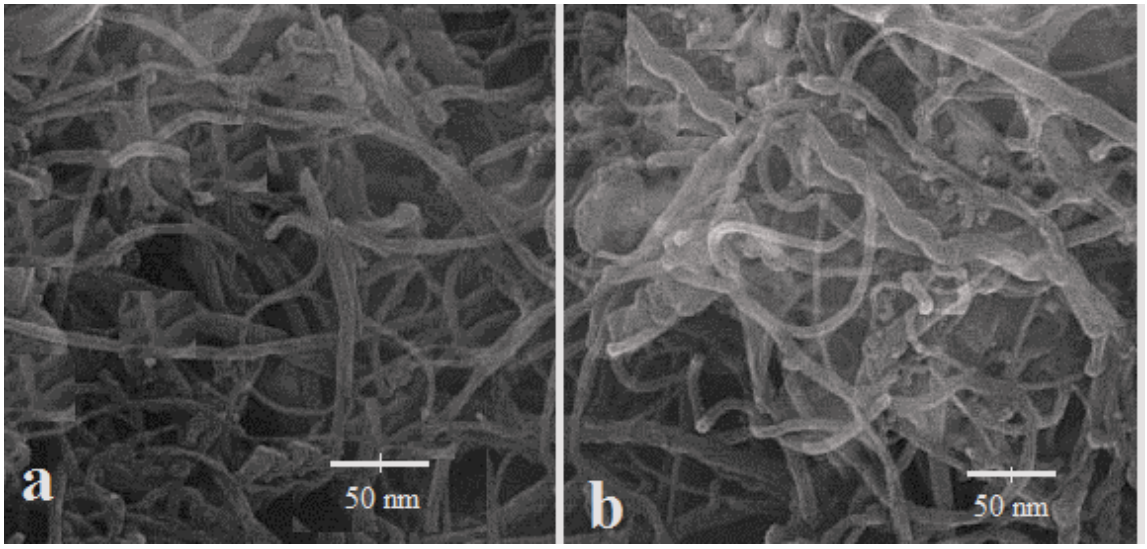

Fig. 4. SEM of images of a) MWCNTs and b) MWCNTs-DJKA

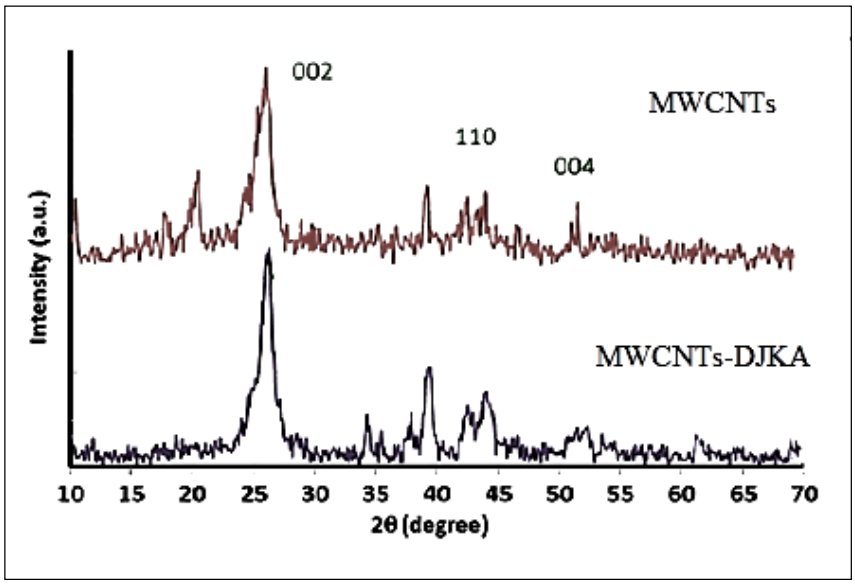

Fig. 5. The X-ray diffraction (XRD) of MWCNTs and MWCNTs-DJKA

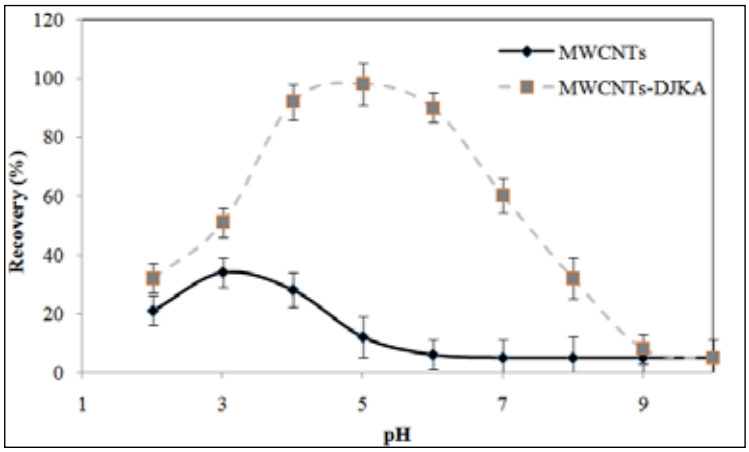

Fig. 6. The effect of pH on aluminum extraction by MWCNTs and MWCNTs-DJKA

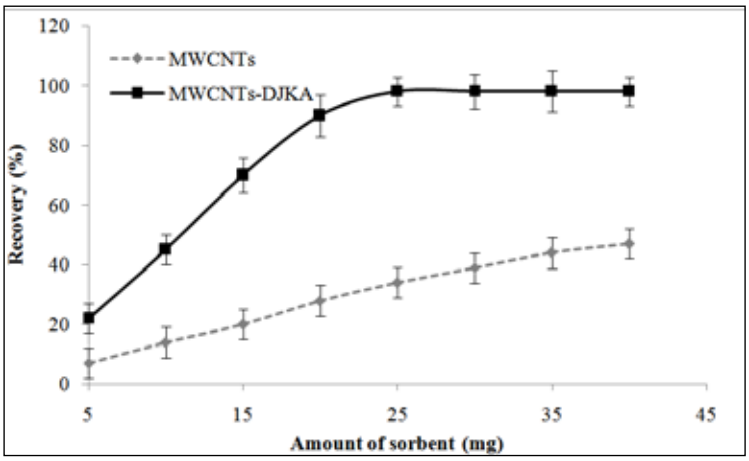

Fig. 7. The effect of amount of MWCNTs and MWCNTs-DJKA for aluminum extraction in serum and water samples

be physically extracted by MWCNTs at pH=3 up to 34%. The mechanism of extraction was carried out based on the coordination of covalent bond between positively charged of Al^{3+} and sulfur of DJKA which is highly dependent on pH.

3.6. The effect of Ionic liquids and sonication time

The different hydrophobic ionic liquids such as [OMIM][PF6], [HMIM][PF_6] and [BMIM][PF_6] were used for separation of MWCNTs and MWCNTs-DJKA from samples. The amounts of ILs on the separation of MWCNTs and MWCNTs-DJKA sorbents were tested between 0.01-0.2 g in Al concentration from 0.3 µg L^{-1} as LLOQ and 12.8 µg L^{-1} as ULOQ. The results showed the the best recovery was obtained by 0.1 g of [OMIM][PF_6]. Therefore, 0.12 g of [OMIM][PF_6] was used as optimum IL for separation of aluminum in water and serum samples.

3.7. Optimazation of amount of MWCNTs-DJKA sorbent

For optimization of extraction, the amount of MWCNTs and MWCNTs-DJKA was studied at pH=5. For this purpose, the amounts of MWCNTs and MWCNTs-DJKA between 1—40 mg were evaluated for Al(III) extraction by the USA-D-µ-SPE procedure. By results, the high recoveries in water and serum samples were achieved from 22 mg of MWCNTs-DJKA by proposed procedure. So, 25 mg of MWCNTs-DJKA was selected as optimum amount of sorbent (**Fig. 7**). The higher amount of MWCNTs-DJKA had no effect on the extraction recovery for Al(III) in water samples.

3.8. The effect of elution and sample volume

The volume/ concentration of elution for back extraction Al ions from MWCNTs-DJKA were studied at pH of 5. So, the different solutions such as HCl, HNO_3, H_2SO_4 and NaOH with different volume (0.2-1.0 mL) and concentration (0.1-0.5 M) was used for back extraction Al(III) from sorbents by USA-D-µ-SPE procedure. The results showed that 0.2 mol L^{-1} HNO_3(0.5 mL) was quantitatively back-extracted aluminum from MWCNTs-DJKA.The sample volume based on MWCNTs-DJKA was evaluated for aluminum extraction between 1-20 mL serum and water samples in ranges (0.3-12.8 µg L^{-1}). The results showed us the efficient extraction were obtained for 10 mL of samples. By

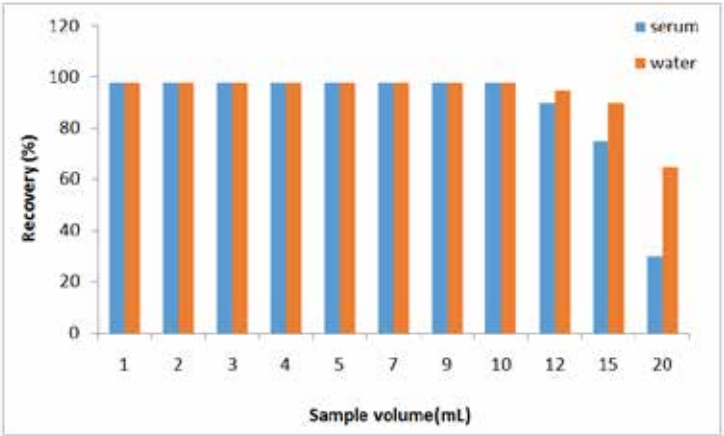

Fig. 8. The effect of sample volume on aluminum extraction by USA-D-μ-SPE procedure

increasing sample volume, the extraction recovery was decreased (**Fig. 8**).

3.9. The effect of interfernce ions in extraction

The effect of interference of coexisting ions for aluminum extraction in water and serum samples was investigated by USA-D-μ-SPE procedure. So, the different concentrations of the interfering cations and anions added to 10 mL of aluminum standard solution based on MWCNTs-DJKA at in ranges of 0.3-12.8 μg L^{-1} at pH=5. The results showed us that the most of the concomitant ions have no effect on the extraction recovery of Al (III) ions by USA-D-μ-SPE procedure (**Table 2**).

Table 2. The effect of interferences ions on extraction of Al(III) based on MWCNTs-DJKA in water/serum samples by USA-D-μ-SPE procedure

Interfering Ions (I)	Mean ratio (C_I /$C_{Al(III)}$)	Recovery (%)
	Pb(II)	Pb(II)
Ni^{2+}, Co^{2+}, Cd^{2+}	600	97.4
Zn^{2+}, Cu^{2+}	900	98.2
Mo^{2+}, V^{3+}, Cr^{3+}	700	96.7
Hg^{2+}, Ag^{+}	100, 200	98.3
Br^{-}, F^{-}, Cl^{-}, I^{-}	900	99.2
Na^{+}, K^{+}	1000	99.4
CO_3^{2-}, PO_4^{3-}, NO_3^{-}	1100	98.0
Ca^{2+}, Mg^{2+}	550	97.1
Pb^{2+}, Se^{2+}	750	96.9
S^{2-}, SO_3^{2-}	850	98.6

3.10. Validation of methodology

The ultra-trace aluminum in human serum and water samples were evaluated by the USA-D-μ-SPE procedure. As results in **Table 3**, the Al (III) ions in human serum and water samples was efficiently extracted based on MWCNTs-DJKA with high recovery. The results showed us that the proposed procedure was well validated by spiking of standard solution between 0.3 μg L^{-1} to 12.8 μg L^{-1} with the high accuracy. The obtained recoveries of spiked samples demonstrated that MWCNTs-DJKA adsorbent can be used as applied and simple procedure for aluminum separation in different samples in short time. Moreover, the validating of methodology was obtained based on the standard reference materials (SRM) and ICP-MS analysis for aluminum determination in water and serum samples by USA-D-μ-SPE

Table 3. Method validation for aluminum extraction/ determination in water and serum samples by spiking samples

Sample	Added (μg L^{-1})	*Found (μg L^{-1})	Recovery (%)
Water 1	---	0.524 ± 0.023	---
	0.5	1.012 ± 0.053	97.6
Water 2	---	5.536 ± 0.247	---
	5.0	10.602 ± 0.503	101.3
Water 3	---	6.464 ± 0.288	---
	6.0	12.231 ± 0.573	96.1
Serum 1	---	0.398 ± 0.021	---
	0.5	0.901 ± 0.043	100.6
Serum 2	---	3.241 ± 0.152	---
	3.0	6.132 ± 0.332	96.4
Serum 3	---	7.207 ± 0.346	---
	5.0	12.155 ± 0.574	98.9

*Mean of three determinations of samples ± confidence interval (P = 0.95, n =10)

Table 4. Validation of methodology for aluminum extraction in water and serum samples by the standard reference materials (SRM) and ICP-MS

Sample	Added(µg L^{-1})	*Found(µg L^{-1})	Recovery (%)
SRM 1643	--------	7.52 ± 0. 34	97.7
	5.0	12.36 ± 0. 58	96.8
SRM 1643d	--------	2.61± 0. 12	102.7
	2.0	4.54± 0. 19	96.5
[a] Serum SRM	--------	4.96 ± 0.22	95.4
	5.0	9.88 ± 0.48	98.4

*Mean of three determinations of samples ± confidence interval (P = 0.95, n =10)

SRM 1643, aluminum in water, 77± 1 µg g^{-1}, 1 g of sample diluted in 100 mL of DW with HNO_3 (2%) after dilution 10 mL of stock solution was used as 7.7± 0. 1 µg L^{-1}

SRM 1643d, aluminum in water: 127.6 ± 3.5 µg L^{-1}, after dilution with DW (1:50) was used as 2.54± 0. 08 µg L^{-1}

[a]ICP-MS: Serum aluminum concentration was obtained 5.2 ± 0.11 µg L^{-1}

procedure (**Table 4**). Analytical results in serum and water samples were confirmed by SRM and ICP-MS.

4. Conclusions

In this study, a novel MWCNTs-DJKA adsorbent was used for aluminum extraction/ separation and preconcentration from water and human serum samples in pH=5 by USA-D-µ-SPE procedure. The ionic liquid of [OMIM] [PF6] was dispersed in samples for separating of MWCNTs-DJKA from liquid phase. The adsorption capacity of the MWCNTs-DJKA and MWCNTs sorbent was achieved 122.6 mg g^{-1} and 33.7 mg g^{-1} for 20 min, respectively. The mean aluminum in drinking water and serum samples was obtained 48.56 ± 2.92 and 11.64 ± 0.73 µg L^{-1} which was lower than reference value in drinking water and human biological samples. The methodology was validated with SRM and ICP-MS analyzer.

5. Acknowledgment

The authors are thank to the Iranian Petroleum Industry Health Research Institute and IAUPS for preparation human serum samples based on the world medical association declaration of Helsinki (R.IAU.SN.1396.944000978).

6- References

[1]C. Exley, Human exposure to aluminium, Environ. Sci. Process. Impacts., 15 (2013) 1807-1816.

[2] G. Bassioni, F.S. Mohammed, E. Al Zubaidy, I. Kobrsi, Risk assessment of using aluminum foil in food preparation, Int. J. Electrochem. Sci., 5 (2012) 4498-4509.

[3] C. Grassie, V.A. Braithwaite, J. Nilsson, T.O. Nilsen , H.C. Teien, S.O. Handeland, S.O. Stefansson , V. Tronci, M. Gorissen, G. Flik, L.O. Ebbesson, Aluminum exposure impacts brain plasticity and behavior in Atlantic salmon (Salmo salar), J. Exp. Biol., 216 (2013) 3148-55.

[4] M. Ogawa, F. Kayama. A study of the association between urinary aluminum concentration and pre-clinical findings among aluminum-handling and non-handling workers, J. Occup. Med. Toxicol., 10 (2015) 13.

[5] C. Exley, what is the risk of aluminium as a neurotoxin, Expert rev. Neurother., 14 (2014) 589–591.

[6] M. Jaishankar, T. Tseten, N. Anbalagan, B.B. Mathew, K.N. Beeregowda, Toxicity mechanism and health effects of some heavy metals. Interdiscip. Toxicol., 2 (2014) 60-72.

[7] L.H. Shaaban, H.H. Zayet, H.H. Aboufaddan, S.A. Elghazally, Respiratory hazards: clinical and functional assessment in aluminum industry workers, Egypt. J. Chest. Dis. Tuberc., 2 (2016) 537-543.

[8] G. Switkes, Foiling the aluminum industry: A toolkit for communities, activists, consumers, and workers, Int. Rivers. Network., Berkeley,

CA 2005.
[9] C.V. Ieggli, D.Bohrer, P.C. do Nascimento, L.M. de Carvalho, L.A. Gobo, Determination of aluminum, copper and manganese content in chocolate samples by graphite furnace atomic absorption spectrometry using a microemulsion technique, J. Food. Compost. Anal., 3 (2011) 465-468.
[10] L.B. Santos, M.T. de Souza, A.T. Paulino, E.E. Garcia, E.M. Nogami, J.C. Garcia, N.E. de Souza. Determination of aluminum in botanical samples by adsorptive cathodic stripping voltammetry as Al-8-hydroxyquinoline complex, J. Microchem., 112 (2014) 50-55.
[11] E.J. Santos, E.B. Fantin, R.E. Paixão, A.B. Herrmann, R.E. Sturgeon. Spectrophotometric determination of aluminium in hemodialysis water, J. Braz. Chem. Soc., 11 (2015) 2384-2388.
[12]. A. Zioła-Frankowska, J. Kuta, M. Frankowski Application of a new HPLC-ICP-MS method for simultaneous determination of Al3+ and aluminium fluoride complexes, Heliyon, 2 (2015) e00035.
[13] M.H. Negaoka, T. Maitani, Speciation of aluminium in human serum investigated by HPLC/high resolution inductively coupled plasma mass spectrometry (HR-ICP-MS): Effects of sialic acid residues of the carbohydrate chain on the binding affinity of aluminium for transferrin, J. Health. Sci., 2 (2009) 161-8.
[14] T.S. Tsaya, Y.L. Huangb, W.C. Tsenga, Determination of aluminum, cadmium and lead in whole blood by Simultaneous atomic absorption spectrometry with oxygen charring, J. Chin Chem. Soc., 56 (2009) 135-41.
[15] R. Gajek, F. Barley, J. She, Determination of essential and toxic metals in blood by ICP-MS with calibration in synthetic matrix, J. Anal. Methods, 9 (2013) 2193-202.
[16] H. Shirkhanloo, H. Z. Mousavi and M. Mohamadi, In-vitro Aluminum Determination and Preconcentration in Blood of Dialysis Patients Based on Ionic Liquid Dispersive Liquid-Liquid Biomicroextraction by 2-Amino-3-(1H-imidazol-4-yl) propanoic Acid, J. Chin. Chem. Soc., 8 (2014) 921-928.
[17] A. Khaligh, H.Z. Mousavi, H. Shirkhanloo, A.M. Rashidi, Speciation and determination of inorganic arsenic species in water and biological samples by ultrasound assisted-dispersive-micro-solid phase extraction on carboxylated nanoporous graphene coupled with flow injection-hydride generation atomic absorption spectrometry, J. RSC. Adv., 113 (2015) 93347-59.
[18] H. Abdolmohammad-Zadeh and E. Rahimpour, CoFe2O4 nano-particles functionalized with 8-hydroxyquinoline for dispersive solid-phase micro-extraction and direct fluorometric monitoring of aluminum in human serum and water samples, J. Anal. Chim. Acta, 881 (2015) 54-64.
[19] S. Khazaeli, N. Nezamabadi, M. Rabani and H.A. Panahi, A new functionalized resin and its application in flame atomic absorption spectrophotometric determination of trace amounts of heavy metal ions after solid phase extraction in water samples, J. Microchem., 106 (2013) 147-153.
[20] NJ Simpson. Solid-phase extraction: principles, techniques, and applications. CRC press; 2000.
[21] H. Abdolmohammad-Zadeh, Z. Talleb, Dispersive solid phase micro-extraction of dopamine from human serum using a nano-structured Ni-Al layered double hydroxide, and its direct determination by spectrofluorometry, J. Microchim. Acta, 179 (2012) 25-32.
[22] C. Nethravathi, M. Rajamathi, Chemically modified graphene sheets produced by the solvothermal reduction of colloidal dispersions of graphite oxide, Carbon, 14 (2008) 1994-1998.
[23] G. Chen, S. Zhai, Y. Zhai, K. Zhang, Q. Yue, L. Wang, J. Zhao, H. Wang, J. Liu, J. Jia, Preparation of sulfonic-functionalized graphene oxide as ion-exchange material and its application into electrochemiluminescence analysis, J. Biosens. Bioelectron., 7 (2011) 3136-3141.

Anal. Method Environ. Chem. J. 3 (2) (2020) 92-107

AMECJ

Research Article, Issue 2
Analytical Methods in Environmental Chemistry Journal
Journal home page: www.amecj.com/ir

A new kinetic models analysis for CO adsorption on palladium zeolite nanostructure by roll-coating technique

Nastaran Mozaffari [a], Alireza Haji Seyed Mirzahosseini [a,*] and Niloofar Mozaffari [b]

[a] *Department of Environmental Engineering, Faculty of Natural Resources and Environment, Science and Research Branch, Islamic Azad University, Tehran, Iran*
[b] *Department of Physics, Faculty of Sciences, Science and Research Branch, Islamic Azad University, Tehran, Iran*

ARTICLE INFO:

Received 19 Feb 2020
Revised form 25 Apr 2020
Accepted 20 May 2020
Available online 30 Jun 2020

Keywords:
Carbon monoxide (CO),
Toxic gas analysis,
Adsorption,
Alumina palladium zeolite composite films,
Kinetic models

ABSTRACT

The aim of this article was the fabrication of *zeolite@Pd*/Al_2O_3 nanostructure through roll-coating technique for CO gas adsorption from air. Transmission electron microscopy (TEM), field-emission scanning electron microscopy (FESEM), X-ray diffraction (XRD), and energy-dispersive x-ray spectroscopy (EDX) were performed to investigate the morphological, structural, and elemental properties of *zeolite@Pd*/Al_2O_3 adsorbent. A continues carbon monoxide gas analyzer KIGAZ 210 was applied for analyzing of CO gas adsorption on as-present adsorbent in an experimental set-up. The adsorption capacity at equilibrium time for CO molecules was studied by *zeolite@Pd*/Al_2O_3 adsorbent. The Elovich, Avrami, and Fractional power kinetic models were used for this study. The equal value of experimental and theoretical adsorption capacity at equilibrium time as well as the unit value of regression coefficient was indicated that the Avrami kinetic model was the suitable model to describe CO removal from air through *zeolite@Pd*/Al_2O_3 nanostructure. The results showed us, the CO molecules were efficiently removed by catalytic zeolite adsorbent more than 95% from air at optimized conditions.

1. Introduction

The clean and high quality air is essential for human health. The main contributors to climate change belong to emission of toxic gases CO, CO_2, NO_x, So_x [1, 2]. Operations of industries and factories, transportation, agricultural activities and post/pre combustion of fuels are major reasons behind the emissions of CO and CO_2 in environment air. Carbon Monoxide (CO) as a main ecological pollutant, can be formed by incomplete burning of industrial fuels, automobiles and caused to a serious of symptoms including dizziness, naupathia and dyspnea [3, 4]. The acceptable limit of CO exposure has reported by ACGIH chemical substances [5]. The development of efficient and robust techniques for air purification has been boosting attention over the past few decades [6]. Among these techniques, the process of adsorption shows a fundamental surface phenomenon in which the attachment of solute (adsorbate) into a solid surface (adsorbent) can remove pollutants selectively from air atmosphere [6, 7]. According to the previous studies, some of toxic gases such as CO, CO_2, SO_2, O_3, VOC_s, etc., have more concentration in air [3]. Nowadays, excellent properties of nanomaterials such as high surface area and high adsorption

* Corresponding Author: Alireza Haji Seyed Mirzahosseini
Email: mirzahosseini@gmail.com
https://doi.org/10.24200/amecj.v3.i02.106

caused to use for air purification [8-10]. According to the most valence of equilibrium cycle, the cycle of adsorption/desorption process can be identified approximately when the adsorbent is started that the model of isotherm as fluctuation of temperature and or pressure can be applied for appraising of the maximum capacity of equilibrium axle. Moreover, the regeneration procedure can be estimated through adsorbents' recognizable characteristic like thermal behavior of electricity. Electric swing adsorption (ESA), moisture swing adsorption (MSA), temperature swing adsorption (TSA), and pressure swing adsorption (PSA), or techniques like temperature vacuum-pressure swing adsorption (TVPSA) that can be made by compilation of these above methods [11]. Pressure/Vacuum swing adsorption (PSA/VSA) and temperature swing adsorption (TSA) techniques was used for trapping of gas pollutions by above methods [12-15]. Carbon-based adsorbents such as activated carbons are commercially cheaper than other adsorbents, and also have known for toxic gas removal because of its useful properties such as eco-dependence, consistency of thermic and chemic, conductance of heat and electricity, or high resistance [16-19]. However, its disadvantages such as lack of low thermal and mechanical stability rather than other materials should not be ignored [6]. Recently, varieties of nonporous including metal-organic frameworks (MOFs) [20-23], mesoporous alumina (MA) [24, 25], and mesoporous silica (MS) [26,27] have been used for detection and adsorption of toxic gases, and are regarded as alternatives to commercial adsorbents [28,29]. Metal-organic frameworks (MOFs) are confirmed to be a significant adsorbent due to its unique properties such as large specific surface area, ultra-high porosities, controllable architectures, and low density [30, 31]. As an important factor, the porosity of MOFs can help to adsorb and desorbs micro molecules by providing a fast and handy path [32,33]. Although considerable fabricated and natural adsorbents such as activated carbon [26], fly ash [25], natural/modified clays [24], biomaterials [4], metal-organic-frameworks (MOFs) [23], zeolites [22,21], and nanomaterials [27] have been studied for a long period of time, there is still needs for advancements of adsorption technology and developing recyclable, cost-effective, high efficient adsorbents that have high capacity. Mesoporous alumina and other alumina-based substances have high adsorption capacity because of their interconnected channels, uniformed porous structures, and united pore size [34,35]. In particular, γ-Phase nano-Al_2O_3 is the best candidate for gas molecules capturing rather than other alumina phases known as "transition alumina" owing to its pore-volume, large surface area, and great catalytic activity [36, 37, 38]. The properties with high surface area and acidic surface make the gamma-alumina (γ-Al_2O_3) a unique material with extensive application ranging from adsorbents to heterogeneous catalysis [39-42]. The phases including δ-, η-, θ-, and γ - Al_2O_3 indicates one of various metastable stages (polymorphs) of alumina [39, 43, 44]. A higher CO adsorption and great capacity of adsorbents can be occurred by covering of the small particle size of Pd clusters on the Al_2O_3 surface [45]. The application of palladium is restricted due to its high material cost, even though there has been extensive investigation of nanopalladium or its alloy groups [46]. Therefore, in this study, nano-scale palladium II nitrate has used due to its similar unique and useful characteristics with palladium nanoparticles, and because of being cost-effective and easy to access compared to palladium. The mesoporous silicates are one of the promising kinds of nanoscale materials that become well-known for researchers due to their potential abilities and utilizations [47-53]. Several researchers have been reported the advantages of applying nanoscale zeolite (NPs) over micro-scale zeolite (MPs). [54-58] For example, according to results of comparing nano-scale (30-40 nm) and micro-scale (2000 nm) of H-ZSM-5 for its catalytic performance, it has found that the catalyst lifetime for H-ZSM-5 in nano-scale particles is longer than itself in micro-scale particles [58]. Synthesizing and utilizing nanosized zeolite attract great interests compared to zeolite with micron size, recently [54-62]. The properties of high external surface

area and high availability of active sites have been made nanoscale zeolites better catalytic proficiency and age of catalyst. Either a particular type of nanoadsorbents like CNTs [63,64], or some kinds of pollutants including heavy metal, antibiotic and so on [65, 66], or organic and inorganic pollutants removal [67] have totally been focused by most of recent review articles even though over 500 technical papers published between 2000 to 2019 indicate the rapid growth of interest in this research area. Hence, the current study concentrates on the adsorption of carbon monoxide as a toxic gas by nanomaterial based composite films. The present study's aim is firstly loading three nanoparticles γ-Al_2O_3, $Pd(NO_3)_2$ and zeolite on glass substrates through the roll-coating method, in order to enhance the span of reactions between CO gas molecules and adsorbents surface, and improve the ability of adsorbents for CO capturing. Then, the Elovich, the Avrami, and the Fractional power kinetic models for CO adsorption by zeolite@Pd/Al_2O_3 nanoadsorbent were studied and analyzed.

2. Experimental

2.1. Materials

Nanoshel chemicals was provided alumina nanoparticles (CASN: 1344-28-1, Molar mass: 101.96 g mol^{-1} γ-Al_2O_3 with purity >99.9%) and zeolite nanoparticles (CASN:1318-02-01, Al_2O_{34} SiO_2 H_2O with purity 99%). Merck chemicals and Sigma-Aldrich were two sources that 1-methyl-2-pyrrolidone and palladium nitrate ($Pd(NO_3)_2$) were bought from them, respectively. There were no needs for purification of received chemicals in order to use them.

2.2. Preparation of Adsorbent

The roll-coating technique has been used to deposit zeolite@Pd/Al_2O_3 as composite films on glass substrates. Four glass substrates (2 cm × 8 cm) were used in this study. Disinfectant materials such as acetone, ethanol and deionized water were consumed for washing glass substrates three times in an ultrasonic device. Then, the washed substrates dried at room temperature. As the process of samples preparation, firstly 1 g of Al_2O_3, 1 g of zeolite and 1 g of $Pd(NO_3)_2$ were mixed in a container, then 1-methyl-2-pyrrolidone was added dropwise into it as 10 mL in order to make the adhesion of materials on the substrates easy and stronger. After 1 day, the prepared coated substrates were desiccated at room temperature. Finally, a hollow cubic container was fabricated through attaching these four Al_2O_3/$Pd(NO_3)_2$/Zeolite coated substrates to each other whereby this tunnel-like shape helps CO gas molecules to be channeled and trapped readily [68]. In this case, the adsorption capacity and efficiency will be greatly affected by enhancing the rate of interaction between gas molecules and adsorbents.

2.3. Characterization

Transmission Electron Microscopy (TEM) was used in order to determine the shape and grain distribution of nanoparticles with high resolution. X-ray diffraction (XRD, STOE STADI MP) was applied for extracting the crystalline structure of pure initial materials. Topography and morphology of as-present adsorbent (before and after adsorption process) were determined through field emission scanning electron microscope (FESEM, MIRA3 TESCAN), while energy-dispersive X-ray spectroscopy (EDX) analysis was used in order to specify and measure chemical elemental contents of the sample.

2.4. Adsorption of CO

The schematic of designed experimental setup for testing CO adsorption consists of main three sections as a CO gas capsule, a compartment (20 cm length and 7 cm internal diameter) where an adsorbent is placed, and a carbon monoxide gas analyzer KIGAZ 210 (Sauermann Co, CO sensor protection by solenoid valve) based on tunable diode laser (TDL, LOD=1 ppm) for CO Measurement for detection of 1-120 ppm CO and evaluation of target gas (CO 99,999%) concentration [68]. The temperature of 0-250 °C (23-482 °F); optional (for probe installation) 0-600 °C (0-1112 °F) with additional thermal barrier was used. The constant pressure 1.5 bar was applied in this study. The

concentration of inlet CO gas and the saturation level of CO gas concentration were 150 mg L^{-1} and 5 mg L^{-1}, respectively.

2.5. Adsorption mechanism of CO by Zeolite@ Pd/Al_2O_3

Generally, movable and fixed bed are two types as classification of the adsorption/desorption by $Al_2O_3/Pd(NO_3)_2$/Zeolite. The molecules of gases like CO can attach to the adsorbent surface of $Al_2O_3/Pd(NO_3)_2$/Zeolite when the molecules of these gases achieve decreased free energy while the molecules come towards the surface of adsorbent. The value of CO molecules that come close to the surface of $Al_2O_3/Pd(NO_3)_2$/Zeolite adsorbent will be increased by decreasing of entropy that occurs by interplay between solid surface and CO molecules. The adsorption process based on van der Waals forces called physically adsorption, while chemical bond formation obtained between surface of $Al_2O_3/Pd(NO_3)_2$/Zeolite adsorbent and adsorbate. So, there are different mechanisms of physio-chemisorption for adsorption procedure which must be optimized. The MOFs' surface has several functional groups caused to act chemical reaction in mechanism adsorption [16]. In Order to achieve efficient elimination of CO, the adsorbent substance should possess some essential properties which are demonstrated as follow: 1) Since the proficiency of adsorption can specify how many adsorbents are required whereby the adsorption column's volume can be measured, it possesses high importance for determining the main cost of the adsorption mechanism. However, the value of adsorbent and size of equipment for adsorption process must be minimized due to high CO concentration. 2) The ratio of CO to another gas capacity shows the selectivity CO gas. 3) Another parameter for grading the adsorbents' efficiency is the kinetics of adsorption/desorption that the fast rate of adsorption/desorption kinetics for CO will be required by the adsorbents. The cycle of time will be controlled by processes of regeneration and the adsorption's kinetics that can form two types of curves that are a sharp breakthrough curve for CO which indicates a fast kinetics, and a budged breakthrough curve occurs if there is slow kinetics for CO. The transfer of mass through the surface of adsorbent, the functional group on the surface of adsorbent, and carbon monoxide's reaction kinetics can together influence on the kinetics of CO adsorption on the porous substances. 4) In order to keep high kinetics, it is necessary to have a property of the mechanical stability for adsorbent. 5) The demanded energy for regeneration of adsorbents should be measured. The range of -25 to -50 kJ mol^{-1} is allocated to heat of physisorption and chemisorption cases possess the heat of -60 to -90 kJ mol^{-1} [17]. Regarding the chemical adsorbents, physical adsorbents such as carbonaceous and non-carbonaceous substances need low energy desire for CO removal due to the no generation of new bonds between these gases and the adsorbents' surface whereby the regeneration of these gases requires less energy (Fig.1).

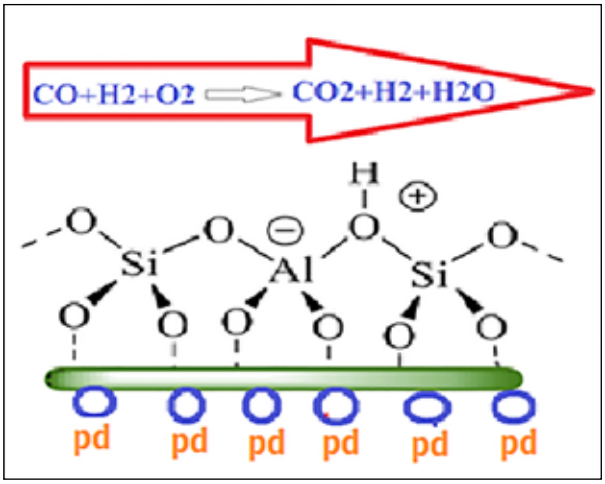

Fig.1. The adsorption mechanism of CO by zeolite@ Pd/Al_2O_3 adsorbent

3. Results and discussion

3.1. TEM analysis

Figure 2a demonstrates the results of TEM analysis of pure Al_2O_3 nanoparticles (γ-Al_2O_3) that three dimensional porous structure are made up by interconnected rod-like particles [69]. It is obviously shown that the shape of nanoparticles does not look accurately spherical [70]. The TEM for nanoparticles of zeolite and zeolite@Pd/Al_2O_3 was shown in Figure 2b and 2C, respectively.

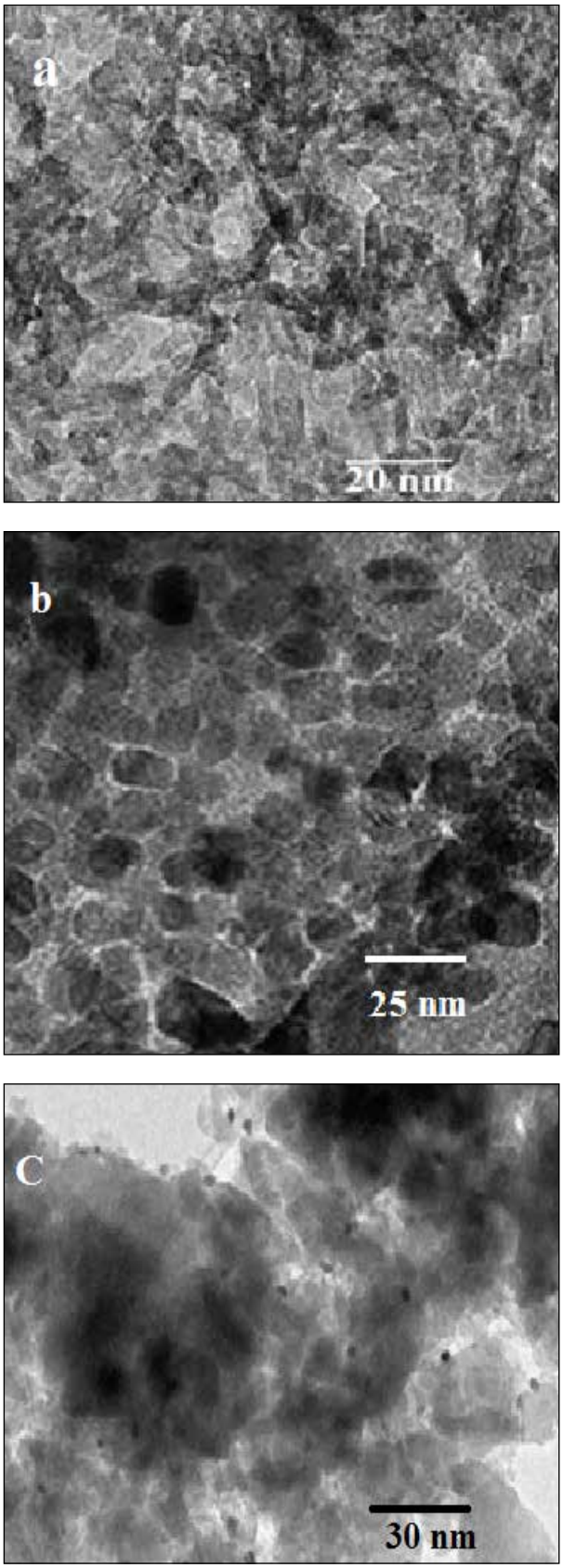

Fig. 2. The TEM for different nanoparticles **a)** γ-Al_2O_3 **b)** Zeolite **c)** Zeolite@Pd/Al_2O_3

3.2. XRD spectra

Figure 3 shows the XRD patterns of pure initial materials which are Al_2O_3, $Pd(NO_3)_2$ and zeolite. An X-ray diffractometer with Cu Kα source (λ = 1.5405 Å) and a scan step size of 0.01° was used for recording XRD patterns. The range of scanning (2θ) was recorded between 10° and 90°. As it is shown, the structure of pure zeolite nanoparticles is more crystalline than pure Al_2O_3 and $Pd(NO_3)_2$ nanoparticles that confirm an appropriate property of zeolite to have a high adsorption capacity due to its porosity. The diffraction peaks of the pure Al_2O_3 appeared at 2θ of 31.93°, 39.49°, 45.49° and 66.76° which are well distributed to the crystalline preferred orientation of 220, 222, 400 and 440, respectively. The peak positions of $Pd(NO_3)_2$ were considered as 24.079 and 68.08, which are corresponding to 011 and 220, respectively. The diffraction peaks 10.34, 16.56, 21.79, 29.39 and 31.58, corresponding to the reflection from 220, 212, 203, 451 and 002 are observed in zeolite nanoparticles. The characteristic peaks of pure zeolite are well matched and consistent with the corresponding peaks of all samples, and there are no other observed phases. [71] According to XRD patterns of pure zeolite, there is no considerable alteration in the framework and no lost in solid pure zeolite's crystallinity as well as the host frame stays intact at the end of the mechanism. [72] Al_2O_3 nanoparticles (Ref 00-029-0063), $Pd(NO_3)_2$ (Ref 00-005-0681 and 01-087-0643) and zeolite (Ref 01-080-0922) are in good agreement with the candidate references (Table 1). Regarding the fact that available commercial nanomaterials of γ-Al_2O_3 produced through boehmite thermal dehydration, thus determining the crystal structure of γ-Al_2O_3 is difficult as well as it indicates poor crystallinity and impurities. Also, this fact can include other alumina polymorphs that have similar crystal formations. The appropriate structure for analysis belongs to large, clean γ-Al_2O_3 single-crystals that typically cannot produced commercially. Oxidizing single-crystal NiAl (110) under appropriate-controlled conditions would make single-crystal γ-Al_2O_3 films with more than 80 nm thick able to be grown

Table 1. The obtained crystalline regions and peaks of the zeolite@Pd/Al_2O_3 composite film ($Al_2O_3/Pd(NO_3)_2$/zeolite) through XRD patterns[73]

Al_2O_3	**hkl**	**220**	**222**	**400**	**440**	
	2θ (Degree)	31.93°	39.49°	45.49°	66.76°	
$Pd(NO_3)_2$ 2 (Degree)	**hkl**	**011**	**-----**	**-----**	**220**	
	2θ (Degree)	24.079°	-----	-----	68.08°	
Zeolite 2 (Degree)	**hkl**	**220**	**212**	**203**	**451**	**002**
	2θ (Degree)	10.34°	16.56°	21.79°	29.39°	31.58°

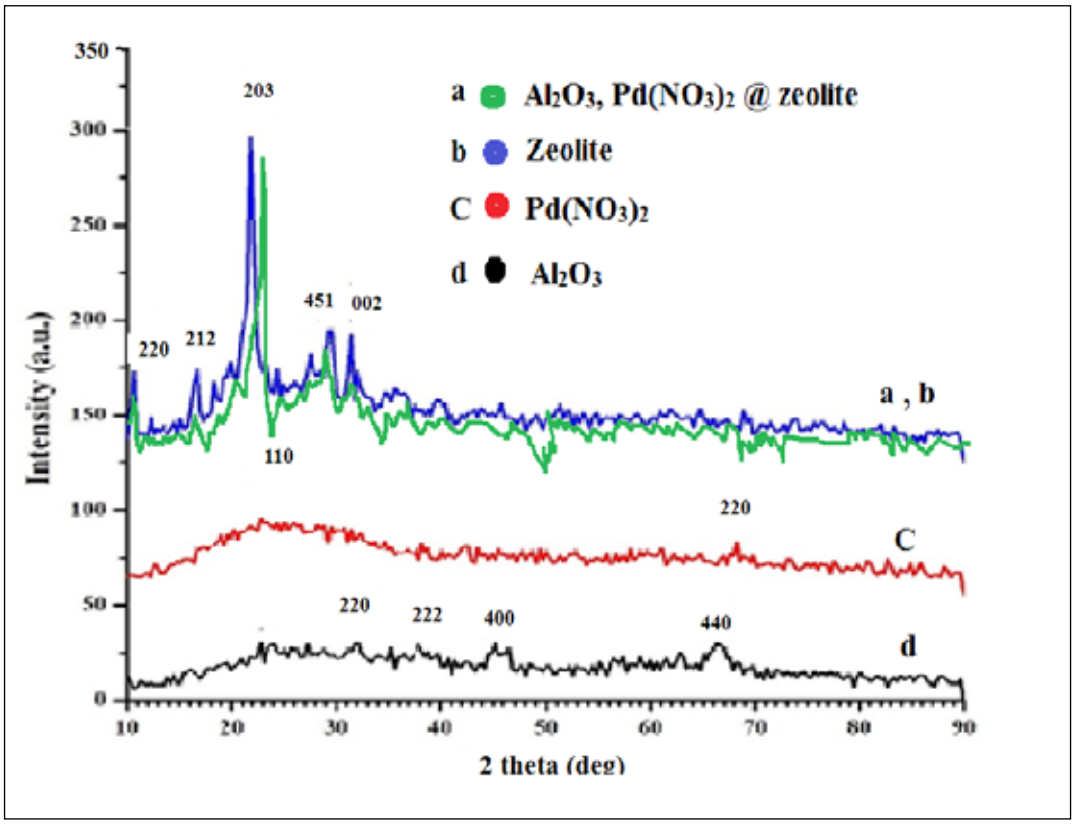

Fig. 3. The results of XRD analysis for pure initial materials including a) $Al_2O_3/Pd(NO_3)_2$/zeolite b) zeolite, c) $Pd(NO_3)_2$ and d) Al_2O_3 nanoparticles

which is demonstrated by Zhang et al which were worked on Al_2O_3 with γ-shape structure on Ni-Al. Since γ-Al_2O_3 fabricated by this technique is well crystalline and does not possess hydrogen or water in bulk structure, it is suitable for considered structural analysis, unlike the material boehmite-originated γ-Al_2O_3 [73].

3.3. FESEM spectra

The surface morphology, microstructure, particle size and distribution of the as-prepared product are determined by field emission scanning electron microscope (FESEM). Figure 4 indicates the FESEM images of the $Al_2O_3/Pd(NO_3)_2$/Zeolite sample at a 1 μm scale of magnification before

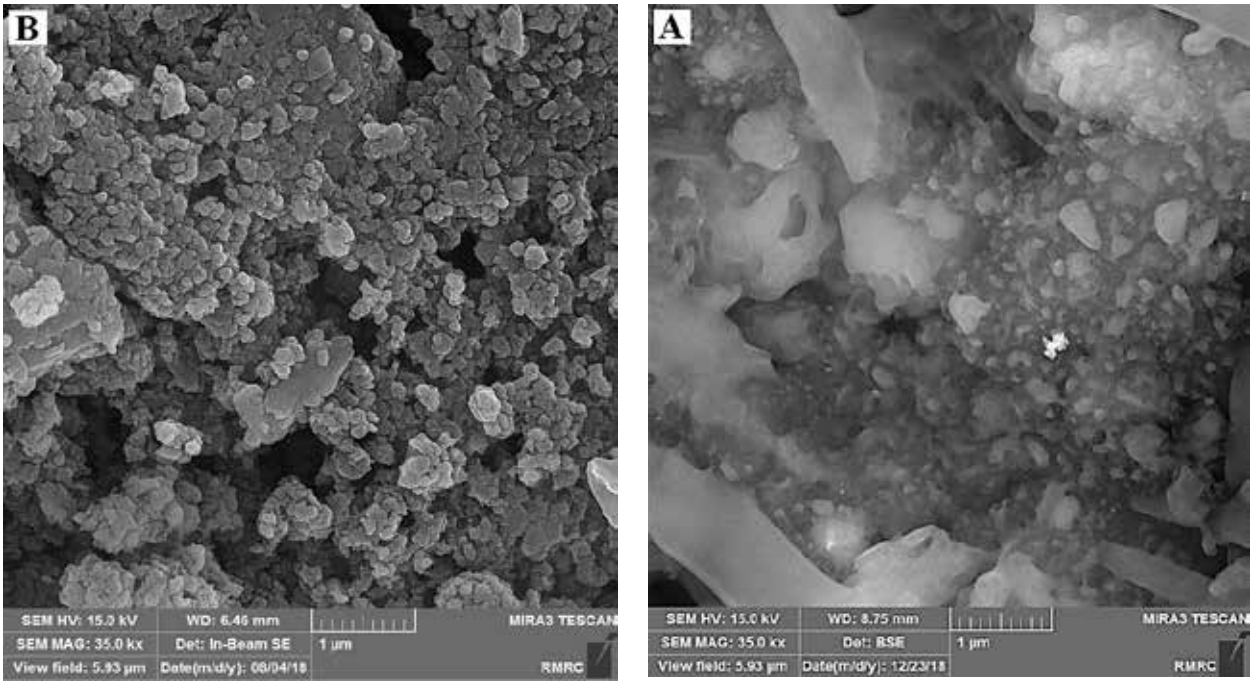

Fig. 4. Obtained images from FESEM of Al_2O_3/$Pd(NO_3)_2$/zeolite adsorbent a) Before b) after CO gas adsorption at 1 µm scales of magnification.

and after CO gas adsorption. The FESEM results revealed that the united porous structures along with regular interlinked channels are developed throughout the adsorbents after adsorption. Also, homogenous dispersion and well particle size repartition of adsorbent after the adsorption process make it incomparable than its virgin version. Hence, a high surface area and whereby a very high CO adsorption is noticed because of these properties.

3.4. Energy-dispersive X-ray spectroscopy

The percentage of elemental content was determined by energy-dispersive X-ray spectroscopy (EDX). Figure 5 illustrates the existence of Al, O, Si, Pd, and N in the sample before the adsorption process that was utilized to fabricate as-present adsorbent. Since Al_2O_3 and zeolite (aluminum silicates) nanoparticles were used in this study, a notable increase in the spectral position of Al EDX peak is observed. The weight and atomic percentages of ingredients are extracted from EDX patterns of virgin adsorbent that include Al, O, Pd, N, and Si at wt.% for each element. (Table 2) The peak of Ca corresponds to glass substrates.

3.5. Kinetic models analysis

The inlet CO gas concentration into an experimental set-up considered as 150 mg L^{-1}. The evaluation of various concentrations of adsorbed CO versus time for Al_2O_3/$Pd(NO_3)_2$/Zeolite adsorbent's results indicates the increase of adsorbed CO concentration (mg L^{-1}) with passing time until reaching saturation levels [68]. The relation between adsorbed CO gas concentration and contact time was illustrated in Figure 6. This diagram indicated the effect of passing time on the speed of CO adsorption that becomes slower while time is reaching saturation level. As it is obvious, the adsorbed CO gas concentration is decreased as range of 150-70, 69-11 and 10-5 mg L^{-1} at rate of 1 s, 2 s and 3 s, respectively.

Table 2. Statistical analysis EDX results of Al_2O_3/$Pd(NO_3)_2$/zeolite with its atomic and weight values.

Elements	Al K_a	O K_a	Pd K_a	N K_a	Si K_a	Ca K_a
wt.%	8.21	26.46	45.01	0.53	1.62	0.48
at%	7.78	42.33	10.83	0.59	1.47	0.31

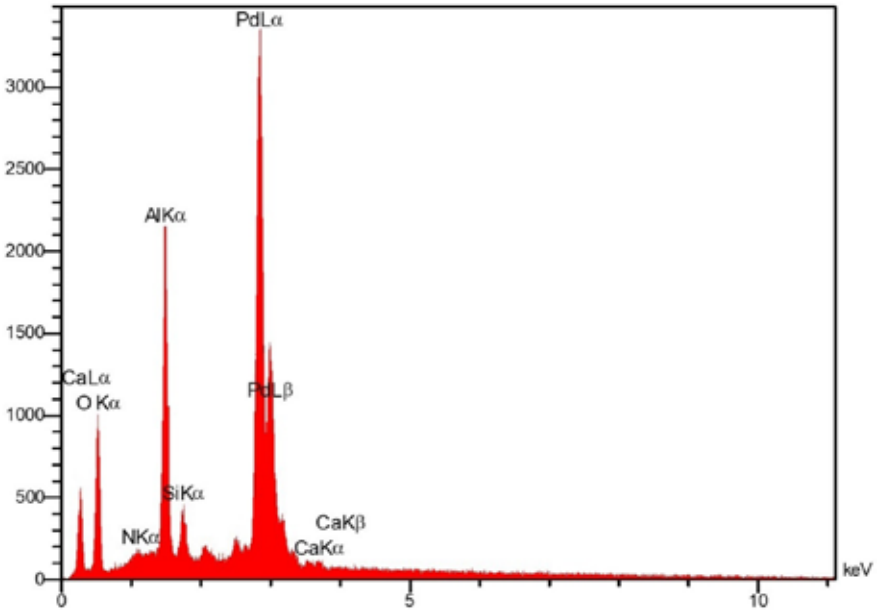

Fig. 5. EDX patterns of the made $Al_2O_3/Pd(NO_3)_2$/zeolite adsorbent

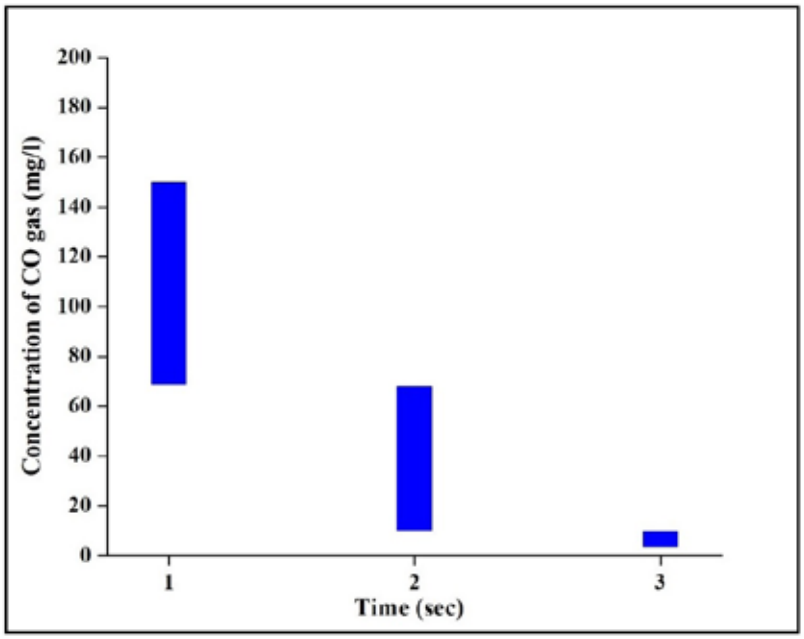

Fig. 6. The diagram of relation between adsorbed CO gas concentration and contact time (mg L^{-1}, sec)

To explore the chemisorption kinetic of gases onto a solid surface, Elovich kinetic model is describe [74, 75]. The Elovich kinetic introduced in Equation 1 [76].

$$q_t = \frac{1}{\beta} Ln(\alpha\beta) + \frac{1}{\beta} \mathrm{Ln}\, t \qquad \text{(Eq. 1)}$$

Where q_t is adsorption capacity at time t (mg g^{-1}), the Elovich coefficient α in the primary rate of adsorption (mg g^{-1} min^{-1}), and the Elovich coefficient β is desorption rate constant (g mg^{-1}) that is associated to the extent of energy activation as well as surface covering for chemisorption process.

The amount of α and β are obtained from intercept (β^{-1} Ln(αβ)) and slope (β^{-1}) of q_t vs. Ln t linear plot (Fig. 7). It should be noted that the number of remained sites after adsorption process can be specified by the value of β^{-1}, and adsorption quantity in Ln t = 0. It can be shown by β^{-1} Ln(αβ) value that the closeness of this value with experimental value indicates the best fitting of kinetic data to the Elovich model [77], however, in this research work, the values have significant difference. The obtained parameters were listed in Table 3. Regarding Mozaffari et al. 2020 [68], the amount of experimental equilibrium adsorption capacity at 216 s is 111.16 mg. g^{-1} that is not in agreement with the theoretical adsorption capacity at equilibrium time calculated through this model. The low regression coefficient (R^2) value and unequal value of $q_{e.exp}$ as well as $q_{e.cal}$ demonstrate the scantiness Elovich model of for description of CO removal by $Al_2O_3/Pd(NO_3)_2$/Zeolite nano-adsorbent.

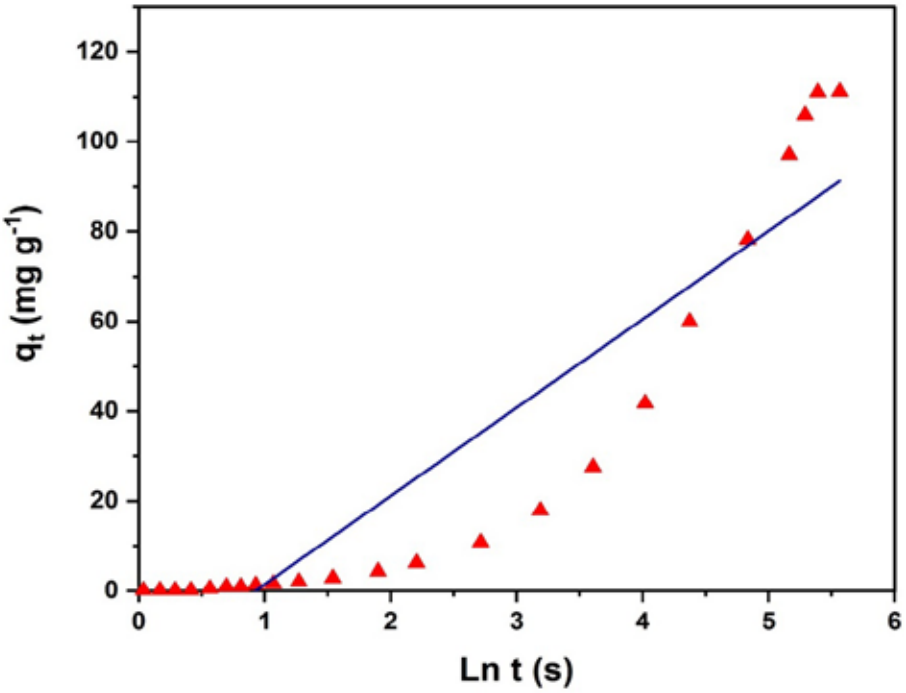

Fig. 7. The Elovich kinetic model for carbon monoxide adsorption by $Al_2O_3/Pd(NO_3)_2$/Zeolite nano-adsorbent

Table 3. The calculated parameters of the Elovich, Avrami, and Fractional power kinetic models

$q_{e,exp}$ (mg.g^{-1})		111.16		[99]	
Elovich Model		**Avrami Model**		**Fractional Power Model**	
$q_{e,cal}$	91.94	$q_{e,cal}$	111.16	$q_{e,cal}$	129.93
α	٣,٥	k_{AV}	4.54	k	1.048
β	٠,٠٣٦	n_{AV}	1.12	v	0.896
β^{-1}	28.096	R^2	0.99	R^2	0.98
β^{-1} [Ln(αβ)]	58.29				
R^2	0.85				

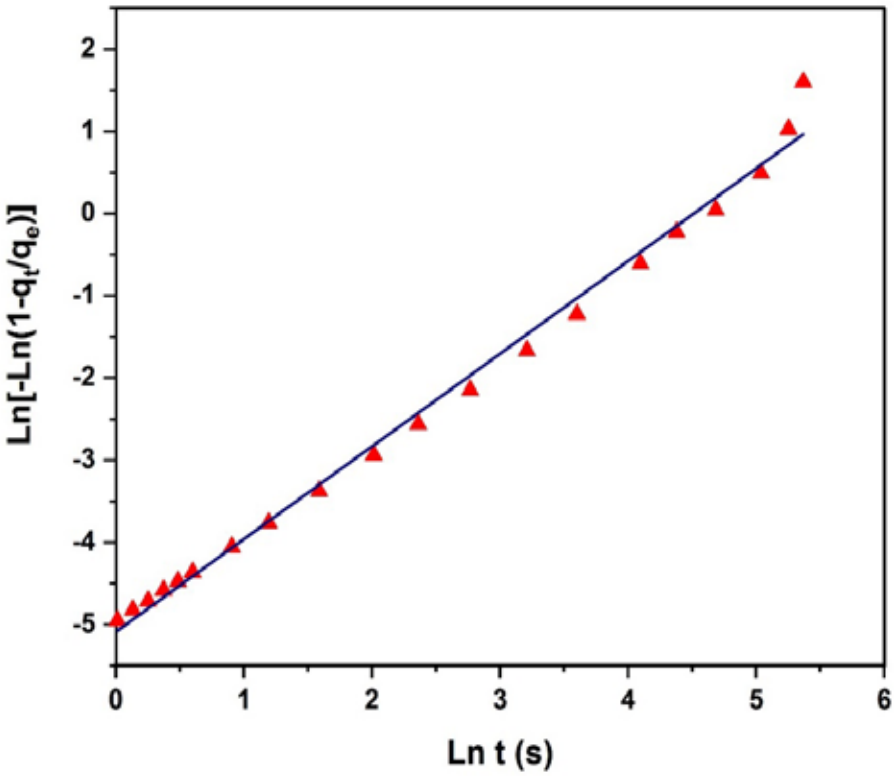

Fig. 8. The Avrami kinetic model for carbon monoxide adsorption by Al_2O_3/$Pd(NO_3)_2$/Zeolite nano-adsorbent

For simulation of phase transition as well as the growth of crystallite in adsorbent, Avrami kinetic model is investigated [78]. The Avrami kinetic is expressed in equation 2 [79]:

$$Ln\left[Ln\left(1-\frac{q_t}{q_e}\right)\right] = n_{AV}k_{AV} + n_{AV}Ln\ t \quad \textbf{(Eq. 2)}$$

Where K_{AV} is the Avrami kinetic constant, the n_{AV} is the Avrami exponent to hypothesize the mechanism of alteration during the process of adsorption [109]. The amount of K_{AV} and n_{AV} are acquired from intercept and slope of $Ln[-Ln\left(1-\frac{q_t}{q_e}\right)]$ vs. Ln linear plot.

Figure 8 demonstrates the plot of $Ln[-Ln\left(1-\frac{q_t}{q_e}\right)]$ versus. The regression coefficient (R^2) is close to unity that shows the best fit of data. The value of theoretical adsorption capacity at (equilibrium time) was obtained as 111.16 mg g^{-1} that is match with the experimental equilibrium adsorption capacity which was reported by Mozaffari et al 2020 [68]. Table 3 gives the calculated parameters of this model. Therefore, the unit value of R^2 and identical value of and indicate the best applicability of Avrami kinetic model to describe carbon monoxide adsorption through $Al_2O_3/Pd(NO_3)_2$/Zeolite nano-adsorbent.

The modified form of the Freundlich equation is Fractional power model [80]. Fractional power kinetic model is defined as equation 3 [110].

$$Lnq_t = Ln\ k + vLn\ t \quad \textbf{(Eq. 3)}$$

Where k and v are constants and v should be less than unity. The sorption rate at is defined as kv [80]. The plot of versus is demonstrated in Figure 9. The amount of k and v are obtained from intercept (Ln k) and slope (v) of vs. linearplot.

The calculated constants are tabulated in Table 3. The value of v was obtained as 0.89 that is positive and less than unity and regression coefficient (R^2)

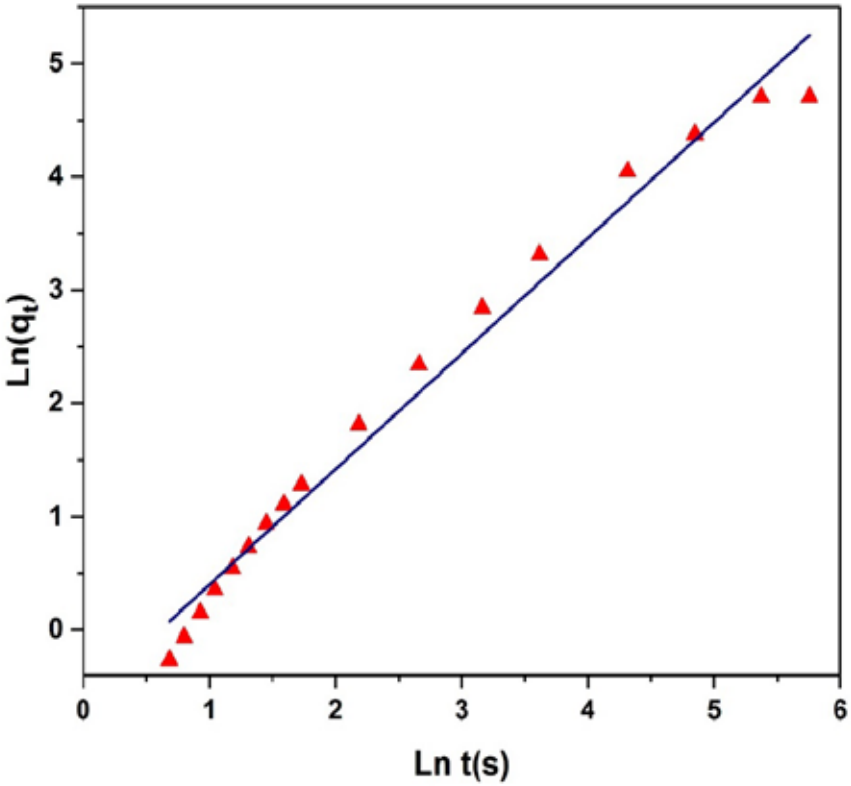

Fig. 9. The Fractional power kinetic model for carbon monoxide adsorption by $Al_2O_3/Pd(NO_3)_2$/Zeolite nano-adsorbent

is almost close to unity. However, experimental adsorption capacity at equilibrium time that was obtained by [99] is not in a good agreement with calculated adsorption capacity. Thus, this model is not sufficient to describe carbon monoxide by $Al_2O_3/Pd(NO_3)_2$/Zeolite nano-adsorbent.

4. Conclusions

In this article, $Al_2O_3/Pd(NO_3)_2$/zeolite adsorbent was prepared by roll coating method to investigate its ability to remove CO gas. It was shown that the effect of passing time on the speed of CO adsorption that becomes slower while time is reaching saturation level. To study the kinetic models for CO removal through this adsorbent, the Elovich, Avrami, and Fractional power kinetic models were explored. The investigation of Avrami kinetic model illustrated that the experimental and theoretical adsorption capacity value at equilibrium time was identical. Furthermore, the regression coefficient value (R^2) was close to unity. Therefore, the Avrami kinetic model was the best model to describe CO removal through $Al_2O_3/Pd(NO_3)_2$/zeolite adsorbent. The porous structure of $Al_2O_3/Pd(NO_3)_2$/zeolite adsorbent which was obtained from FESEM analysis is responsible for high values of adsorption efficiency and adsorption capacity. The result of XRD patterns of pure initial materials was applied to confirm their purity and crystalline structures. Elemental content of materials of adsorbent before adsorption was specified by EDX analysis to show the existence of Al, O, Pd, Si, N and Ca that the last one was referred to glass substrates.

5. Acknowledgement

This study was carried out in Natural Recourses College Lab, Environment Science and Research Department.

6. References

[1] J. Cleland, World population growth; past, present and future, Environ. Res. Econ., 55 (2013) 543–554.

[2] M. Hussain, G. Liu, B. Yousaf, R. Ahmed, F. Uzma, M. U. Ali, H. Ullah, A. R. Butt, Regional and sectoral assessment on climate-change in Pakistan: Social norms and indigenous perceptions on climate-change adaptation and mitigation in relation to global context, J. Clean. Prod., 200 (2018) 791–808.

[3] S, Mahajan. S, Jagtap, Metal-oxide semiconductors for carbon monoxide (CO) gas sensing. Materials. Rev., 18 (2020) 100483.

[4] C. Qin, B. Wang, N. Wu, C. Han, C. Wu, X. Zhang, Q. Tian, S. Shen, P. Li, Y. Wang, Metal-organic frameworks derived porous Co_3O_4 dodecahedrons with abundant active Co^{3+} for ppb-level CO gas sensing, Appl. Surf. Sci., 506 (2019) 144900.

[5] ACGIH Chemical Substances TLV Committee, Notice of intended change - carbon monoxide, Appl. Occup. Environ. Hyg., 6 (1991) 621–624.

[6] A. M. Awad, R. Jalab, A. Benamor, M. S. Naser, M. M. Ba-Abbad, M. El-Naas, A. W. Mohammad, Adsorption of organic pollutants by nanomaterial-based adsorbents: An overview. J. Mol. Liq., 301 (2019) 112-335.

[7] M. N. Rashed, Adsorption technique for the removal of organic pollutants from water and wastewater, Organic Pollutants-Monitoring, Risk and Treatment, Intech. Open, (2013) 167-194.

[8] P. K. Gautam, A. Singh, K. Misra, A. K. Sahoo, S. K. Samanta, Synthesis and applications of biogenic nanomaterials in drinking and wastewater treatment, J. Environ. Manage., 231 (2019) 734–748.

[9] C. Santhosh, V. Velmurugan, G. Jacob, S. K. Jeong, A. N. Grace, A. Bhatnagar, Role of nanomaterials in water treatment applications: A review, Chem. Eng. J., 306 (2016) 1116– 1137.

[10] Y. Zhang, B. Wu, H. Xu, H. Liu, M. Wang, Y. He, B. Pan, Nanomaterials-enabled water and wastewater treatment, Nano Impact, 3 (2016) 22–39.

[11] R. Zhao, S. Deng, S. Wang, L. Zhao, Y. Zhang, B. Liu, H. Li, Z. Yu, Thermodynamic research of adsorbent materials on energy efficiency of vacuum pressure swing adsorption cycle for CO capture, Appl. Thermal Eng., 128 (2018) 818–829.

[12] K. T. Chue, J. N. Kim, Y. J. Yoo, S. H. Cho, R. T. Yang, Comparison of activated carbon and zeolite 13X for CO_2 recovery from flue gas by pressure swing adsorption, Ind. Eng. Chem. Res., 2 (1995) 591– 598.

[13] R, Krishna, Adsorptive separation of CO_2/CH_4/CO gas mixtures at high pressures, Micropor. Mesopor. Mater., 156 (2012) 217–223.

[14] M. Clausse, J. Bonjour, F. Meunier, Adsorption of gas mixtures in TSA adsorbers under various heat removal conditions, Chem. Eng. Sci., 17 (2004) 3657–3670.

[15] J.-R. Li, R. J. Kuppler, H. C. Zhou, Selective gas adsorption and separation in metal–organic frameworks, Chem. Soc. Rev., 5 (2009) 1477.

[16] M., Bui, C. S. Adjiman, A. Bardow, E. J. Anthony, A. Boston, S. Brown, et. Al., Carbon capture and storage (CCS): the way forward, Energ. Environ. Sci., 5 (2018) 1062–1176.

[17] A. Samanta, A. Zhao, G. K. H. Shimizu, P. Sarkar, R. Gupta, Post combustion CO_2 capture using solid sorbents: a review, Ind. Eng. Chem. Res., 4 (2011) 1438–1463.

[18] D. Lozano-Castelló, D. Cazorla-Amorós, A. Linares-Solano, D. F. Quinn, Activated carbon monoliths for methane storage: influence of binder, Carbon, 15 (2002) 2817–2825.

[19] P. Bilalis, D. Katsigiannopoulos, A. Avgeropoulos, G. Sakellariou,

Noncovalent functionalization of carbon nanotubes with polymers, RSC Adv., 6 (2014) 2911– 2934.
[20] Y. K. Mishra, R. Adelung, ZnO tetrapod materials for functional applications, Mater. Today, 21 (2018) 631-651.
[21] X. Wang, W. Tian, T. Zhai, C. Zhi, Y. Bando, D. Golberg, Cobalt (II, III) oxide hollow structures: fabrication, properties and applications, J. Mater. Chem., 22 (2012) 23310-23326.
[22] N. S. Bobbitt, M. L. Mendonca, A. J. Howarth, T. Islamoglu, J. T. Hupp, O. K. Farha, R. Q. Snurr, Metal–organic frameworks for the removal of toxic industrial chemicals and chemical warfare agents, Chem. Soc. Rev., 46 (2017) 3357-3385.
[23] D. Britt, D. Tranche Montagne, O. M. Yaghi, Metal–organic frameworks with high capacity and selectivity for harmful gases, Proc. Natl. Acad. Sci., 105 (2008) 11623–1162.
[24] S. E. Lehman, S. C. Larsen, Zeolite and mesoporous silica nanomaterials: greener syntheses, environmental applications and biological toxicity, Environ. Sci. Nano, 1 (2014) 200-213.
[25] N. Moitra, P. Trens, L. Raehm, J.O. Durand, X. Cattoen, M. Wong Chi Man, Facile route to functionalized mesoporous silica nanoparticles by click chemistry, J. Mater. Chem., 21 (2011) 13476-13482.
[26] C. Yeom, Y. Kim, Mesoporous alumina with high capacity for carbon monoxide adsorption, Korean J. Chem. Eng., 35 (2017) 587–593.
[27] A. Walcarius, L. Mercier, Mesoporous organosilicon adsorbents: Nano engineered materials for removal of organic and inorganic pollutants, J. Mater. Chem., 20 (2010) 4478–4511.
[28] C. Yeom, R. Selvaraj, Y. Kim, Preparation of nonporous alumina using aluminum chloride via precipitation templating method for CO adsorbent, J. Ind. Eng. Chem., 67 (2017) 132-139.
[29] Z. Li, J.C. Barnes, A. Bosoy, J.F. Stoddart, J.I. Zink, Mesoporous silica nanoparticles in biomedical applications, Chem. Soc. Rev., 41 (2012) 2590–2605.
[30] T. Kitao, Y. Zhang, S. Kitagawa, B. Wang, T. Uemura, Hybridization of MOFs and polymers, Chem. Soc. Rev., 46 (2017) 3097–348.
[31] X. Lian, Y. Fang, E. Joseph, Q. Wang, J. Li, S. Banerjee, C. Lollar, X. Wang, H. Zhou, Enzyme-MOF (metal-organic framework) composites, Chem. Soc. Rev., 46 (2017) 3386-3401.
[32] L. Peng, J. Peng, Z. Xue, B. Han, J. Li, G. Yang, Large-pore mesoporous Mn_3O_4 crystals derived from metal-organic frameworks, Chem. Commun., 49 (2013) 11695-11697.
[33] R. K. Bhakta, J. L. Herberg, B. Jacobs, A. Highley, R. B. Jr, N. W. Ockwig, J. A. Greathouse, M. Alendorf, Metal-organic frameworks as templates for nanoscale NaAlH4, J. Am. Chem. Soc., 131 (2009) 13198–13199.
[34] S. Rengaraj, Y. Kim, J-W. Yeon, W-H. Kim, Application of Mg-mesoporous alumina prepared by using magnesium stearate as a template for the removal of nickel: kinetics, isotherm, and error analysis, Ind. Eng. Chem. Res., 46 (2007) 2834-2842.
[35] L. Dejam, S. Solaymani, A. Achour, S. Stach, S. Talu, N. Beryani Nezafat, V. Dalouji, A.A. Shokri, A. Ghaderi, Correlation between surface topography, optical band gaps and crystalline properties of engineered AZO and CAZO thin films, Chem. Phys. Lett., 719 (2019) 78-90.
[36] P. Souza Santos, H. Souza Santos, S.P. Toledo, Standard transition alumina. Electron microscopy studies, Mat. Res., 3 (2000) 104-114.

[37] M. Macêdo, C. Bertran, C. Osawa, Kinetics of the γ → α -alumina phase transformation by quantitative X-ray diffraction, J. Mater. Sci., 42 (2007) 2830–2836.

[38] C.H., Shek, J.K.L. Lai, T.S. Gu, G.M. Lin, Transformation evolution and infrared absorption spectra of amorphous and crystalline nano-Al_2O_3 powders, Nanostruct. Mater., 8 (1997) 605-610.

[39] J.L. Peng, L.D. Lai, X. Jiang, W.J. Jiang, B. Lai, Catalytic ozonation of succinic acid in aqueous solution using the catalyst of Ni/Al_2O_3 prepared by electroless plating-calcination method, Sep. Purif. Technol,. 195(2018) 138–148.

[40] N. Mozaffari, N. Mozaffari, S. M. Elahi, S. Vambol, V. Vambol, N. A. Khan, N. Khan, Kinetics study of CO molecules adsorption on Al_2O_3/Zeolite composite films prepared by roll-coating method, Surface Engineering. (2020) 1-10. https://doi.org/10.1080/02670844.2020.1768628

[41] M. Trueba, S.P. Trasatti, γ-Alumina as a support for catalysts: a review of fundamental aspects, Eur. J. Inorg. Chem., 17 (2005) 3393-3403.

[42] G. Busca, The surface of transitional aluminas: a critical review, Catal. Today, 226 (2014) 2-13.

[43] I. Levin, D. Brandon, Metastable alumina polymorphs: crystal structure and transition sequences, J. Am. Ceramic Soc., 81 (1998) 1995-2012.

[44] N. Mozaffari, S. Solaymani, A. Achour, S. Kulesza, M. Bramowicz, N. B. Nezafat, Ş. Ţălu, N. Mozaffari, S. Rezaee, New insights into SnO_2/Al_2O_3, Ni/Al_2O_3, and $SnO_2/Ni/Al_2O_3$compositefilms for CO adsorption: building a bridge between microstructures and adsorption properties, J. Phys. Chem. C, 124 (2020) 3692–3701.

[45] I. W. Davies, L. Matty, D. L. Hughes and P. J. Reider, Are heterogeneous catalysts precursors to homogeneous catalysts, Chem. Soc., 123 (2001) 10139-10140.

[46] I. Saldan, Y. Semenyuk, I. Marchuk, O. Reshetnyak, Chemical synthesis and application of palladium nanoparticles, J. Mater. Sci., 50 (2015) 2337-2354.

[47] N. Ono, The Nitro Group in Organic Synthesis; Wiley-VCH: Weinheim, 392, (2001). https:/doi: 10.1021/op010046s.

[48] G. Yan, M. Yang, Recent advances in the synthesis of aromatic nitro compounds. Org. Biomol. Chem., 11 (2013) 2554-2566.

[49] P. LaBeaume, M. Placzek, M. Daniels, I. Kendrick, P. Ng, M. McNeel, R. Afroze, A. Alexander, R. Thomas, A. E. Kallmerten, G. B. Jones, Microwave-accelerated fluorodenitrations and nitrodehalogenations: expeditious routes to labeled PET ligands and fluoropharmaceuticals, Tetrahedron Lett., 51 (2010) 1906-1909.

[50] X.-F. Wu, J. Schranck, H. Neumann, M. Beller, Convenient and mild synthesis of nitroarenes by metal-free nitration of arylboronic acids, Chem. Commun., 47 (2011) 12462-12463.

[51] J. P. Das, P. Sinha, S. Roy, A Nitro-Hunsdiecker Reaction: From Unsaturated Carboxylic Acids to Nitrostyrenes and Nitroarenes, Org. Lett., 4 (2002) 3055-3058.

[52] J. J. Song, J. T. Reeves, F. Gallou, Z. Tan, N. K. Yee, C. H Senanayake, Organometallic methods for the synthesis and functionalization of azaindoles, Chem. Soc. Rev., 36 (2007) 1120-1132.

[53] S. Mohan, P. Dinesha, S. Kumar, NOx reduction behaviour in copper zeolite catalysts for ammonia SCR systems: A review, Chem. Eng. J., 384 (2019) 123253.

[54] L. Tosheva, V.P. Valtchev, Nanozeolites: synthesis, crystallization mechanism, and applications, Chem. Mater., 17 (2005) 2494-2513.

[55] G. T. Vuong, V. T. Hoang, D. T. Nguyen, T. O. Do, Synthesis of nanozeolites and nanozeolite-based FCC catalysts, and their catalytic activity in gas oil cracking reaction, Appl. Catal. A, 382 (2010) 231-239.

[56] H. Konno, T. Okamura, T. Kawahara, Y. Nakasaka, T. Tago, T. Masuda, Kinetics of n-hexane cracking over ZSM-5 zeolites – Effect of crystal size on effectiveness factor and catalyst lifetime, Chem. Eng. J., 207–208 (2012) 490-496.

[57] T. Tago, H. Konno, Y. Nakasaka, T. Masuda, Size-controlled synthesis of nano-zeolites and their application to light olefin synthesis, Catal. Surv. Asia, 16 (2012) 148-163.

[58] T. Tago, H. Konno, M. Sakamoto, Y. Nakasaka, T. Masuda, Selective synthesis for light olefins from acetone over ZSM-5 zeolites with nano-and macro-crystal sizes, Appl. Catal., A, 403 (2011) 183-191.

[59] K. Na, C. Jo, J. Kim, K. Cho, J. Jung, Y. Seo, R.J. Messinger, B.F. Chmelka, R. Ryoo, Directing Zeolite Structures into Hierarchically Nanoporous Architectures, Sci., 333 (2011) 328-332.

[60] J. He, D. Chen, N. Li, Q. Xu, H. Li, J. He, J. Lu, Controlled fabrication of mesoporous ZSM-5 Zeolite-supported PdCu alloy nanoparticles for complete oxidation of toluene, Appl. Catal. B: Environ., 265 (2019) 118560. http://doi: 10.1016/j.apcatb.2019.118560.

[61] S. van Donk, A.H. Janssen, J.H. Bitter, K.P. de Jong, Generation, characterization, and impact of mesopores in zeolite catalysts, Catal. Rev., 45 (2003) 297-319.

[62] R. Chun, S. Kim, S. H. Han, A. K. Pandey, N. K. Mishra, I. S. Kim, Site-selective C−H nitration of *N*-aryl-7-azaindoles under palladium(II) catalysis, Tetrahedron Lett., 59 (2018) 3848-3852.

[63] S. Zhang, T. Shao, The impacts of aggregation and surface chemistry of carbon nanotubes on the adsorption of synthetic organic compounds, Environ. Sci. Technol., 43 (2009) 5719-5725.

[64] V. Sabna, S.G. Thampi, S. Chandrakaran, Adsorption of crystal violet onto functionalised multi-walled carbon nanotubes: Equilibrium and kinetic studies, Ecotoxicol. Environ. Saf., 134 (2016) 390–397.

[65] H. Anjum, K. Johari, N. Gnanasundaram, M. Ganesapillai, A. Arunagiri, I. Regupathi, M. Thanabalan, A review on adsorptive removal of oil pollutants (BTEX) from wastewater using carbon nanotubes, J. Mol. Liq., 277 (2019) 1005–1025.

[66] S. Mallakpour, S. Rashidimoghadam, 9 - Carbon Nanotubes for Dyes Removal, Composite Nanoadsorbents, Micro Nano Technol., Elsevier, (2019) 211-243. http://doi: 10.1016/B978-0-12-814132-8.00010-1.

[67] D.P. Dutta, R. Venugopalan, S. Chopade, Manipulating carbon nanotubes for efficient removal of both cationic and anionic dyes from wastewater, Chem. Select., 2 (2017) 3878–3888.

[68] N, Mozaffari. A, H, S, Mirzahosseini. A, H, Sari. L, F, Aval. Investigation of carbon monoxide gas adsorption on the Al_2O_3/$Pd(NO_3)_2$/zeolite composite film. Journal of Theoretical Appl. Phys., 14 (2019) 65–74.

[69] L. Samain, A. Jaworski, M. Edén, D. M. Ladd, D. K. Seo, F. J. Garcia-Garciad, U. Häussermanna, structural analysis of highly porous γ-Al2O3, J. Solid State Chem., 217 (2014)1–8.

[70] M. Shayesteh, M. S. Afarani, A. Samimi1, M. Khorram, Preparation of γ-Al_2O_3 and prioritization of affecting factors on the crystallite size using taguchi method, Trans. Phenom. Nano Micro Scales, 1 (2013) 45-52.

[71] J. Liu, j. Zhang, H. Zhang, F. Zhang, M. Zhu, N. Hu, X. Chen, H. Kita, Synthesis of hierarchical zeolite T nanocrystals with the assistance of zeolite seed solution, J. Solid State Chem., 285 (2020) 121228.

[72] N. M. Mahmoodi, M. H. Saffar-Dastgerdi, Zeolite nanoparticle as a superior adsorbent with high capacity: Synthesis, surface modification and pollutant adsorption ability from wastewater, Microchem. J., 145 (2019) 74-83.

[73] J.H. Kwak, J. Hu, D. Mei, C.W. Yi, D.H. Kim, C.H. Peden, L.F. Allard, J. Szanyi, Coordinatively unsaturated Al^{3+} centers as binding sites for active catalyst phases of platinum on gamma-Al_2O_3, Sci., 325 (2009) 1670-1673.

[74] S. Arnis, F. Belaib, M. Bencheikh Lehocine, H.-A Menian, Progress in clean energy, analysis and modeling,, Equilbrium and kinetic studies of adsorption of Cd(II), Zn(II), and Cu(II) from aqueous solution into cereal by-products, chapter 4, volume 1, Springer Publishing, (2015). https:// doi: 10.1007/978-3-319-16709-1

[75] D.M. Ruthven, principle of adsorption and desorption process, Wiley, New York, (1984).

[76] S.H. Chien, W.R. Clayton, Application of elovich equation to the kinetics of phosphate release and sorption in soils, Soli Sci. Soc. Am. j., 44 (1980) 265-268.

[77] A.O. Dada, D. F. Latona, O. J. Ojediran, O. O. Nath, Adsorption of Cu (II) onto bamboo supported manganese (BS-Mn) nanocomposite: effect of operational parameters, kinetic, isotherms, and thermodynamic studies, J. Appl. Sci. Environ. Manage., 20 (2016) 409 –422.

[78] S. Karka, S. Kodukula, S. V. Nandury, U. Pal, Polyethylenimine-modified zeolite 13X for CO_2 capture: adsorption and kinetic studies, ACS Omega, 4(2019) 16441 – 16449.

[79] A.A. Inyinbor, F.A. Adekola, G.A. Olatunji, Kinetics, isotherms and thermodynamic modeling of liquid phase adsorption of Rhodamine B dye onto Raphia hookerie fruit epicarp, Water Res. Ind., 15 (2016) 14–27.

[80] Y.S. Ho, G. McKay, Application of kinetic models to the sorption of copper (II) on to peat, Adsorp. Sci. Technol., 20 (2002) 797-815.